



National Library
of Canada

Acquisitions and
Bibliographic Services Branch

395 Wellington Street
Ottawa, Ontario
K1A 0N4

Bibliothèque nationale
du Canada

Direction des acquisitions et
des services bibliographiques

395, rue Wellington
Ottawa (Ontario)
K1A 0N4

Your file Votre référence

Our file Notre référence

NOTICE

The quality of this microform is heavily dependent upon the quality of the original thesis submitted for microfilming. Every effort has been made to ensure the highest quality of reproduction possible.

If pages are missing, contact the university which granted the degree.

Some pages may have indistinct print especially if the original pages were typed with a poor typewriter ribbon or if the university sent us an inferior photocopy.

Reproduction in full or in part of this microform is governed by the Canadian Copyright Act, R.S.C. 1970, c. C-30, and subsequent amendments.

AVIS

La qualité de cette microforme dépend grandement de la qualité de la thèse soumise au microfilmage. Nous avons tout fait pour assurer une qualité supérieure de reproduction.

S'il manque des pages, veuillez communiquer avec l'université qui a conféré le grade.

La qualité d'impression de certaines pages peut laisser à désirer, surtout si les pages originales ont été dactylographiées à l'aide d'un ruban usé ou si l'université nous a fait parvenir une photocopie de qualité inférieure.

La reproduction, même partielle, de cette microforme est soumise à la Loi canadienne sur le droit d'auteur, SRC 1970, c. C-30, et ses amendements subséquents.

UNIVERSITY OF ALBERTA

STRESS INDUCED PERMEABILITY CHANGES
OF ATHABASCA OIL SANDS

BY



KAZIMIERZ OLDAKOWSKI

A thesis submitted to the Faculty of Graduate Studies and Research in partial fulfillment
of the requirements for the degree of MASTER OF SCIENCE
IN
GEOTECHNICAL ENGINEERING

DEPARTMENT OF CIVIL ENGINEERING

Edmonton, Alberta

SPRING 1994



National Library
of Canada

Acquisitions and
Bibliographic Services Branch

395 Wellington Street
Ottawa, Ontario
K1A 0N4

Bibliothèque nationale
du Canada

Direction des acquisitions et
des services bibliographiques

395, rue Wellington
Ottawa (Ontario)
K1A 0N4

Your file Votre référence

Our file Notre référence

The author has granted an irrevocable non-exclusive licence allowing the National Library of Canada to reproduce, loan, distribute or sell copies of his/her thesis by any means and in any form or format, making this thesis available to interested persons.

L'auteur a accordé une licence irrévocable et non exclusive permettant à la Bibliothèque nationale du Canada de reproduire, prêter, distribuer ou vendre des copies de sa thèse de quelque manière et sous quelque forme que ce soit pour mettre des exemplaires de cette thèse à la disposition des personnes intéressées.

The author retains ownership of the copyright in his/her thesis. Neither the thesis nor substantial extracts from it may be printed or otherwise reproduced without his/her permission.

L'auteur conserve la propriété du droit d'auteur qui protège sa thèse. Ni la thèse ni des extraits substantiels de celle-ci ne doivent être imprimés ou autrement reproduits sans son autorisation.

ISBN 0-612-11314-0

Canada

UNIVERSITY OF ALBERTA
RELEASE FORM

NAME OF AUTHOR: KAZIMIERZ OLDAKOWSKI

TITLE OF THESIS: STRESS INDUCED PERMEABILITY
CHANGES OF ATHABASCA OIL SANDS

DEGREE: MASTER OF SCIENCE

YEAR THIS DEGREE GRANTED: SPRING 1994

Permission is hereby granted to the University of Alberta Library to reproduce single copies of this thesis and to lend or sell such copies for private, scholarly or scientific research purposes only.

The author reserves all other publication and other rights in association with the copyright in the thesis, and except as hereinbefore provided neither the thesis nor any substantial portion thereof may be printed or otherwise reproduced in any material form whatever without the author's prior written permission.

Kazimierz Oldakowski

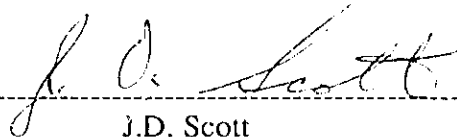
#C412, 17116 - 64 Avenue
Edmonton, Alberta
T5T 2C9

April 19, 1994


UNIVERSITY OF ALBERTA

FACULTY OF GRADUATE STUDIES AND RESEARCH

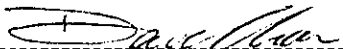
The undersigned certify that they have read, and recommend to the Faculty of Graduate Studies and Research for acceptance, a thesis entitled STRESS INDUCED PERMEABILITY CHANGES OF ATHABASCA OIL SANDS submitted by KAZIMIERZ OLDAKOWSKI in partial fulfillment of the requirements for the degree of MASTER OF SCIENCE in GEOTECHNICAL ENGINEERING.



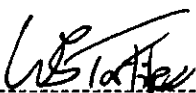
J.D. Scott



D.C. Sego



D. Chan



W.S. Tortike

April 14, 1994

ABSTRACT

This study investigates the influence of stress-induced deformations and porosity changes on changes in the permeability of the Athabasca McMurray Formation oil sands.

The measurements performed on bitumen-free reconstituted oil sands show that the absolute permeability change is a function of porosity change. This function is the same whether the porosity change is caused by isotropic unloading or dilation resulting from shear stresses. The Kozeny and Carman's equation has been found to represent well the experimental absolute permeability - porosity relationship. For the range of porosity changes occurring during testing a linear relationship between absolute permeability and porosity is also proposed.

The measurements made on preserved oil sands cores at the in situ temperature of 8 °C show that the effective permeability to water is mainly a function of water porosity for oil sands expansion caused by isotropic stress relief as well as by shear dilation. A linear semilogarithmic relationship between effective permeability to water and water porosity is formulated for water porosities lower than 15 %. Deviations from this relationship occur for cores containing a high amount of fines.

The mode of oil sands deformations which involve compression in one direction and lateral expansion in the other direction can cause effective permeability to water enhancement even when water porosity does not increase. This type of permeability enhancement ceases to predominate when the specimen volume starts to increase by shear dilation.

ACKNOWLEDGEMENTS

I would first like to acknowledge the support of my supervisor Dr. J.D. Scott who aroused my interest in the subject and provided guidance throughout this research.

The technical assistance provided by Gerry Cyre and Steve Gamble is appreciated.

I would like to express my gratitude to Sam Proskin who readily took part in discussions on many subjects during my work and gave me a lot of encouragement.

Indispensable help in mastering the secrets of the English language was provided by Nathan A. LaRoy for which I am grateful.

The financial support was provided by the Alberta Oil Sands Technology and Research Authority which I greatly appreciate.

Lastly, I would like to thank my wife, Barbara, and our children, Anna and Konrad, to whom this work is dedicated, for understanding and loving support throughout my years of study.

TABLE OF CONTENTS

Chapter	Page
1. INTRODUCTION	
1.1 Statement of Problem	1
1.2 Objective of Thesis	3
1.3 Outline of Thesis	3
2. LITERATURE REVIEW	
2.1 Oil Sands	4
2.1.1 Geology of the Athabasca Oil Sands	4
2.1.2 Characteristics of Athabasca Oil Sands	8
2.1.3 Formation Fluids	8
2.2 Permeability of Oil Sands	11
2.2.1 General	11
2.2.2 Indirect Determination of Permeability	13
2.2.2.1 Use of Indirect Methods for Oil Sands	18
2.2.3 Oil Sands Permeability Reported in Literature	19
2.2.3.1 Sources of Permeability Data	19
2.2.3.2 Reported Oil Sands Permeabilities	21
2.2.4 Factors Affecting Laboratory Measurements of Permeability	21
2.2.5 Effect of Isotropic and Anisotropic Stress Changes on Oil Sands Porosity and Permeability	25
2.3 Summary	29

3.	ABSOLUTE PERMEABILITY OF ATHABASCA MCMURRAY FORMATION OIL SANDS	
3.1	Introduction.....	37
3.2	Experimental Program.....	38
3.2.1	Test Conditions and Stress Paths	38
3.2.2	Grain Size of Sand Specimens	39
3.3	Equipment.....	40
3.3.1	Triaxial Cell and Load Frames.....	40
3.3.2	Pressure Systems	41
3.3.3	Flow System.....	41
3.3.4	Electronic Instrumentation and Data Acquisition System.....	42
3.3.5	Instrument Calibration and Compliance Testing.....	43
3.4	Specimen Preparation.....	43
3.5	Test Procedures	44
3.5.1	Saturation and Isotropic Compression.....	44
3.5.2	Isotropic Stress Change Test	46
3.5.3	Shear Stress Change Tests.....	46
3.5.3.1	Triaxial Compression Strain-Controlled Test.....	46
3.5.3.2	Triaxial Compression Stress-Controlled Test	47
3.5.3.3	Anisotropic Unloading Test	47
3.6	Results.....	48
3.6.1	Degree of Saturation and Compressibility.....	48
3.6.2	Absolute Permeability and Volume Changes	49
3.6.2.1	Isotropic Unloading	51
3.6.2.2	Triaxial Shear.....	51

3.7	Discussion	54
3.7.1	Volume Changes	54
3.7.2	Absolute Permeability	55
3.7.2.1	Initial Permeability of Specimens	55
3.7.2.2	Extrapolation from Laboratory Tests to Reservoir Conditions.....	57
3.7.2.3	Permeability Changes Caused by Isotropic and Shear Stress Changes.....	58
3.7.2.4	Calculations of Change in Absolute Permeability for Reservoir Modeling.....	59
3.7.2.5	Comparison with Other Experimental Works	62
3.7.3	Shear Strength.....	64
3.8	Summary.....	67
3.8.1	Observations	67
3.8.2	Conclusions.....	68
4.	EFFECTIVE PERMEABILITY TO WATER - TEST PROCEDURES AND RESULTS	
4.1	Introduction	94
4.2	Testing Program	95
4.2.1	Stress Paths.....	96
4.2.2	Tested Material	97
4.2.3	Equipment.....	99
4.3	Specimen Preparation and Mounting in Triaxial Cell	99
4.4	Index Testing.....	100
4.5	Experimental Procedures and Results.....	102
4.5.1	Specimen Saturation and Isotropic Compression.....	102

4.5.2	Isotropic Unloading, Stress Path A_p and A_u	103
4.5.3	Triaxial Compression Tests, Stress Paths B_σ and B_ϵ	105
4.5.4	Confining Stress Unloading Tests, Stress Path G_p and G_u	109
4.5.5	Constant p' Tests, Stress Path D_p and D_u	114
4.6	Summary	117
5.	EFFECTIVE PERMEABILITY TO WATER - DISCUSSION OF TEST RESULTS	
5.1	Specimen Saturation and Compressibility	139
5.2	Volume Changes.....	141
5.2.1	Isotropic Unloading Tests	142
5.2.2	Triaxial Shear Tests	143
5.3	Effective Permeability to Water	145
5.3.1	Bitumen Mobility	145
5.3.2	Influence of Fines on Permeability	146
5.3.3	Initial Permeability of Oil Sand Cores.....	147
5.3.4	Isotropic Unloading	150
5.3.5	Triaxial Shear Tests	151
5.3.5.1	Effect of Stress Path on Effective Permeability to Water.....	152
5.3.5.2	Effect of Water Porosity on Effective Permeability to Water.....	153
5.3.6	Comparison with Other Experimental Works	154
5.3.6.1	Triaxial Shear Test on Oil Sands	154
5.3.6.2	Absolute Permeability Versus Porosity and Effective Permeability to Water Versus Water Porosity.....	155
5.3.6.3	Effective Permeability to Water Versus Water Saturation.....	157

5.4	Shear Strength of Athabasca McMurray Formation Oil Sands.....	158
5.5	Summary	160
5.5.1	Observations	160
5.5.2	Conclusions	162
6.	SUMMARY AND CONCLUSIONS	
6.1	Factors Affecting Permeability of Oil Sands	177
6.2	Experimental Apparatus and Procedures	178
6.3	Absolute Permeability of Athabasca Oil Sands	179
6.4	Effective Permeability to Water of Athabasca McMurray Formation Oil Sands	180
6.5	Shear Strength of Athabasca Oil Sands	182
6.6	Suggestions for Future Work	182
	REFERENCES	184
	APPENDIX A - Initial Tests on Oil Sand Cores, Stress Path Bσ	193
	APPENDIX B - Frictionless Porous Stones.....	202
	APPENDIX C - Effect of Rubber Membrane on Triaxial Test Results.....	207
	APPENDIX D - Bitumen Mobility During Testing	212
	APPENDIX E - Compression Curves for Specimens S19 to S23	217
	APPENDIX F - Grain Size Analysis	221

LIST OF TABLES

Table	Page
2.1 Various Sources of Permeability Estimation	32
2.2 Permeability Data Reported in Literature for Alberta Oil Sands	33
3.1 Specimen Data - Series PI.....	70
3.2 Specimen Conditions After Consolidation	71
3.3 Isotropic Unloading Test Results	72
3.4 Compression Shear Test Results.....	73
3.5 Anisotropic Unloading Test Results	73
4.1 Specimen Initial Conditions	119
4.2 Isotropic Unloading After Consolidation Under 5.6 to 6.0 MPa	120
4.3 Specimen Conditions at the Beginning of Shear Tests.....	121
4.4 Triaxial Shear Test Results	122
4.5 Grain Size Distribution Data	123
D.1 Bitumen Mobility Analysis	215

LIST OF FIGURES

Figure	Page
2.1 Geology of Athabasca Oil Sands at UTF Site (Phase A).....	36
3.1 Stress Paths Followed During Triaxial Tests on Reconstituted Oil-Free Oil Sands Specimens	74
3.2 Grain Size Distributions - PI Specimens	75
3.3 Grain Size Distributions - Sn-D and Ss-D Specimens.....	75
3.4 Schematic Diagram of the Triaxial System for Permeability Measurement	76
3.5 Volume Change During Isotropic Unloading.....	77
3.6 Absolute Permeability - Volume Change, Isotropic Unloading	77
3.7 Volume Change During Isotropic Unloading.....	78
3.8 Absolute Permeability - Volume Change, Isotropic Unloading	78
3.9 Absolute Permeability - Porosity, Isotropic Unloading	79
3.10 Absolute Permeability - Porosity, Isotropic Unloading	79
3.11 Stress Path B_{ϵ} , Volume Change	80
3.12 Stress Path B_{σ} , Volume Change	80
3.13 Stress Path F_u , Volume Change	81
3.14 Volume Change During Anisotropic Unloading.....	81
3.15 Stress Path B_{ϵ} , Absolute Permeability - Volume Change.....	82
3.16 Stress Path B_{ϵ} , Absolute Permeability - Porosity.....	82
3.17 Stress Path B_{σ} , Absolute Permeability - Volume Change	83
3.18 Stress Path B_{σ} , Absolute Permeability - Porosity.....	83
3.19 Stress Path F_u , Absolute Permeability - Volume Change	84
3.20 Stress Path F_u , Absolute Permeability - Porosity	84
3.21 Initial Absolute Permeability of Oil-Free Reconstituted Oil Sand Specimens.....	85

3.22	Isotropic Test Results Compared with Kozeny and Carman's Theory	86
3.23	Shear Test Results Compared with Kozeny and Carman's Theory	86
3.24	Absolute Permeability Change - Porosity Change, Isotropic Unloading.....	87
3.25	Absolute Permeability Change - Porosity Change, Triaxial Shear	87
3.26	Absolute Permeability Change - Porosity Change, Comparison	88
3.27	Stress Path $B\varepsilon$, Stress Ratio - Axial Strain.....	89
3.28	Stress Path $B\varepsilon$, Deviatoric Stress - Axial Strain.....	89
3.29	Stress Path $B\sigma$, Stress Ratio - Axial Strain	90
3.30	Stress Path $B\sigma$, Deviatoric Stress - Axial Strain	90
3.31	Stress Path $B\varepsilon$, Failure Envelope	91
3.32	Stress Path $B\sigma$, Failure Envelope.....	91
3.33	Stress Path F_u , Effective Stress Ratio.....	92
3.34	Stress Path F_u , Failure Envelope	92
3.35	Failure Envelope for Oil-Free Reconstituted Oil Sand Specimens	93
4.1	Stress Paths Followed During Triaxial Tests on Oil Sands Core	124
4.2	Stress Paths A_p and A_u , Volume Change - Effective Confining Stress	125
4.3	Stress Paths A_p and A_u , Effective Permeability to Water - Volume Change....	125
4.4	Stress Paths A_p and A_u , Effective Permeability to Water - Water Porosity	126
4.5	Stress Path $B\varepsilon$, Stress Ratio - Axial Strain	127
4.6	Stress Path $B\varepsilon$, Deviatoric Stress - Axial Strain	127
4.7	Stress Path $B\varepsilon$, Volume Change - Axial Strain	128
4.8	Stress Path $B\varepsilon$, Failure Envelope.....	128
4.9	Stress Path $B\varepsilon$, Effective Permeability to Water - Volume Change.....	129

4.10	Stress Path B _e , Effective Permeability to Water - Water Porosity	129
4.11	Stress Path G _p , Effective Stress Ratio - Axial Strain	130
4.12	Stress Path G _p , Deviatoric Stress - Axial Strain	130
4.13	Stress Path G _p , Volume Change - Axial Strain.....	131
4.14	Stress Path G _p , Failure Envelope	131
4.15	Stress Path G _p , Effective Permeability to Water - Volume Change	132
4.16	Stress Path G _p , Effective Permeability to Water - Water Porosity	132
4.17	Stress Path G _u , Effective Stress Ratio - Axial Strain	133
4.18	Stress Path G _u , Deviatoric Stress - Axial Strain.....	133
4.19	Stress Path G _u , Volume Change - Axial Strain.....	134
4.20	Stress Path G _u , Failure Envelope	134
4.21	Stress Path G _u , Effective Permeability to Water - Volume Change	135
4.22	Stress Path G _u , Effective Permeability to Water - Water Porosity	135
4.23	Stress Paths D _p and D _u , Effective Stress Ratio - Axial Strain	136
4.24	Stress Paths D _p and D _u , Deviatoric Stress - Axial Strain.....	136
4.25	Stress Paths D _p and D _u , Volume Change - Axial Strain	137
4.26	Stress Paths D _p and D _u , Stress Envelope	137
4.27	Stress Paths D _p and D _u , Effective Permeability to Water - Volume Change....	138
4.28	Stress Path D _p and D _u , Effective Permeability to Water - Water Porosity	138
5.1	Saturation of Specimens by Pore Pressure Increase.....	164
5.2	Relation Between Pore Pressure Parameter B and Compressibility of Oil Sands Core.....	164
5.3	Isotropic Compressibility of Oil Sands Specimens (Unloading Phase).....	165
5.4	Isotropic Compressibility of Oil Sands Specimens - Curve Fit (Unloading Phase).....	165
5.5	Volume Change During Isotropic Unloading, S19-S23	166

5.6	Pore Volume Change During Isotropic Unloading	166
5.7	Volume Change During Triaxial Shear.....	167
5.8	Pore Volume Change During Triaxial Shear	167
5.9	Effect of Water Porosity on Initial Effective Permeability to Water	168
5.10	Effect of Fines Content on Initial Effective Permeability to Water.....	168
5.11	Effect of Isotropic and Triaxial Shear Volume Changes on Effective Permeability	169
5.12	Increase in Effective Permeability Caused by Deformation During Specimen Contraction.....	169
5.13	Effect of Water Porosity on Effective Permeability to Water During Isotropic and Shear Tests.....	170
5.14	Effective Permeability to Water of Oil Sands Cores Compared to Absolute Permeability Test Results.....	171
5.15	Comparison of Experimental Results with Numerical Model	172
5.16	Failure Envelope for Athabasca McMurray Formation Oil Sands	173
5.17	Stress Path B ϵ in p' - q Stress Field.....	174
5.18	Stress Path B ϵ and A, Void Ratio - Mean Effective Stress	174
5.19	Stress Paths D and G in p' - q Stress Field.....	175
5.20	Stress Paths D and G, Void Ratio - Mean Effective Stress.....	175
5.21	Effective Stress Ratio at Failure Versus Effective Confining Stress.....	176
A.1	Stress Path B σ , Volume Change - Axial Strain.....	197
A.2	Stress Path B σ , Deviatoric Stress - Axial Strain.....	197
A.3	Stress Path B σ , Volume Change - Axial Strain.....	198
A.4	Stress Path B σ	198
A.5	Stress Path B σ , Effective Permeability to Water - Water Porosity.....	199

A.6	Stress Path B σ , Effective Permeability to Water - Volume Change.....	199
A.7	Volume Change During Isotropic Compression	200
A.8	Shape of Specimens S1 and S2 After Failure	201
B.1	Assembly of Frictionless Porous Stones	205
B.2	Dimensions of Specimen S4 After Test as an Example of Specimen Deformations with Conventional Porous Stones	206
B.3	Schematic Diagram of Specimen S5 with Frictionless Porous Stones After Failure.....	206
C.1	Measurement of Extension Modulus of Rubber Membrane	209
C.2	Calculation of Confining Pressure Correction	210
C.3	Rubber Membrane Extension Test, 0.67 mm thick.....	211
C.4	Rubber Membrane Extension Test, 0.28 mm thick.....	211
D.1	Relationship Between Water Content and Amount of Fines Measured on Trimmings.....	216
D.2	Comparison of Amount of Fines Measured on Trimmings and Specimens	216
E.1	Isotropic Unloading and Recompression, Specimen S19	218
E.2	Isotropic Compression and Unloading, Specimen S20.....	218
E.3	Isotropic Compression and Unloading, Specimen S21.....	219
E.4	Isotropic Compression and Unloading, Specimen S22.....	219
E.5	Isotropic Compression and Unloading, Specimen S23.....	220
F.1	Grain Size Distribution, Specimens S1 and S2	222
F.2	Grain Size Distribution, Specimens S3 - S5	222
F.3	Grain Size Distribution, Specimens S6 - S8	223
F.4	Grain Size Distribution, Specimen S9	223
F.5	Grain Size Distribution, Specimens S10 and S11	224
F.6	Grain Size Distribution, Specimens S12 and S13	224

F.7	Grain Size Distribution, Specimens S14 and S15	225
F.8	Grain Size Distribution, Specimens S16 - S18	225
F.9	Grain Size Distribution, Specimens S19 and S20	226
F.10	Grain Size Distribution, Specimens S21 and S22	226
F.11	Grain Size Distribution, Specimen S23	227

LIST OF SYMBOLS

A, A_0, A_1, A_2, A_v	constants
A_s	cross-sectional area, m^2
a	constant
a_s	piston cross-sectional area, m^2
B	pore pressure parameter relating pore pressure response with total confining stress change
b	constant
B_0, B_1, B_2, B_v	constants
C	shape factor representing the composite effect of the pore shape and the surface roughness of the grains (Kozeny and Carman equation)
C, C_0, C_1, C_2	constants
c_b	compressibility of bitumen
c_s	compressibility of oil sands structure or matrix
$c_w = 0.46 \cdot 10^{-6} \text{ kPa}^{-1}$	compressibility of water
Da	experimentally obtained coefficient
d	average diameter of grains
e	void ratio
F	finer content, %
$f_1(d)$	function indicating the effect of grain size on permeability
$f_2(\phi)$	function indicating the effect of porosity on permeability
g	gravitational acceleration, $g=9.81 \text{ m/s}^2$
H	Henry's constant

(h_2-h_1)	difference between outlet and inlet fluid heads, m
$i = (h_2-h_1)/l$	hydraulic gradient in the direction of flow
K	coefficient of permeability (hydraulic conductivity), m/s
$K'=(\sigma_3-u)/(\sigma_1-u)$	effective stress ratio
k	absolute permeability, $m^2, \mu m^2$
k_i	in situ permeability, μm^2
k_o, k_1	initial permeability, μm^2
k_2	increased permeability, μm^2
k_{ew}	effective permeability to water, μm^2
$k_{rw} = k_{ew}/k$	relative permeability to water
k_{ro}	relative permeability to oil
l	distance in the direction of flow, m
m	constant
N	piston load, N
n	constant
p	pressure, Pa
$p' = (\sigma_1' + \sigma_2' + \sigma_3')/3$	mean principal effective stress
Q	flow rate, m^3/s
$q = \sigma_1 - \sigma_3 = \sigma_1' - \sigma_3'$	deviatoric stress
S_o	initial degree of saturation
S_w	water saturation ratio
S_{wi}	irreducible water saturation
$s' = (\sigma_1' + \sigma_3')/2$	parameter used in MIT (Massachusetts Institute of Technology) stress path plot
$t = (\sigma_1 - \sigma_3)/2$	parameter used in MIT stress path plot
u	pore pressure

u_a	initial absolute pressure, Pa
u_s	saturation pressure, kPa
V_{po}	initial volume of pores
V_o	initial total volume of specimen
$v = Q/A_s$	average flow velocity, m/s
z	vertical location, m
α	constant
β	constant
Δp	differential pressure across flow section (pressure drop), Pa
Δu	pore pressure change
$\Delta V/V_{po} = \epsilon_{vp}$	pore volume change
$\Delta V/V_o = \epsilon_v$	volume change
$\Delta \sigma$	confining pressure (cell pressure) change
ϵ_v	volumetric strain
ϵ_{vp}	pore volume change
κ	constant
μ	dynamic viscosity of fluid, Pa•s
μ_w	dynamic viscosity of water, Pa•s
$\sigma' = (\sigma'_1 + 2\sigma'_3)/3$	mean principal effective stress for triaxial cell conditions
$\sigma_1, \sigma_2, \sigma_3$	principal total stresses
$\sigma'_1, \sigma'_2, \sigma'_3$	principal effective stresses
$\sigma_1 = \sigma_v$	vertical total stress, Pa
$\sigma_3 = \sigma_2 = \sigma_h$	horizontal total stress in triaxial cell
$\sigma'_3 = \sigma_3 - u$	effective confining stress
ρ	fluid density, kg/m ³
ρ_w	density of water, kg/m ³

ϕ	porosity = volume of pores/total volume of specimen
ϕ_i	in situ porosity
ϕ_o, ϕ_1	initial porosity
ϕ_2	increased porosity
ϕ_b	bitumen porosity = volume of bitumen/total volume of specimen
ϕ_w	water porosity = volume of water/total volume of specimen
ϕ'	angle of shearing resistance

Chapter 1. INTRODUCTION

1.1 Statement of Problem

The vast majority of Alberta oil sand deposits are buried too deep to be exploited with open-pit mining operations; this necessitates the use of in situ extraction technology. Because the viscosity of the bitumen contained in the oil sands is high ($>10^6$ mPa·s in Athabasca), the bitumen is practically immobile under natural conditions. However, viscosity declines exponentially with increases in temperature, so that technology can enhance bitumen mobility by injecting hot fluid into an oil sands formation. Hot bitumen flows more readily into production wells as the result of gravity or the combined effect of gravity and steam drag.

The injection of steam or water into a formation at high temperatures and pressures changes the initial state of stresses not only by increasing pore pressure but also through thermal expansion of the sand structure. These changes, in turn, result in deformations and an increase in pore volume and permeability, not only in the zone of increased temperature but also in the cold reservoir in front of the advancing steam chamber. Some applied technologies intentionally disturb the sand matrix by increasing injection pressure above the minimum total stress, causing formation fracture, in order to obtain communication channels between the injection and production wells. The development of the fracture by fluid injection reduces the effective stress along fracture walls to a very low value, bringing about sand shear failure and shear dilation, and hence an increase in porosity and permeability. The interpenetrative grain structure characteristic of oil sands, with its peculiar grain to grain contacts, once disturbed, cannot be reinstated, with the result that porosity will not return to its initial state upon pore pressure decrease.

The shear deformations and porosity enhancement, as induced by extraction processes, may be beneficial for bitumen recovery through increasing absolute permeability or increasing effective permeability to water, thus enhancing the propagation of hot fluid into the formation. Taking these permeability changes into account can help provide reasonably accurate predictions of bitumen production rates through the mathematical modeling of the reservoir.

Difficulties in restoring the initial porosity of disturbed oil sands poses problems in terms of obtaining laboratory permeability measurements that would be representative of oil sands under in situ conditions. Laboratory measurements are conducted on cores which are always disturbed, to some degree, during drilling by confining stress reduction, pore pressure relief, and gas evolution. Laboratory permeability values need to be extrapolated to reservoir conditions.

The types of problems addressed in this research can be summarized as:

- Evaluating the magnitude of the volumetric changes of oil sands under stress conditions encountered in reservoir engineering practice (including at very low effective confining stresses).
- Finding relationships between oil sands volumetric deformations and changes in the absolute permeability or effective permeability to water.
- Demonstrating methods of extrapolation of permeability values obtained in the laboratory to reservoir conditions.
- Investigating whether deformations alone can enhance effective permeability to water.

1.2 Objective of Thesis

The main objective of this thesis is to investigate the influence of stress-induced deformations and porosity changes on changes in the permeability of the Athabasca McMurray Formation oil sands. The testing program is divided into two major parts:

1. Investigation of changes in absolute permeability in response to deformations resulting from different stress paths. The tests were performed in a triaxial cell on bitumen-free reconstituted Athabasca McMurray Formation oil sands at room temperature (23 °C).
2. Investigation of changes in effective permeability to water in response to deformations induced by different stress paths. The tests were performed in a triaxial cell on Athabasca McMurray Formation oil sands cores from the Underground Test Facility Phase A Pilot site at the in situ temperature of 8 °C.

The investigation of the relationships between deformation and permeability change are conducted in the context of the stress paths followed and the fines content of the oil sands.

The secondary objective of this research is to investigate the stress-strain relationship of tested specimens and evaluate the strength of bitumen-free reconstituted oil sands and Athabasca McMurray Formation oil sands cores.

1.3 Organization of Thesis

A review of the literature pertaining to the subject of this research constitutes Chapter 2. Geological background, oil sand structure and composition, formation fluids and their distribution, data on oil sands permeability, and factors affecting laboratory permeability measurements are presented in this chapter.

Chapter 3 describes the procedures and results of the triaxial tests, which follow three different effective stress paths, performed on bitumen-free Athabasca oil sands. The test results are discussed and a relationship is formulated between absolute permeability and changes in porosity caused by isotropic stress reduction and by shear dilation of the sand. An equation allowing for the extrapolation of laboratory initial absolute permeability results to in situ conditions is presented. The testing equipment adopted for the whole study is also described in this chapter.

Chapter 4 describes a series of triaxial tests performed on preserved oil sands core material at in situ temperatures. Measurements of stresses, stress induced deformations, and changes in permeability to water during testing over four different effective stress paths are presented.

Chapter 5 contains discussion and analysis of the results of the tests described in Chapter 4. An equation has been formulated relating changes in the effective permeability to water to the water porosity changes resulting from isotropic stress reduction and by shear dilation. The same equation can be used to extrapolate laboratory measurements of the initial permeability of oil sands cores to reservoir conditions. Permeability changes induced only by deformation and not associated with an increase in porosity are also shown.

Chapter 6 concludes with a final summary of the major findings of this research program.

Chapter 2. LITERATURE REVIEW

2.1 Oil Sands

2.1.1 Geology of the Athabasca Oil Sands

The Athabasca Deposit is the richest of the Alberta bitumen reservoirs. It contains $212 \cdot 10^9 \text{ m}^3$ of bitumen in three different geologic horizons: the McMurray/Wabiskaw, Grand Rapids and Grosmont/Nisku formations. The majority of recoverable reserves is contained in the Lower Cretaceous sands of the McMurray Formation and the Wabiskaw Member of the Clearwater Formation; $114 \cdot 10^9 \text{ m}^3$ of bitumen is spread over an area of 46800 km^2 with a mean thickness of 34 m (Wightman et al., 1989). The thicknesses of overburden ranges from 0 to 750 m. The Suncor and Syncrude open-pit mining operations are situated in the northern portion of the Athabasca region where the McMurray Formation lies closest to the surface. It has been estimated that only about 10 % of Athabasca oil sands deposits are surface-mineable; thus the vast majority of Alberta bitumen will be recovered by means of in situ extraction technology.

The McMurray Formation rests unconformably on the Upper Devonian Waterways Formation consisting of interbedded shales and limestones. The McMurray Formation is usually subdivided into three stratigraphic units (lower, middle and upper member) to reflect changes in the environment during deposition (Mattison, 1987). These environments, as a result of rising sea level, range from continental, fluvial, and floodplain environments to a shoreline estuarine complex (channels, point bars), (Mossop, 1980; Wightman et al., 1989). The McMurray Formation is overlain by Wabiskaw sands of the Clearwater Formation, which were deposited during transgression of the Clearwater Sea from the north. The rest of the Clearwater Formation

is made up of thick marine shales which, in turn, are capped by sands and shales of the Grand Rapids Formation. Thin Quaternary deposits comprise gravels and tills.

The geologic profile illustrating stratigraphy at the AOSTRA Underground Test Facility (UTF) located 50 km northwest of Fort McMurray is shown in Figure 2.1. Cores from wells at this site were used in laboratory tests designed for effective permeability to water measurements under changing stress conditions. The lower McMurray member is absent here and the middle member rests on the Devonian limestone at a depth of 163 m. The McMurray Formation consists of mixed oil sands and shales, approximately 37 m thick. The stratigraphic section of the formation was informally divided into 6 units, denoted alphabetically from B to G (Rottenfusser et al., 1988), each displaying differences in lithology, porosity, and bitumen and water saturation. The thickness of these units vary within the UTF reservoir.

Unit B, directly underlying the Wabiskaw sands, has a thickness of about 7 m. It consists of soft shales mixed with sand, in proportions of 65 % and 35 %, respectively. The sand fills horizontal burrows and sometimes creates sand lenses. The unit average porosity is 31.8 % and average water saturation is 77 %.

Unit C varies in thickness from 4 m to 7 m. It consists of fine to medium grained sands interbedded with shales. The average proportion of oil sand and shale is 70 % and 30 %, respectively. Breccias of angular shale fragments and thin cemented sandstone layers are often found in this unit. Average porosity for unit C is 32.4 %. Water saturation varies broadly from 35 % to 12.5 %. Bitumen content ranges from 2.9 % to 6.0 % of the total mass. Units C and B originated in a marine environment.

Unit D ranges in thickness from 6.2 m to 10.4 m. It consists of dark brown bitumen-saturated oil sands interbedded with light brown shale laminae. Cemented sands and shale breccias are present within the unit. The average content of oil sands and shales is 80 % and 20 %. Average porosity is 33 % and average water saturation is 28 %.

Bitumen content ranges from 5.1 % to 10.9 %. The unit was deposited along the channel margins.

Unit E and Unit G are of the same origin. They were deposited in tidal channels. Unit E varies from 5.6 m to 10.9 m in thickness and unit G from 3.3 m to 6.3 m. Unit E consists of rich oil sands and layers of shale breccia composed of shale fragments varying in diameter from less than 1 mm to 6 cm, suspended in an oil sand matrix. The average proportional content of this unit is 90 % oil sand and 10 % shale. Average porosity is 31 % and average water saturation is 13 %. Bitumen content varies from 9.0 % to 13.0 %. The lithology and thickness of unit G is more variable, within the reservoir, compared to other units. Bitumen content of unit G ranges from 1.8 % to 12.5 %.

Unit F is composed mostly of shales (70 %) and oil sands (30 %). The shales were deposited in a brackish swamp. Unit F separates units E and G, both bitumen rich.

In the above descriptions, porosity was calculated as an average value derived from neutron and density logs, without any shale correction. The water saturation derived from logs was shown as a percentage of pore space occupied by water. The calculated values represent the average for each unit. Because water is not uniformly distributed (for example, it fills all pore spaces in shales), water saturation is lower for pure oil sands. It can be as low as 6 % (1 % of the total mass). The bitumen contents were presented as a percentage of the total oil sands mass. The richest oil sands were deposited at the lower part of the McMurray Formation at the UTF. They are composed of medium to fine grained, well-sorted sands. Moving upward from this point, the average grain size decreases as the deposition of very fine-grained sands, sandy silts, silts and clays becomes heavier.

2.1.2 Characteristics of Athabasca Oil Sands

The mineralogy of the Athabasca oil sands from the McMurray Formation is usually characterized as extremely mature and stable. Generally, rich oil sands consist of approximately 95 % quartz, 2 to 3 % feldspar, 2 to 3 % mica and clay minerals, and traces of other minerals (Mossop, 1980). The clay fraction in units D and E is 45 % illite and 55 % kaolinite at the UTF (Rottenfusser et al., 1989). Quartz grains are mainly sub-angular and sub-rounded. Grain surfaces display a rugose texture, solution concavities, and recrystallization overgrowth (Dusseault and Morgenstern, 1979). Coarser grains of oil sands tend to be smoother than the finer grains. The grain to grain contact area is large, and there are large numbers of concavo-convex contacts. The interpenetrative structure of the Athabasca oil sands developed during the time of burial due to diagenesis in the form of dissolution and recrystallization of quartz at grain boundaries. This structure is responsible for higher shear strength, smaller strain at failure, and higher rates of dilation, compared to younger Quaternary sand deposits with similar mineralogy and porosity.

2.1.3 Formation Fluids

Three types of fluids can occupy pore space in the oil sands reservoirs: bitumen, water and gas. The gas in a free state appears only under special circumstances (i.e., when pore pressure is lowered below gas saturation pressure). The gas in oil sand formations in natural conditions is usually dissolved in the bitumen with a small amount in the water. Occasionally gas pockets are found trapped beneath thick shale strata.

It is generally accepted that the bitumen invaded the presently occupied areas from distant sources when it had the consistency of a lighter hydrocarbon. Following this migration, the bitumen underwent in situ degradation, increasing bitumen viscosity to its

present level (Wightman et al., 1989). Migrating into the McMurray Formation, crude oil displaced water from pore spaces, entering only areas from which water could be easily drained. As a result, some areas within the formation remained unsaturated with bitumen, for instance, where permeability was especially low (in shale) or where water was trapped before it could drain.

Water contained in an oil sand reservoir can be divided into different types, each with a distinctive chemical composition (Gunter and Bird, 1989):

1. Water found at the base of oil sand deposits (absent at UTF).
2. Water occurring in isolated pockets of high water saturation within the oil-saturated zone.
3. Water contained within shale beds and trapped because of the low permeability of the shales. Composition can differ substantially from that of other types of water.
4. Water contained within shale stringers. Composition can differ from that of water contained in shale beds. Shale beds can have contact with sources beyond the reservoir.
5. Water remaining in the oil-saturated zone, known as connate or irreducible water.

In bitumen rich oil sands, the irreducible water content is about 2 % of total oil sand mass. In this experimental program, measurements as low as 1.1 % were encountered. If the porosity of an oil sand equals 33 %, irreducible water occupies only about 12 % of the pore space. The remainder of pore space is filled with bitumen. In leaner oil sands, water content is significantly higher. A direct relationship was observed between water content and the amount of fine particles (smaller than 45 μm). The higher the fines content, the higher the water saturation and the lower the bitumen saturation. Several structural models were created by researchers to explain the mutual arrangement of sand grains, fines, water and bitumen in oil sands (Cottrell, 1963; Dusseault and Morgenstern, 1978; Mossop, 1980; Takamura, 1982). In the most advanced model

proposed by Takamura, all quartz grains are in direct contact with one another, creating a stable framework, but the fine particles occur in isolated clusters within that framework, rather than adhering directly to grain surfaces, as in Dusseault and Morgenstern's model. Such an arrangement provided a better explanation of the direct relationship between water content and fines content. In Takamura's model, the connate water, as an irreducible wetting phase, occurs in three configurations:

1. Pendular rings surrounding particle to particle contact points.
2. Water film surrounding quartz grains and separating them from bitumen.
3. Water saturating isolated clusters of fine particles, the amount of which varies with fines content and their mode of distribution.

Thickness of the water film is stabilized principally by double-layer repulsive forces acting between charged surfaces of sand and bitumen. In cases where sand surfaces are covered with clay mineral precipitates, clay particles are also covered by the water film because their zeta potentials are close to that of quartz in NaCl solution, as encountered in oil sands. The water film thickness is less than 15 nm (as calculated by Takamura), so that permeability through this layer can be considered negligible. The volume of water contained in the water film represents less than 0.05 % of pore volume. In high grade oil sands, the amount of fine clusters is small and the pore space is filled mostly with bitumen and water. Water occupies usually between 10 % and 15 % of pore space. Pendular rings cover around 30 % of the sand surface while the remaining 70 % is covered with water film. When water saturation increases, pendular rings expand until a continuous wetting phase is formed. This state is referred to as equilibrium saturation to the wetting phase. At even higher levels of water saturation, the flow of the wetting phase becomes possible; such saturation is called funicular (Bear, 1972, p.444).

The above description is an idealization of the real situation. In practice, the distribution of the pendular rings on grain surfaces is irregular and many contacts

between them can occur at a much lower saturation. Moreover, the applied differential pressure during permeability tests can push bitumen aside at water channel throats and help open paths for flowing water. Even at low in situ temperatures (8 °C at the UTF), bitumen is still a fluid, although one of very high viscosity (up to 10^7 mPa·s after Peacock, 1988); however, under pressure, it can deform slowly with time. Changes in effective permeability to water with changes in water saturation are expected to be rather smooth and they can be dependent on time and on differential pressure magnitude.

2.2 Permeability of Oil Sands

2.2.1 General

The term "permeability" is usually defined as the ability of a porous medium to conduct fluids. When fluid flowing through the porous medium fully saturates it, this is referred to as the absolute permeability of the medium. If more than one fluid type is present and the fluids are immiscible, the concept of effective permeability is utilized.

The equation used to describe the flow of a fluid through a porous medium was formulated on the basis of observations made by French engineer Henry P. Darcy in 1856. He observed that, under steady-state conditions of water flow through beds of sand, the rate of flow was always proportional to the hydraulic gradient:

$$v = -K(h_2 - h_1)/l \quad 2.1$$

where: $v = Q/A_s$ - average flow velocity, m/s

Q - flow rate, m³/s

A_s - cross-sectional area, m²

$(h_2 - h_1)/l = i$ - hydraulic gradient in the direction of flow

l - distance in the direction of flow, m

$(h_2 - h_1)$ - difference between outlet and inlet fluid heads, m

K - coefficient of permeability (hydraulic conductivity), m/s

The constant of proportionality K , called the coefficient of permeability, is a function of both soil and fluid properties. In more general form, Darcy's law for the laminar flow of an incompressible fluid in an arbitrary direction l , within an isotropic incompressible medium, can be written as:

$$Q = -(kA_s/\mu)(dp/dl + \rho g dz/dl) \quad 2.2$$

where: μ - dynamic viscosity of the fluid, Pa·s

ρ - fluid density, kg/m³

g - gravitational acceleration, $g = 9.81 \text{ m/s}^2$

p - pressure, Pa

z - vertical location, m

k - absolute permeability, m²

The constant of proportionality k in Equation 2.2 is called absolute permeability or simply the permeability of a porous medium. Assuming there is no reaction between fluid and rock, permeability is a function only of the pore structure of the medium. The unit of permeability in the SI system is m² or μm^2 and in the cgs system is the darcy or millidarcy. The relationship between these units is defined as:

$$1\text{d} = 1000\text{md} = 0.987 \cdot 10^{-12} \text{ m}^2 = 0.987 \mu\text{m}^2$$

The absolute permeability of soils and rocks can assume an extremely wide range of values (from $10^5 \mu\text{m}^2$ for coarse gravel to $10^{-8} \mu\text{m}^2$ for shale); this explains why permeability is so sensitive to differences in the state of the granular medium. "With sands even a slight change in the void ratio or the washing-out of a portion of the fine

fraction may substantially impair the results of the permeability test" (Kezdi, 1974, p. 134).

In oil sands, pores are filled with two or more fluids; hence the concept of effective permeability finds an application. Effective permeability to a fluid is a measure of the ability of a porous medium to conduct that fluid when two or more fluid types are present in the void space. Each fluid phase has its own effective permeability. Effective permeability is a function of the degree of saturation and of the properties of the rock and fluid, including initial pore-system geometry, fluid distribution within the system, and physico-chemical interaction of the mineral grains and the pore fluids. By analogy to Equation 2.2, the effective permeability to water (k_{ew}) can be expressed in the equation:

$$Q_w = - (k_{ew} A_s / \mu_w) (dp_w/dl + \rho_w g dz/dl) \quad 2.3$$

The effective permeability is often presented as a relative permeability, which is defined as the ratio of the effective permeability at a given saturation to the effective permeability at 100 % saturation (absolute permeability). The relative permeability to water (k_{rw}) can be calculated from the equation:

$$k_{rw} = k_{ew} / k \quad 2.4$$

The relative permeability to a fluid is usually plotted versus degree of saturation of that particular fluid.

2.2.2 Indirect Determination of Permeability

Darcy's law is utilized to calculate permeability on the basis of the direct measurement, in field or laboratory tests, of all the variables appearing in Equations 2.2 or 2.3. In the absence of direct measurements, several empirical formulas have been

proposed to estimate permeability when porosity and grain size distribution are known. To develop these formulas, flow in a real soil matrix is represented by various models (capillary tube models, fissure models, hydraulic radius models, resistance to flow models, and statistical models). Bear (1972) provides a review of these models. The characteristics of these models were briefly described by Rajani (1988).

All formulas for permeability calculation may be expressed in the following general form:

$$k = C \cdot f_1(d) \cdot f_2(\phi) \quad 2.5$$

where: C - shape factor representing the composite effect of the pore shape and the surface roughness of the grains

$f_1(d)$ - function indicating the effect of grain size

d - average diameter of grains

$f_2(\phi)$ - function indicating the effect of porosity

ϕ - porosity

The formula which has been found particularly applicable for sandy and silty soils takes the form:

$$k = C \cdot d^2 \cdot \phi^3 / (1 - \phi)^2 \quad 2.6$$

This formula was developed by Kozeny and Carman on the basis of the model which considers soil to be a bundle of capillary tubes with a common hydraulic radius. Since the capillary tube model is a simplified scheme for depicting porous media, it often cannot take into account the influence on permeability of such factors as fines content, the grading of grain sizes, and the presence of a second fluid in the pores. The Kozeny-Carman formula clearly reflects the influence of porosity on the permeability of soils. Because factor C changes only slightly with porosity (Kezdi, 1974, p.135) and has little influence on calculated permeability (Rajani, 1988), Equation 2.6 can be used to predict,

for a given soil, the value of permeability at any porosity through the application of the conversion relationship:

$$k_2 = k_1 \cdot f(\phi_2) / f(\phi_1) \quad 2.7$$

where: $f(\phi_1) = \phi_1^3 / (1 - \phi_1)^2$ and $f(\phi_2) = \phi_2^3 / (1 - \phi_2)^2$

In the event that the volumetric strain (ϵ_v) is known, the new permeability can be calculated from the following equation (Tortike and Farouq Ali, 1991):

$$k_2 = k_1 \cdot (1 + 3\epsilon_v / \phi_1 + 3\epsilon_v^2 / \phi_1^2 + \epsilon_v^3 / \phi_1^3) / (1 + \epsilon_v) \quad 2.8$$

Equation 2.8 can be derived from Equation 2.7 if the following relationship between the new porosity (ϕ_2), old porosity (ϕ_1), and volumetric strain is applied:

$$\phi_2 = (\phi_1 + \epsilon_v) / (1 + \epsilon_v) \quad 2.9$$

Monicard (1980) suggested the following correlation for field studies in reservoir engineering:

$$\phi = A_0 \cdot \log(k) + B_0 \quad 2.10$$

where A_0 and B_0 are constants.

Monicard also noted that there are sometimes two line segments for the $\log(k)$ - ϕ correlation. Rajani (1988) demonstrated that Equation 2.10 can be derived from the Kozeny-Carman equation or from a more general permeability - porosity relationship of the form:

$$k = C_0 \cdot \phi^a / (1 - \phi)^b \quad 2.11$$

where: $C_0 = C \cdot f_1(d)$ (from Equation 2.5)

a, b - constants.

Taking the natural logarithm on both sides of Equation 2.11, expressing the logarithmic terms in series form, and neglecting terms of ϕ^3 and higher order, the following equation can be obtained:

$$\ln(k) = \ln(C_0) + A_1 + B_1 \cdot \phi + C_1 \cdot \phi^2 \quad 2.12$$

where A_1 , B_1 , C_1 are constants.

In terms of a logarithm to base ten and with one constant including C_0 and A_1 , this equation can be written:

$$\log(k) = A_2 + B_2 \cdot \phi + C_2 \cdot \phi^2 \quad 2.13$$

where A_2 , B_2 , and C_2 are new constants.

For small porosities, the term $C_2 \cdot \phi^2$ can be neglected and an equation can be obtained which is practically the same as Equation 2.10. Rajani demonstrated that for permeability measurements on oil sand samples from the Orinoco Heavy Oil Belt in Venezuela, a bilinear fit seems to be most appropriate. The Kozeny-Carman equation gave the best fit in the high porosity range ($\phi > 25-28\%$). Below this range, a linear semi-logarithmic relationship expressed by Equation 2.10, gave the best fit to the data. The parabolic semi-logarithmic relation expressed by Equation 2.13 gave a smooth transition from one region to another. Rajani postulated that the mechanism of flow in each of these ranges must be fundamentally different. Monte and Krizen (1976) also found that the bilinear semi-logarithmic relation between permeability and void ratio provided the best fit for their experimental data obtained from clay specimens.

Chardabellas found the following relationship between permeability and void ratio (e) (Monicard, 1980):

$$k = \beta \cdot e^x \quad 2.14$$

where: β and κ are constants

The equation indicates that the plot of $\log(k)$ versus $\log(e)$ is a straight line.

Jacquin found the following relationship for Fontainebleau sandstone (Monicard, 1980):

$$k = \alpha \cdot \phi^{(2m-1)} \quad 2.15$$

where: k is expressed in md and ϕ in %

α and m are experimentally derived constants

When two fluids occupy pore space, reservoir engineers apply the coefficient of relative permeability as defined by Equation 2.4. Numerous empirical equations relate relative permeability to water to the saturation ratio (S_w). The general shape of the water relative permeability curve is most often expressed in the form (Honarpour et al., 1986):

$$k_{rw} = A \cdot (S_w)^n \quad 2.16$$

For example, The Petroleum Production Handbook (1962) suggests the following water-oil relative permeability equations:

1. For unconsolidated (non-cemented) sand, well sorted:

$$k_{rw} = (S_w^*)^3 \quad k_{ro} = (1 - S_w^*)^3 \quad 2.17$$

2. For unconsolidated sand, poorly sorted:

$$k_{rw} = (S_w^*)^{3.5} \quad k_{ro} = (1 - S_w^*)^2 (1 - (S_w^*)^{1.5}) \quad 2.18$$

where: $S_w^* = (S_w - S_{wi}) / (1 - S_{wi})$

S_{wi} - irreducible water saturation

2.2.2.1 Use of Indirect Methods for Oil Sands

The oil sands tested in this study, originating from the Athabasca McMurray Formation at the UTF site, are unconsolidated, fine, dense sands. They are well sorted (uniform grain size) with d_{50} ranging from 0.11 to 0.25 mm, fines content (particles $<45\mu\text{m}$) from 1 to 6 % by weight, and porosity ranging from 32.5 to 35.0 %. Absolute permeability of these sands is expected to be mainly a function of porosity. Therefore, the Kozeny-Carman formula will be evaluated to determine if it can reasonably predict absolute permeability changes with stress induced changes in porosity.

In rich oil sands, the larger part of the pore space is occupied by bitumen which, at an in situ temperature of 8 °C, can be considered immobile due to its high viscosity ($10^7 \text{ mPa}\cdot\text{s}$). In such oil sands, any stress induced volume changes may increase the water saturation ratio (S_w) from its initial values of 10 to 15 %. At such low water saturations the linear semi-logarithmic relationship between effective permeability to water and water porosity (defined as the ratio of the pore volume occupied by water to the total specimen volume) may be applicable. Therefore Equation 2.10 will be evaluated to determine if it can predict the increase in effective permeability to water with water porosity increase.

A plot of k_{ew} versus S_w will be compared with the relationship described by Equation 2.17. When making this comparison it must be born in mind that the changes in S_w occurring in this experimental program result from shearing strains and differ from those for which Equation 2.17 was developed. In this testing program, S_w increases because of an increase in specimen porosity resulting from a pore volume increase whereas Equation 2.17 was obtained for S_w decreasing from an initial value of unity as a result of an increase in oil saturation under conditions of constant porosity. However, different saturation cycles, imbibition in this testing and drainage in tests from which

Equation 2.17 was developed, should not have a large influence on the water permeability-porosity relationships as water is the wetting phase in all cases.

2.2.3 Oil Sands Permeability Reported in Literature

2.2.3.1 Sources of Permeability Data

Formations containing bitumen originated in depositional environments which changed from continental to shoreline and marine, with the result that the properties of deposits vary vertically and horizontally. The oil sands deposits are cross-bedded and often interbedded with shale laminae, or containing shale breccias, shale beds or stringers. During geological history there was extensive loading and subsequent unloading due to the deposition and erosion of overlying sediments or due to the advancing and retreating of continental glaciers. Of the three principal stresses, the horizontal stress is usually the highest to a depth of 290 m (Dusseault, 1977). At the UTF, in the McMurray Formation, the ratio of the maximum horizontal effective stress to vertical effective stress is about 1.5 (Harris and Graham, 1989). As a result of all these factors, the oil sands deposits are generally nonhomogeneous and anisotropic. Their permeability tensor forms an ellipsoid and, to describe it, three permeability values are required measured in the three principal directions. In practice, it is not easy to determine the principal directions of the ellipsoid; even if this is known, the laboratory measurements give permeability for an extremely small portion of the reservoir, a measurement which may not represent the average values within the whole reservoir.

To estimate permeability values for reservoir engineering calculations, three major measurement techniques are utilized: wireline-log analysis, well testing, and laboratory testing of core samples (Ahmed et al., 1991). These various techniques give various measurements of permeability, a fact which should be taken into account when

permeability values found in the literature are compared. The important factors that should be considered are measurement scale, environment, and physics. The volumes being investigated can vary from 2.5 cm long by 2.5 cm diameter for a specimen tested in a laboratory, through wireline-log measurements involving 0.5 m to several meters of a well and 0.2 m to 0.5 m into a deposit, to a radius of investigation reaching tens to hundreds of meters in well testing. The range of well tests covers large scale heterogeneities; the horizontal permeability calculated from such a test is a gross average over a vast volume and represents total reservoir permeability under truly in situ conditions. Wireline-log measurements provide level-by-level permeability values. Although its accuracy of permeability prediction is often unsatisfactory, this technique delivers an excellent relative value for comparing different layers. Laboratory core analysis provides measurements of permeability for a particular specimen measured under controlled laboratory conditions. The in situ conditions of pressure and temperature can be simulated. However, it is impossible to restore the in situ density by the application of an effective confining stress without grain crushing, which may change saturation and permeability conditions. Two different techniques are most often applied in laboratories to measure the permeability of oil sands: the steady state and the pressure pulse technique (Wong et al., 1991, Kwan et al., 1986). Air or water are commonly used in absolute permeability measurements. Air permeability is higher than liquid permeability, necessitating correction (Klinkenberg effect).

Table 2.1 presents measurement techniques and factors affecting permeability estimation.

2.2.3.2 Reported Oil Sands Permeabilities

Some published data on the permeability of Athabasca and Cold Lake oil sands, measured with different techniques, are presented in Table 2.2. The lowest reported effective permeability to water of the Athabasca oil sands is $10^{-5} \mu\text{m}^2$ (Wong et al., 1991). This permeability was measured on an exceptionally well-preserved core. Minimal sample disturbance took place probably because of the low dissolved gas content in the borehole. The sample water saturation was 13 % and porosity about 37 %. It can be calculated that the water content, expressed as a percentage of the total mass, was 2.4 %. Because lower in situ porosities are relatively common, even lower water saturations can be encountered in oil sands. This indicates that smaller in situ permeabilities of rich oil sands can also be expected. However, this is not confirmed by well tests, which give permeability values about two orders of magnitude larger, $10^{-3} \mu\text{m}^2$ (Leshchyshyn and Sayer, 1990; Hackbarth and Nastasa, 1979). The differences between permeabilities measured with these two techniques arise from differences in measurement scale and physics. During well tests, flow is in the horizontal direction, in which permeability is usually higher than in the vertical direction. Well tests measure the permeability of large volume deposits, which are nonhomogeneous and contain layers more pervious to water.

The reported absolute permeability values range from $1 \mu\text{m}^2$ to $5 \mu\text{m}^2$; however, in some cases, the absolute permeability was as low as $0.06 \mu\text{m}^2$. Low absolute permeabilities are associated with larger fines content in tested samples.

2.2.4 Factors Affecting Laboratory Measurements of Permeability

The permeability of soil depends on many factors. We can divide these factors into those related to the properties of an individual soil and those related to the experimental method applied in the laboratory. The following factors belong to the first

group: particle size, fines content, void ratio, composition (especially clay content and type), fabric, and degree of saturation (Lambe and Whitman, 1979). In the second group we can include: flow velocity, type and chemical composition of the fluid, applied stresses, and the effects of core handling and preservation. If the effective permeability is measured, other important factors, such as wettability of soil grains, saturation history, temperature, interfacial tension and fluid density, can affect obtained permeability values (Hycal, 1990). The influence of all these factors on permeability has been broadly investigated and discussed. Some findings pertaining to this experimental project will be briefly presented.

Darcy's law, as expressed by Equation 2.1, is valid only for laminar flow, so that flow rate cannot exceed some critical value. For soils, this critical flow rate takes place when Reynold's number reaches a value between 1 and 10. There is another reason to limit flow velocity. Several researchers (Coskuner, 1988; Gruesbeck and Collins, 1982; Gabriel and Inamdar, 1983) have illustrated that there is a critical flow velocity at which physical fines migration occurs. Concentration of fines in pore throats can restrict flow through a soil (Muecke, 1979). Excessive flow rates and pressure gradients can also affect the effective permeability by disturbing the interface positions between different fluids (fingering) through local perturbations in fluid velocity (Hycal, 1990). The flow rate also has an influence on the "end effects", i.e. nonuniform distribution of saturation in a tested specimen. At the end of the specimen, water saturation tends to be higher than deeper in the specimen (Batycky et al., 1981). In the latter case, higher flow rates are advantageous, as they reduce the end effect.

Proper core handling and preservation is extremely important when oil sand properties are to be tested. Unconsolidated oil sands are highly susceptible to expansion as the result of pore pressure and stress relief during sampling. Dissolved gasses in pore fluids start to evolve causing expansion of the core. The best method utilized thus far to

prevent this damage is freezing of the core, contained in a plastic liner, as soon as it is taken out of the core barrel. The freezing of the core limits its disturbance by increasing the solubility of the gas contained in bitumen and pore water, increasing the bitumen viscosity to a very high value, and providing a tensile resistance to expansion by frozen pore water (McKay, 1989). However the freezing of the oil sand core can also have negative effects, such as altering grain structure and clay structure due to the expansion of water as it freezes (Torsaeter and Beldring, 1987); it can also enhance the physical adsorption of heavy oil components making samples more oil-wet than they actually are (Hycal, 1990).

Saturation history affects the effective permeability because permeability is not a simple function of saturation but also depends on whether saturation is approached from a higher or a lower value (relative permeability hysteresis). Hysteresis in oil-water systems is more pronounced in the non wetting phase than in the wetting phase (Hycal, 1990).

The type of fluid involved can influence permeability results. Absolute permeability is independent of fluid viscosity and density but can be affected by polarity (Wei et al., 1986; Lambe and Whitman, 1979, p. 289). It was found that permeability decreased with increasing liquid polarity. The mobility of the fluid immediately adjacent to the soil particles depends on the polarity of the pore fluid (Lambe and Whitman, 1979). Wei et al. views the dispersion of fine particles, as the result of fluid polarity, as a main reason for the permeability decrease mentioned above.

Many researchers have noted the influence on permeability of non-equilibrium brines used as a permeant (Nasr-El-Din et al., 1991; Coskuner and Maini, 1988; Kwan et al., 1988). Generally, when fresh water followed brine in cores which were susceptible to permeability damage, a considerable decrease in permeability resulted. The same occurred when salt concentration dropped below a critical value (CSC - Critical Salt

Concentration). The CSC was found to be a function of the initial salt concentration, the charge or valency of a cation, type of the monovalent cation, and temperature. The CSC was found to decrease with decreasing temperature. The permeability damage was attributed to fines migration, which is enhanced by the deflocculation or alteration of clay structures when fluids are injected which are chemically incompatible with the existing connate water. All oil sands contain some amount of fines (particles smaller than 45 μm) and clay minerals, although this amount can vary from place to place within a reservoir. Two different types of clay found in oil sands can be distinguished: detrital and authigenic (Coskuner and Maini, 1988). The detrital clays, which are immobile, originated outside the sand deposits and now form part of its structure. The authigenic clay minerals are distributed in a different way within the sand matrix. They occur as pore lining, pore fillings, or can be deposited at pore throats. The authigenic clays are free to expand or move without disaggregating the soil structure. The authigenic clays can be further divided into expanding and nonexpanding types. The most common nonexpanding clays are kaolinite, illite and chlorite. The expanding clays can be represented by smectite, which swells upon contact with an incompatible fluid. The expanding clays are not present in large amounts in oil sands; hence permeability damage is attributed mainly to the movement of nonexpanding clays and other fine particles (Coskuner and Maini, 1988; Cerda et al. 1988). Under natural conditions, clay minerals are in an agglomerated or flocculated state. Permeability reduction follows two steps. First, deflocculation, dispersion, and entrainment of particles into the fluid stream take place, following by deposition in pore throats and plugging (Nasr-El-Dim et al., 1990). The entrainment and deposition of clay minerals and other fine particles present in pores depend on their distribution and location within the pores, the amount of fines present, the size and shape of grains, and the fluid flow velocity (Selby et al., 1988).

Other factors that can influence fines migration and permeability impairment during laboratory tests are extraction processes and sample preparation. Repacked Cold Lake oil sands samples (regardless of whether the bitumen was extracted prior to or after mounting and packing the sample) exhibited much lower initial absolute permeabilities and displayed larger permeability reductions with fresh water injection (Kwan et al., 1988). In comparison, the absolute permeability of the preserved core was not significantly affected when brine was replaced with water.

The degree of permeability damage is also related to the value of the initial absolute permeability of a soil. Sand with higher permeability is less susceptible to damage (Coskuner and Maini, 1988).

It was also found that nonextracted cores are not sensitive to the sequence of brine and water flow (Coskuner and Maini, 1988). In tests performed on Berea sandstones (Mungan, 1965), the rock was saturated with crude oil to the point of irreducible water saturation (water-wet rock), after which the oil was displaced with brine to the point of residual oil; under these conditions, permeability was not affected when the flow was changed to distilled water. It was concluded that the mere presence of residual oil can prevent permeability reduction by fresh water flow. The reported experiments also indicate that, with gradual and continuous decreases in sodium chloride concentration, even a core as sensitive as that of Berea sandstone was not damaged.

2.2.5 Effect of Isotropic and Anisotropic Stress Changes on Oil Sands Porosity and Permeability

The major objective of this research was to investigate the influence of stress changes on the permeability of oil sands. Therefore, findings on this topic require separate discussion.

Oil sands subject to decreasing hydrostatic stresses, or distorted by shearing stresses at confining effective stresses remaining below some critical value, increase in volume. The critical value of the confining effective stress depends on grain mineralogy and sand density. It is intuitively understood that volumetric changes affect permeability, and that the effective permeability to water will be affected to a higher degree than absolute permeability as volume change results in a change in volume of water but not in volume of bitumen.

Field observations performed during high-pressure fluid injection operations confirmed that substantial volumetric changes take place within a reservoir. Bitumen recovery techniques depending on the injection of pressurized steam or hot water into deposits alter in situ stress conditions. At the surface, changes that occur within the reservoir manifest themselves as surface heave (Hassan, 1990; Smith, 1990; Gronseth, 1990). Some recompaction was observed after pressure had been released, but, for the most part, deformations were irrecoverable. The uplifts measured at Cold Lake were much larger than could be explained by thermal expansion or tensile fracturing of the formation. The steam injectivity was also larger than might be expected, based on in situ reservoir properties (Beattie et al., 1989). The irrecoverable volumetric strains proved that shear deformations and dilation of oil sands took place in the reservoir. Only after taking into account these irrecoverable deformations was Beattie able to successfully reproduce, in his mathematical model, the observed steam-injection pressures and rates.

Extensive data on oil sands behavior during in situ recovery processes was gathered at the Phase A Pilot AOSTRA Underground Test Facility. The UTF was developed to test steam-assisted gravity drainage techniques with horizontal wells drilled from tunnels situated beneath the oil sands deposit. Extensive instrumentation was installed capable of measuring the distribution of temperature, pore pressure, and horizontal and vertical deformations (Laing et al., 1988; Scott et al., 1991b). Data

analysis indicated limited possibilities of oil sands expansion in the horizontal direction, due to the relatively high stiffness of the deposit. On the other hand, vertical deformations were much higher than could be calculated only on the basis of oil sands thermal expansion (Scott et al., 1992). It was concluded that vertical deformations were caused by shear strains resulting from a large increase in horizontal total stresses and a decrease in effective vertical stresses due to increased pore pressure.

While oil sands volumetric changes associated with in situ bitumen extraction operations are recognized and their influence on permeability appreciated, there is still insufficient knowledge about how to quantitatively relate these volumetric changes to permeability changes. Researchers pointed to the need for more experimental work (Settari et al., 1990; Beattie et al., 1989).

Experimental work performed on sand grouted with silicate grout showed that a significant permeability increase (two orders of magnitude) occurred as a result of triaxial compression at relatively low confining stresses (0.5 MPa). An increase in permeability was also observed in the case of loose sands when no dilation took place (Mori and Tamura, 1986). The experiments showed that permeability enhancement can also take place due to flow channels which develop during shear deformations, without an increase in soil volume. Since oil sands can dilate during shear, this will produce additional permeability enhancement (Dusseault and Rothenburg, 1988). Dusseault et al. predicted that an increase in porosity from 29-30 % to 35-36 % would result in an absolute permeability increase of 50 % and a 12-fold increase in effective permeability to water. They concluded that effective permeability to water, measured in a laboratory on disturbed specimens (35-36 % porosity), could be two orders of magnitude higher than the permeability of oil sands in situ. Tests performed in a triaxial cell on preserved Athabasca oil sand cores, using the pressure pulse-decay method (Wong et al., 1991) showed that 1 % shear dilation can increase the effective permeability to water 50 times.

despite the fact that shear deformation was localized in a shear band 4-6 mm thick inclined at 70° . The same study investigated changes in effective permeability to water with changes in effective isotropic stress. The effective permeability to water increased 18 times, from $0.01 \cdot 10^{-3} \mu\text{m}^2$ to $0.18 \cdot 10^{-3} \mu\text{m}^2$, with a decrease in effective confining stress from 2.1 MPa to 0.4 MPa. The absolute permeability, for the same range of stresses, increased from $0.87 \mu\text{m}^2$ to $1.68 \mu\text{m}^2$, i. e., by 70 %. Agar (1984) demonstrated a decrease in absolute permeability from $4.1 \mu\text{m}^2$ to $2.3 \mu\text{m}^2$, with an increase of effective confining stresses from 2 MPa to 18 MPa. Absolute permeability then increased to $2.6 \mu\text{m}^2$ during unloading to 2 MPa. Other tests performed on Cold Lake oil sands showed a decrease in absolute permeability, from about $1.9 \mu\text{m}^2$ to $1.6 \mu\text{m}^2$, for an increase in effective confining stress from 1.4 MPa to 12.4 MPa (Nasr-El-Din, 1991). The change in permeability during isotropic unloading generally follows the trend in volume or compressibility changes which are more pronounced at lower confining stresses.

Numerous studies performed on other sands investigated the influence of isotropic stress changes on absolute permeability (Aggour et al., 1989; Gobran, 1981; Zoback, 1975) and granular rocks (Rhett and Teufel, 1992; Wei et al., 1986). All of these studies confirmed the marked reduction in absolute permeability with an increase in confining effective stresses, as well as the increase in permeability with unloading. The influence of isotropic stresses on effective permeability to water was not so widely studied; however, it seems very likely that changes in porosity and alterations in internal flow geometry, brought about by isotropic stresses, can have an even larger influence on effective permeability than on absolute permeability.

Tests investigating the influence of shear stresses on permeability were mostly performed on consolidated rocks (Rhett and Teufel, 1992; Holt, 1990; Morita et al., 1984). The triaxial failure tests on Berea sandstone showed that permeability decreased

initially during axial loading but increased close to failure, as the result of dilation of the rock (Morita et al., 1984). Tests on Red Widmoor sandstone (North Sea) showed permeability reduction during axial loading in the triaxial cell. Other interesting laboratory measurements, performed on two types of North Sea sandstone, demonstrated that compressibility and permeability are highly stress-path dependent (Rhett and Teufel, 1992). Triaxial compression tests were carried out with pore pressure (u) and cell pressure (σ_3) decreased in such a way that a constant ratio of stress changes (K') was maintained ($K'=(\sigma_3-u)/(\sigma_1-u)$). Under nonhydrostatic loading, in which K' was lower than 0.5, permeability increased with increasing effective stress. The increase in permeability was greater for stress paths that followed a lower stress ratio. Dilation of rock specimens during these tests was found to be negligible.

The permeability changes of rock specimens are associated with changes in porosity but can also be influenced by microcracking, which does not have to be reflected in specimen total volume changes. In the case of granular soils, pore volume changes (contraction or dilation) have the principal influence on permeability. Whether sand dilates during shear depends on the strength of its grain material, its density, structure (very pronounced in the case of the Athabasca oil sands), and the effective confining stress magnitude.

2.3 Summary

1. Oil sands are a nonhomogeneous and anisotropic geotechnical material. They are generally composed of uncemented quartz sands with associated shales occurring in different forms: beds, stringers, layers, laminations, lenses, breccias, or separate shale fragments of different sizes.

2. Oil sands grains are water-wet and oil sands pores are filled with varying proportions of bitumen and formation brines. Recovered cores also contain gas, which has evolved from water and bitumen. The volume of pores filled with gas is an indication of the degree of sample disturbance. The in situ porosity of rich oil sands varies from 30 % to 35 % and oil saturation is up to 18 % by weight.
3. Oil sands geotechnical properties (high strength and dilation during shear) are influenced by their specific, interpenetrative fabric.
4. The in situ effective permeability to water of rich oil sands can be of the order of $10^{-5} \mu\text{m}^2$ or even lower. The absolute permeability of Athabasca and Cold Lake oil sands assumes values of the order of $1-5 \mu\text{m}^2$.
5. Core disturbance during recovery, storage, and specimen preparation can significantly alter the effective permeability to water.
6. The absolute permeability can sharply decrease when flow is changed from brine to fresh water. The permeability change depends on the rate of change in NaCl concentration. The sensitivity of a core to salt concentration changes can differ from field to field and must be checked every time a core from a new place is tested. The effective permeability to water of bitumen-rich oil sands is probably not significantly sensitive to the sequence of brine and water flow.
7. The unloading of rocks and sands through a decrease in isotropic effective stress causes elastic volume increase and permeability enhancement.
8. Shear stresses cause distortion and dilation of oil sand specimens if confining effective stresses remain below some critical value. This dilation is reflected in an increase in permeability.

9. In some instances (grouted sands (Mori and Tamura, 1986), some sandstones from North Sea (Rhett and Teufel, 1992)), anisotropic loading or unloading caused permeability enhancement without an increase in total volume.
10. Factors that should be taken into account during permeability tests on oil sands in a laboratory include: technique of specimen preparation, flow rate, sensitivity to fluid salinity, specimen full saturation, specimen reconsolidation, and bitumen mobility.

Table 2.1 Various Sources of Permeability Estimation

Table 2.1 Various Sources of Permeability Estimation						
Measurement Technique	Permeability	Measurement Method	Description	Scale	Environmental and Physics	Comments
Wireline-Log Analysis	Absolute	Empirical Correlations	Empirical correlation of permeability with porosity and surface area	Megascopic (scale of grid-blocks in simulation models)	In situ conditions with the exception of reservoir fluid saturation owing to mud filtrate invasion	Presents an excellent relative value for correlating between layers and zones.
		NML Measurements	Measurement of producible formation fluid with the nuclear magnetism log			
		GLT Measurements	Estimate of mineral concentrations by the geochemical logging tool			
	Effective	Stoneley-Wave Attenuation and Dispersion	Correlation of permeability with Stoneley wave velocity by acoustic logging tools			
		RFT Measurements	Pressure/time measurement of formation fluids with the formation tester tool			
Well Testing	Effective	Short Term Testing	Involving DST, IMPULSE testing and transient-rate and transient-pressure testing (TRAP)	Gigascope (total formation or regional scale represented by well-test area of investigation)	Truly in situ conditions	Horizontal permeability calculated is a gross average over vast volume and represents total reservoir flow behaviour but it lacks foot-by-foot resolution.
		Conventional Testing	Classic pressure drawdown and buildup involving single or step rate			
		Advanced Test Techniques	Layered reservoir testing, vertical interference testing, multiwell interference testing			
Core Analysis	Absolute	Steady-State Technique	Permeability calculated with Darcy equation	Macroscopic (conventional core plug scale)	Standard ambient or in situ pressure and temperature conditions can be simulated (saturation is rarely simulated correctly).	Air or water can be used as the fluid medium. Air permeability requires correction. Pressure pulse has to be smaller than the capillary pressure. Small specimen sizes can bias it in heterogeneous form. (perm. can vary from one spec. to another).
		Pulse-Decay Method	Pressure transient falloff is measured and analyzed for permeability			
	Effective and Relative	Steady-State Technique	Oil and water flowing together in proportion to maintain the desired water saturation			
		Displacement Technique	Oil satur. specimen is displaced with water while pressure and flow rates are monitored			
		Pulse-Decay Method				

Note: Data contained in this table is presented after Ahmed et al.(1991).

Table 2.2 Permeability Data Reported in the Literature for Alberta Oil Sands					
Author	Source of Core or Well Test Location	Reported Permeability Value	Test Technique	Reported Oil Sand Properties	Comments
Wong et al., 1991	Athabasca oil sands, McMurray Formation OSLO lease 41 site 10 km north of Fort McMurray core from depth: 70-105 m	Absolute: Change from 0.87 μm^2 to 1.97 μm^2 for change in σ_3' from 2.08 MPa to 180 kPa	Lab. test *constant flow rate	Density (core recovered): 2.039 kg/m ³ Density (at σ_3' =0.3 MPa): 2.041 kg/m ³	Tests on well preserved core
		Effective to water: Change from 0.01*10 ⁻³ μm^2 to 0.18*10 ⁻³ μm^2 for σ_3' change from 2.08 MPa to 0.38 MPa Change from 0.05*10 ⁻³ μm^2 to 0.52*10 ⁻³ μm^2 with shear stress 1% at constant σ_3' =106 MPa	Lab.test *pressure pulse-decay	Density (neutron log): 2.04-2.05 kg/m ³ Porosity(at σ_3' =0.3 MPa): 36.89 % Water saturation: 13.01 % Bitumen saturation: 86.99 %	Pressure pulses of 70 -140 kPa Shear deformations located along a shear band of 4 - 6 mm thick at an inclined angle of 70 °
Nasr-El-Din et al., 1991	Cold Lake oil sands: Frog Lake-McLaren field	Absolute: Change from 1.9 μm^2 to 1.6 μm^2 for change in σ_3' from 1.38 MPa to 12.42 MPa	Lab. tests *steady state	Mineral composition: Quartz 91% Feldspar 5 % Clays: kaolinite 3 % illite 1% chlorite (traces)	Preserved extracted cores, Flow rates up to 70.8 ml/min of 1% KCl had no significant effect on permeability. Injection of a deionized water caused gradual decrease in perm. from 1.9 to 0.7 μm^2 for 180 pore volumes injected.
		Effective to mineral oil at connate water saturation: 60*10 ⁻³ μm^2		Quartz 52 % Feldspar 33 % Clays: kaolinite 8 % illite 3 % chlorite 4 % Fines with dia. smaller than 2 μm : Smectite 64 %, Kaolinite 26 % Illite 7 %, Quartz 2 %, Feldspar 1%	Deionized water damaged permeability significantly due to causing swelling of the smectite.

Leshchynsky and Seyer, 1990	Althabasca Oil Sands, McMurray Formation at PCEJ Hengstone project, depth 300 m Reservoir pressure 2MPa	Effective: 1.47*10 ⁻³ μm ² (0.67-0.92)*10 ⁻³ μm ² (407-440)*10 ⁻³ μm ² 5.1*10 ⁻³ μm ² Effective: (0.0-5.0)*10 ⁻³ μm ²	Well tests: *falling head *constant rate *high rate stress test: early time data *late time data Lab. tests	Typical properties of oil sand: Porosity 33 % Absolute perm. 1.5 μm ² Bitumen content 8-16 % Average oil saturation 80 % Reservoir temperature 8 -16 °C Bitumen viscosity 10 ⁶ mPa*s	Test fluid: saline water Results from combination of tests in the low permeability oil sands are more conclusive than individual tests.
Rottenfusser et al., 1989	Althabasca oil sands McMurray Formation UTF site -Unit D -Unit E	Absolute: 0.4 μm ² (range from v. small to 3.9 μm ²) 1.4 μm ² (range from v. small to 5.9 μm ²)	Well logs	Porosity 22.6 % Porosity 26.6 %	The values are arithmetic averages of a large number of points. Porosity values are probably to low in the shallower units. The authors have little faith in log derived permeabilities.
Kwan et al., 1988	Cold Lake oil sands, Clearwater Formation	Absolute: 1 - 3 μm ² (preserved and extracted cores) 0.06 - 0.21 μm ² (repacked and extracted cores)	Lab. tests: *steady state	Bitumen content 12 % Fines content 10 %	Tests carried on at 10.3 MPa total conf. stress and 1.38 MPa back pr. Repacked specimens susceptible to severe fresh water induced permeability damage. Absolute permeability of the preserved core is not significantly affected by fresh water.
Coskuner and Maini, 1988	Cold Lake oil sands, Lower Grand Rapids Formation, Lindbergh field	Absolute: 0.062 - 0.17 μm ²	Lab. tests *steady state	Composition of core: Quartz 85 %, Illite 2 % Kaolinite 12 %, feldspar 1 % Average formation porosity 33 % Oil viscosity 10 ⁵ mPa*s at reservoir temperature 24°C Average oil sands absolute permeability 2 - 3 μm ²	Core sensitive to the salinity of the injected fluid. Critical velocity (affecting fines movement) decreases as the effective confining stress increases.

Kwan et al. 1986	Cold Lake oil sands	Effective to oil at irreducible water saturation, $T=19.2^{\circ}\text{C}$: $0.63 \mu\text{m}^2$ Absolute: $0.78 \mu\text{m}^2$	Lab. tests *pressure pulse-decay *steady state	Core porosity 31.2 % Oil saturation 81% Bitumen viscosity 99960 mPa*s	Test fluids: dewatered produced Cold Lake bitumen and distilled deaerated water.
Agar, 1984	Athabasca oil sands McMurray Formation	Absolute: $3.0 \mu\text{m}^2$ at $\sigma_v' = 3 \text{ MPa}$	Lab. tests *constant flow rate (oedometer tests)	Extracted reconsolidated oil sand recompacted in consolidometer to dry density 1.67 kg/m^3 and porosity 37 %	Test fluid: water
		Absolute: Change from 4.1 to $2.23 \mu\text{m}^2$ over stress range $2 - 18 \text{ MPa}$ Change from 2.23 to $2.57 \mu\text{m}^2$ over stress range $18 - 2 \text{ MPa}$		Preserved extracted oil sand, initial specimen porosity 35 %	
		Effective: $(9-12) \cdot 10^{-3} \mu\text{m}^2$ at $\sigma_v' = 3 \text{ MPa}$		Preserved oil sand bitumen saturation 81 - 88 % Oil viscosity $3 \cdot 10^5 \text{ mPa*s}$	
Mainland, 1983	Cold Lake oil sands ESSO Resources Canada Limited Lease	Absolute: $1.5 \mu\text{m}^2$	Lab. tests		
Hackbarth and Nastasa, 1979	Athabasca oil sands	Effective to water: Average $0.01 \mu\text{m}^2$ (range: 10^{-3} to $1 \mu\text{m}^2$)	Well tests		

Note: σ_3' - effective confining stress in triaxial cell tests

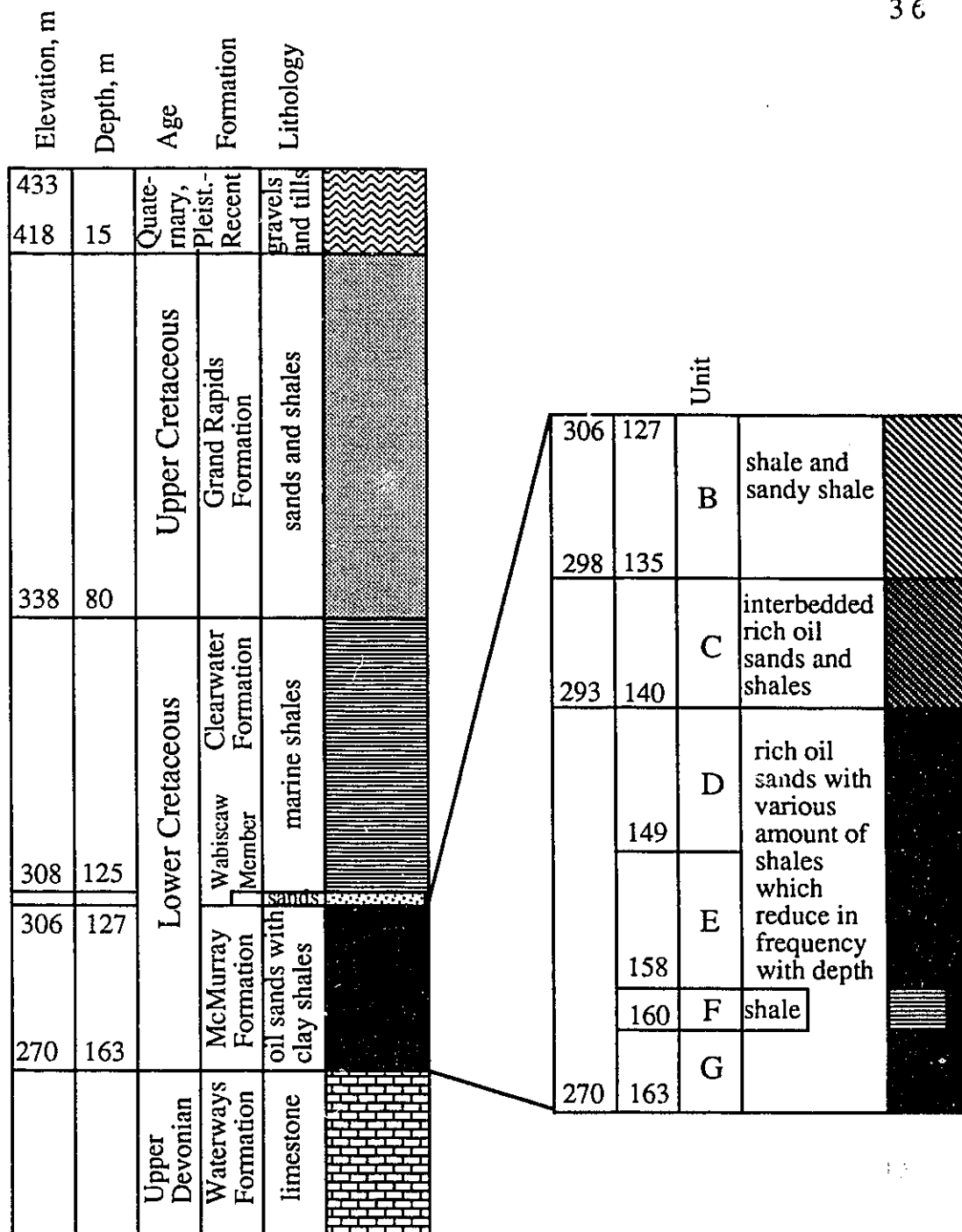


Figure 2.1 Geology of Athabasca Oil Sands at UTF Site (Phase A)

Chapter 3. ABSOLUTE PERMEABILITY OF ATHABASCA MCMURRAY FORMATION OIL SANDS

3.1 Introduction

Permeability is an important parameter in reservoir engineering analysis. Understanding the influence that bitumen recovery processes have on permeability is necessary to obtain reasonably accurate predictions of bitumen production rates. The influence of oil sands compressibility on permeability is better understood and generally applied in reservoir simulation calculations. Other aspects of the geomechanical behavior of unconsolidated sands, such as shear dilation and irrecoverable strains and their impact on permeability, have only recently attracted the attention of reservoir engineers (Tortike and Farouq Ali, 1991).

This chapter discusses results of laboratory experiments investigating the influence of variations in the state of stress on volume change and absolute permeability. Tests were performed with a triaxial cell on specimens of reconstituted bitumen-free oil sands. Isotropic stress as well as shear stress conditions were investigated.

The series of tests denoted PI was carried out by the author of this thesis. The remaining series, denoted Sn-D, Ss-D, PI-D, were performed by Adhikary (1991), who worked on the same testing program.

3.2 Experimental Program

3.2.1 Test Conditions and Stress Paths

Injection of steam or water into petroleum reservoirs during bitumen recovery processes alters the existing in situ state of stress. The oil sands matrix response to increased pore pressure depends on the character of the initial existing stresses. In the case of isotropic stresses, pore pressure injection causes a decrease of the effective isotropic stresses and the formation expands by reason of elastic unloading. If the stress field within a reservoir is anisotropic, with higher horizontal stresses than vertical, as at the UTF site, the pore pressure increase causes a reduction in all principal effective stresses by the same amount which results in shear deformations. As the Athabasca McMurray Formation oil sands dilate during shear an increase in porosity will take place.

This model of stress changes was used to design stress paths for the experimental program. It does not take into account thermal expansion of the sand matrix or consider the resistance of the surrounding formation to local volume changes. These factors will also result in stress changes within a reservoir but they can only alter the sequence or rate of change of the three principal stresses.

Figure 3.1 shows the stress paths followed in this experimental study in the p' - q stress field. The p' and q stand for:

$$p' = (\sigma_1' + \sigma_2' + \sigma_3')/3 \text{ - mean principal effective stress}$$

$$q = \sigma_1 - \sigma_3 = \sigma_1' - \sigma_3' \text{ - deviatoric stress}$$

$$\sigma_1, \sigma_2, \sigma_3 \text{ - principal total stresses}$$

$$\sigma_1', \sigma_2', \sigma_3' \text{ - principal effective stresses}$$

In a triaxial cell both of the principal horizontal stresses are assumed to be the same and equal to the cell pressure ($\sigma_2 = \sigma_3 = \sigma_h = p$). The vertical stress σ_1 (σ_v) is equal to the sum of

the cell pressure (confining pressure) and the deviatoric stress. The isotropic unloading, stress path A_U , was accomplished by increasing the pore pressure (back pressure) in steps and keeping the cell pressure at a constant value. The deviatoric stress remained equal to zero. During anisotropic unloading, stress path F_U , the deviatoric stress was set at a predetermined value, kept constant during the test, and the pore pressure was increased in steps until the specimen failed. Compression shear tests (stress path B) are the most common laboratory triaxial test. The two types of compression shear tests, denoted B_E and B_σ , differed from each other only in the manner of strain control. During B_E tests, specimens were sheared with a constant strain rate. During B_σ tests, vertical stresses were increased in steps, so that axial strains also changed in steps. An additional stress was applied when the axial strain became constant.

All tests were carried out at room temperature, 22 °C. Additional data on test conditions are contained in the subsection devoted to test procedures.

3.2.2 Grain Size of Sand Specimens

The grain size distribution, fines content, grain shape and texture are factors that, amongst others, affect permeability and can be controlled in a laboratory. To eliminate natural differences that would appear if specimens were taken from a core, all specimens (except specimens PI) were made from one batch of extracted oil sands.

Sand from the Athabasca McMurray Formation deposits was used to prepare specimens for testing. A sample of extracted sand was sieved to obtain several fractions of grain sizes. These fractions were then mixed in such proportion to prepare a sand sample with a grain size distribution considered to be "typical" for the McMurray Formation sand. Results of grain size analyses performed after triaxial tests are shown in

Figures 3.2 and 3.3. The grain size distributions of PI specimens slightly differ from others since the sand sample for making PI specimens was prepared separately.

3.3 Equipment

A conventional high pressure triaxial cell was used to measure the permeability of oil sands under changing stress conditions. The triaxial cell and auxiliary equipment allow for controlling cell pressure and pore pressure and increasing the vertical load (deviatoric stress) on a specimen. Different stress paths were achieved by changing the cell pressure, vertical load, or pore pressure in a predetermined manner. The cell pressure and back pressure could only be changed manually by means of regulator relief valves. In practice they were changed in steps. The minimal range of the pressure change was determined by the regulators' capability for controlling pressure changes and setting pressure at a predetermined value. The vertical load was controlled in two ways. When the Bellofram load frame was used to apply deviatoric stress, the vertical load was changed manually in steps. When a constant strain rate loading frame was used, the load was changed continuously. Figure 3.4 shows a schematic layout of the test facility. It includes the following major components: triaxial cell, load frame, back and cell pressure systems, flow system, electronic measuring devices and data-logging system.

3.3.1 Triaxial Cell and Load Frames

A Wykeham-Farrance WF40020 high pressure triaxial cell was selected for this test program. The cell was designed for cell pressures up to 14 MPa. The Wykeham-Farrance constant shear strain rate, electric motor driven load frame was used for strain-controlled tests. It can supply shear strain rates from 6.25 mm/min to 0.0008 mm/min.

The maximum load capacity is 440 kN. Another load frame, with a Bellofram air diaphragm cylinder, was used for stress-controlled tests. The load is applied by compressed air.

3.3.2 Pressure Systems

Pressure systems used to apply cell pressure, pore pressure, and vertical loads (with the Bellofram load frame) are schematically shown in Figure 3.4. The pressure systems contain a series of "Dynareg" regulator relief valves driven by a nitrogen booster pump. A compressed air system drives the nitrogen booster pump and also feeds the Bellofram. Nitrogen for the system is supplied from a nitrogen bottle. Two nitrogen over water accumulators and two "Ennis Measuring Accumulators" (EMA) were used for maintaining pressures, dampening pressure spikes, and allowing changes from the gas system to a water system. The EMA is provided with a piston that separates the nitrogen from the water. The piston is connected to a Linear Variable Differential Transformer (LVDT) which measures displacement of the piston and can indicate the amount of water flowing in or out of the EMA. One of the Ennis Measuring Accumulators was used to maintain cell pressure and to monitor specimen volumetric changes.

3.3.3 Flow System

A constant flow rate of water was maintained and the pressure drop across the specimen was monitored during permeability tests. A LC-5000 syringe pump was used. The pump is designed for applications requiring precise, pulse free delivery of liquids. It has the capability of giving flow rates from 0.06 ml/hr to 400 ml/hr and working under pressures up to 25.5 MPa. The syringe pump was connected to a port in the triaxial cell

base pedestal that accesses the specimen from the bottom. Water was drained to one of the accumulators through a top cap. The back pressure (pore pressure) in the specimen was maintained by setting a required pressure in this accumulator. Fresh water was used as a permeant.

3.3.4 Electronic Instrumentation and Data Acquisition System

The cell pressure and back pressure (downstream and upstream) were measured by three strain gauge pressure transducers designed for pressures ranging from 0 to 7 MPa. Axial deformations of specimens were measured by means of an LVDT that was fastened to the triaxial cell load piston. The applied vertical load was measured with a 22 kN capacity strain gauge load cell placed between the cell piston and the load frame. The water pressure drop across the specimen was monitored by means of a Validyne differential pressure transducer that could measure pressures over a wide range by inserting a diaphragm with an appropriate capacity.

Excitation voltages for the electronic instruments were supplied by a signal conditioner. The output voltage signals from the instruments were received by the signal conditioner and sent to a data acquisition system. A "HP-3497A Data Acquisition Control Unit" was used for scanning transducers and sending the signals to a Macintosh IIfx desktop computer where data were stored, processed, and displayed on screen during tests. The "Lab View" program was used for data processing.

3.3.5 Instrument Calibration and Compliance Testing

Calibrations of all instruments and compliance testing were completed prior to conducting tests. In addition, calibration checks were carried out periodically and the compliance testing was repeated after any element of the triaxial system was changed.

The purpose of the compliance measurements was to isolate apparatus deformations, stresses, and system pressure loss, which were included with external measurements of specimen behavior (e.g., cell and tubing pressure expansions, piston friction, system differential pressure loss). Special attention was directed to finding proper relationships between cell pressure and cell volume since the volumetric changes of specimens were measured by means of the EMA placed in the cell pressure system. The system pressure loss was found to be a linear function of the flow rate. For a flow rate of 400 ml/hr, the system pressure loss was about 1.4 kPa, making up a significant part of the total pressure drop across specimens during absolute permeability tests (about 40% for a permeability of $3.8 \mu\text{m}^2$).

3.4 Specimen Preparation

Before specimen preparation was started, the sand sample was partly saturated with water to change it into a "rigid body" after freezing. The degree of saturation was kept lower than 80 % to provide space for water expansion during freezing. The water content of all specimens remained within limits from 12.0 % to 16.6 %.

The specimens were formed in a three piece, steel split mold, 38.1 mm in diameter and 127 mm in length. The mold was assembled and lined with a latex membrane passed through the center of the mold and stretched over the ends. The mold was then fitted over a steel base pedestal to support the specimen. The sand was placed in

the mold in 20 mm layers. Each layer was tamped with a steel rod. Filling of the mold was stopped when the sand reached a height of about 80 mm. An aluminum "plug" with 2 mm diameter holes drilled through it and a 5 kg weight were placed on top of the specimens. Next, the mold was held on a vibrating table for 4 to 5 minutes. (Specimens Sn-D, Ss-D, PI-D were vibrated during filling of the mold without an additional weight on the sand.) The specimens were placed in a cold room, with temperatures maintained in the range from -20 °C to -25 °C, and left overnight. A 5 kg weight was placed on top of the plug to help minimize heaving of the specimens during freezing. The specimens taken out of the mold required little final preparation. Only the top of the specimens covered with the plug had to be slightly smoothed with a file. The final size of the specimens was 38.1 mm diameter by 76.2 mm long.

Specimen mounting in the triaxial cell was also carried out in the cold room. The cell was transported there for chilling one hour earlier. The height, diameter and weight of a specimen were measured before it was set on the pedestal. In view of the high confining stresses applied and the angularity of sand grains, two latex membranes, 0.70 mm and 0.33 mm thick, were used to enclose the specimen. A drainage tube was attached between the top cap and a port in the triaxial cell base. The upper part and the base of the cell were fastened together, and the cell was transported to the testing laboratory.

3.5 Test Procedures

3.5.1 Saturation and Isotropic Compression

The triaxial cell was placed in a load frame, and the cell pressure line and the water line from the syringe pump were connected. The cell was filled with water and a confining pressure of 200 kPa applied. The specimen was left for two hours to thaw.

Then, with the back pressure line opened, water flow, at a rate of 400 ml/hr, was instigated to flush air from the tubing and the specimen and to increase the specimen's initial water content. Flushing was performed for 40 minutes to 3 hours, thus exceeding the typical flushing time for sand specimens recommended by Caney (1980). (Specimens Sn-D, Ss-D and Pi-D were saturated without initial flushing with water.) Next, the back pressure line was closed, and cell and back pressures were increased in steps to complete saturation of the pore fluid. The pore water pressure necessary to accomplish this was calculated from the theoretical equation (Love and Johnson, 1960):

$$u_s = u_a(1-S_0)(1-H)/H \quad 3.1$$

where: u_a - initial absolute pressure, kPa

S_0 - initial degree of saturation

H - Henry's constant

u_s - saturation pressure, kPa

Henry's constant for water at room temperature is equal to the ratio of 0.02 cm³ of air to 1 cm³ of water. Assuming that a degree of saturation of 90% was reached after the specimen was flushed, the required back pressure (u_s) was calculated to be 497 kPa. To reduce the time needed to dissolve free air in specimen voids, a 3 MPa back pressure was applied and continued overnight.

The pore pressure parameter B was measured to check saturation conditions for specimens. Full saturation was defined as the point at which B becomes constant with increasing back pressure.

Once the specimen was fully saturated, cell and back pressures were increased in increments of 200 kPa until a cell pressure of 5 MPa was reached. Cell pressure was always maintained at a higher level than back pressure by about 200 kPa. Specimen isotropic compression was performed by reducing pore pressure in stages down to

1000 kPa. Cell pressure was kept constant. Specimen volumetric changes were monitored by the EMA placed in the cell pressure system. Two cycles of isotropic pressure increase and decrease were carried out. Cyclic compression was intended to compress the specimen to a higher density, closer to in situ porosity values. The volume compressibility coefficient was measured as an index of sample quality.

3.5.2 Isotropic Stress Change Test

After the specimen was consolidated under an effective stress of 4 MPa and stabilized for at least one hour, a permeability test was started. The syringe pump was turned on and distilled water was pumped through the specimen at a constant flow rate of 400 ml/hr. Pressure drop across the specimen was monitored. When the differential pressure across the specimen was stabilized, the flow was stopped and the back pressure increased. The permeability test was repeated at a number of effective stress values. Cell pressure and specimen volumetric changes were monitored as in 3.5.1.

3.5.3 Shear Stress Change Tests

3.5.3.1 Triaxial Compression Strain Controlled Test

The Wykeham-Farrance load frame was used to apply a vertical shear force to a specimen in the triaxial compression strain-controlled test. After the isotropic unloading was finished, the specimen was reconsolidated at a predetermined confining effective stress and the flow of water through the specimen was begun. When the pressure drop across the specimen was stable, the load frame motor was turned on. The motor speed provided a constant rate of displacement of 0.5 % strain per hour. Axial displacements of the triaxial cell piston, vertical loads on the piston, cell pressure, back pressure, and

differential pressure across the specimen were continuously recorded and displayed on a computer screen. Water flow through the specimen to measure permeability was continuous during testing.

3.5.3.2 Triaxial Compression Stress Controlled Test

During the triaxial compression stress controlled test, the Bellofram load frame, equipped with a pressure chamber with "Bellofram" rolling seals, was used to apply constant vertical loads on the specimen independent of its deformation. In this test, the confining effective stress was kept constant and the axial stress was changed in increments until the specimen failed. Permeability measurements were carried on at each level of vertical stress. Displacements, vertical loads, pressures, and volume changes were monitored.

3.5.3.3 Anisotropic Unloading Test

A constant effective stress ratio was maintained during this test. The cell was set in the Bellofram load frame. A predetermined effective confining pressure was applied to a specimen and the axial load was increased to a precalculated value to obtain the desired stress ratio. The specimen was brought to failure by increasing the pore pressure in several stages. At each back pressure level, permeability was measured. Vertical and volumetric deformations and pressure changes were monitored.

3.6 Results

3.6.1 Degree of Saturation and Compressibility

In permeability measurements, it is important to obtain complete specimen saturation, thus eliminating obstructions to flow caused by bubbles of gas. The presence of air in specimen pores reduces the "active" volume available to flowing water. Permeability can be affected even more by the accumulation of bubbles at pore throats and at the specimen outlet. In these tests, the degree of saturation was monitored by observing pore pressure response (with back pressure lines closed) to confining pressure increments. The pore pressure parameter B was calculated from the equation:

$$B = \Delta u / \Delta \sigma \quad 3.2$$

where: Δu - back pressure change

$\Delta \sigma$ - confining pressure (cell pressure) change

If several successive equal increments of confining pressure gave similar values of B , despite the increase in the magnitude of back pressure during this process, specimen saturation was considered acceptable. (Each consecutive increment of confining pressure was preceded by the adjustment of the back pressure to restore an initial confining effective stress of 200 kPa.)

Table 3.1 presents values of the pore pressure parameter B obtained during the PI series of tests. The values of B , ranging from 0.87 to 0.90, are significantly lower than unity. Neglecting compressibility of soil grains, the coefficient B can be defined by the theoretical relationship:

$$B = 1 / (1 + \phi c_w / c_s) \quad 3.3$$

where: ϕ - porosity

c_s - compressibility of soil skeleton, kPa^{-1}

$c_w = 0.46 \cdot 10^{-6} \text{ kPa}^{-1}$ - compressibility of water

Table 3.1 shows compressibility of the soil skeleton calculated as a slope of the curve representing the relationship between volumetric strain and isotropic effective stress at the initial stages of the isotropic compressibility tests. On the basis of these values, a theoretical coefficient B for 100 % saturation was calculated: its value varied from 0.978 to 0.983. Even at relatively low effective confining stresses, such as 400 kPa to 600 kPa, specimen material can be classified as a stiff soil after Black and Lee (Head, 1985, page 793). For sand with such low compressibility, they obtained a coefficient B value of 0.8 at a degree of saturation of 99.7 %. This saturation level was considered satisfactory for these experiments. A pore pressure coefficient B larger than 0.85 was obtained by flushing the specimen with water and applying a 3 MPa back pressure for more than 12 hours. The measured coefficient B is considered to be a lower boundary of its true value, since the measured pore pressure changes were affected to some degree by changes in the volume of the back pressure system, e.g., deformations of the pressure transducer diaphragm and the 1 m long steel tubing. Table 3.1 also shows specimen compressibility calculated at confining stresses around 4 MPa at the end of the first and second loading cycles.

3.6.2 Absolute Permeability and Volume Changes

The absolute permeability was calculated from the equation based on Darcy's law:

$$k = (Q \cdot \mu / A_s) (\Delta l / \Delta p) \quad 3.4$$

where: Q - flow rate, m^3/s

A_s - cross sectional flow area, m^2

Δp - differential pressure across flow section (pressure drop), Pa

μ - dynamic viscosity, Pa•s

l - length, m

k - absolute permeability, m²

Absolute permeability is, in principle, independent of the nature of the flowing fluid, pressure gradient and macroscopic dimensions; it is a function only of the pore structure of the medium, which is affected by grain size, porosity, the manner in which grains are packed, and the shape characteristics of voids. In these tests, an attempt was made to maintain similar grain size distributions and grain shape characteristics for all specimens. Porosity was calculated at all stages of testing, however, control of this parameter was not equally successful throughout all tests. This will be discussed later. Flow rate was kept constant during each test. The dynamic viscosity of water at 22 °C was taken from thermodynamic tables. Specimen length and cross sectional area were calculated on the basis of the initial dimensions and the axial and volumetric deformations measured during testing. The pressure drop was monitored by a differential pressure transducer.

The term volume change, as used in this thesis, refers to the percent volume change of the total specimen. To convert volume change into pore volume change, the parameter commonly used in petroleum engineering, the following relationship must be applied:

$$\Delta V/V_{p0} = (\Delta V/V_0)/\phi_0$$

where: $\Delta V/V_{p0}$ - pore volume change

$\Delta V/V_0$ - volume change

V_{p0} - initial volume of pores

V_0 - initial total volume of specimen

ϕ_0 - initial porosity

3.6.2.1 Isotropic Unloading

The characteristics of specimens at the beginning of isotropic unloading are tabulated in Table 3.2. The summary of the isotropic unloading test results is presented in Table 3.3.

Figures 3.5 and 3.7 show the relationship between effective confining stress and volumetric change for ten experiments. The initial effective confining stress in eight cases was about 4 MPa; the other two cases measured 3.2 MPa and 1 MPa. All the curves have similar characteristics, displaying similar slopes at corresponding stress levels. The effective stress change from 4 MPa to about 200 kPa resulted in a volume increase of 1.2 % to 1.5 %; a change from 1 MPa to 250 kPa resulted in a 0.45 % volume increase.

The influence of volumetric changes on permeability is shown in Figures 3.6 and 3.8. The relationship between absolute permeability and porosity is shown in Figures 3.9 and 3.10. The initial permeability in most cases varied from $0.4 \mu\text{m}^2$ to $3.8 \mu\text{m}^2$. The maximum permeability increase was 70 %. In most cases, higher permeability increases were associated with lower initial permeability values (except the test conducted on specimen Sn 3-D which gave untypical results).

3.6.2.2 Triaxial Shear

Figures 3.11 and 3.12 show the relationship between volumetric changes and axial strains for the compression strain-controlled and stress-controlled tests, respectively. In all cases but two, at the beginning of testing, specimens underwent a decrease in volume; when axial strains from 1% to 2 % were reached the volume started to increase.

The stress-controlled tests could be carried out only until specimens reached their maximum strength. From that point on, deformation took place in an uncontrolled

manner. The maximum measured volumetric changes for the four specimens were: 2.15, 1.45, 1.1 and 0.74 % at axial strains of 7.1, 3.6, 3.2 and 4.5 % respectively. The volume changes at failure are related to the effective confining stress at failure. The lower the confining stress, the higher the volume increase that took place. For example, specimen Ss 4-D, which sheared under an effective confining stress of 120 kPa, expanded by 2.2 %, whereas specimen Ss 3-D, sheared under a 550 kPa effective confining stress, dilated by only 0.7 %.

The strain-controlled tests were continued in the post-peak range of strain. For the two dilating specimens, the tests were conducted up to 11 % and 12 % axial strains, at which point the respective maximum volumetric changes were 3.2 % and 2.4 %. In both tests, the effective confining stress was 150 kPa. Two specimens (Sn 3-D and Sn 4-D) did not behave typically. Specimen Sn 4-D contracted from the beginning of the test in the characteristic manner of loose sands. Specimen Sn 3-D expanded at the beginning but when the axial strain reached about 1% it started to contract. It is hypothesized that these specimens might have been accidentally unloaded through an excessive increase in back pressure or that the specimens might have thawed during the set-up in the triaxial cell prior to the application of an initial confining pressure. The density of these specimens was probably lower than was calculated.

Figure 3.13 shows volumetric changes measured during the anisotropic unloading tests. It can be seen that the volume started to increase sharply at the beginning of the tests and that its rate of change decreased with increasing axial strain. The anisotropic unloading tests were also stress-controlled but they were carried on to higher levels of strain than the compression stress-controlled tests. This procedure was possible because back pressure increments were lower during these series of tests and because specimen weakening, due to decreases in the effective confining stress, was largely counter-balanced by increases in cross-sectional area due to deformation. For two

specimens, PI 3 and PI 4, volumetric changes of 2.6 % and 3.8 % at axial strains of 13 % and 18 % were recorded.

The relationships between absolute permeability and volume change during compression shear tests are shown in Figures 3.15 and 3.17. The relevant data on permeability changes are contained in Tables 3.4 and 3.5. During the strain-controlled tests, permeability measurements were performed on three specimens: Sn 1-D, Sn 3-D and Sn 4-D. Specimen Sn 1-D dilated during testing and experienced a permeability increase of 27 %. Specimens Sn 3-D and Sn 4-D contracted during shearing and their permeability decreased by 33 % and 46 % respectively. During the stress-controlled tests, lower permeability changes were recorded (from 11 % to 28 %) since specimens experienced smaller volumetric changes. Absolute permeability versus porosity plots for the compression shear tests are shown in Figures 3.16 and 3.18.

Figure 3.19 presents relationships between absolute permeability and volume changes for the anisotropic unloading shear tests. The permeability of specimen PI 1-D departed from the permeability of all other specimens. Its magnitude was from 15 to 100 times lower and its change during the shear test (4 %) was relatively small (Table 3.5). The results of the test on the specimen were discarded from further analysis. Three specimens, PI 2-D, PI 3 and PI 4, were subjected to deformations beyond the failure point; they displayed permeability increases of 19 %, 30 %, and 42 % respectively. The permeability increases were only 15 %, 6 %, and 28 % respectively, at the moment the specimens reached their maximum strength. The permeability changes were confirmed to be a function of the volumetric changes and the initial permeability. Absolute permeability versus porosity plots for the anisotropic unloading shear tests are shown in Figure 3.20.

3.7 Discussion

3.7.1 Volume Changes

During the triaxial compression shear tests, the specimens contracted at the beginning and then, in most cases, they expanded at higher axial strains. At the end of testing, specimen volume was larger than it had been initially. To explain this volumetric behavior, it is convenient to make reference to the concept of two components of stress states: mean principal effective stress and deviatoric stress. For triaxial cell stress conditions, the mean principal effective stress is defined as:

$$\sigma' = (\sigma'_1 + 2\sigma'_3)/3 \quad 3.5$$

According to the theory of elasticity, the mean component of stress causes "pure" volume change of the specimen whereas the deviatoric component causes shear strain. In the case of sand, the shear strain results in dilation or contraction depending on sand density and confining stress.

In the triaxial compression test (stress path B) on dense sand, both components of the state of stresses increase but their influence on volumetric changes is different. At the beginning of the test, contraction dominates due to the increase in the mean effective stress. At larger deviatoric stresses, dilation due to specimen shear distortion exceeds this contraction and the specimen displays a net increase in volume. Figures 3.11 and 3.12 show behavior of this kind. If sand is loose or confining stresses are high, both components of the state of stress generate soil contraction.

In the anisotropic unloading test (stress path F_U), the vertical and horizontal total stresses remained constant at a pre-chosen ratio and the pore pressure was increased in increments until the specimen failed. During this test, the deviatoric stress was constant (but not equal to zero) and the hydrostatic effective stress was decreased in steps; hence

both components of the state of stress tended to cause specimen expansion. It can be seen in Figure 3.13 that all specimens started to expand at the very beginning of the test. Figure 3.14 illustrates specimen volume changes with changes in mean effective stress. If the deviatoric component of stress had no influence on specimen volume, the plotted changes in specimen volume would be similar to those during isotropic unloading tests (Figures 3.5 and 3.7) at corresponding stress levels. The dilation caused by deviatoric stress is especially pronounced when stress conditions are approaching their state at failure and in the post-failure region. At the beginning of anisotropic unloading, deviatoric stress seems to cause contraction and it hinders the expansion caused by the reduction in the mean effective stress. This observation indicates that the way in which deviatoric stress influences specimen volume (contraction or expansion) depends not only on the specimen density and the magnitude of the mean effective stress but also on the degree of specimen shear distortion.

3.7.2 Absolute Permeability

3.7.2.1 Initial Permeability of Specimens

The initial permeabilities of all specimens measured in this study (as well as results of three tests reported by others) are shown in Figure 3.21. The permeability values are consistent with the permeability increasing with an increase in porosity.

All points in Figure 3.21, representing results of tests performed in this study, come together in two groups. One group is composed mainly of results of tests performed on specimens of series PI and the other group contains most of the results of all other tests. To saturate the specimens of series PI, they were subjected to flushing with water for 40 minutes to 3 hours, under an effective confining stress of 200 kPa, which may have washed out some fine particles and resulted in higher permeabilities.

Specimen PI 4 was tested with frictionless porous stones, which might have led to errors in pressure drop calculations. Specimens of the other series were not flushed before compression.

Another reason for the two groups of results is that the specimens of series PI were vibrated after placement of sand in the mold was finished, with a confining weight of 5 kg on top of the specimens, while the other series were vibrated during preparation, when sand was placed in the mold, without any confining weight on the sand. The differences in preparation could generate differences in specimens (anisotropy) that could lead to generally lower permeabilities measured on specimens of the second group.

The scatter of points on the permeability-porosity plot confirms that it is difficult, during testing, to control all factors having an influence on sand permeability. Although an effort was made to ensure similar grain size distributions for all specimens, the initial permeability of the fourteen specimens varied from $0.42 \mu\text{m}^2$ to $3.8 \mu\text{m}^2$ despite relatively similar porosities ranging from 36.7 % to 39.5 %. Figures 3.2 and 3.3 show the results of the sieve analyses performed after triaxial testing. The grain size distribution curves are fairly similar. The percent smaller than $75 \mu\text{m}$ (U.S. sieve No. 200) was less than 6 % for all specimens. However, the fine material smaller than $75 \mu\text{m}$ may have been different for the two groups of specimens.

In summary, the permeability variation between the two groups of specimens probably arose from differences in grain size distribution of particles smaller than $75 \mu\text{m}$, and possibly from differences in specimen preparation and saturation techniques and equipment head loss.

3.7.2.2 Extrapolation from Laboratory Tests to Reservoir Conditions

The two lines which are plotted in Figure 3.21, passing through the two groups of points, follow Kozeny and Carman's theoretical relationship between permeability and porosity (Equation 2.6). In the equations written in Figure 3.21, the two parameters C and d^2 used in Equation 2.6 are expressed as one constant. Because the difference between the average particle diameters of the two groups of specimens is small, the theoretical difference in permeability between the two groups of specimens arises from constant C , that is, the shape characteristics of the voids and the grains.

The good agreement between Kozeny and Carman's theoretical equation and the measured changes in initial permeability with changes in porosity makes possible extrapolation of the permeability values from laboratory tests to in situ conditions. Such extrapolation is of importance in the case of oil sands, because it is not only difficult to recover relatively undisturbed core from the formation but the in situ porosity of the core can not be restored upon application of a confining pressure in the laboratory. The tests performed on core from the UTF site in this study (Chapter 4) showed in situ porosities varying from 33 % to 35 % with an average value of 34 %. Confining pressures of 6 to 7 MPa, applied in the triaxial cell, reduced specimen disturbance, however, specimen porosity remained higher than the in situ porosity by 1.5 to 2 %.

To perform the extrapolation of the permeability value (k_l) measured in the laboratory on a specimen with a porosity (ϕ_l), coefficient C_o can be calculated from the following equation:

$$C_o = k_l / (\phi_l^3 / (1 - \phi_l)^2) \quad 3.6$$

Using the obtained value of C_o , the in situ permeability (k_i) can be calculated for the in situ porosity (ϕ_i):

$$k_i = C_o \cdot \phi_i^3 / (1 - \phi_i)^2 \quad 3.7$$

To illustrate the permeability extrapolation, the typical experimental results in Section 3.7.2.4 shows that $k_i = 2.69 \mu\text{m}^2$ at $\phi_i = 39 \%$. Coefficient C_o , calculated from Equation 3.6, is equal to $16.9 \mu\text{m}^2$. The initial permeability at the average in situ porosity of 34 % would then be:

$$k_i = 16.9 \cdot 0.34^3 / (1 - 0.34)^2 = 1.52 \mu\text{m}^2$$

These laboratory tests therefore indicate the initial in situ absolute permeability of relatively low fines Athabasca McMurray Formation oil sands is $1.52 \mu\text{m}^2$. Similar extrapolations from laboratory tests can be made for higher fines oil sands.

3.7.2.3 Permeability Changes Caused by Isotropic and Shear Stress Changes

Results of permeability measurements during isotropic stress unloading tests are shown in Figure 3.22, and during triaxial shear tests in Figure 3.23. In these figures, four Kozeny and Carman's theoretical curves are shown for comparison. The curves were drawn through four points with common abscissa (39 % porosity) and different ordinates (1, 2, 3 and $4 \mu\text{m}^2$).

For the specimens with the higher initial permeabilities ($>2 \mu\text{m}^2$), agreement between the test results and the theoretical equations is good. For specimens with lower initial permeabilities ($<2 \mu\text{m}^2$), the experimental curves deviate more from the theoretical plots.

It can be seen in Figures 3.22 and 3.23 that the change in permeability slopes for all the experimental results are similar. On the basis of this observation the slopes of the experimental curves are plotted for comparison in Figures 3.24 and 3.25. The best linear

fits were constructed on both plots and the best fit lines are compared in Figure 3.26. The following relationships were found between permeability change and porosity change:

$$1. \text{ For isotropic unloading: } \Delta k = 32 \cdot \Delta \phi \text{ } \mu\text{m}^2 \quad 3.8$$

$$2. \text{ For triaxial shear: } \Delta k = 29 \cdot \Delta \phi \text{ } \mu\text{m}^2 \quad 3.9$$

Because the slopes of both lines are very similar, the average change in permeability with change in porosity for both types of tests can be expressed with one equation:

$$\Delta k = 31 \cdot \Delta \phi \text{ } \mu\text{m}^2 \quad 3.10$$

It can be concluded that the change in absolute permeability is a function of change in porosity and is independent of the stress path followed to induce this porosity change. This conclusion is for low fines Athabasca McMurray Formation oil sands and limited to the magnitude of porosity changes which would take place during bitumen recovery processes.

3.7.2.4 Calculations of Change in Absolute Permeability for Reservoir Modeling

In reservoir simulation practice the question arises whether the absolute permeability changes brought about by in situ bitumen recovery processes are significant and how they can be calculated when an increase in porosity takes place. The change in porosity can be determined from volumetric strains obtained by geomechanical modeling. Geomechanical modeling simulates stress changes and subsequent volumetric strains which occur in a reservoir during bitumen recovery operations by utilizing geomechanical constitutive models which incorporate the oil sands geomechanical properties obtained from laboratory tests. Two different equations are given below which allow the change in

absolute permeability to be calculated when a change in porosity has been determined by modeling.

Procedure Based on Kozeny and Carman Theory

The results of tests performed in this study, that displayed an unique relationship between permeability change and porosity change independent of initial permeability values and stress paths followed, indicate that the following Kozeny and Carman equation can be used to calculate permeability increase:

$$k = Co \cdot \phi^3 / (1 - \phi)^2 \quad 3.11$$

On the basis of Equation 3.11, the increased absolute permeability induced by an increase in porosity can be calculated from equation:

$$k_2 = k_1 + \Delta k = k_1 + Co \cdot (\phi_2^3 / (1 - \phi_2)^2 - \phi_1^3 / (1 - \phi_1)^2) \mu m^2 \quad 3.12$$

where: k_1 - initial (in situ) permeability, μm^2

k_2 - increased permeability, μm^2

ϕ_1 - initial (in situ) porosity

ϕ_2 - increased porosity

Co - coefficient

Co can be determined based on the experimental findings discussed in Section 3.7.2.3 where it was shown that all the ratios $\Delta k / \Delta \phi$ are similar. The Kozeny and Carman equation with this slope at a typical experimental ϕ of 39 % has the coefficient $Co = 16.9 \mu m^2$. This coefficient gives an in situ permeability of $1.52 \mu m^2$ at the in situ porosity of 34 %.

The increase in absolute permeability can then be calculated from Equation 3.12:

$$k_2 = k_1 + 16.9 \cdot (\phi_2^3 / (1 - \phi_2)^2 - \phi_1^3 / (1 - \phi_1)^2) \mu m^2$$

With an initial in situ ϕ_1 of 34 % and a volumetric strain of 6 % (this amount of volumetric strain is typical during shear as will be shown later with tests on UTF core), the increased porosity can be calculated from Equation 2.9:

$$\phi_2 = (\phi_1 + \epsilon_v)/(1 + \epsilon_v) = (0.34 + 0.06)/(1 + 0.06) \cdot 100 \% = 38 \%$$

Taking the initial in situ $k_1 = 1.52 \mu\text{m}^2$ from above:

$$\begin{aligned} k_2 &= (1.52 + 16.9 \cdot (0.38^3/(1-0.38)^2 - 0.34^3/(1-0.34)^2)) \mu\text{m}^2 \\ &= (1.52 + 0.89) \mu\text{m}^2 \\ &= 2.41 \mu\text{m}^2 \end{aligned}$$

Therefore this amount of volumetric strain has increased the absolute permeability by 59%.

Empirical Procedure Based on Test Results

A more direct, simpler procedure for the calculation of changes in absolute permeability is to directly use Equation 3.10 which is based on the test results. A new permeability for Athabasca oil sands would be calculated with the equation:

$$k_2 = k_1 + Da \cdot (\phi_2 - \phi_1) \quad 3.13$$

where: $Da = 31 \mu\text{m}^2$ (from Equation 3.10)

This latter method gives slightly larger permeability increases than the Kozeny and Carman procedure but is simpler and appears to be more accurate as it fits the laboratory results better. It also does not vary with the initial porosity and did not require a choice of porosity as Equation 3.12 did.

With the initial in situ $\phi_1 = 34 \%$ and $k_1 = 1.52 \mu\text{m}^2$ and a volumetric strain of 6 %,

$$\begin{aligned}
 k_2 &= (1.52 + 31 \cdot (0.38 - 0.34)) \mu\text{m}^2 \\
 &= (1.52 + 1.24) \mu\text{m}^2 \\
 &= 2.76 \mu\text{m}^2
 \end{aligned}$$

This is an increase in absolute permeability of 82 %.

3.7.2.5 Comparison with Other Experimental Works

Initial Permeability

Agar (1986) measured the absolute permeability of remolded samples of oil-free Athabasca McMurray Formation oil sands. The sample was recomacted in the consolidometer to a porosity of 37 % and was then confined under an effective stress of 3 MPa. The permeability of this specimen at room temperature (20 °C) was $3.0 \mu\text{m}^2$, which falls within the range of permeabilities measured in this study (Figure 3.21).

Agar (1986) also performed one test on an undisturbed Athabasca oil sands core specimen. It was confined in a consolidometer under an effective vertical stress of 2 MPa and deprived of bitumen through flushing with benzene. The porosity of the flushed specimen was 35 % and its initial permeability to water was $4.1 \mu\text{m}^2$.

The absolute permeability of the Athabasca oil sands reported by Wong et al. (1991) measured on extracted core with a porosity of 36.6 % was $0.87 \mu\text{m}^2$ which can be placed in the lower range of permeabilities (second group of points in Figure 3.21) obtained in these tests.

The absolute permeabilities measured by Agar and Wong fall within the same range of magnitudes as those measured in this study (Figure 3.21). It can be further concluded that absolute permeabilities measured on reconstituted oil sands or on oil sand cores are not appreciably different if porosities are similar.

Change in Permeability

Agar (1986) continued his absolute permeability test on an extracted core over a range of effective stresses from 2 MPa to 18 MPa. The permeability changed from $4.1 \mu\text{m}^2$ to $2.2 \mu\text{m}^2$ during loading and then increased to $2.5 \mu\text{m}^2$ during unloading back to 2 MPa. The change of permeability over the relatively high range of stresses was not large (about 12%) since the greater part of the elastic volumetric deformations takes place at lower confining stresses. It must be mentioned that Agar's tests were performed in the consolidometer where the lateral deformations of the specimen were restricted.

Wong et al.(1991) plotted absolute permeability against effective confining stress. The permeability was measured in a constant flow rate test on a preserved, bitumen-extracted core specimen. For an effective confining pressure change from about 2 MPa to 180 kPa, the absolute permeability increased from about $0.87 \mu\text{m}^2$ to $1.68 \mu\text{m}^2$, that is, by 93 %.

In Figure 3.26, changes in permeability versus changes in porosity from Agar's and Wang's tests are compared to the best linear fits to data obtained in this study. The slopes of curves from both tests, performed on extracted core, differ substantially from slopes of curves obtained in our experimental study. The large permeability changes during the tests on cores could not result only from changes in porosity and other test factors must be influencing the results. It is significant that in case of Agar's test, the slope of the plot decreased and became similar to the slopes of experimental plots obtained in this study as porosity changes increased. Agar's and Wong's results can not be extrapolated over a wider range of porosities. To determine the factors that caused these large absolute permeability changes, more tests on extracted cores or on natural, bitumen-free oil sands cores need to be performed. It is speculated that the core extraction processes could involve changes in specimens which allowed fines movement and led to the measured high permeability changes.

The differences in the rates of change in permeability may also be partially due to the difference in sand fabric between reconstituted specimens and core specimens. It would appear, however, that the locked structure of in situ oil sands may have a greater volume increase during shear which would result in a larger permeability increase but probably a similar rate of change with the increase in porosity.

No data was found in the literature on absolute permeability changes during triaxial shear tests.

3.7.3 Shear Strength

Investigation of the shear strength of the oil sands was not the main objective of this experimental program; nevertheless, recorded data allowed for the appropriate calculations and for plotting stress-strain curves. A summary of the compression shear test results is presented in Table 3.4 and the anisotropic unloading test results are shown in Table 3.5.

A principal stress ratio failure criterion, defined as the maximum ratio of vertical effective stress to confining effective stress, is preferable to a deviatoric stress criterion, defined as the maximum deviatoric stress. The maximum effective stress ratio criterion can provide a better correlation of specimen shear strength as measured in different types of tests. The maximum deviatoric stress criterion could not be applied for anisotropic stress unloading tests since its magnitude was kept constant during testing. However, plotting the deviatoric stress versus axial strain provides other information useful for analyses: it shows clearly that the maximum deviatoric stress that a specimen can withstand, before failing in shear, depends on the effective confining stress. The higher the confining stress the higher deviatoric stress a soil can resist (Figures 3.28, 3.30). The effective stress ratio versus axial strain plot shows that at lower confining stresses, higher

stress ratios are reached before failure (Figure 3.27, 3.29). This indicates that the failure envelope is not linear and that the angle of shearing resistance is a function of applied stresses.

The effective stress ratio against axial strain plots for the compression strain-controlled tests are shown in Figure 3.27. The deviatoric stress against axial strain plots for the same four tests are shown in Figure 3.28. The two specimens that dilated during shear (Sn 1-D and Sn 2-D) failed at 4.5 % axial strain and reached a peak effective stress ratio of 4.4. Figure 3.31 shows the stress paths followed and the failure envelope in the $s'-t$ stress field.

The compression stress-controlled test results are shown in Figures 3.29 and 3.30. These tests could not be continued in the post-peak strain region. The last reading taken when pressure was increased in steps was considered to correspond with the maximum strength. The relationship between effective confining stress and effective stress ratio or deviatoric stress was the same as observed in the strain-controlled tests. At higher confining stresses, specimens appear to be stronger than in strain-controlled tests. One reason for this was the lower density of the two accidentally-unloaded specimens (Sn 3-D and Sn 4-D). The failure envelope and stress paths followed are shown in Figure 3.32.

The anisotropic unloading test results, the effective stress ratio against axial strain, are shown in Figure 3.33. Two specimens, PI 1-D and PI 2-D, tested under initial confining stresses of 920 and 845 kPa were unloaded to effective confining stresses of 95 kPa and 300 kPa. Axial deformations were 22 % and 14 % respectively. These specimens experienced a volumetric change of approximately 1 % and behaved like loose sand. Specimens PI 1-D and PI 2-D withstood higher stress ratios (4.5 and 3.9) than specimens PI 3 and PI 4, tested under initial effective stresses of 1470 kPa and 2000 kPa respectively. Effective stress ratio peak values for the last two specimens were 3.5 and

3.8. A low stress ratio decrease with further increases in axial strain was noted during these tests. One specimen (PI 1) failed early, as the result of an excessive back pressure increase. The failure envelope and stress paths for anisotropic unloading tests are shown in Figure 3.34.

The summary of shear strength tests is shown in Figure 3.35, where points representing the state of stresses at maximum effective stress ratios are plotted on the $s' - t$ stress field. Two failure envelopes are shown to indicate possible differences between triaxial compression and anisotropic unloading by pore pressure injection tests. To draw these curves, the results of the two strain-controlled tests conducted at higher confining stresses were not taken into account, since the densities of these specimens were much smaller than all other specimens. The results of one pore pressure injection test was also discarded because the last reading in this test was taken before the peak stress was reached. Both envelopes exhibit distinct curvature which alters with changes in stress. The test data for all types of tests give an angle of shearing resistance ϕ' of 42° at low effective confining stresses. At higher stresses, the slope of the tangent to the failure envelopes decreases and the angle of shearing resistance varies from 31° for pore pressure injection tests to 35° for compression shear tests. The difference in the strength behavior of the oil sands specimens under various stress paths can be attributed to differences in volumetric changes resulting from changing stresses, as discussed in subsection 3.7.1. Following stress path F_u , specimens PI 3 and PI 4 were brought to failure at comparable confining stresses to specimens Ss 1-D and Ss 3-D and demonstrated greater expansion and lower stress ratios at failure than specimens Ss 1-D and Ss 3-D.

The angle of shear resistance at failure (42°) is much lower than the maximum recorded (60°) for undisturbed oil sands (Dusseault and Morgenstern, 1979). The high angle of friction is a result of the characteristic interpenetrative or "locked" structure of the

Athabasca McMurray Formation oil sands. In the reconstituted oil sand specimens, this special fabric is not present and the original density cannot be restored without grain crushing. Therefore, the strength of reconstituted oil sands is similar to other fairly uniformly graded, fine, dense sands with angular grains.

3.8 Summary

3.8.1 Observations

1. The absolute permeability of reconstituted bitumen-free oil sands specimens compacted to porosities ranging from 36.7 % to 39.5 % varied from $0.4 \mu\text{m}^2$ to $3.8 \mu\text{m}^2$. The variations in absolute permeability did not correspond strictly with variations in porosity.
2. The isotropic unloading from a 4 MPa to 0.2 MPa effective confining stress resulted in an average increase of 1.4 % in specimen volume. The measured absolute permeability increase varied from 13 % to 70%.
3. The volume changes during triaxial shear, as the result of dilation, is more pronounced in the close to peak and post-peak stress ranges. While the average volume increase at failure for dilating specimens was about 1.2 %, it increased to 3 % at 12 % axial strain.
4. The extreme absolute permeability changes measured during triaxial shear ranged from -46 % for a specimen contracting by 2 % to +42 % for a specimen dilating by 2.6 %.
5. The magnitude of the volume change at the moment of specimen failure depends on the stress path it has followed to approach the state of stresses at failure.

3.8.2 Conclusions

1. Experimental results of absolute permeability can be extrapolated from laboratory to in situ porosities using Kozeny and Carman's theory. The number of tests and the variation in the initial densities and grain size distributions, however, do not allow a statistical evaluation of data quality and model fit to better prove this extrapolation.
2. Absolute permeability change is a function of pore volume change and is independent of the stress path a specimen has followed to undergo this volume change. It should be realized, however, that the amount of volume change is a function of stress path.
3. For reservoir modeling purposes, a new permeability resulting from an increase in porosity of the Athabasca McMurray Formation oil sands can be calculated from the equation:

$$k_2 = k_1 + 16.9 \cdot (\phi_2^3 / (1 - \phi_2)^2 - \phi_1^3 / (1 - \phi_1)^2)$$

4. The new permeability also can be calculated by using the equation:

$$k_2 = k_1 + 31 \cdot (\phi_2 - \phi_1)$$

which agrees better with the experimental results.

5. The absolute permeability measured on reconstituted oil-free oil sands and on extracted oil sand cores fall within the same range when the porosities are similar.
6. The failure envelope of the reconstituted oil-free Athabasca oil sands is curvilinear. At low effective confining stresses (up to 250 kPa), the angle of shearing resistance ϕ' is equal to 42°. At higher effective confining stresses, its

value is lower and is a function of the stress path followed in the triaxial cell. The shear strength of the reconstituted oil-free Athabasca oil sands is similar to other fine, dense sands with uniform gradation of angular grains.

Table 3.1 Specimen Data - Series PI

	PI 1	PI 2	PI 3	PI 4
Initial Parameters				
Diameter, mm	38.1	38.1	38.1	38.1
Height, mm	73.5	76.3	78.5	80.5
Water Content, %	16.6	16.1	16.6	15.3
Saturation Ratio	0.63	0.64	0.65	0.6
Dry Weight, g	130.6	138	141.4	144.9
Dry Density, g/cm ³	1.56	1.59	1.58	1.58
Porosity, %	41.0	40.1	40.3	40.4
Void Ratio	0.70	0.67	0.676	0.678
Saturation				
Flushing Time (Q = 400 ml/hr), min	180	40	180	60
Back Pressure, kPa	3000	3000	3000	3000
Parameter B (after minimum 12 hr saturation)	0.87	0.87	0.88	0.90
Compressibility				
a) Effective Conf. Stress = 400 kPa				
Coefficient of Compressibility, 10 ⁻⁶ kPa ⁻¹	8.3(600 kPa)	8.3	10.7	10.2
Theoretical Parameter B	0.978	0.978	0.983	0.982
b) Effective Conf. Stress = 4000 kPa - First Cycle				
Coefficient of Compressibility, 10 ⁻⁶ kPa ⁻¹	4.3	3.4	3.9	3.9
Theoretical Parameter B	0.959	0.951	0.956	0.956
c) Effective Conf. Stress = 4000 kPa - Second Cycle				
Coefficient of Compressibility, 10 ⁻⁶ kPa ⁻¹	3.3	2.7	2.6	2.5
Theoretical Parameter B	0.948	0.939	0.937	0.935

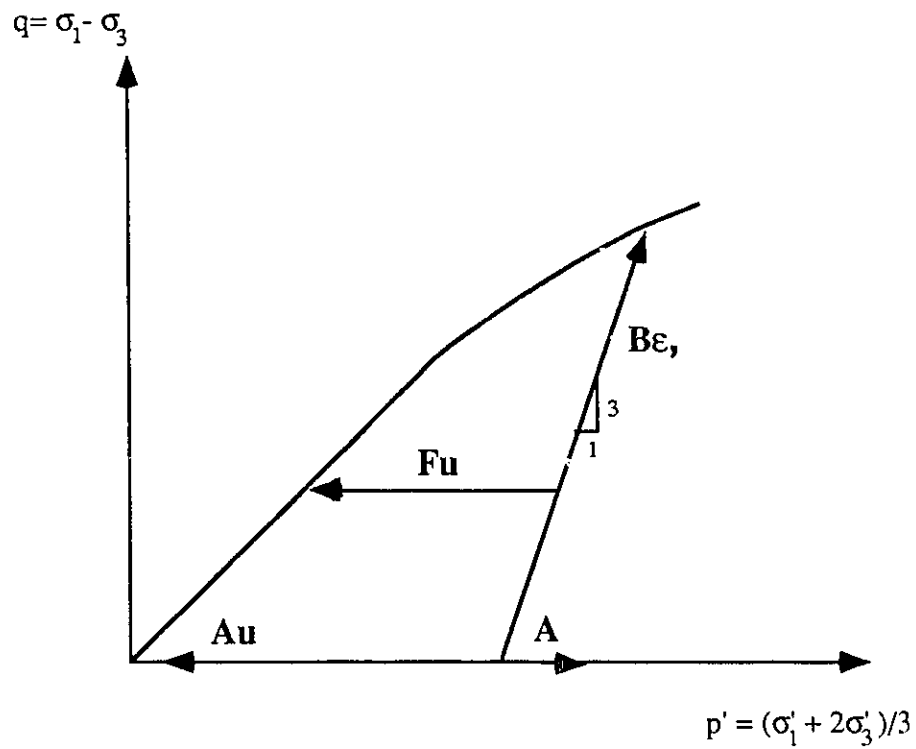
Table 3.2 Specimen Conditions After Consolidation						
Specimen	Bulk Density (g/cm ³)	Dry Density (g/cm ³)	Relative Density (%)	Porosity ϕ_o (%)	Void Ratio, e_o	Max. Effective Conf. Stress (kPa)
Sn1-D	2.05	1.69	92	36.7	0.58	4030
Sn2-D	2.05	1.69	92	36.7	0.58	4120
Sn3-D	2.02	1.64	79	38.3	0.62	4240
Sn4-D	2.02	1.63	75	38.7	0.63	530
Sn5-D	2.03	1.65	79	38.3	0.62	4360
Ss1-D	2.02	1.64	75	38.7	0.63	4050
Ss2-D	2.04	1.67	86	37.5	0.60	4120
Ss3-D	2.04	1.67	86	37.5	0.60	4020
Ss4-D	2.02	1.64	75	38.7	0.63	3970
PI1-D	2.04	1.67	86	37.5	0.60	1000
PI2-D	2.03	1.66	82	37.9	0.61	4400
PI3-D	2.05	1.68	89	37.1	0.59	1000
PI1	2.00	1.60	70	39.5	0.65	4040
PI2	2.02	1.63	80	38.4	0.62	3990
PI3	2.01	1.62	77	38.7	0.63	4280
PI4	2.01	1.62	77	38.8	0.63	4160

Table 3.3 Isotropic Unloading Test Results					
Specimen	Initial Absolute Permeability (μm^2)	Isotropic Effective Stress Change (kPa)	Volume Change (%)	Permeability Change (%)	
Sn1-D	1.0	4050 - 115	1.42	32	
Sn2-D	x	4120 - 230	1.21	x	
Sn3-D	2.3	4240 - 160	1.40	63	
Sn4-D	0.67	x	x	x	
Sn5-D	0.53	4410 - 370	1.11	70	
Ss1-D	x	x	x	x	
Ss2-D	x	x	x	x	
Ss3-D	x	x	x	x	
Ss4-D	x	x	x	x	
PI1-D	x	x	x	x	
PI2-D	0.42	3200 - 500	1.08	58	
PI3-D	0.43	990 - 270	0.44	25	
PI1	3.8	4000 - 440	1.24	3.0	
PI2	3.3	3920 - 290	1.28	6.5	
PI3	3.5	4190 - 240	1.53	13	
PI4	2.0	3990 - 310	1.47	11	

Specimen	Initial Absolute Permeability (μm^2)	Effective Confining Stress (kPa)	Axial Strain at Failure (%)	Volume Change at Failure (%)	Deviator Stress ($\sigma_1 - \sigma_3$) _f (kPa)	Stress Ratio (σ_1 / σ_3) _f	Maximum Volume Change (%)	Maximum Permeability Change (%)
Sn1-D	1.3	150	4.2	1.40	490	4.47	3.12	27
Sn2-D	x	150	4.2	0.95	480	4.30	2.41	x
Sn3-D	3.8	450	4.9	0.18	1180	3.62	-2.16	-33
Sn4-D	0.94	530	4.8	-1.98	1220	3.30	-2.40	-46
Ss1-D	1.1	320	3.2	1.10	1110	4.46	1.10	17
Ss2-D	1.1	150	3.6	1.45	560	4.75	1.45	21
Ss3-D	0.85	550	4.5	0.74	1680	4.06	0.74	11
Ss4-D	1.0	120	7.1	2.15	430	4.60	2.15	28

Note: Sn-D Compression Strain Controlled Test
Ss-D Compression Stress Controlled Test

Specimen	Initial Absolute Permeability (μm^2)	Initial Stress Ratio	Effective Conf. Stress Change (kPa)	Effective Conf. Stress at Failure (kPa)	Axial Strain at Failure (%)	Volume Change at Failure (%)	Stress Ratio at Failure	Permeability Change at Failure (%)	Maximum Volume Change (%)	Maximum Permeability Change (%)
P11-D	0.03	1.4	920 - 95	110	2.7	0.90	4.48	x	1.02	3.9
P12-D	0.52	2.2	845 - 300	360	2.9	0.60	3.90	15	0.97	19
P13-D	0.47	x	x	x	x	x	x	x	x	x
P11	3.8	2.0	1980 - 870	870	2.0	0.64	3.25	5	0.64	5.2
P12	3.4	x	x	x	x	x	x	x	x	x
P13	3.7	2.0	1470 - 430	520	3.6	1.29	3.77	6	3.75	30
P14	1.6	2.0	2000 - 670	710	6.2	1.34	3.54	28	2.59	42



- A - Isotropic Consolidation
- Au - Isotropic Unloading by Pore Pressure Injection
- Fu - Anisotropic Unloading by Pore Pressure Injection
- Be - Compression
- Bσ - Compression

Figure 3.1 Stress Paths Followed During Triaxial Tests on Reconstituted Oil-Free Oil Sands Specimens

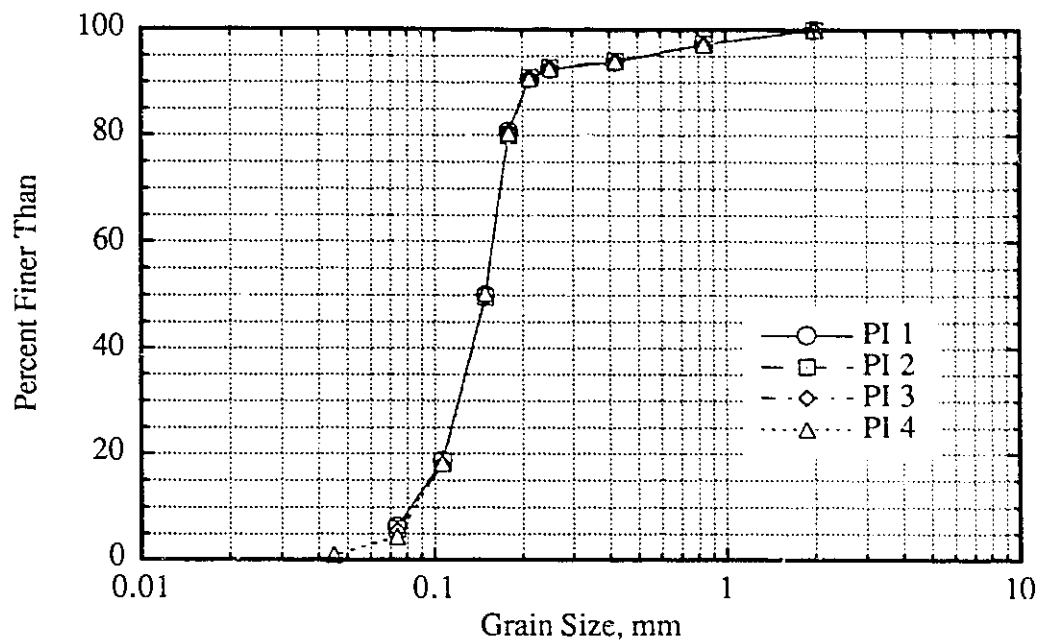


Figure 3.2 Grain Size Distributions- PI Specimens

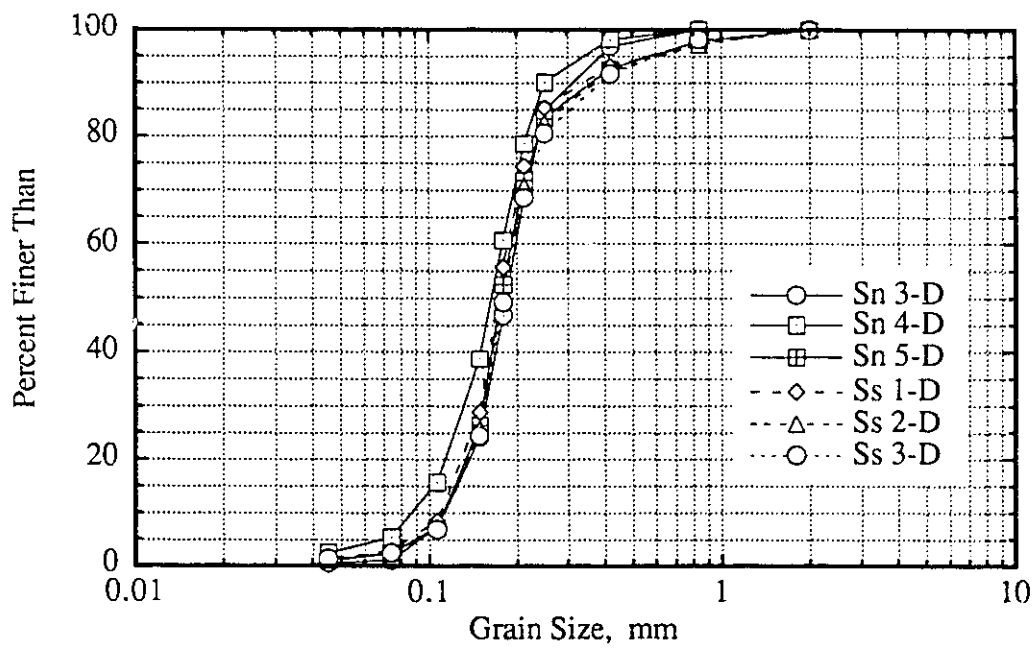


Figure 3.3 Grain Size Distributions - Sn-D and Ss-D Specimens

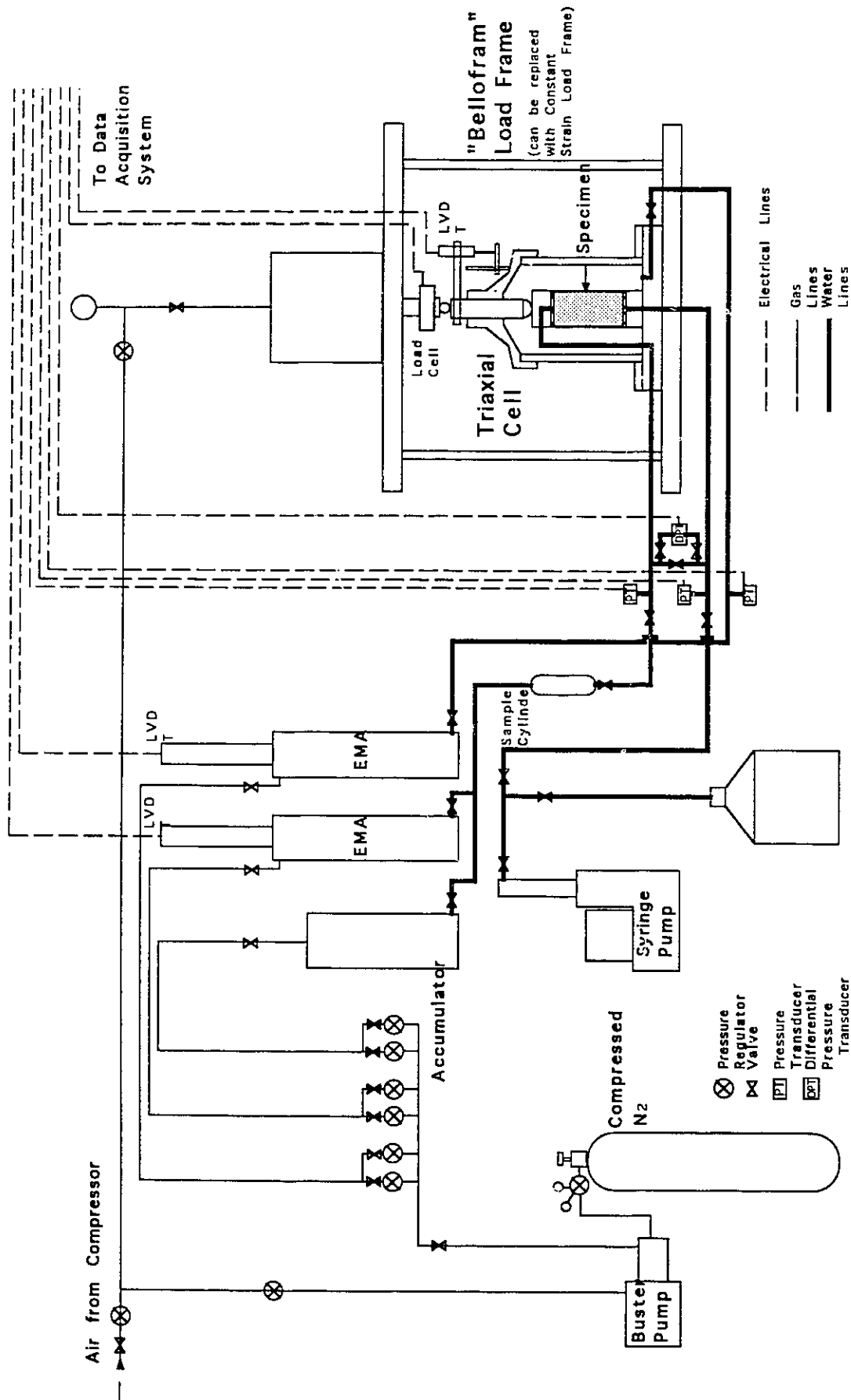


Figure 3.4 Schematic Diagram of the Triaxial System for Permeability Measurement

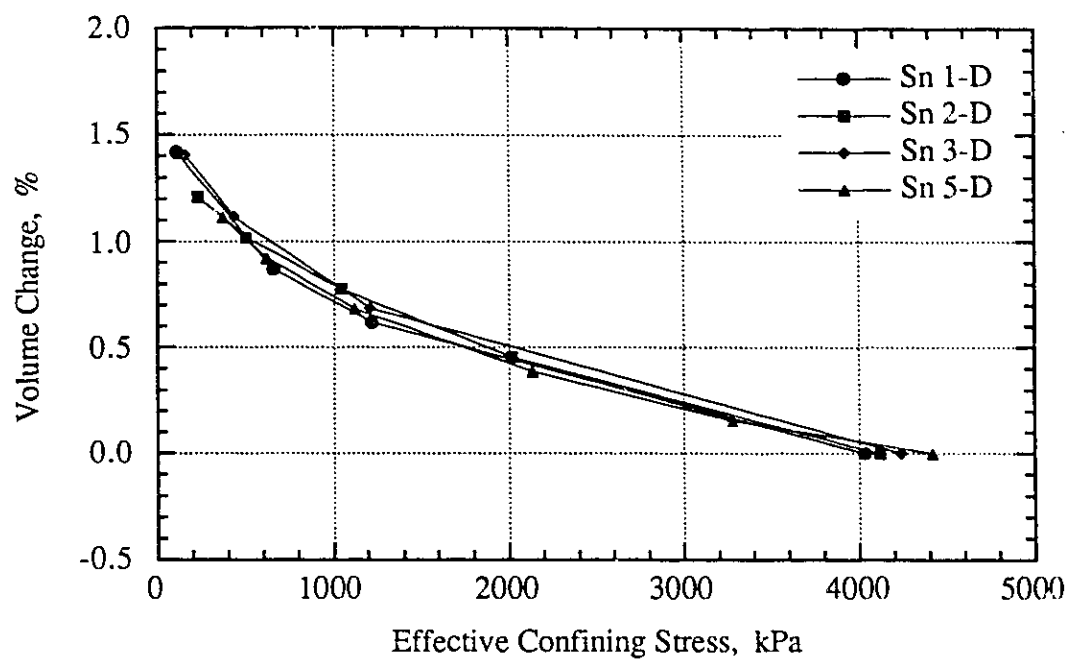


Figure 3.5 Volume Change During Isotropic Unloading

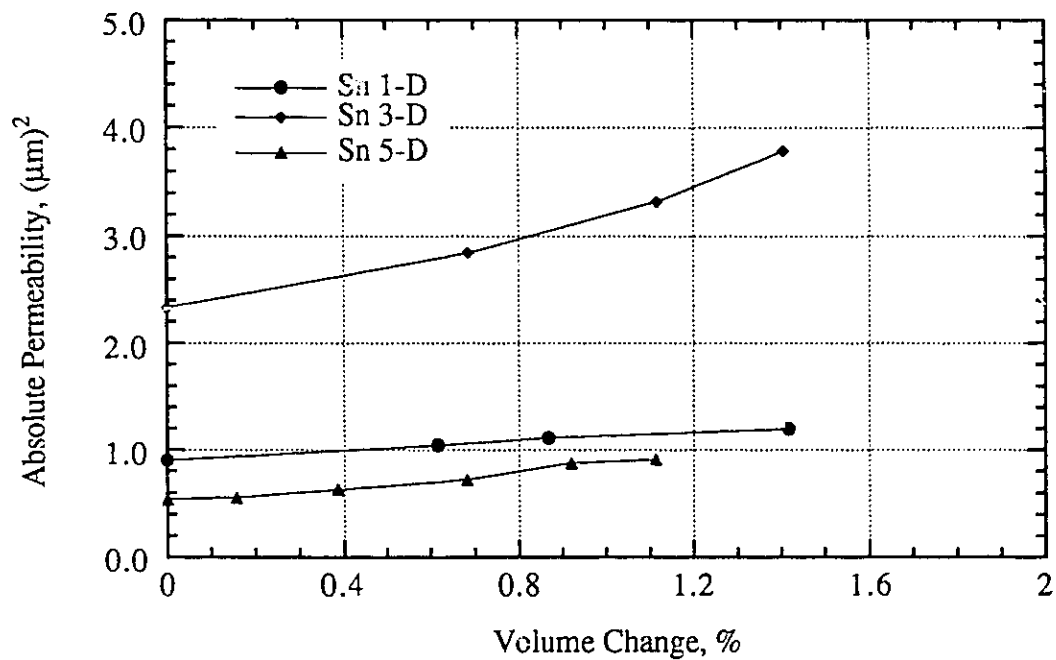


Figure 3.6 Absolute Permeability - Volume Change, Isotropic Unloading

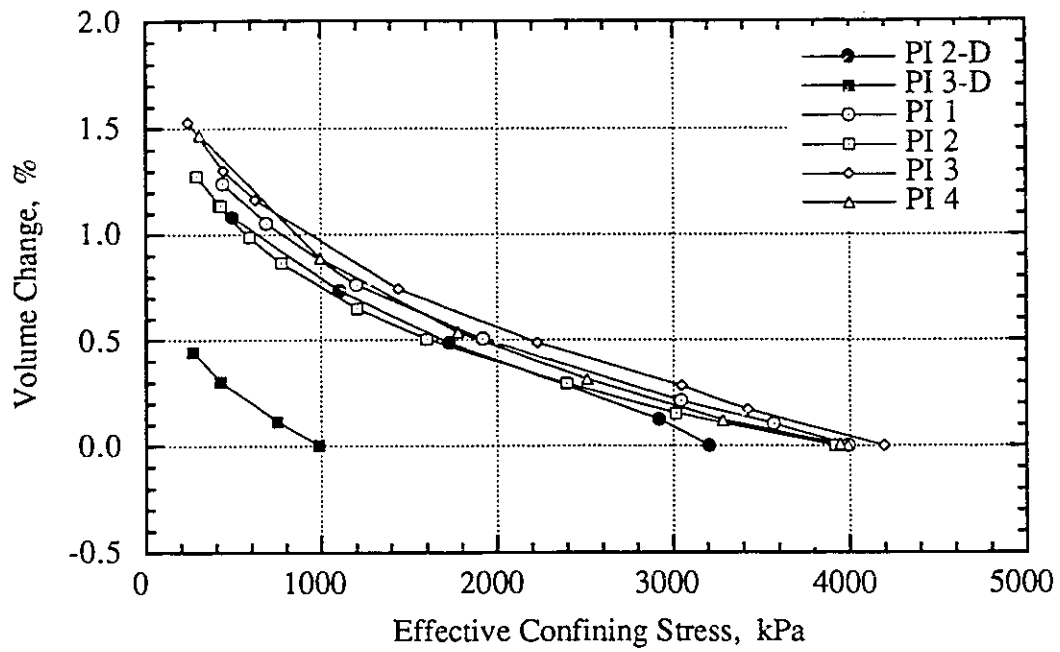


Figure 3.7 Volume Change During Isotropic Unloading

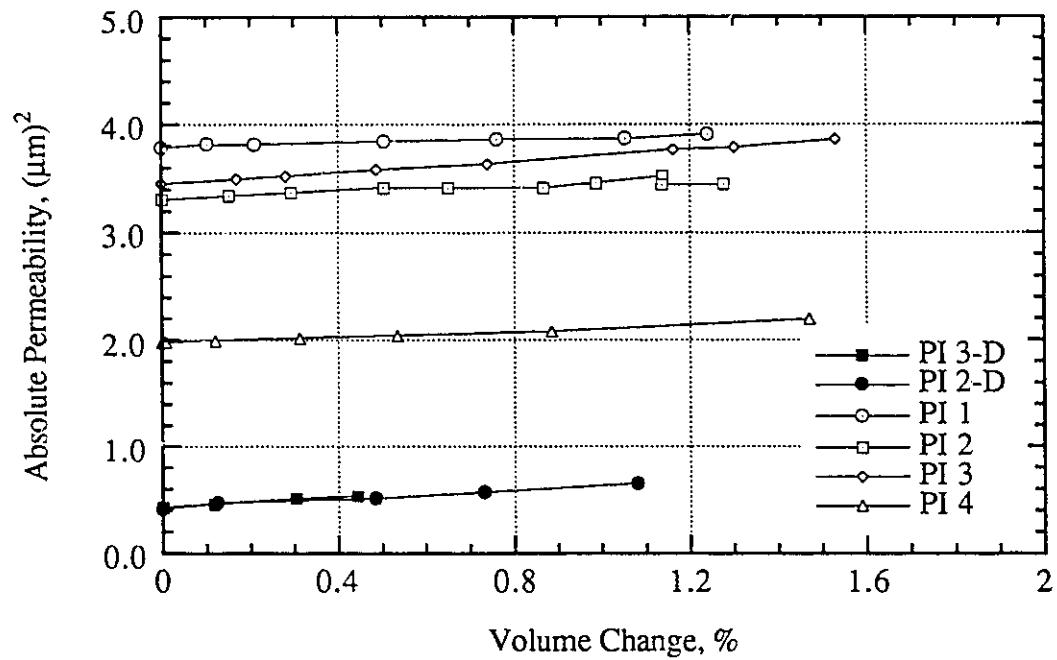


Figure 3.8 Absolute Permeability - Volume Change, Isotropic Unloading

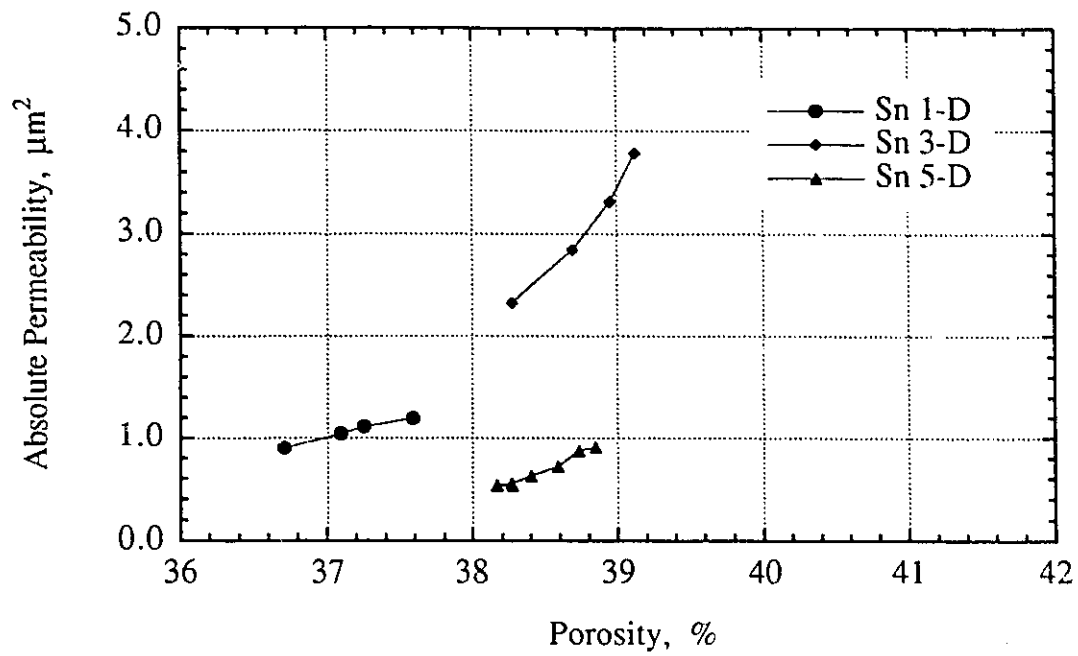
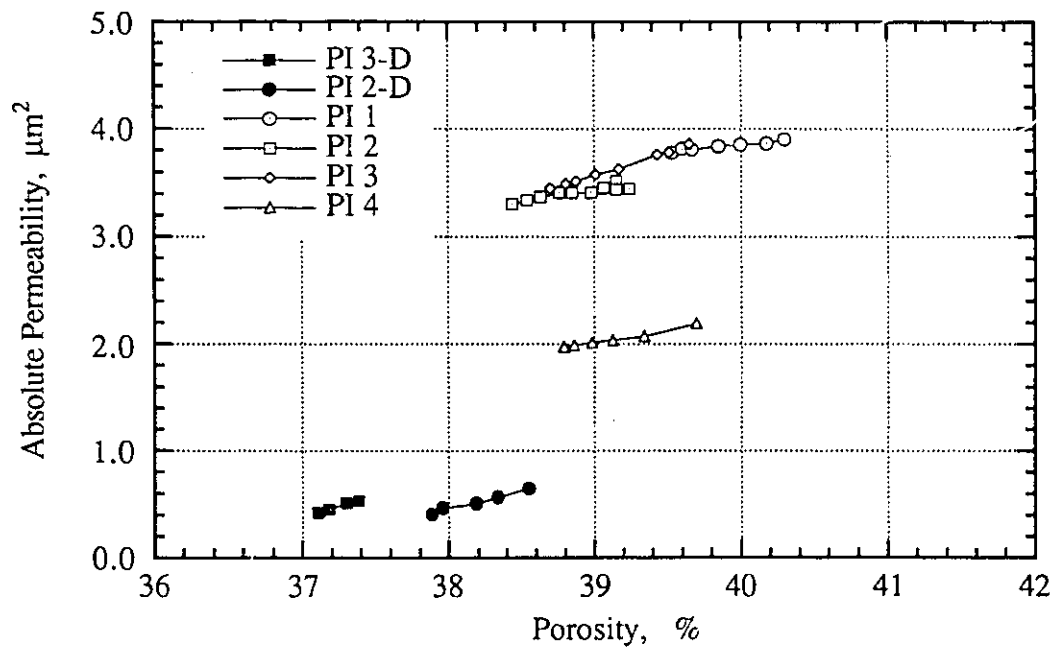
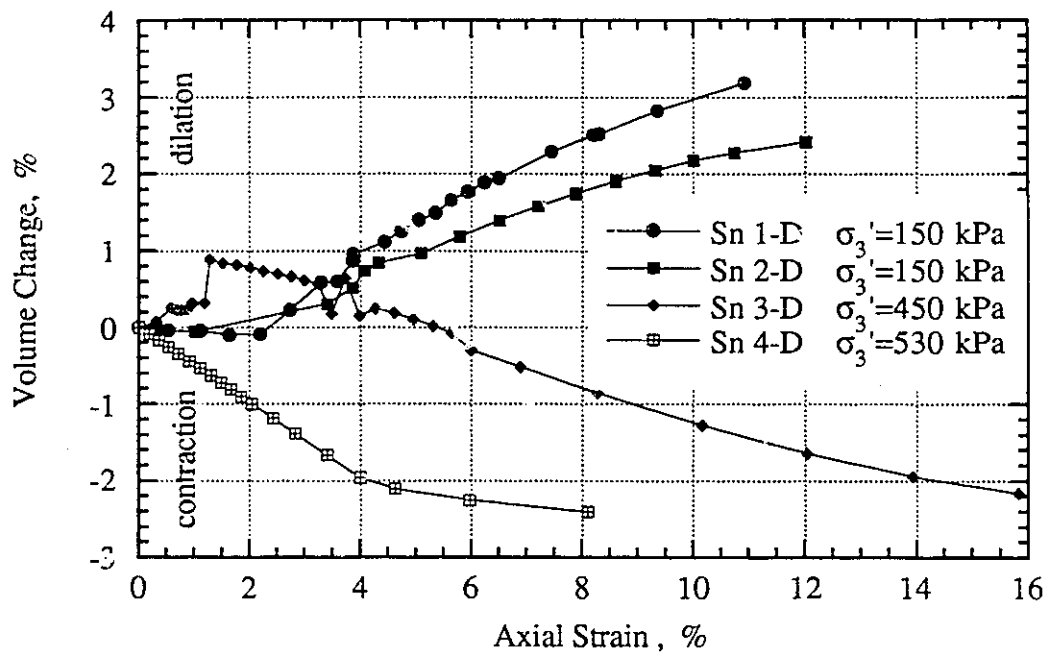
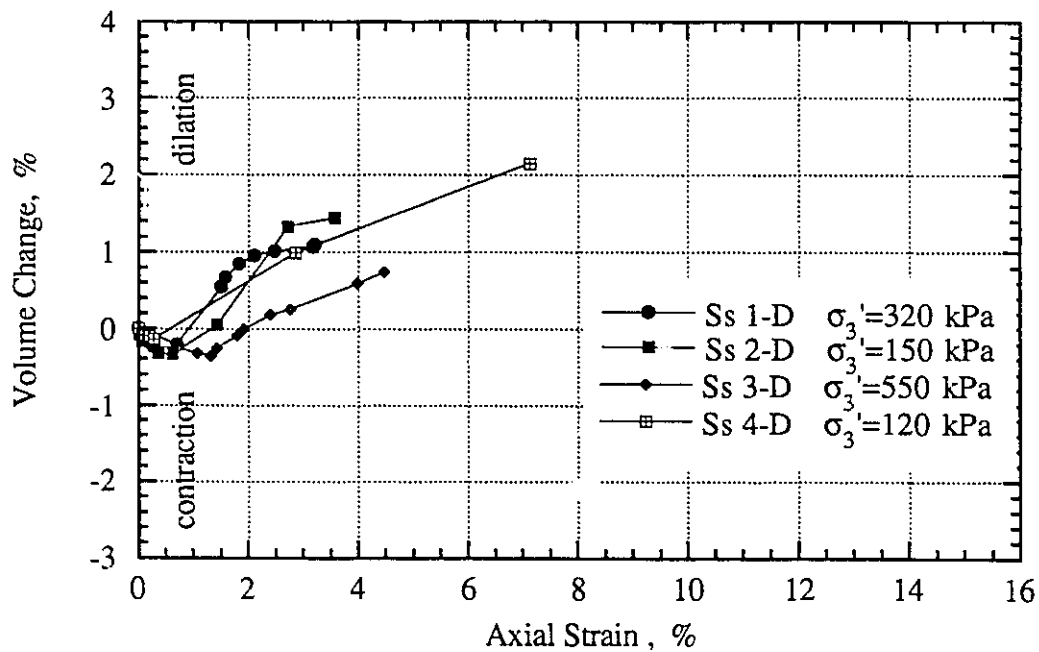


Figure 3.9 Absolute Permeability - Porosity, Isotropic Unloading



Figure 3.11 Stress Path B_ϵ , Volume ChangeFigure 3.12 Stress Path B_σ , Volume Change

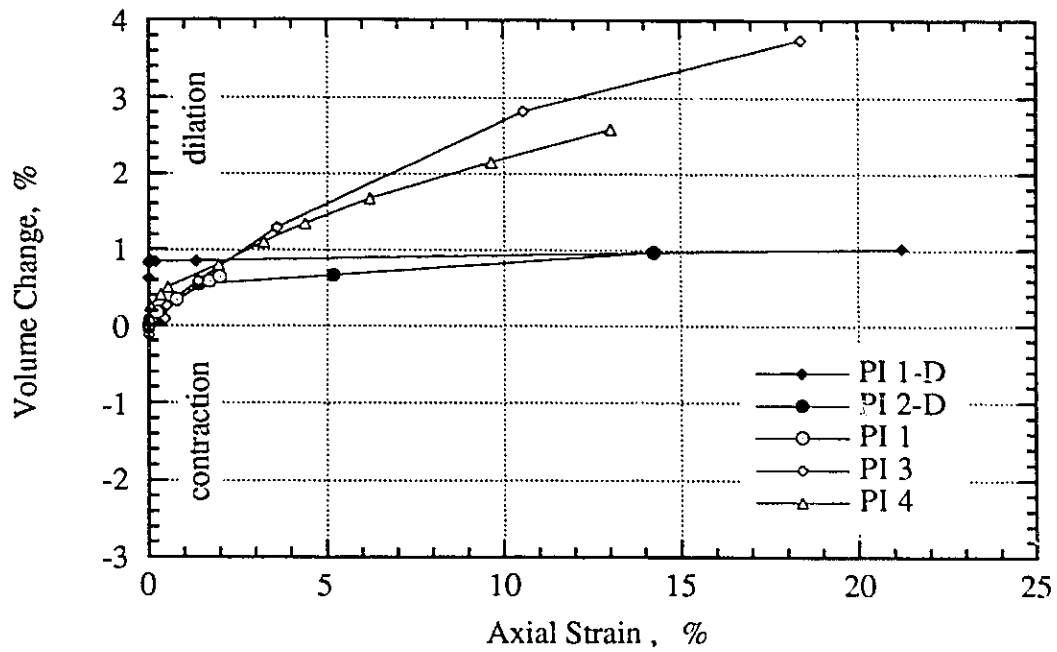
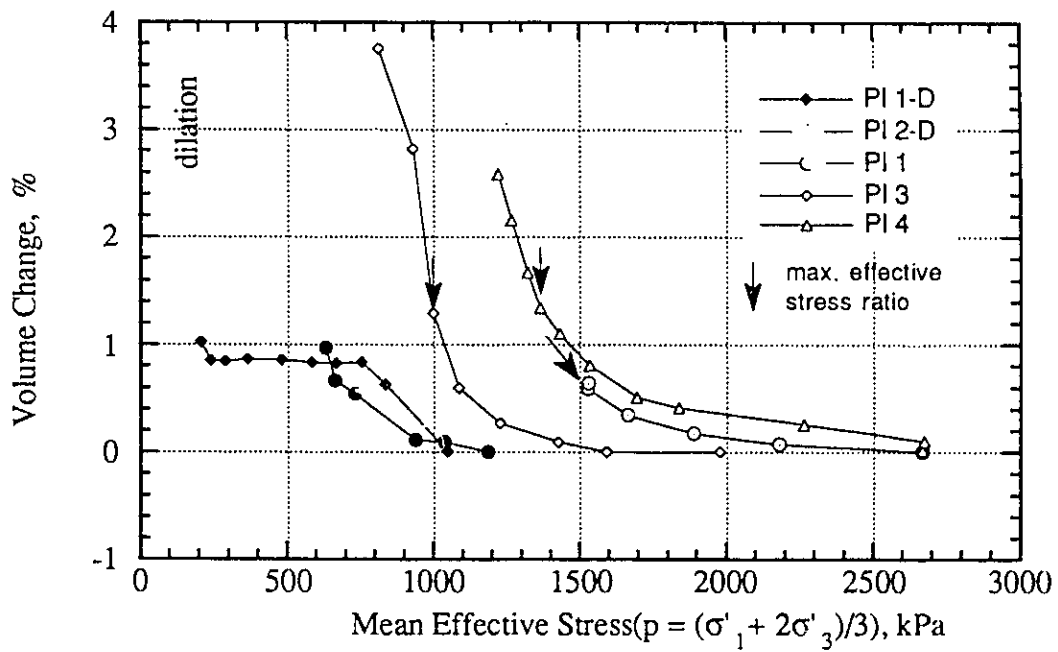
Figure 3.13 Stress Path F_u , Volume Change

Figure 3.14 Volume Change During Anisotropic Unloading

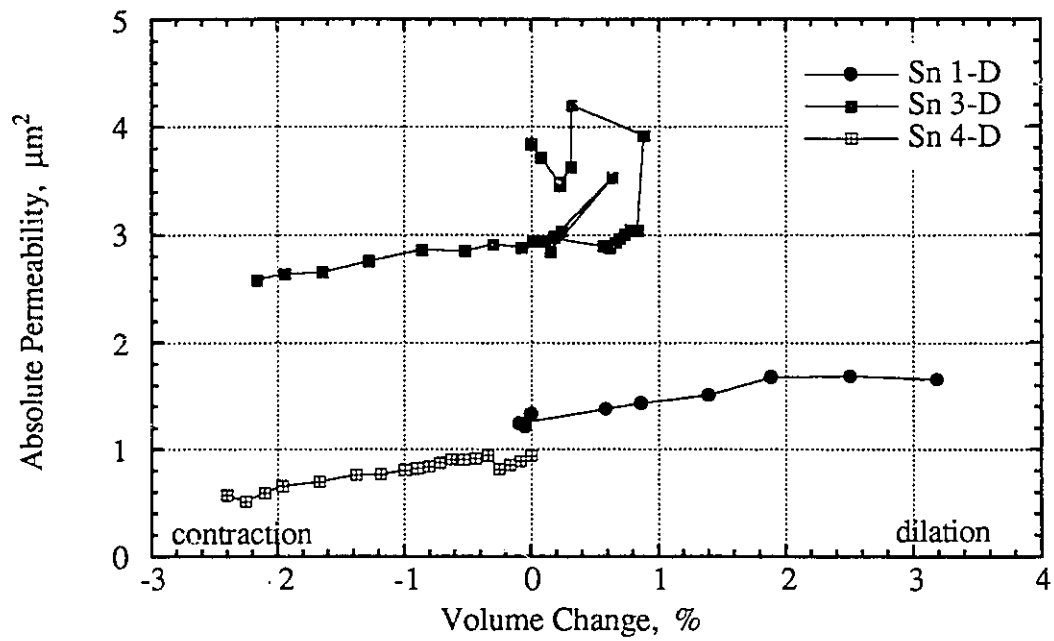


Figure 3.15 Stress Path B_ϵ , Absolute Permeability - Volume Change

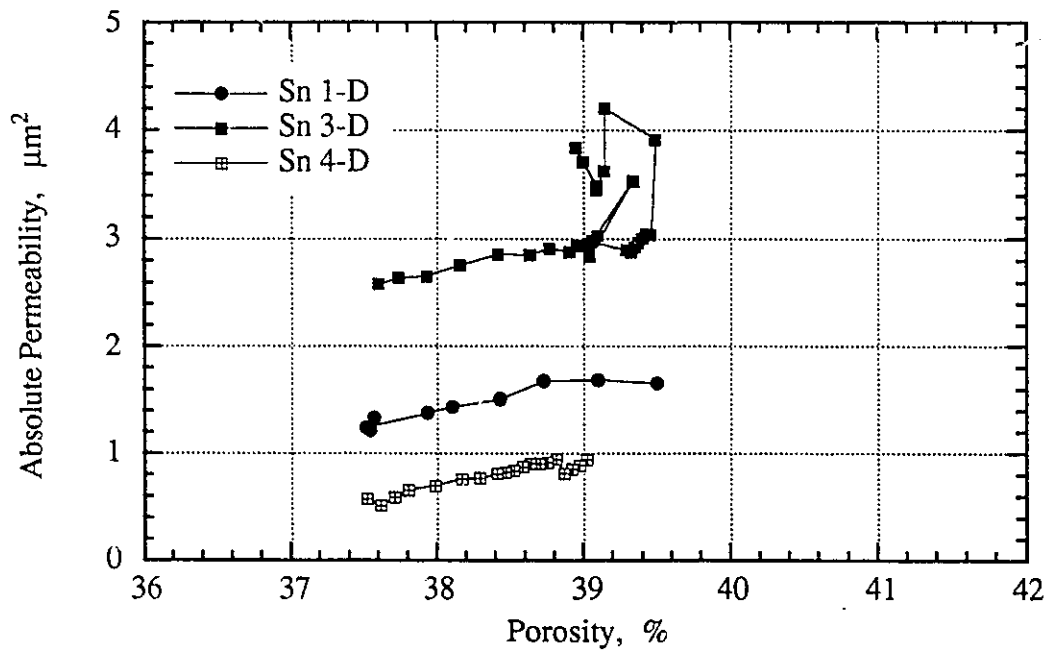


Figure 3.16 Stress Path B_ϵ , Absolute Permeability - Porosity

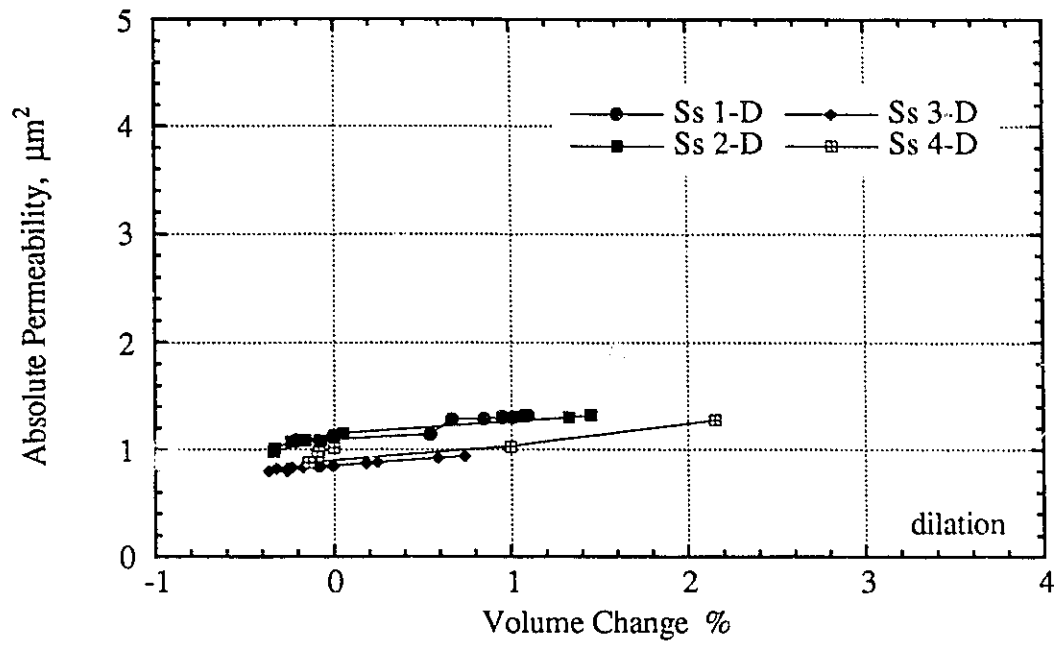


Figure 3.17 Stress Path B_σ , Absolute Permeability - Volume Change

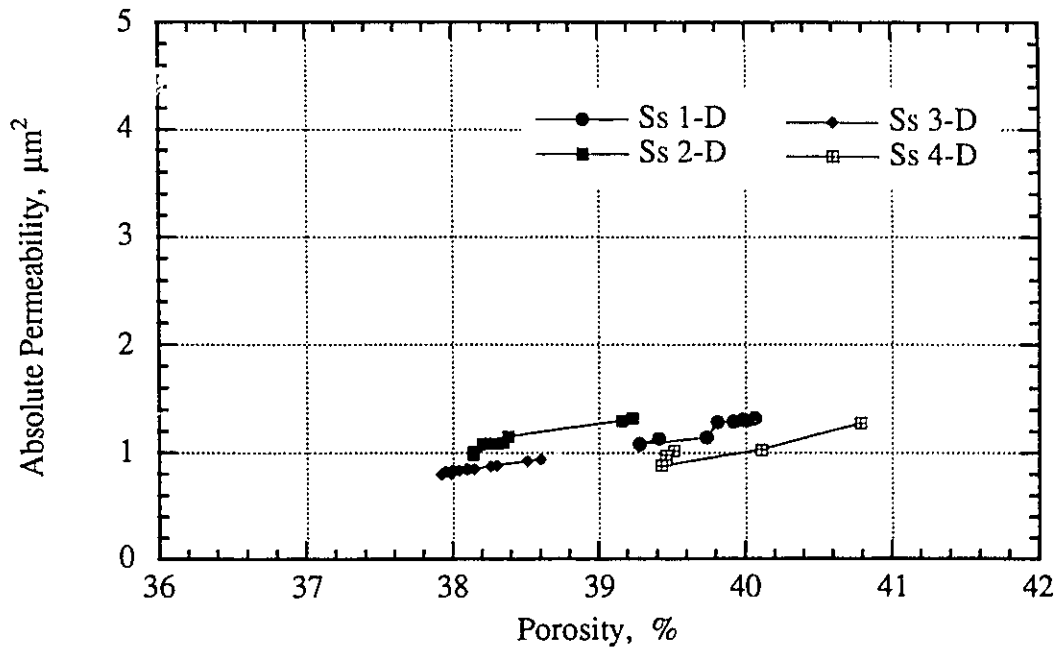


Figure 3.18 Stress Path B_σ , Absolute Permeability - Porosity

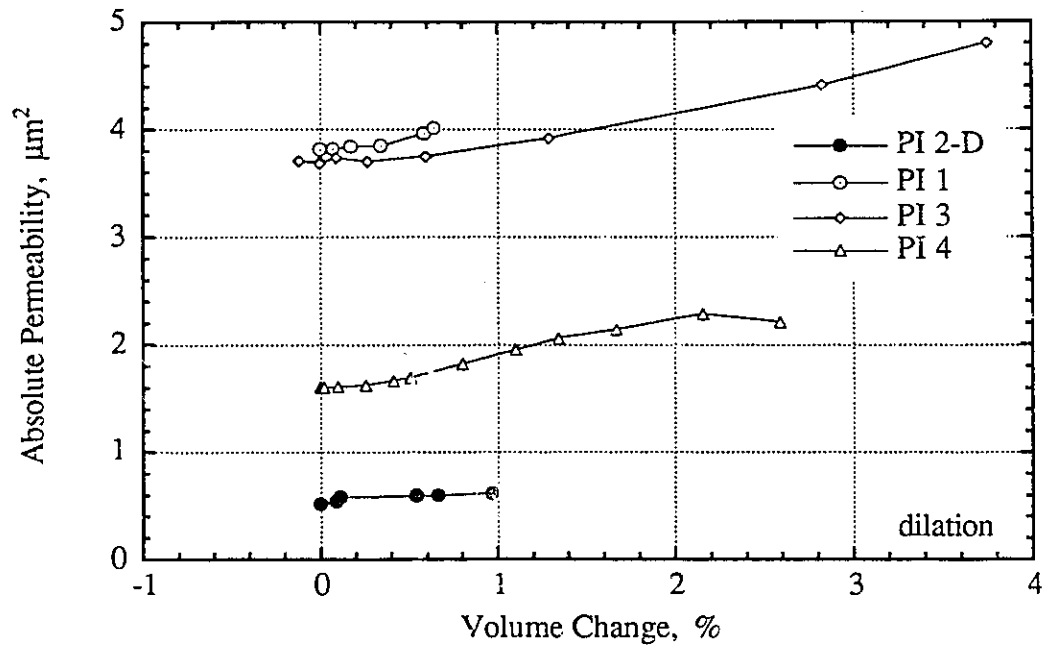


Figure 3.19 Stress Path F_v , Absolute Permeability - Volume Change

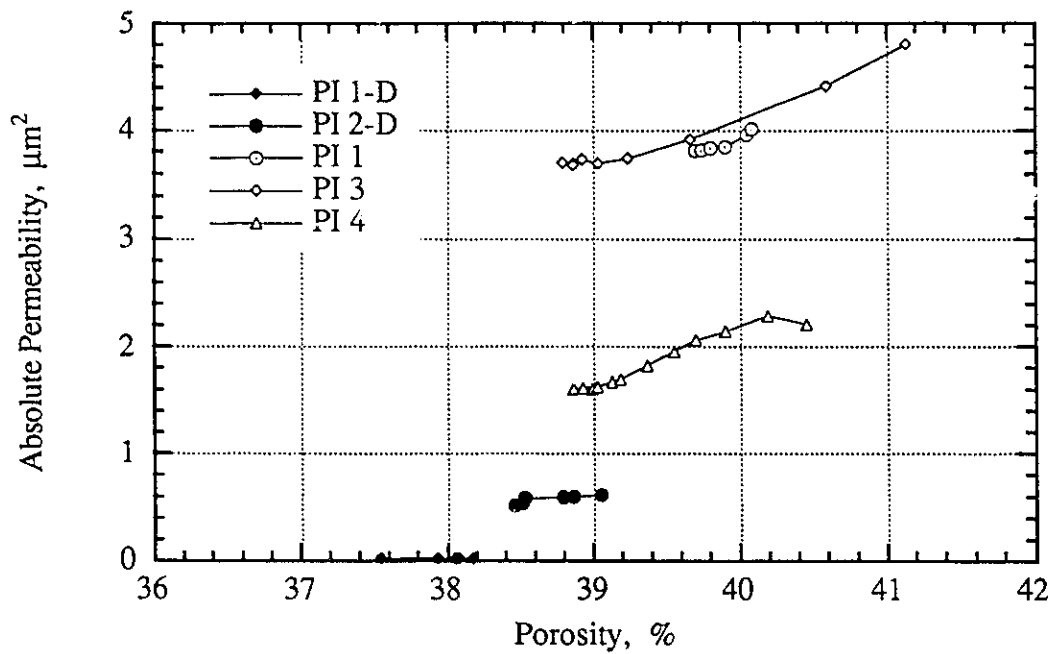


Figure 3.20 Stress Path F_v , Absolute Permeability - Porosity

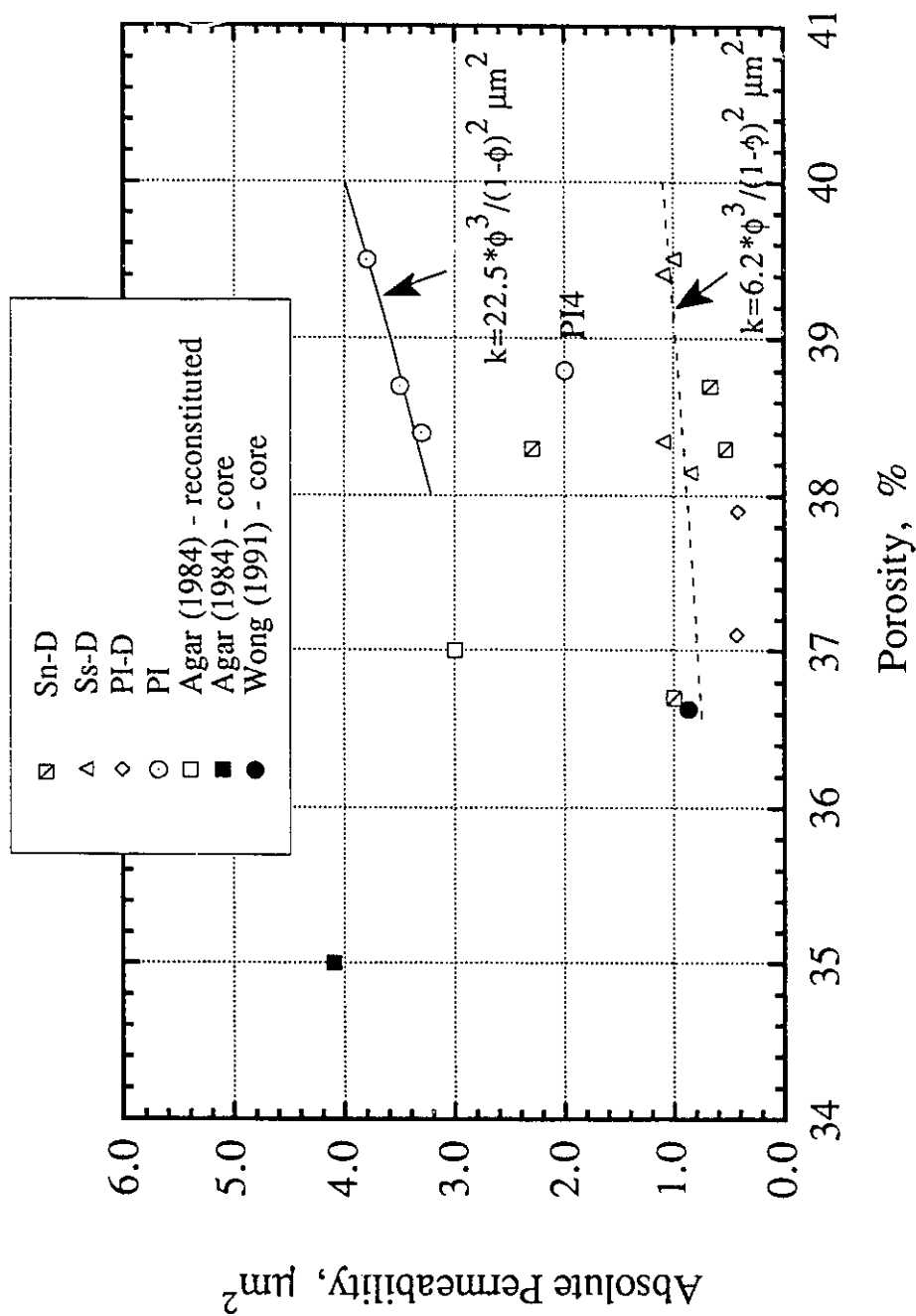


Figure 3.21 Initial Absolute Permeability of Oil-Free Reconstituted Oil Sand Specimens

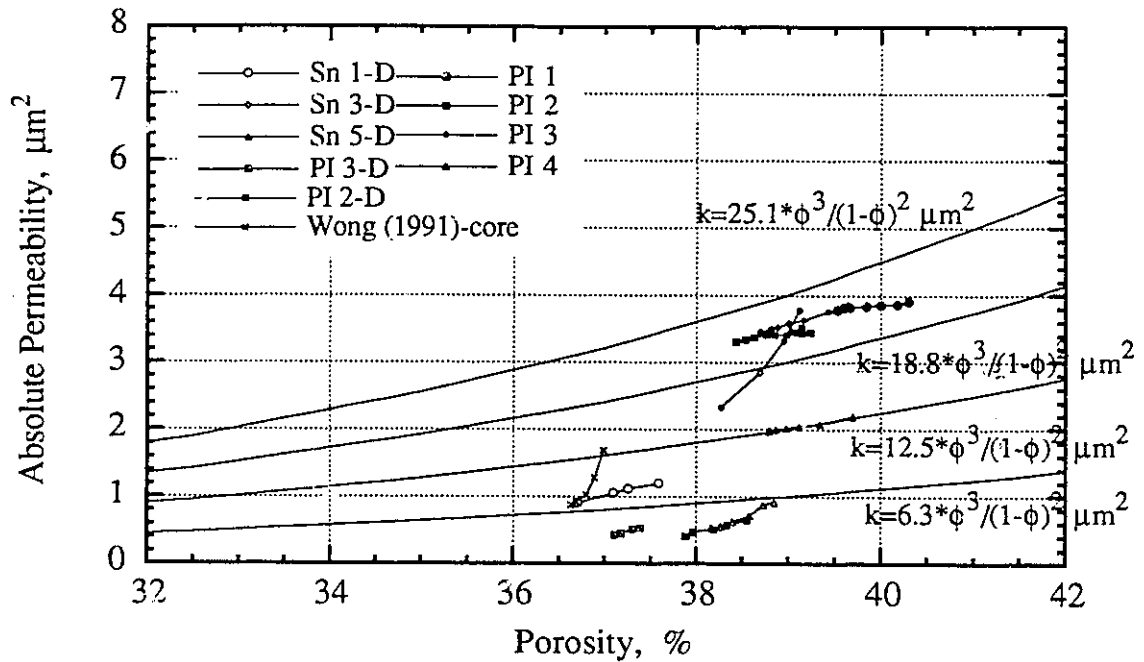


Figure 3.22 Isotropic Test Results Compared with Kozeny and Carman's Theory

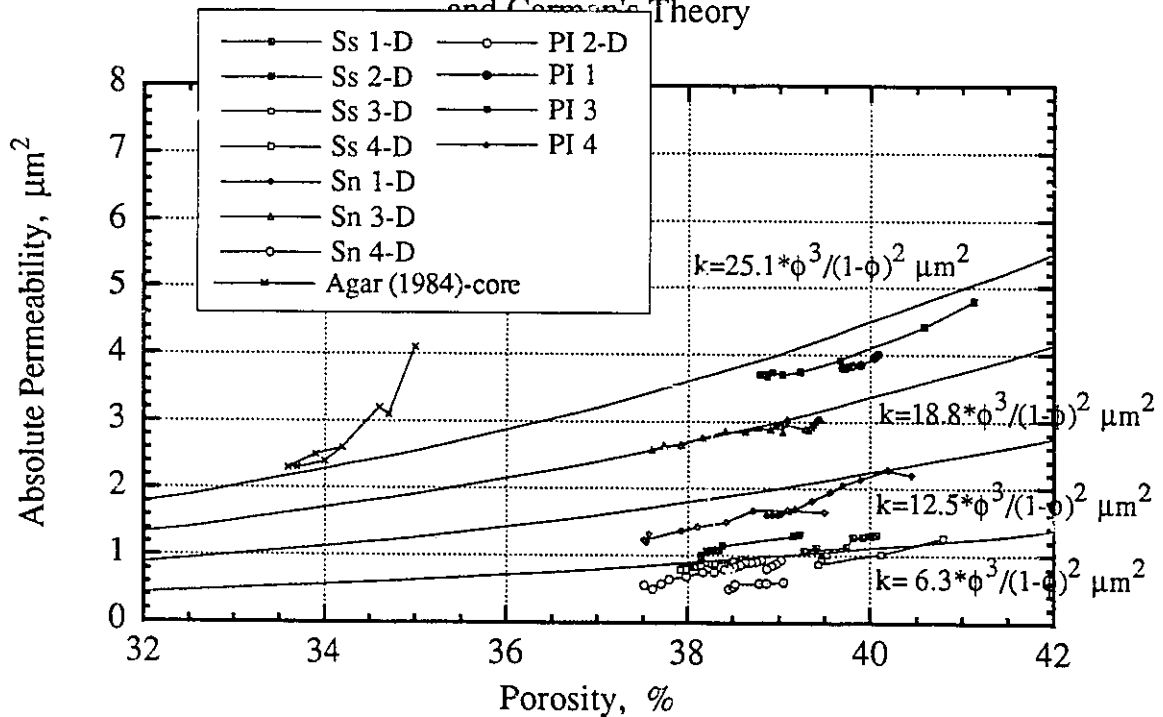


Figure 3.23 Shear Test Results Compared with Kozeny and Carman's Theory

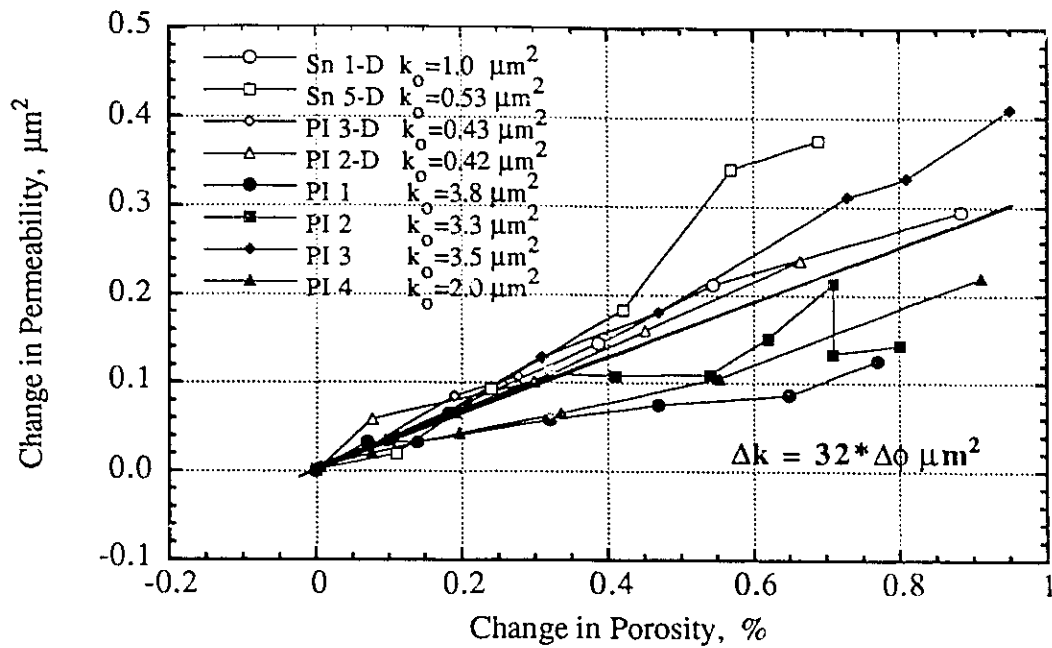


Figure 3.24 Absolute Permeability Change - Porosity Change, Isotropic Unloading

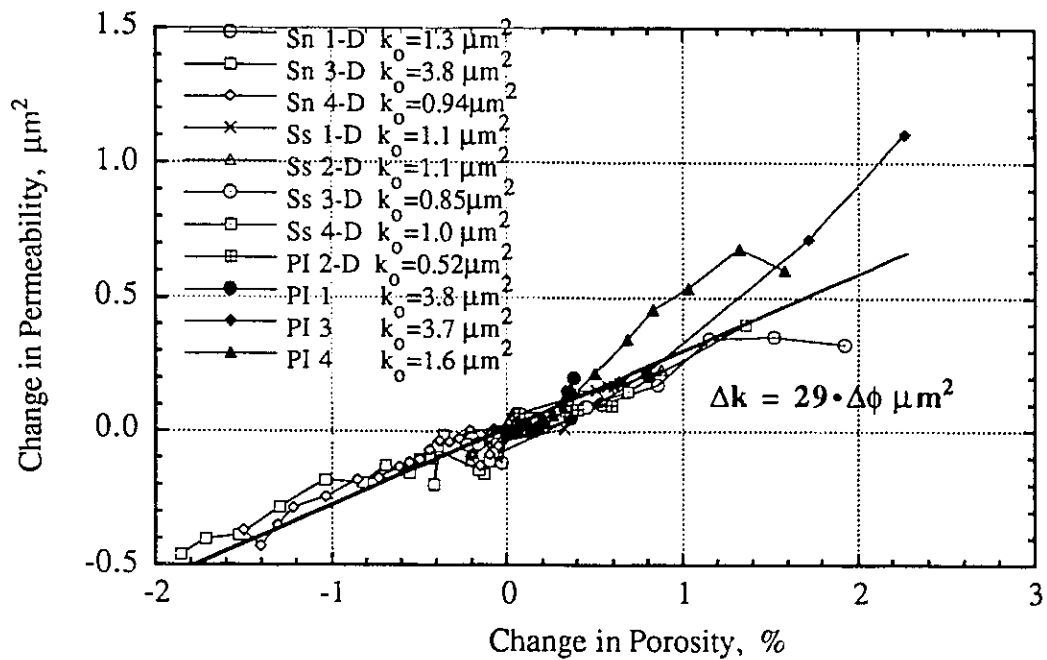


Figure 3.25 Absolute Permeability Change - Porosity Change, Triaxial Shear

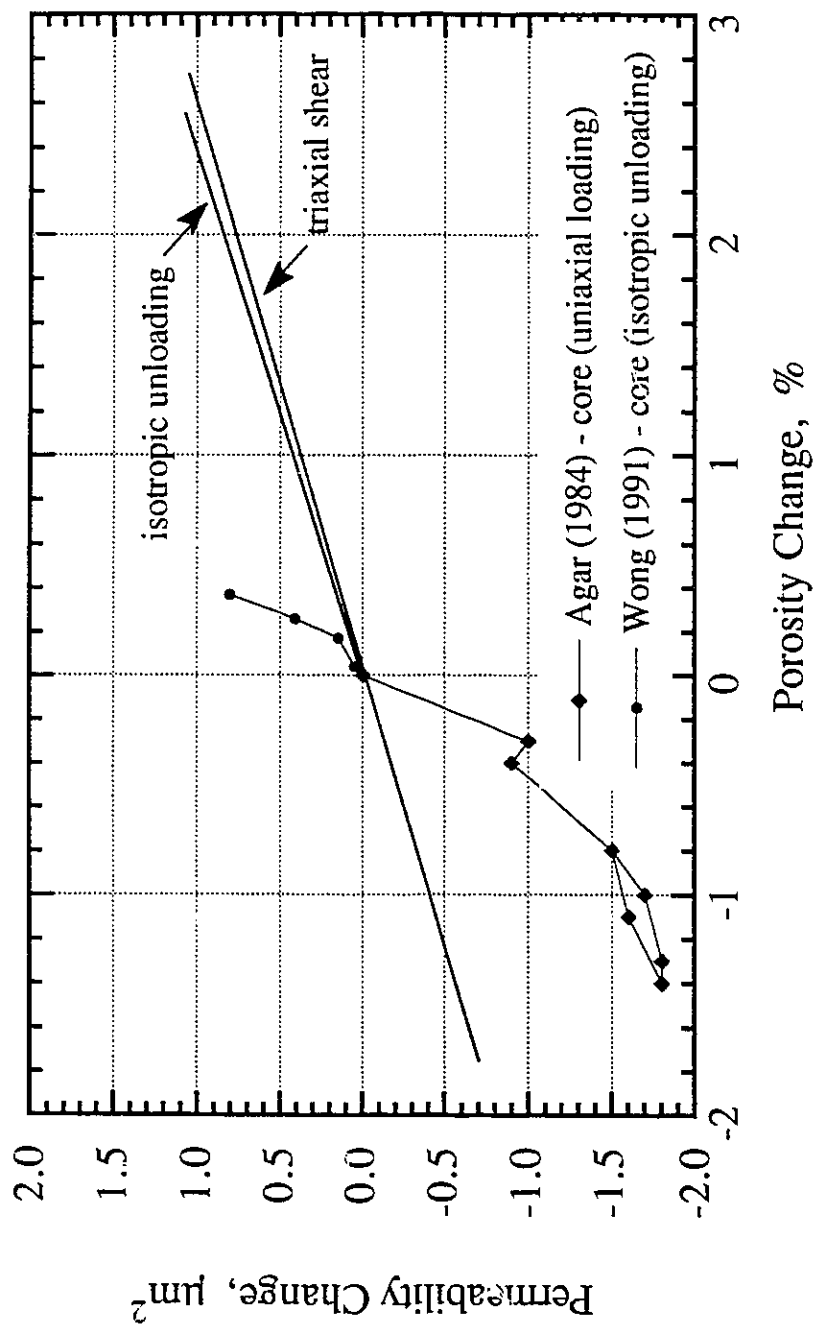


Figure 3.26 Absolute Permeability Change - Porosity Change, Comparison

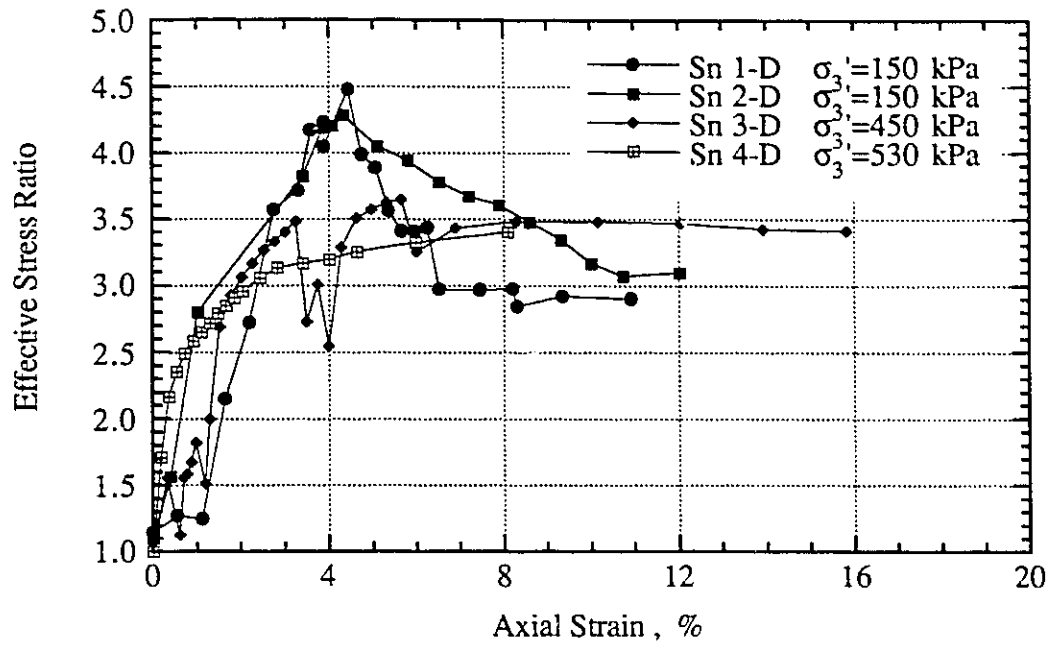


Figure 3.27 Stress Path B_ϵ , Stress Ratio - Axial Strain

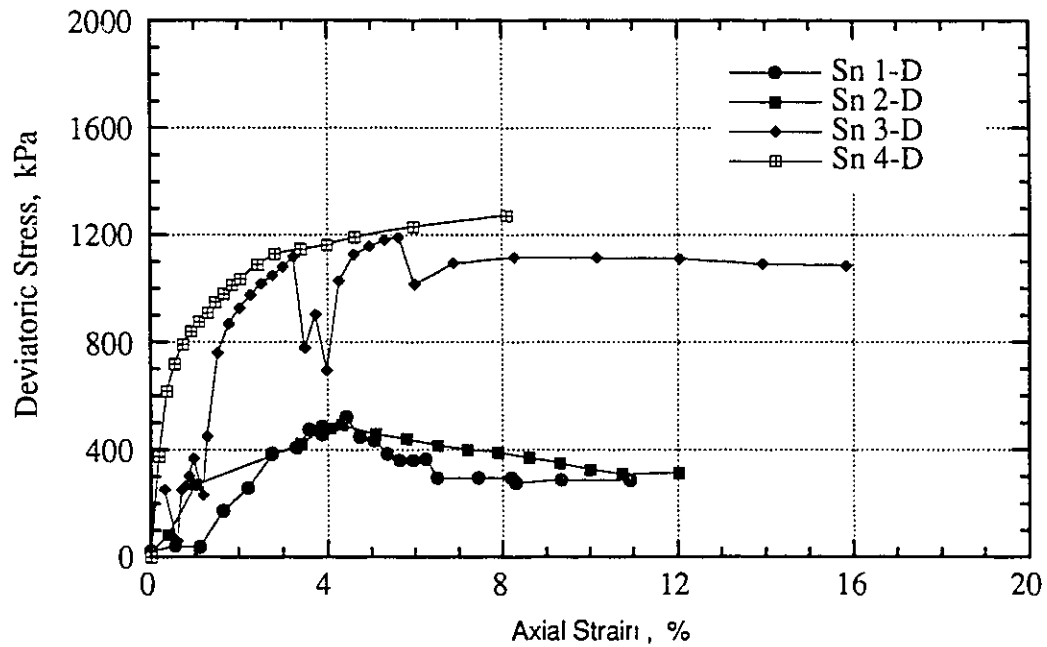


Figure 3.28 Stress Path B_ϵ , Deviatoric Stress - Axial Strain

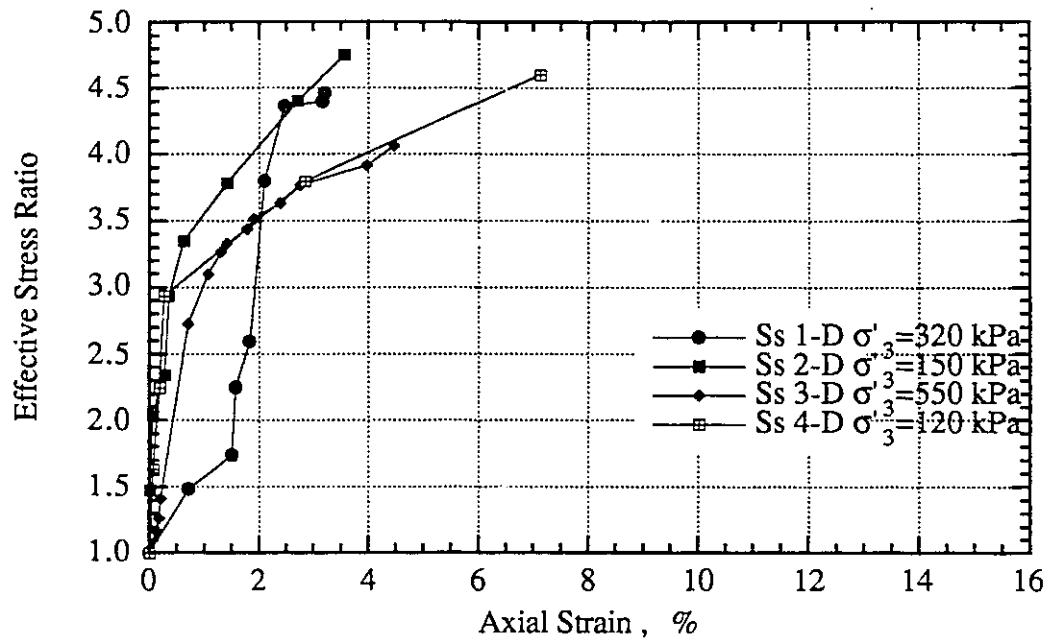


Figure 3.29 Stress Path B_σ , Stress Ratio - Axial Strain

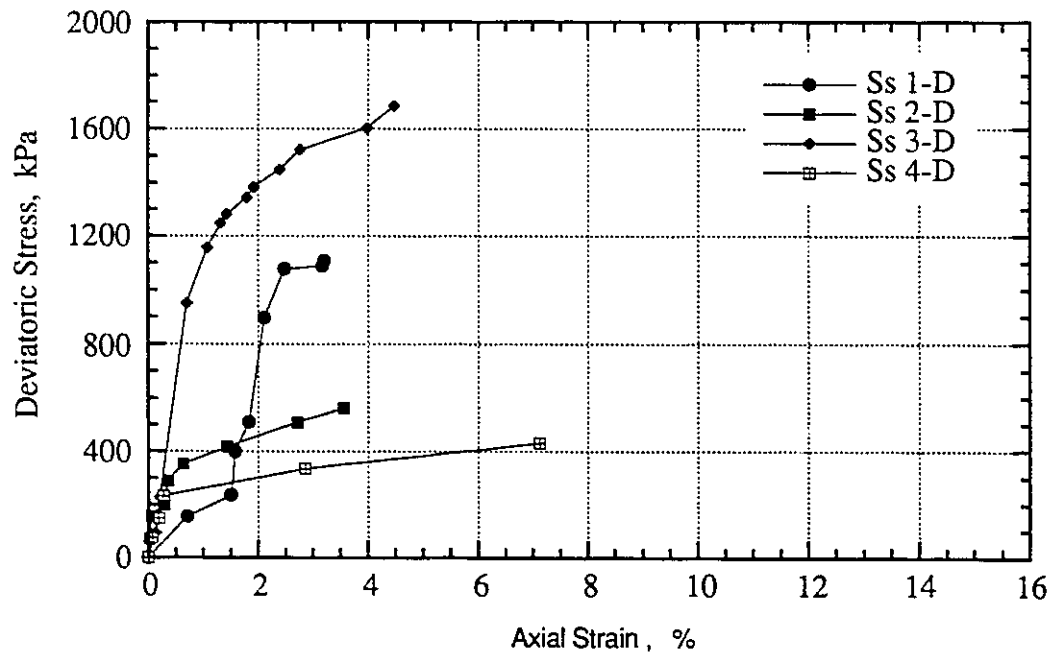
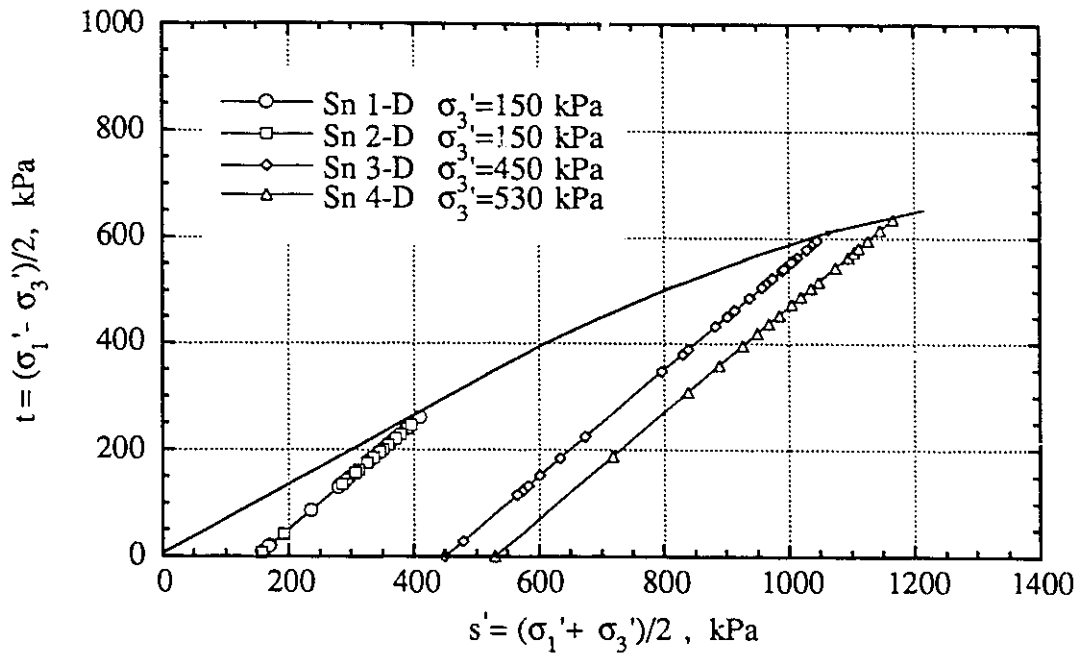
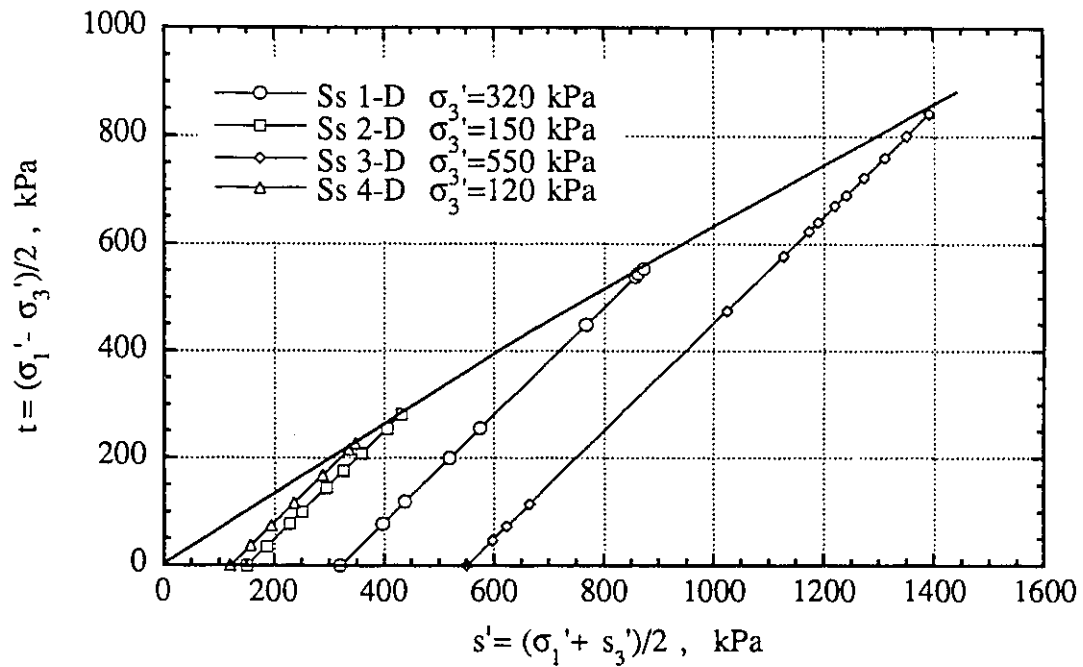
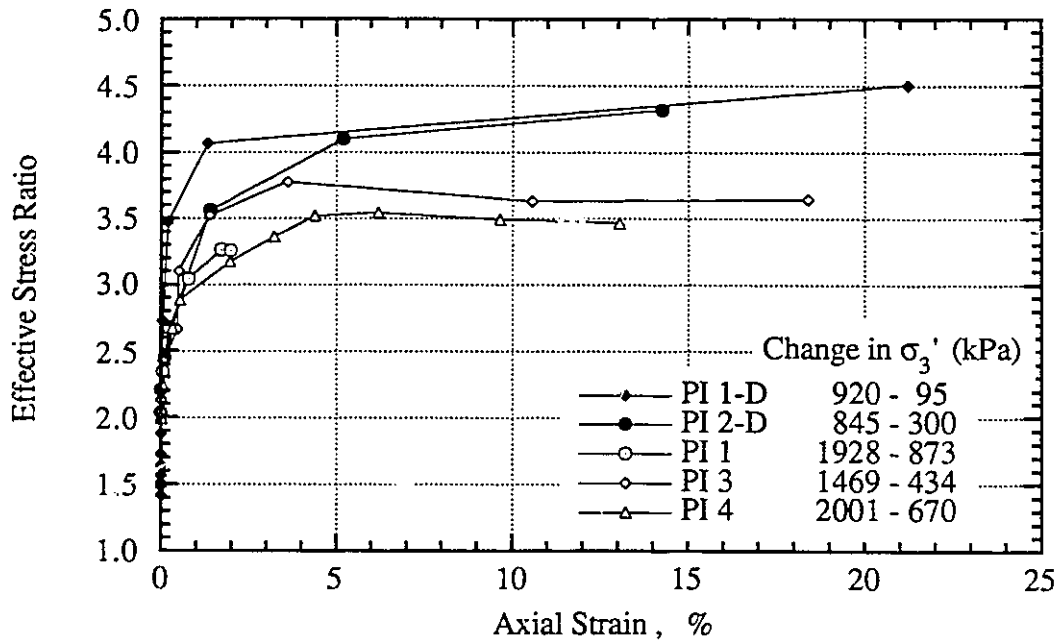
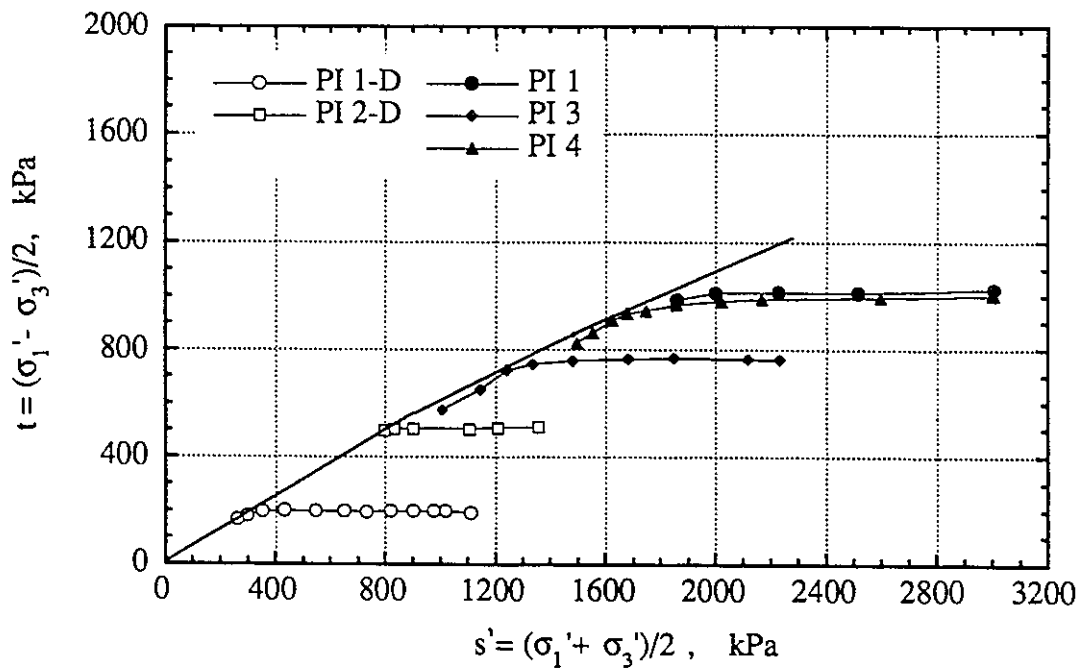


Figure 3.30 Stress Path B_σ , Deviatoric Stress - Axial Strain

Figure 3.31 Stress Path B_e , Failure EnvelopeFigure 3.32 Stress Path B_σ , Failure Envelope

Figure 3.33 Stress Path F_u , Effective Stress RatioFigure 3.34 Stress Path F_u , Failure Envelope

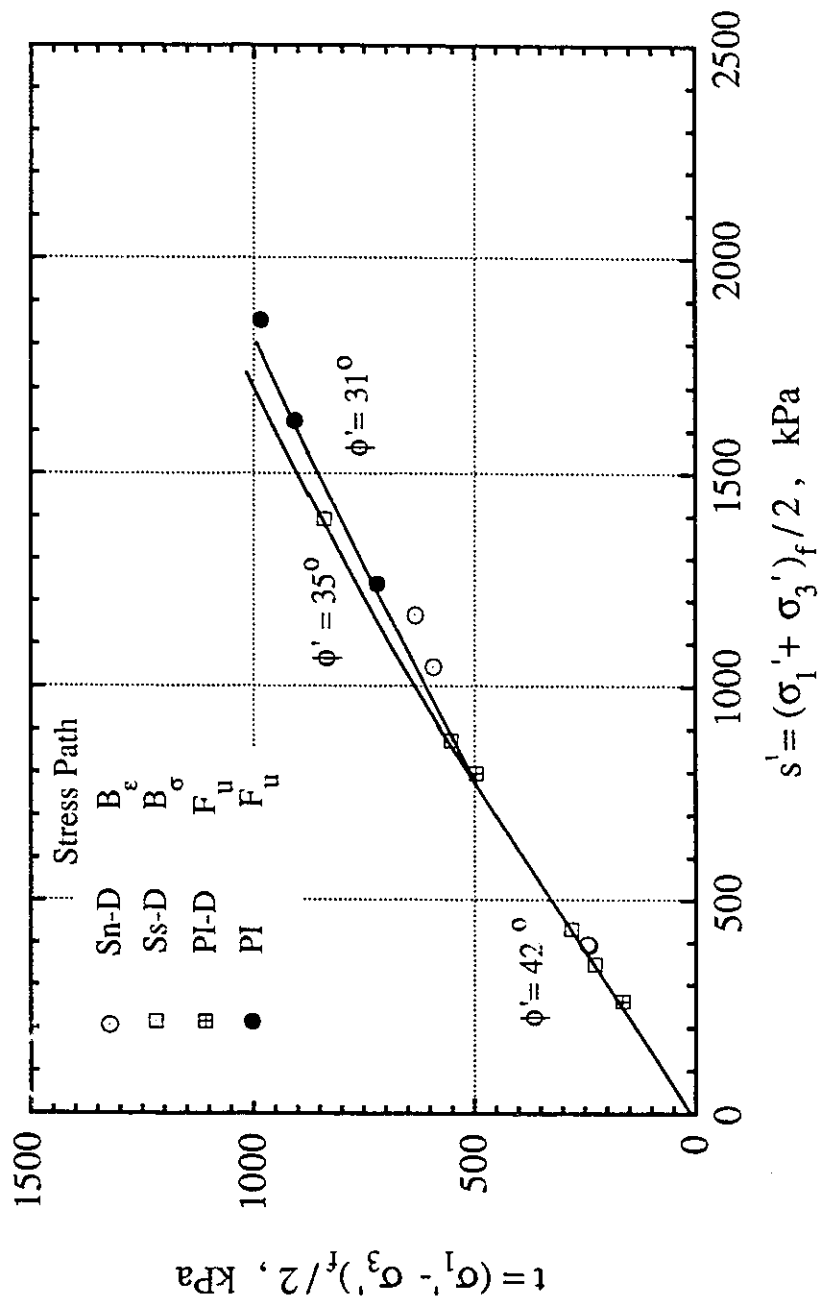


Figure 3.35 Failure Envelope for Oil-Free Reconstituted Oil Sand Specimens

Chapter 4. EFFECTIVE PERMEABILITY TO WATER - TEST PROCEDURES AND RESULTS

4.1 Introduction

This chapter describes a series of triaxial tests performed on preserved oil sands core material at in situ temperatures. The stress paths followed and measurements of stress induced deformations and changes in effective permeability to water are presented. The test results will be compared and discussed in Chapter 5.

The testing program followed in this study deals, in part, with processes that take place in a reservoir in front of the heated zone that develops during steam assisted in situ bitumen recovery. Researchers (Scott et al., 1991a) postulated that a zone of increased horizontal stresses propagates in front of a zone of increased pore pressure which in turn propagates in front of the zone of elevated temperature. According to measurements at the Underground Test Facility, the full steam chamber pressure at a given point in the reservoir was reached before the temperature rose above 20 to 30 °C (Laing et al., 1991). The combination of total stress and pore pressure changes cause complex deformations that, in the case of shear dilation, lead to permanent alterations in oil sands structure and increases in porosity. At an in situ temperature of 8 °C (at UTF), bitumen is practically immobile and all changes in porosity affect water saturation. Because of the heated zone, the elevated pore pressure zone and the elevated total stress zone propagate relatively slowly, it is assumed that increases in oil sands porosity can be accommodated by flow of cold injection water away from the steam chamber. This assumption appears relevant for the gravity drainage process at the UTF because no significant pore pressure changes were measured at the UTF Phase A Pilot that could be related to changes in total stresses. In the case of rich, thick oil sands deposits, however, the ability to conduct water can be

especially low, so that some shear deformations may take place under partly undrained conditions.

The hydraulic fracturing of oil sands deposits also creates conditions under which shear stress can induce dilation. The hydraulic fracturing process is utilized to obtain communication paths between injection and production wells or to obtain more rapid and extensive injectivity. Injection of fluids into an oil sands deposit at a pressure higher than the minimum principal total stress results in fracture development in the form of a shear band of altered sand fabric. The increase in porosity due to shear dilation results in an increase in the effective permeability to water.

Investigation of the enhanced porosity of oil sands due to shear dilation and due to a reduction in the mean principal effective stress, and the associated changes in effective permeability to water were the main objectives of the series of tests described in this chapter. The stress-strain relationships of tested specimens were also measured and will be presented.

4.2 Testing Program

The testing program was designed to investigate relationships between oil sands volumetric deformations and changes in effective permeability to water. These relationships were investigated in the context of the stress paths followed to induce these deformations; isotropic unloading, triaxial shear, and "pure" triaxial shear. The effects of sample quality (disturbance index), and other oil sands parameters such as strength, stress-strain relationship, grain size distribution, and fines content were also evaluated.

4.2.1 Stress Paths

Four different effective stress paths or, in terms of the total stress, seven stress paths were followed during tests performed. The stress paths in the p' - q stress field are plotted in Figure 4.1.

Stress Path A

The isotropic unloading tests were carried out by reducing cell pressure (path A_p) or by increasing pore pressure (path A_u). These tests were conducted on the same specimens used for constant p' tests.

Stress Path B

The triaxial compression shear tests were conducted at different effective confining stresses ranging from 240 kPa to 3000 kPa. Two initial tests were stress-controlled (B_σ) during which the vertical total stress was increased in several increments until specimen failure occurred. These tests will be described in Appendix A. The next eight tests were strain-controlled (B_ϵ) carried on with the load frame delivering a constant vertical strain rate.

Stress Path D

The constant p' tests, during which the mean principal effective stress $p' = (\sigma_1' + 2\sigma_3')/3$ was held constant, were carried on with the constant axial strain rate load frame. During one type of test, a constant p' value was maintained by reducing cell pressure (path D_p), whereas during the other type this was accomplished by pore pressure injection (path D_u).

Stress Path G

The confining stress unloading tests were conducted under constant axial strain and constant vertical effective stress (σ_1'). Four tests were performed by decreasing cell

pressure (path G_p) and four other tests by pore pressure injection (path G_u). Both the cell pressure and the pore pressure were changed in a predetermined way to keep σ_1' constant.

Triaxial compression tests were conducted to investigate the general relationship between volumetric strains generated by deviatoric stresses and changes in the effective permeability to water. As an approximation, the triaxial compression shear tests simulate stress conditions that occur laterally in front of the steam chamber. The oil sands thermal expansion in the steam chamber causes large local increases in the total horizontal stress, whereas the vertical stress remains unchanged or can be even reduced. These stress changes are similar to stress path B.

The triaxial confining stress unloading tests, stress path G, simulate the stress conditions that occur along a hydraulic fracture during hydraulic fracturing. In this process, the minimum principal effective stress is reduced to a very small value resulting in localized shear failure and oil sands dilation. Porosity enhancement due to this dilation affects effective permeability to water in the developed shear band along the fracture.

The constant p' tests, stress path D, were conducted to investigate the influence of "pure" shear strains on permeability enhancement. No change in the mean effective stress occurs along this stress path. The isotropic unloading tests, stress path A, investigated permeability enhancement due to elastic rebound. No shear strains occur along this stress path. These latter two stress paths bound the possible stress paths that could occur in the formation.

4.2.2 Tested Material

The oil sands cores for this experimental study were obtained from wells drilled in 1987 at the AOSTRA Underground Test Facility site. The data on the origin of tested

specimens, including well number, depth and the stratigraphic unit number (Rottenfusser et al., 1988) are shown in Table 4.1. The wells AT3 and AGI4 were cored with the Christensen core barrel with modified liners, giving a core 63 mm in diameter. The PVC inner liner, having a length of 149.3 cm, was designed to reduce radial and longitudinal expansions of the core compared to the standard core liner (McKay, 1989). One specimen was from well AGI1 cored with the Craelius SK6L standard triple tube core barrel which gives a 102 mm diameter core. All plastic liners containing oil sands cores were capped and sealed and placed in dry ice on site and subsequently stored at temperatures well below 0 °C.

The samples for testing were chosen from two stratigraphic units, E and D, which are composed of the richest oil sands at the UTF site. The criterion applied to select a piece of core was its bulk density as measured before specimen preparation. After a piece of core was machined in a lathe to a 38.1 mm diameter, the specimen was cut to a length of 38.1 mm from the part of the machined core that appeared to contain the lowest amount of shale fragments. In spite of this effort, the specimens often contained shale fragments of various sizes from very small to several millimeters in diameter. In some cases, the tested specimen contained shale or silt layers, or lenses up to several mm thick and stretching through the whole cross-section of the specimen or a significant portion of the specimen. The presence of shale and silt fragments and layers was noticeable, in most cases, only after testing, when the specimens were cut into pieces for examination.

The triaxial specimens were machined to a length to diameter ratio of one as short specimens were necessary to reduce the variation of radial effective stress with height, induced by the water flow during permeability tests (Appendix A).

4.2.3 Equipment

The testing equipment used in this experimental study is described in Chapter 3 and is shown in Figure 3.4. The main modification introduced was a brass tubing coiled around the steel triaxial cell, through which cold antifreeze was circulated to lower the cell temperature to the in situ temperature of 8 °C. A cold bath was used to cool down the antifreeze to the required temperature. An attempt to reduce the influence of caps on the specimen ends through the application of frictionless porous stones is described in Appendix B.

4.3 Specimen Preparation and Mounting in Triaxial Cell

Specimen preparation was conducted at a temperature below -20 °C in a cold room in which the cores, sealed in plastic liners, were stored after transportation to the University. Before trimming, the chosen pieces of core were kept in a styrofoam cooler containing dry ice for at least two hours. The core was trimmed to a diameter of 38.1 mm on a lathe using a diamond bit. The trimming was performed in several stages. Between stages the trimmed core and bit were put into dry ice to dissipate the heat generated through friction between the bit and the frozen core during machining. The trimmed core was cut to a desired length with a diamond saw. Specimens S1 and S2 were made 76 mm long and the rest of specimens 38.1 mm long. The specimen ends were finished at right angles to the specimen longitudinal axis in the lathe. After trimming, the specimen was chilled in dry ice and then mounted in the triaxial cell. The mounting process was also carried out in the cold room. The triaxial cell, end cap, porous stones, and membranes were kept in the cold room for at least one hour before the specimen was installed on a cell base with porous stones at both ends, covered with the top cap, and confined with

two latex membranes, 0.67 mm and 0.28 mm thick. After the cell was assembled, it was transferred to a testing room and placed in a loading frame. The cell pressure lines were connected, the cell filled with water, and an initial confining pressure applied to prevent the specimen from softening when it thawed and gas attempted to come out of solution in the bitumen.

4.4 Index Testing

During preparation of a specimen, 200 to 400 g of oil sand from the vicinity of the specimen was retained for index analysis.

Water and bitumen contents were determined using a Dean-Stark apparatus. In this apparatus, vaporized toluene passes through the oil sands core, dissolving bitumen and vaporizing water. The water vapor is condensed and collected in a graduated tube. The weight of the core is measured before and after extraction. The amount of extracted bitumen is calculated as the difference between the total weight of the core and the weight of solids and water.

The weight, diameter and length of each specimen were measured before mounting in the triaxial cell. The bulk density was calculated from these measurements. The mean density of sand grains was assumed to be 2.65 g/cm^3 . (Two grain density tests gave results: 2.642 and 2.647 g/cm^3 .) The density of bitumen was assumed to be 1.03 g/cm^3 . This data could be used to calculate dry density, porosity and saturation ratio. To calculate in situ porosity, the volume occupied by water and bitumen was divided by the specimen volume minus the volume occupied by gas. Zero free gas in situ was assumed. The disturbance index was calculated as the ratio of oil sands porosity increase to oil sands in situ porosity.

Table 4.1 contains the data described above. Bitumen contents for most specimens, as measured on trimmings, ranged from 13.4 % to 15.2 % and water contents ranged from 1.0 % to 2.9 %. In case of specimen S13, bitumen content was as low as 11.7 % and water content 3.5 %. Bitumen and water contents are expressed as a percentage of total specimen weight. Porosity of the specimens varied from 34.7 % to 39.3 %. Calculated in situ porosity varied from 32.5 % to 35.0 %. (Porosity of specimen S13 was 31.4%.) The disturbance index ranged from an exceptionally low 4.8% (specimen S3) to 18.3 %.

Grain size analyses were conducted on each sample extracted for bitumen and initial water content determination, as well as on each specimen extracted after testing. The characteristic grain sizes and coefficients, fines contents and, for comparison, water contents for all specimens are shown in Table 4.5. The grain size distribution curves are contained in Appendix F. It can be seen in Table 4.5 that, in many cases, significant differences occurred between fines content measured on trimmings before triaxial testing and on the corresponding specimen after testing. Differences up to 100 % are not infrequent; sometimes differences are even higher (specimens S6, S8, S20). Because water content in oil sands has been proven to be a function of fines content (Figure 5.7), the differences in measured fines contents correspond to differences in water contents; this means that the initial water contents assumed for specimen saturation and porosity calculations contain some degree of error. In these experiments, it was not possible to reliably estimate this error because of variations in measured water contents for different specimens containing similar amounts of fines.

4.5 Experimental Procedures and Results

4.5.1 Specimen Saturation and Isotropic Compression

Specimens S3-S19

To reduce specimen disturbance and bring the specimens close to the in situ porosity, an isotropic compression test was performed as a first step after the cell pressure line was connected and the triaxial cell filled with water. A confining pressure of 7 MPa was applied to the specimen, while the back pressure system remained opened to atmospheric pressure. The refrigerated bath circulator was turned on just after the cell was filled with water and the cooling tubing connected. The bath temperature was set at a predetermined value necessary to keep the temperature inside the triaxial cell at 8 °C. The specimen was left overnight to thaw and recompress to a higher density. Next, the cell base channels were saturated with a measured quantity of water. The channels were composed of two ports (one to connect the pressure transducer, which measures pore pressure, and the other for the back pressure line) and two holes ending at the porous stone situated at the bottom of the specimen (Figures 3.4 and A.1). In the next step, the pore pressure port was closed and the back pressure line attached to the cell. The back pressure line is composed of an inlet line that transmits water from the syringe pump to the bottom of the specimen and an outlet line that drains water from the top of the specimen and transmits it to an accumulator. A bypass between the inlet and the outlet lines was opened and 3 MPa back pressure (1 MPa for S19) applied in several increments to both ends of the specimen simultaneously. The sample and back pressure lines were saturated overnight. The amount of water flowing into the cell was measured. The amount of water used to saturate the specimen was calculated by subtracting the known volume of gas occupying the back pressure system (before back pressure was applied) from the total amount of water injected into the system. The difference between the

volume of gas contained in the specimen before testing and the volume of water at saturation reflects the specimen volume change as a result of compression. To check the state of specimen saturation, the pore pressure parameter B was measured. If the value of B did not change with changes in the magnitude of the back pressure, when effective confining stress was kept constant, this indicated that the specimen was fully saturated.

Specimens S20-S23

The saturation and compression procedures were changed for the last four specimens to allow direct measurement of specimen volume changes during compression. In the new procedure, a specimen was thawed under an initial confining pressure of about 150 kPa, with the back pressure lines open to atmospheric pressure. Next, to saturate the specimen, the back pressure lines were connected and both cell and back pressures were increased in increments of 100 kPa until a cell pressure of about 7 MPa was reached. The pore pressure parameter B was measured during this process. To compress the specimen, the effective confining stress was increased to 6 MPa by reducing the back pressure in steps. The amount of water that entered the cell during compression indicated specimen volumetric changes.

The isotropic compression results are plotted in Figures E1-E4 contained in Appendix E.

4.5.2 Isotropic Unloading, Stress Paths Ap and Au.

Procedure

An isotropic unloading test was performed on five specimens (S19-S23). Before isotropic unloading, the initial permeability test was continued overnight to allow the differential pressure across each specimen to stabilize under steady-stress conditions. The initial stress conditions for the isotropic unloading tests were a cell pressure of 7 MPa and

a back pressure of 1 MPa. The tests on specimens S19, S21 and S23 were performed by increasing back pressure in steps until effective confining stresses of 140, 154 and 122 kPa respectively were reached. Specimen S20 was unloaded by reducing cell pressure until an effective confining stress of 146 kPa was reached. During the isotropic unloading test on specimen S22, the cell pressure was first changed to about 3 MPa, after which the cell pressure was left unchanged and the back pressure was increased, until an effective confining stress of 115 kPa was reached. At the beginning of all tests, the pressures were changed at intervals of about 1 MPa. At lower effective confining stresses, pressures were changed in smaller intervals.

The flow of water through the specimen was continued during testing. Time intervals between each consecutive pressure change were kept long enough to allow the differential pressure across specimen to stabilize. The length of this time interval, which depended on specimen permeability and an applied flow rate, ranged from 20 minutes, for a flow rate of 1.5 ml/hr, to 3 to 6 hours, for a flow rate of 0.075 ml/hr. The flow rate into the specimen (Q_{in}) was controlled by the syringe pump, designed for precise, pulse-free delivery of liquids. The flow rate out of the specimen (Q_{out}) was calculated taking into account Q_{in} and volumetric changes of the specimen.

Specimen volume changes were measured with the Ennis Measuring Accumulator connected in line with the cell pressure system. EMA volume readings were corrected for triaxial cell expansion brought about by cell pressure changes. The differential pressure between the top and the bottom of the specimen was measured with a differential pressure transducer.

Results

The effective permeability to water was calculated from Equation 3.4. Specimen length and cross-sectional area were calculated on the basis of initial dimensions and measured volume changes during testing, assuming uniform specimen expansion in all

directions. For permeability calculations, average flow rate ($Q_{av}=(Q_{in}+Q_{out})/2$) was used.

The test results are plotted in Figures 4.2 to 4.4. Some test details, such as specimen conditions at the beginning of isotropic unloading, effective confining pressure changes, and volumetric and permeability changes, are listed in Table 4.2.

All plots of volumetric changes against effective confining stresses proved fairly consistent with one other. The average change in volume was 1.7 % for changes in the effective confining stress from about 6 MPa to 150 kPa. The slopes of plotted curves increase as the effective confining stress is decreased. The logarithm of effective permeability to water plotted against volumetric changes or water porosity shows a nearly linear relationship. The slope of the line is less for specimens with a larger initial permeability. A scatter in initial permeability values for different specimens at the same water porosity can be observed in Figure 4.4.

The straight line drawn in Figure 4.4, derived from Equation 5.4, was drawn in all permeability versus porosity plots as a reference for comparison between different types of tests. The physical meaning of this line will be discussed in Section 5.3.3.

4.5.3 Triaxial Compression Tests, Stress Paths B_{σ} and B_{ϵ}

A total of ten triaxial compression tests were carried out. Specimens S1 and S2 were axially compressed with the Bellofram load frame in a stress-controlled mode, stress path B_{σ} . This mode of triaxial compression was found to be unsuitable for volumetric strain-permeability change investigations. The triaxial compression stress-controlled tests are described in Appendix A. Specimens S3 - S10 were compressed in the strain-controlled mode, stress path B_{ϵ} , with the Wykeham-Farrance load frame.

Procedure

After isotropic compression and saturation, each specimen was consolidated under the isotropic confining stress at which triaxial compression was later conducted. Next, upward flow through the specimen was begun at a constant rate. Flow was continued throughout testing, but the flow rate was adjusted, at the beginning, to maintain the pressure drop across the specimen below the upper limit of the differential pressure transducer (140 kPa). The flow rates used in the eight tests were: 0.3, 3.0, 2.0, 0.3, 4.0, 1.5, 0.15, and 0.6 ml/hr. The initial permeability test was conducted until the differential pressure became stabilized. The time required to achieve this stabilization ranged from 2 to 9 hours and was a function of flow rate and specimen permeability. Next, axial compression was applied to the specimen at a constant rate of 0.075 mm/hr (an axial strain of 0.20 %/hr) while pore pressure and cell pressure were kept at a constant level. In the case of specimen S9, the strain rate was as low as 0.05 mm/hr, equaling the lower limit of the load frame capabilities. Application of low strain rates was necessary so that the flow rate through a specimen was not excessively affected by specimen volumetric changes during deformation. In addition, the average flow rate through the specimen was used for calculations to obtain reliable measurements of permeability.

The cell pressure, back pressure, differential pressure, axial displacement, cell liquid volume change, and piston load were monitored by computer throughout testing and recorded at predetermined time intervals, usually of 5 or 10 minutes.

After tests, the bitumen was extracted from specimens and grain size analyses were performed.

Results

Specimens conditions at the beginning of the triaxial compression tests are shown in Table 4.3. The results of eight tests, S3 - S10, are plotted in Figures 4.5 - 4.10; some test details are presented in Table 4.4.

The stress paths in the s' - t diagram are shown in Figure 4.8. A failure envelope was drawn through the points representing specimens with the highest strength. Because the measured stress ratio at failure is affected by specimen disturbance, this failure envelope is believed to be the best representation of the in situ strength. The deviatoric stress versus axial strain plots in Figure 4.6 illustrate the influence of the effective confining stress on the magnitude of the shear stress that the specimens can withstand.

The effective stress ratio versus axial strain plots are shown in Figure 4.5. The specimens reached their peak strength at axial strains ranging from 1.8 % to 4.4 %. The value of an axial strain at failure depends, to a high degree, on specimen disturbance. The disturbance index, however, is only a measure of change in specimen porosity and does not reflect other aspects of specimen disturbance; this is especially notable in the case of specimen S6, the disturbance index of which was lower than those of many other specimens. Nevertheless, the initial slope of the curve representing specimen S6 on the effective stress ratio versus axial strain plot is small, until an axial strain of about 2.2 % is reached. After this point, the slope increases and the effective stress ratio at failure is finally higher than the maximum stress ratio for specimen S8, which also sheared under an effective confining stress of about 2 MPa. Specimen S6 was prepared from a core contained in a thin plastic liner of an internal diameter of 105.6 mm, larger by 3.5 mm than the diameter of the core cut from the deposit. (In modified liners, the gap between the core and the liner was reduced). The free space in the liner allowed the core to expand radially until it filled the liner entirely. During specimen preparation, many longitudinal fissures filled with bitumen were noted. Similar fissures on disturbed specimens have

been observed by other experimenters (Wong et al., 1993). The particular stress-strain behavior of specimen S6 is believed to be a result of the mode of core disturbance described above.

All specimens except S7 displayed strain-softening after failure. Specimen S7 sheared under the lowest initial effective confining stress of all specimens: initial stress was 240 kPa but increased with time due to a self activating increase in cell pressure, and at failure reached a value of 410 kPa. The increase in effective confining stress had an influence on the shape of the stress-strain curve.

Volumetric change versus axial strain plots for seven specimens are shown in Figure 4.7. Specimen S8 volume changes are not plotted because they were disturbed by accidental changes in cell temperature. All specimens displayed initial compression followed by shear dilation. Dilation rates reached their maximum values usually before specimen failure or directly after failure. At higher axial strains, dilation rates became smaller. The relationships between magnitude of volume change, effective confining stress, and specimen density can be observed on the basis of the plots in Figure 4.7 and the data contained in Table 4.3. The specimens that sheared under effective confining stresses of 2 MPa and higher initially underwent a substantial decrease in volume. At failure, specimen volumes were still below their initial values, but at higher axial strains volume changes became positive (dilation). The specimens that sheared under lower effective confining stresses underwent small degrees of compression followed by substantial shear dilation, up to 5.6 % at an axial strain of 6 % (specimen S4). The magnitude of dilation depends on the effective confining stress, specimen density (porosity) and axial strain.

The effective permeability to water is plotted against volume change and water porosity (the latter defined as the ratio between the volume occupied by water and the total volume of the specimen) in Figures 4.9 and in 4.10, respectively. The plot of

logarithm of permeability against volume change or water porosity is almost a straight line in the case of specimens that did not contract during initial stages of testing. The permeability - volume change relationships for contracting specimens are more complicated. During specimen contraction the effective permeability to water decreased less than it increased during specimen dilation. When the specimen volume returned to its initial value, specimen permeability became larger than it was at the beginning of the test. At larger volumetric strains, permeability changes seem to follow the general trend depicted by the straight line shown in the plot.

4.5.4 Confining Stress Unloading Tests, Stress Paths G_p and G_u

The triaxial confining stress unloading test was designed to investigate how the dilation that occurs during hydraulic fracture propagation influences the oil sands effective permeability to water. To be able to monitor post-peak behavior, the specimen was compressed with the constant strain-rate loading frame. During the test, a constant vertical effective stress was maintained and the confining effective stress (σ_3') was reduced until specimen failure occurred. Then, σ_3' was left unchanged until the end of the test .

Two types of confining stress unloading tests were performed:

1. The confining stress unloading test with cell pressure reduction and constant pore pressure, performed on specimens S11-S14 (total stress path G_p).
2. The confining stress unloading test with pore pressure injection and constant cell pressure, performed on specimens S15-S18 (total stress path G_u).

Procedures

After the isotropic compression and saturation described in Section 4.5.1 was finished, each specimen was consolidated under an initial confining stress. Specimens

S11-S14 were consolidated under effective confining stresses of 2930, 1920, 1040, and 560 kPa respectively and specimens S15-S18 under respective effective confining stresses of 2000, 1510, 980, and 2860 kPa. Next, the initial permeability test was conducted until the differential pressure across the specimen became stabilized. The flow rate was adjusted to keep the differential pressure lower than 140 kPa. The respective flow rates applied during testing of S11-S18 were: 4.0, 2.0, 0.03-0.45, 0.3, 0.75, 0.75, 0.60, and 0.60 ml/hr. (During the test on specimen S13, the flow rate was changed several times because of significant changes in permeability.) After the initial permeability measurements were finished, axial compression was started at constant strain rates that ranged from 0.047 to 0.11 mm/hr.

During the tests on specimens S11-S14, the cell pressure was reduced in a predetermined manner to keep the total vertical stress close to its initial value. Since the pore pressure remained unchanged during these tests, the effective vertical stress was also kept at its initial level. The following relationship between piston load, vertical stress, and cell pressure for triaxial stress conditions was derived:

$$N = (\sigma_1 - \sigma_3(1 - a_s/A_s)) \cdot A_s \quad 4.1$$

where: N - piston load, kN

σ_1 - vertical total stress, kPa

σ_3 - confining total stress (= cell pressure), kPa

A_s - specimen cross-sectional area, m²

a_s - piston cross-sectional area, m²

To keep σ_1 constant, the relation between N and σ_3 must follow this equation. In practice during testing, as compression was continued, σ_1 and N were allowed to increase by some amount, whereupon σ_3 was reduced slowly until N reached a value that satisfied Equation 4.1 for a given σ_3 . The σ_3 value was controlled in this way until the peak

strength was reached. The pressure regulators were not accurate enough to allow for confining pressure control in the post-peak region, because this required precise, small pressure increments. As well, tests were conducted for many hours before peak strength was reached, which usually took place late at night. For this reason, in the post peak region, the tests were continued as conventional triaxial compression tests with cell and back pressures remaining unchanged.

The confining stress unloading tests on specimens S15-S18 were performed under constant cell pressure conditions. The pore pressure was changed during these tests in a predetermined manner to keep the vertical effective stress constant. The total vertical stress was changing slightly during these tests. Equation 4.1 was modified to show the pore pressure component (u):

$$N = (u + \sigma_1' - \sigma_3(1 - a_s/A_s))A_s \quad 4.2$$

The N and u values have to follow this equation if σ_1' is to stay at a constant value. The pore pressure was increased manually at certain time intervals, each time in several small steps. Each change in pore pressure involved some reduction in vertical load. The pore pressure increase was stopped when the desired value of N was reached, as described by Equation 4.2, for a given pore pressure. The specimen cross-sectional area (A_s) was corrected at each pore pressure level, since it was known approximately how volumetric changes are related to axial strains, on the basis of tests performed earlier. As during the previous four tests (S11-S14), σ_1' was controlled only until the specimen reached its peak strength. The tests then were conducted as conventional triaxial compression tests. The time interval between consecutive corrections of N , through changes in u (or σ_3), was equal to the time required to obtain stabilization of the differential pressure across the specimen. This factor determined the duration of the test. For specimens with a low

permeability, the axial strain rate had to be set at the lowest possible value of 0.047 mm/hr.

Results

The results of the cell pressure reduction tests are shown in Figures 4.11 to 4.16 and the results of the pore pressure injection tests are shown in Figures 4.17 to 4.22. The stress paths followed are shown in Figures 4.14 and 4.20 in the s' - t stress field. The jagged appearance of the stress-strain plots resulted from the way the confining effective stress was controlled, that is, by pore pressure or cell pressure changes in steps at certain time intervals. For both types of tests, the most striking characteristic of the effective stress ratio versus axial strain plots is the value of the effective stress ratio at failure. The stress paths followed during these tests led to very low effective confining stresses at failure. In the most extreme case (specimen S17), the effective stress ratio at failure was 145 at an effective confining stress of 10 kPa. Although such low values of stress, measured by the difference in readings of two pressure transducers, may have a relatively large error due to limited instrument resolution, the general tendency was for an increase in effective stress ratio with a decrease in effective confining stress. The unexpectedly high stress ratio (for sand) at low effective confining stresses is the result of the high viscosity bitumen in the oil sands specimens. Although the bitumen is not a solid body but a fluid, its very high viscosity (about 10^7 mPa·s) at 8 °C (Peacock, 1988) gives the oil sands an apparent cohesion, that is, some degree of strength at zero confining stress at the strain rates used. The effective stress ratio at failure of oil sands is a function of this factor, the magnitude of effective confining stress, the specimen disturbance and the initial porosity. The latter two parameters also influence the magnitude of axial strain at failure; this was especially noticeable in the case of specimen S12, in which cracks and fissures were visible before testing. For specimens S11 - S14, axial strain at failure ranged from 1.9 % to 4.8 %. For specimens S15 - S18, axial strain at failure ranged

from 0.8 % to 1.9 %. The difference in the magnitude of axial strains at failure as measured in these two types of tests, is obvious, although the causes of this differential are not well understood. It could be speculated that the difference may be associated with the low permeability of oil sands. If the cell pressure is reduced, the specimen undergoes expansion because of the instantaneous drop in effective confining stress. But this, in turn, results in a reduction in pore pressure if the specimen permeability is low, and the equalization of pore pressure requires some time, so that water can fill the increased voids. When water fills these voids, the pore pressure returns to its initial value and, in effect, the effective confining stress decreases. Hence, after each cell pressure reduction, one cycle of confining effective stress increase and decrease takes place, which strengthens the specimen. If the pore pressure is increased, the effective confining stress is reduced by the amount by which the pore pressure has increased, so that no cycle of confining effective stress can take place. This could be the reason that, in the pore pressure injection tests, specimens failed at lower axial strains and experienced larger volume changes at corresponding axial strains than in the cell pressure reduction tests.

The volume change versus axial strain plots are shown in Figures 4.13 and 4.19. Dilation at failure for both series of tests ranged between 2.0 % and 4.7 %. The largest volumetric changes at higher strains, measured during these tests, ranged from 4.9 % to 8.7 %. The highest rates of volume change occurred in the region where the specimens reached their peak stress ratio. At higher axial strains, the curve representing the relation between volumetric strain and axial strain tends to level off. The volumetric strains at failure constituted about 1/3 to 2/3 of their largest measured values.

The effective permeability to water versus volume change plots are shown in Figures 4.15 and 4.21. The effective permeability to water versus porosity plots are shown in Figures 4.16 and 4.22. The tests on specimens S15 - S18 gave rather consistent results mainly because their initial permeabilities were close to one another

(some differences in slopes of different plots can be noticed). Differences in the initial permeabilities of specimens S11-S14 were much greater. The difference between the maximum and minimum values of effective permeability to water for specimens S11 and S13 was equal to two orders of magnitude ($8.0 \cdot 10^{-6}$ versus $6.8 \cdot 10^{-4} \mu\text{m}^2$). Specimen S13 contained about four times more fines than other specimens from the same series. The reason for the high permeability of specimen S11 (which was ten times higher than the permeability of specimen S14, which had a similar water porosity) was not easy to identify. Specimen S14 had only a slightly higher content of fines, defined as particles smaller than $45 \mu\text{m}$, but had more than twice the content of fines smaller than $75 \mu\text{m}$. Probably the latter factor and the mode of fines distribution led to the difference in permeability. The effective permeabilities to water of specimens S12 and S14 were consistent with their water content and with the general tendency for permeability to change as a function of water porosity.

4.5.5 Constant p' Tests, Stress Paths D_p and D_u

The objective of this series of tests was to measure volumetric changes due to "pure" shear deformations under a constant mean effective stress ($p' = (\sigma_1' + 2 \cdot \sigma_3')/3$) and the effect of these changes on permeability. The constant p' tests were performed on specimens S19 - S23, previously used in isotropic unloading tests.

Two types of constant p' tests were conducted:

1. The confining pressure unloading test, performed on specimens S19 and S20. During these tests, pore pressure was maintained constant and cell pressure was reduced.
2. The pore pressure injection test, performed on specimens S21 to S23. During these tests, cell pressure was maintained constant and pore pressure was increased.

Procedure

After the isotropic unloading tests, specimens S19 and S20 were recompressed under an effective confining stress of 6 MPa and then unloaded to 3 MPa and 890 kPa respectively at a back (pore) pressure of 3 MPa. Specimens S21, S22 and S23 were recompressed under effective confining stresses of 1950, 570, and 1480 kPa respectively at a back (pore) pressure of 3 MPa.

During both types of tests the specimens were axially loaded at constant strain rates and pressures were changed in a predetermined way to maintain mean effective stresses at constant values. The following relationship between the external load on the cell piston, cell pressure, pore pressure, and mean effective stress was derived:

$$N = (3(p' + u) - \sigma_3(3 - a_s/A_s)) \cdot A_s \quad 4.3$$

where: p' - mean effective stress, kPa

u - pore pressure, kPa

σ_3 - cell pressure, kPa

a_s - piston cross-sectional area, m²

A_s - specimen cross-sectional area, m²

N - piston load, monitored by load cell, kN

Equation 4.3 must be satisfied by all variables and constants in order to maintain the mean effective stress (p') at a constant value. The cross-sectional area for the first test was assumed to be constant. In the next tests, the cross-sectional area was corrected on the basis of estimated specimen deformation at a given axial strain. The cell pressure was changed manually in steps, in the same manner as during the confining stress unloading tests. During the constant p' pore pressure injection tests, the mean effective stress was maintained constant by manually increasing the pore pressure. Permeability measurements were continuous throughout every test.

Results

The constant p' test data are included in Table 4.4. The test results are plotted in Figures 4.23 to 4.28. Figure 4.26 show the effective stress paths followed during the constant p' tests in the s' - t stress field. The way in which the pressures were changed resulted in the saw-tooth plot shapes. Constant p' values were maintained only until specimens reached their peak strength. This process usually took several hours. Specimen compression in the post-peak strength region was continued overnight unattended, with cell and pore pressures left unchanged. In the s' - t plot, the stress paths follow the standard triaxial compression stress path after the specimens reached their maximum strength. The effective stress ratio versus axial strain plots are shown in Figure 4.23 for all constant p' tests. Maximum effective stress ratios occurred at axial strains ranging from 1.2 % to 3.5 %. The value of the maximum stress ratio is a function of the effective confining stress at failure. The lower the effective confining stress, the higher the peak stress ratio that was reached. Deviation from this rule in the case of specimens S20 and S22 was caused by differences in their porosity. The disturbance indexes for these two specimens were very similar. The deviatoric stress versus axial strain plots are shown in Figure 4.24. The initial slopes are similar for the three tests that were carried out under higher initial effective confining stresses. For the two tests that were started at lower initial effective confining stresses, the curves are less regular and their initial slopes are smaller.

The volumetric change versus axial strain plots are shown in Figure 4.25. Only one test (S19), carried out under an initial effective confining stress of 3000 kPa, differs substantially from all other test results, that is, its dilation is less than half of the dilation of other specimens. The confining effective stress at failure of specimen S19 was relatively high (1160 kPa) compared to the confining stresses at failure of specimens S20 to S23, which were: 94, 360, 81 and 250 kPa respectively. At the beginning of axial

strain, the volume changes were increasing but relatively slowly. They started to increase in volume significantly at 0.5 % to 1.5 % axial strain and usually reached their maximum rate before the peak stress ratio. At larger axial strains, the rate of volume change became low again and the volumetric change-axial strain curves tended to level off. The average volume change at peak stress ratio for the four tests was 2.1 % and was 6 % at 5 % axial strain. The logarithm of effective permeability to water versus volume change is plotted in Figure 4.27 and versus water porosity in Figure 4.28. It is interesting that, in spite of different initial permeabilities and water porosities, the general trend of permeability increase with volume increase is similar. In two cases (specimens S20 and S22), the slope of the curves are substantially higher in the initial stages of the tests (up to a 2% volume change), but at larger strains the slopes again follow the general trend. Specimen S20 contained the largest amount of fines of all specimens. Specimen S22 contained less fines than specimen S20, but the common characteristic of both of them concerned the mode of fines distribution, which was in layers instead of in small pockets. The continuity of these impermeable layers was broken by shear deformation and dilation at the beginning of shear and the specimens then behaved similarly to the specimens without shale layers.

4.6 Summary

The experimental procedures followed in the triaxial tests on oil sand cores and the results of these tests have been described in this chapter. A total of 28 triaxial tests were carried out on 23 different specimens, following four different effective stress paths: isotropic unloading, triaxial compression, confining stress unloading, and constant p' . For each stress path, effective stress ratio, deviatoric stress, and volumetric strain were plotted against axial strain. Similarly, plots for each stress path were

constructed for effective permeability to water versus volumetric strain and versus water porosity. The stress paths followed are depicted in the s' - t stress field. The test results are compared and discussed in the next chapter.

Table 4.1 Specimen Initial Conditions

Specimen Number	Well Number	Geologic Unit (Depth, m)	Water (%)**	Bitumen (%)**	Solids (%)**	Saturation Ratio (%)	Dry Density (g/cm ³)	Bulk Density (g/cm ³)	Porosity (%)	In-situ Porosity (%)	Disturb. Index (%)	In-situ Water Porosity (%)
S1	AG14	E (153.4-153.7)	1.1	15.1	83.8	78.8	1.62	1.94	38.8	33.3	16.4	2.3
S2	AG14	E (153.2-153.4)	1.0	15.2	83.8	76.9	1.61	1.92	39.3	33.0	18.3	2.1
S3	AG14	E (152.1-153.0)	1.4	14.7	83.9	93.1	1.73	2.06	34.7	33.1	4.8	2.9
S4	AG14	E (152.1-153.0)	1.4	14.7	83.9	82.1	1.65	1.97	37.6	33.1	13.6	2.9
S5	AG14	E (152.1-153.0)	1.4	14.7	83.9	83.5	1.67	1.98	37.2	33.1	12.4	2.9
S6	AG11*	E (152.4-152.8)	1.3	15.2	83.5	87.3	1.67	2.00	36.8	33.7	9.2	2.7
S7	AT3	D (149.4-149.6)	2.3	14.6	83.1	86.0	1.64	1.98	38.0	34.5	10.1	4.9
S8	AT3	D (149.4-149.6)	2.3	14.6	83.1	85.5	1.64	1.98	38.1	34.5	10.5	4.9
S9	AG14	E (155.2-155.3)	2.3	15.0	82.7	90.0	1.66	2.00	37.5	35.0	6.9	4.8
S10	AG14	D (149.0-149.2)	1.7	14.9	83.4	89.2	1.68	2.02	36.5	33.9	7.7	3.6
S11	AT3	D (149.0-149.2)	1.9	14.6	83.5	82.1	1.63	1.96	38.3	33.4	13.5	4.0
S12	AT3	D (148.6-148.8)	2.7	14.6	82.8	84.7	1.62	1.96	38.8	35.0	11.0	5.5
S13	AT3	D (148.4-149.6)	3.5	11.7	84.9	81.2	1.69	1.99	36.3	31.4	15.6	7.4
S14	AT3	D (147.5-147.7)	2.0	13.8	84.2	83.9	1.68	1.99	36.7	32.7	12.2	4.2
S15	AT3	D (147.5-147.7)	2.0	13.8	84.2	87.3	1.70	2.02	35.7	32.7	9.3	4.2
S16	AT3	D (147.2-147.4)	1.4	14.5	84.1	83.1	1.67	1.99	37.0	32.8	12.8	2.9
S17	AT3	D (147.2-147.4)	1.4	14.5	84.1	85.1	1.67	2.00	36.4	32.8	11.1	2.9
S18	AT3	D (147.2-147.4)	1.4	14.5	84.1	85.8	1.69	2.01	36.2	32.8	10.5	3.0
S19	AT3	D (147.0-147.1)	2.9	13.9	83.3	86.4	1.66	1.99	37.5	34.2	9.8	6.0
S20	AT3	D (147.1-147.3)	2.3	13.4	84.3	83.1	1.68	1.99	36.7	32.5	12.9	4.9
S21	AT3	D (146.6-151.1)	1.7	14.5	83.8	87.7	1.69	2.02	36.2	33.3	8.9	3.6
S22	AT3	D (150.9-151.1)	2.0	14.5	83.5	84.7	1.65	1.98	37.6	33.8	11.2	4.1
S23	AT3	D (150.8-150.9)	1.5	14.4	84.1	82.6	1.67	1.98	37.1	32.8	13.3	3.3

* core ø 10.2 cm, in thin plastic liner

** content by mass

Table 4.2 Isotropic Unloading After Consolidation Under 5.6 to 6.0 MPa

Stress Path	Specimen Number	Initial Dry Density g/cm ³	Initial Bulk Density g/cm ³	Initial Porosity %	Disturbance Index %	In. Water Porosity %	Initial Perm. to Water μm^2	Eff. Confining Pressure Change, kPa	Volume Change %	Permeability to Water Change, %
Au	S19	1.69	2.06	36.2	5.8	8.9	$2.1 \cdot 10^{-4}$	5860 to 140	1.72	106
Ap	S20	1.73	2.08	34.9	7.4	8.3	$5.3 \cdot 10^{-6}$	5720 to 150	1.59	500
Au	S21	1.74	2.09	34.5	3.6	5.4	$7.7 \cdot 10^{-5}$	5960 to 160	1.60	258
Ap, Au	S22	1.70	2.07	35.9	6.2	7.2	$1.2 \cdot 10^{-5}$	5610 to 120	1.62	500
Au	S23	1.71	2.08	35.3	7.6	6.9	$5.3 \cdot 10^{-5}$	5660 to 120	1.73	214

Table 4.3 Specimen Conditions at the Beginning of Shear Tests

Stress Path	Specimen	Effective Confining Stress kPa	Bulk Density g/cm ³	Dry Density g/cm ³	Porosity %	Disturbance Index %	Water Saturation %	Water Porosity %	Effective Permeability to Water μm^2	Pore Pressure Coefficient B	Effective Conf. Stress During Measuring of B (kPa)
A σ	S1	820	2.04	1.67	36.9	10.6	22.7	8.5	$1.9 \cdot 10^{-3}$	0.86*	370
A σ	S2	1850	2.04	1.65	37.6	13.3	22.8	8.6	$1.5 \cdot 10^{-4}$	0.90*	240
A ϵ	S3	1300	2.07	1.74	34.4	3.9	13.9	4.8	$7.5 \cdot 10^{-5}$	0.38	1900
A ϵ	S4	480	1.98	1.68	36.7	11.0	22.4	8.2	$1.4 \cdot 10^{-3}$	0.36	4170
A ϵ	S5	970	2.00	1.69	36.2	8.7	20.7	7.5	$4.7 \cdot 10^{-4}$	0.52	2990
A ϵ	S6	2030	2.01	1.69	36.3	7.6	17.8	5.8	$4.3 \cdot 10^{-5}$	0.54	2060
A ϵ	S7	240	1.99	1.66	37.2	7.8	23.6	8.8	$2.3 \cdot 10^{-3}$	0.43	4300
A ϵ	S8	1970	2.00	1.68	36.6	6.0	21.5	7.9	$2.9 \cdot 10^{-4}$	0.40	4000
A ϵ	S9	2980	2.01	1.67	37.0	5.6	20.8	7.8	$1.4 \cdot 10^{-5}$	0.37	4070
A ϵ	S10	2960	2.09	1.73	34.7	2.4	13.8	4.8	$7.3 \cdot 10^{-5}$	0.34	4130
Gp	S11	2930	2.06	1.69	36.4	7.8	20.4	7.4	$6.8 \cdot 10^{-4}$	0.36	3780
Gp	S12	1920	2.04	1.67	37.2	6.3	23.8	8.9	$2.9 \cdot 10^{-4}$	0.39	3470
Gp	S13	1040	2.06	1.70	35.8	11.2	29.6	10.7	$8.0 \cdot 10^{-6}$	0.30	3860
Gp	S14	560	2.08	1.73	34.8	6.4	21.0	7.3	$5.7 \cdot 10^{-5}$	0.61	760
Gj	S15	2000	2.08	1.72	35.2	7.6	22.1	7.8	$1.6 \cdot 10^{-4}$	0.30	3860
Gj	S16	1510	2.06	1.69	36.2	10.4	21.6	7.8	$2.0 \cdot 10^{-4}$	0.41	3760
Gj	S17	980	2.07	1.70	35.8	9.1	20.4	7.3	$9.0 \cdot 10^{-5}$	0.32	4130
Gj	S18	2860	2.08	1.72	35.3	7.6	18.6	6.6	$3.5 \cdot 10^{-5}$	0.36	3890
Dp	S19	3000	2.06	1.68	36.5	6.7	25.4	9.3	$2.5 \cdot 10^{-4}$	0.32	5920
Dp	S20	890	2.07	1.71	35.4	8.9	25.3	9.0	$1.9 \cdot 10^{-5}$	0.92*	60
Du	S21	1950	2.08	1.72	35.0	5.1	17.4	6.1	$1.8 \cdot 10^{-4}$	0.95*	60
Du	S22	570	2.05	1.68	36.7	8.6	22.8	8.4	$4.9 \cdot 10^{-5}$	0.92*	50
Du	S23	1390	2.07	1.70	35.9	9.5	21.5	7.7	$1.4 \cdot 10^{-4}$	0.92*	50

Note: * measurement before consolidation

Table 4.4 Triaxial Shear Test Results

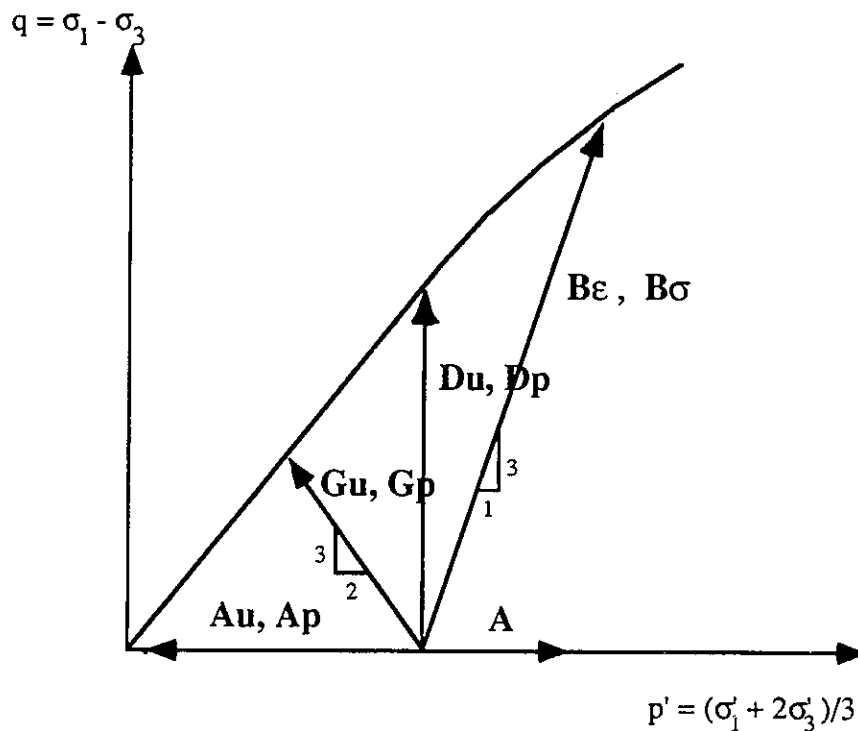
Stress Path	Specimen Number	Eff. Conf. Stress at Failure (kPa)	Effective Stress Rat. at Failure	Dev. Stress at Failure (kPa)	Axial Strain at Failure (%)	Volume Change at Failure (%)	Effect Perm to Water at Failure (μm^2)	k_{wf}/k_{wi}	Max. Volume Change Measured (%)	Max. Effect. Permeability to Water (k_{wmax}) (μm^2)	k_{wmax}/k_{wi}
B σ	S1	810	5.0	3200	5.1	1.2	3.0×10^{-3}	1.6			
	S2	1840	4.4	6200	3.5	-0.08	1.5×10^{-4}	1.0	0.67	2.1×10^{-4}	1.4
B ϵ	S3	1290	10.6	12400	1.8	0.38	2.0×10^{-4}	2.7	3.5	1.5×10^{-3}	20
	S4	480	8.5	3600	2.3	1.9	5.4×10^{-3}	3.9	5.6	4.3×10^{-2}	31
	S5	990	6.1	5100	2.3	1.1	1.3×10^{-3}	2.8	3.6	9.0×10^{-3}	19
	S6	2090	7.1	12700	4.4	-0.2	9.0×10^{-5}	2.1	1.3	2.2×10^{-4}	5.1
	S7	300	6.3	1600	3.6	1.1	6.0×10^{-3}	2.6	2.4	1.1×10^{-2}	4.8
	S8	2010	5.6	9200	3.3	-0.4	3.4×10^{-4}	1.2	0.2	5.2×10^{-4}	1.8
	S9	3000	5.0	12200	3.2						
	S10	2870	7.8	19500	2.6	-0.75	1.3×10^{-4}	1.8	1.0	5.5×10^{-4}	7.5
	S11	70	41	2800	1.9	3.0	2.7×10^{-3}	4	6.0	3.2×10^{-2}	47
	S12	63	28	1750	4.8	3.6	2.0×10^{-3}	6.9	6.6	1.0×10^{-2}	34
Gp	S13	26	52	1350	1.9	3.4	5.0×10^{-4}	62	4.4	1.0×10^{-3}	125
	S14	24	36	860	3.0	4.7	1.5×10^{-3}	26	6.9	6.2×10^{-2}	1090
	S15	42	55	2300	1.9	2.6	1.2×10^{-3}	7.5	7.5	4.2×10^{-2}	263
	S16	19	75	1420	1.0	4.0	2.3×10^{-3}	12	8.5	1.0×10^{-2}	50
	S17	10	145	1450	0.8	2.7	1.6×10^{-3}	18	8.7	2.0×10^{-1}	2222
	S18	58	56	3220	1.0	2.0	4.0×10^{-4}	11	4.9	1.1×10^{-2}	314
Dp	S19	1160	5.7	5480	3.5	1.5	4.7×10^{-4}	1.9	3.2	1.4×10^{-3}	5.6
	S20	94	27	2500	2.2	1.9	2.7×10^{-4}	14	5.7	2.4×10^{-2}	1260
Du	S21	360	14	4800	1.6	1.9	1.1×10^{-3}	6.1	6.4	1.9×10^{-2}	100
	S22	81	23	1760	1.7	2.8	1.6×10^{-3}	33	6.3	2.7×10^{-2}	550
	S23	250	14	3210	1.2	1.8	4.6×10^{-4}	3.3	6.6	2.5×10^{-2}	180

Note: k_{wi} - initial effective permeability to water

Table 4.5 Grain Size Distribution Data

Sample No.		Grain Size mm				Uniformity Coefficient $C_u = D_{60}/D_{10}$	Curvature Coefficient $C_c = D_{30}^2/D_{10}/D_{60}$	Fines Content		Water Content % (by weight)
		D10	D30	D60	D50			% < 0.075mm	% < 0.045mm	
P11	A	0.086	0.13	0.16	0.153	1.86	1.23	6.30		
P12	A	0.086	0.13	0.16	0.153	1.86	1.23	5.90		
P13	A	0.086	0.13	0.16	0.153	1.86	1.23	5.60		
P14	A	0.086	0.13	0.16	0.153	1.86	1.23	6.30		
S1	B	0.15	0.215	0.255	0.24	1.70	1.21	2.10	1.00	1.11
	A	0.16	0.215	0.24	0.224	1.50	1.20	2.50	1.30	
S2	B	0.15	0.22	0.265	0.255	1.77	1.22	2.70	1.50	1.01
	A	0.097	0.183	0.25	0.23	2.58	1.38	6.40	3.60	
S3	B-I	0.126	0.21	0.24	0.228	1.90	1.46	2.20	0.90	
	B-II	0.14	0.197	0.248	0.236	1.77	1.12	2.40	1.20	1.39
	A	0.086	0.124	0.19	0.167	2.21	0.94	5.30	1.80	
S4	A	0.114	0.165	0.22	0.21	1.93	1.09	2.70	0.90	
S5	A	0.093	0.16	0.22	0.204	2.37	1.25	6.20	1.00	
	B	0.104	0.15	0.18	0.172	1.73	1.20	1.80	0.70	1.29
S6	A	0.085	0.134	0.173	0.162	2.04	1.22	6.80	2.10	
	B	0.12	0.18	0.21	0.2	1.75	1.29	4.60	2.30	2.30
S7	A	0.1	0.12	0.215	0.204	2.15	0.87	7.10	4.70	
	B	0.083	0.16	0.19	0.18	2.29	1.62	8.80	5.80	
S9	B-I	0.124	0.153	0.24	0.22	1.94	0.79	5.30	2.40	2.30
	B-II	0.09	0.205	0.244	0.23	2.71	1.91	2.90	1.50	1.81
	A	0.073	0.112	0.173	0.15	2.37	0.99	9.90	4.10	
S10	B-II	0.09	0.12	0.158	0.147	1.76	1.01	6.00	2.90	1.51
	B-I	0.11	0.15	0.179	0.167	1.63	1.14	4.00	2.50	1.92
	A	0.092	0.123	0.165	0.156	1.79	1.00	6.00	2.50	
S11	A	0.1	0.132	0.172	0.159	1.72	1.11	4.00	2.10	
S12	B-I	0.083	0.107	0.14	0.128	1.69	0.99	7.50	3.50	2.66
	B-II	0.077	0.101	0.128	0.118	1.66	1.04	5.40	2.10	2.87
	A	0.08	0.1	0.122	0.114	1.53	1.02	6.60	2.30	
S13	B-I	0.06	0.135	0.19	0.128	3.17	1.60	12.00	5.80	2.49
	B-II	0.068	0.105	0.144	0.118	2.12	1.13	12.10	9.00	4.46
	A	0.04	0.088	0.12	0.114	3.00	1.61	20.70	11.60	
S14	B	0.08	0.112	0.142	0.132	1.78	1.10	8.50	2.20	1.99
	A	0.077	0.115	0.152	0.14	1.97	1.13	9.00	2.70	
S15	A	0.083	0.127	0.158	0.15	1.90	1.21	7.90	2.70	
S16	B	0.072	0.104	0.139	0.128	1.93	1.08	10.60	2.30	1.39
	A	0.065	0.104	0.137	0.128	2.11	1.21	13.80	3.00	
S17	A	0.071	0.096	0.13	0.118	1.83	1.00	11.50	2.40	
S18	A	0.066	0.097	0.126	0.115	1.91	1.13	13.50	4.30	
S19	B-I	0.065	0.116	0.147	0.142	2.26	1.41	11.40	7.50	4.26
	B-II	0.064	0.116	0.155	0.136	2.42	1.36	12.00	6.90	3.41
	A	0.073	0.105	0.135	0.127	1.85	1.12	10.00	3.90	
S20	B	0.03	0.1	0.13	0.12	4.33	2.56	17.40	12.20	4.32
	A	0.072	0.1	0.125	0.117	1.74	1.11	10.60	4.10	
S21	B	0.09	0.12	0.153	0.143	1.70	1.05	4.80	1.60	1.14
	A	0.088	0.122	0.153	0.144	1.74	1.11	6.30	2.60	
S22	B	0.102	0.13	0.162	0.152	1.59	1.02	3.30	1.50	1.96
	A	0.09	0.112	0.138	0.129	1.53	1.01	5.60	2.60	
S23	B-I	0.08	0.109	0.145	0.14	1.81	1.02	7.80	1.80	1.40
	B-II	0.082	0.115	0.152	0.129	1.85	1.06	7.60	2.50	2.25
	A	0.076	0.109	0.145	0.129	1.91	1.08	9.20	2.90	

Note B - grain size analysis performed on binnings
A - grain size analysis performed on specimens after tests



- A** - Isotropic Compression
- Au** - Isotropic Unloading by Pore Pressure Injection
- Ap** - Isotropic Unloading by Decreasing Confining Pressure
- Be** - Compression
- Bσ** - Compression
- Dp** - Constant p' , Compression with Decreasing Confining Pressure
- Du** - Constant p' , Compression with Pore Pressure Injection
- Gp** - Confining Stress Unloading, Compression with Decreasing Confining Pressure (Constant σ_1' and σ_3')
- Gu** - Confining Stress Unloading, Compression with Pore Pressure Injection (Constant σ_1')

Figure 4.1 Stress Paths Followed During Triaxial Tests on Oil Sands Core

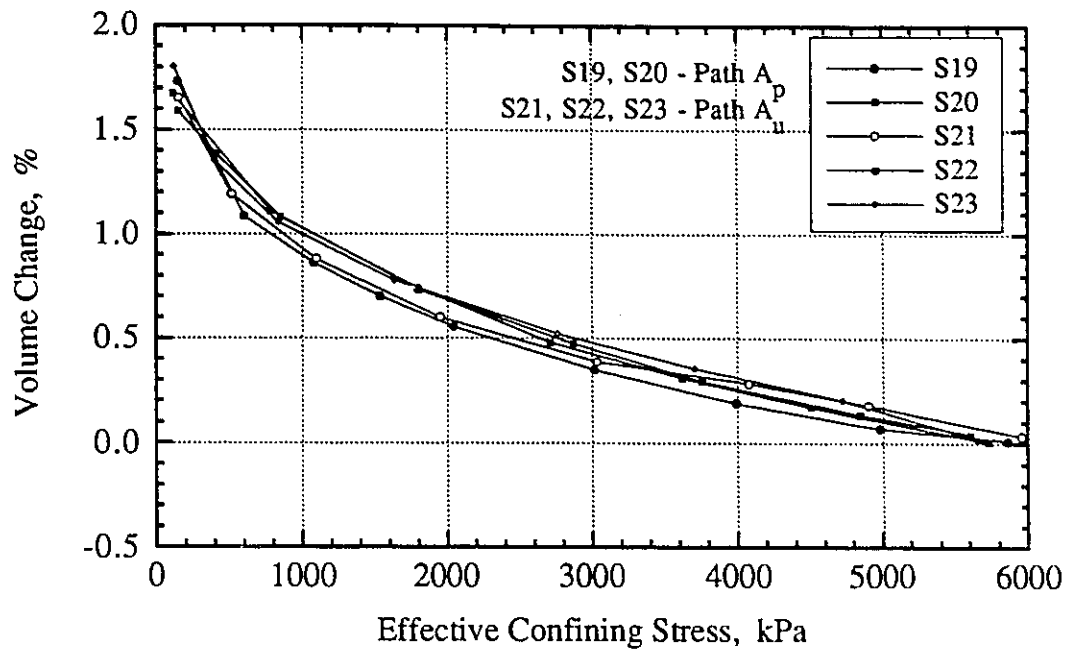


Figure 4.2 Stress Paths A_p and A_u, Volume Change - Effective Confining Stress

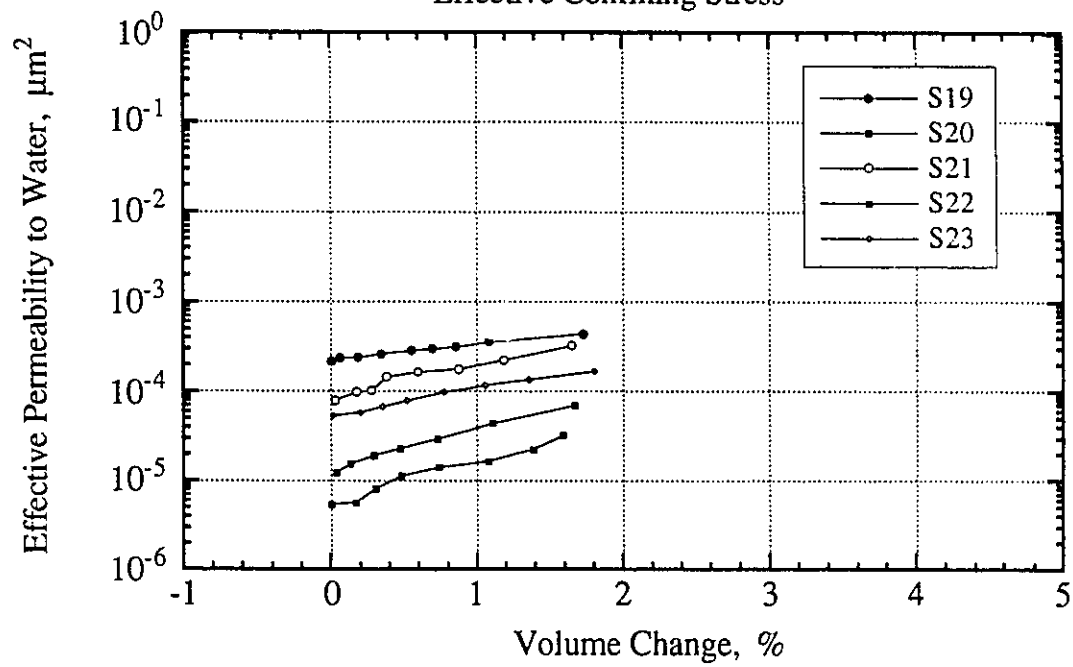


Figure 4.3 Stress Paths A_p and A_u, Effective Permeability to Water - Volume Change

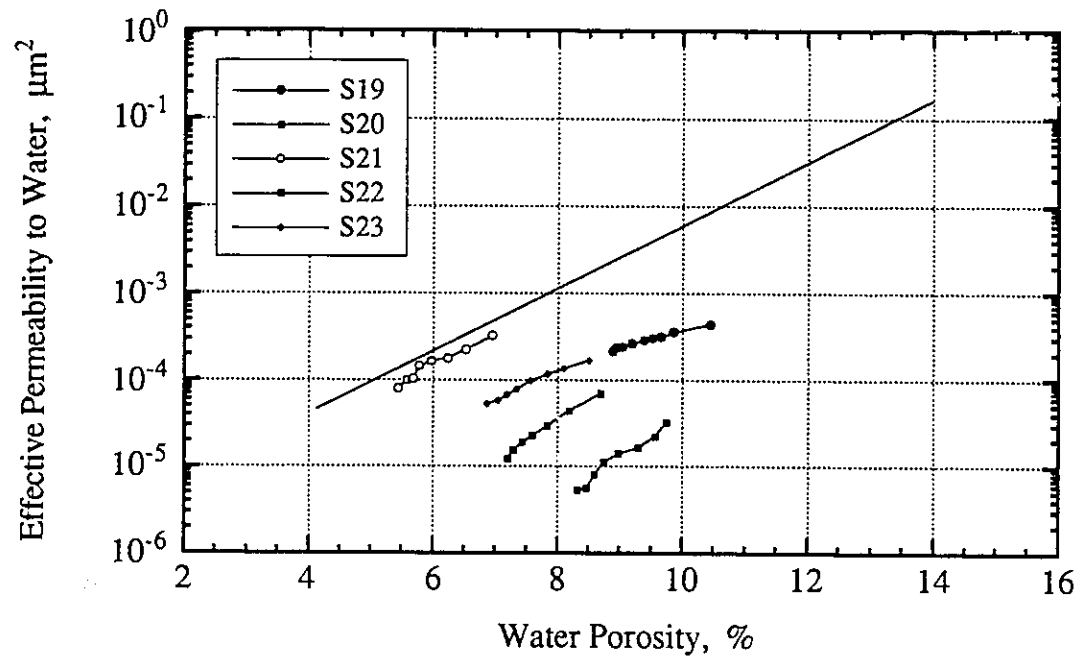
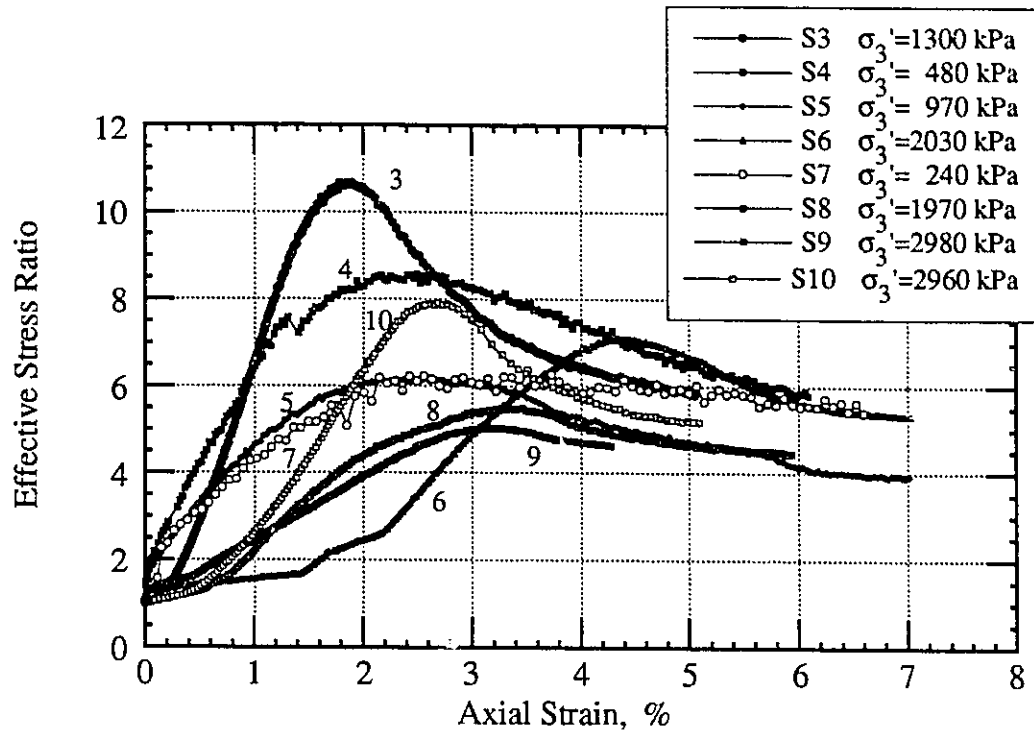
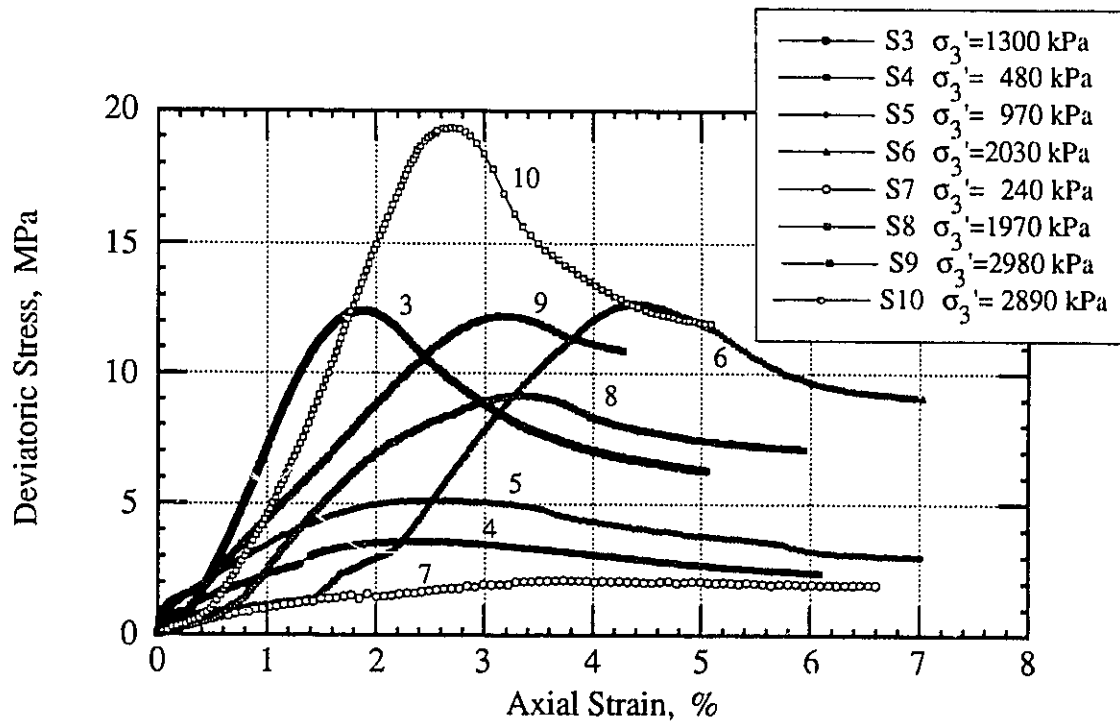
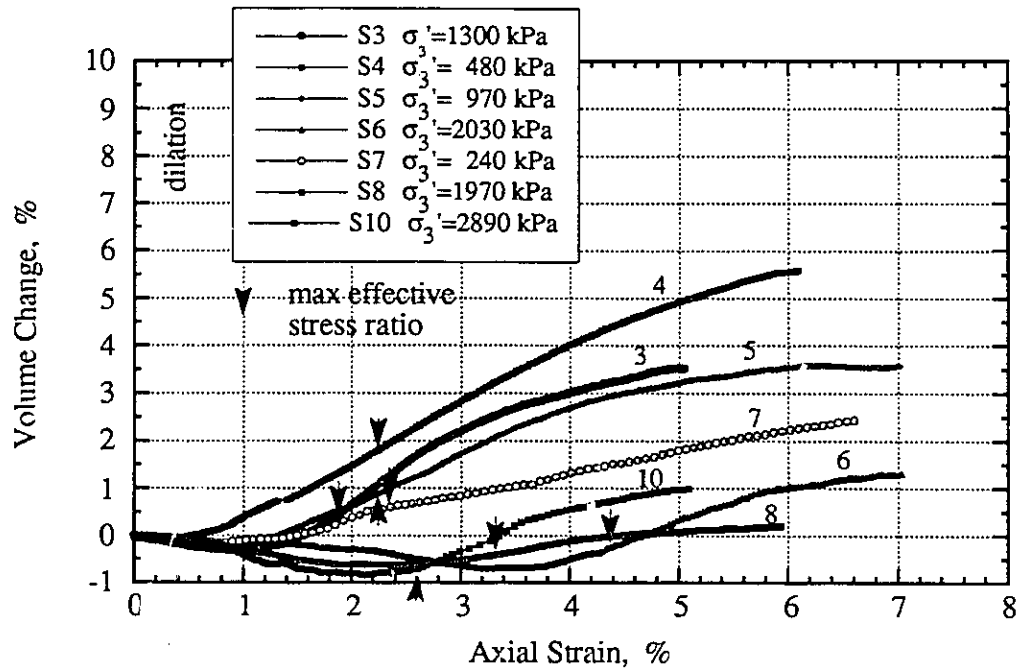
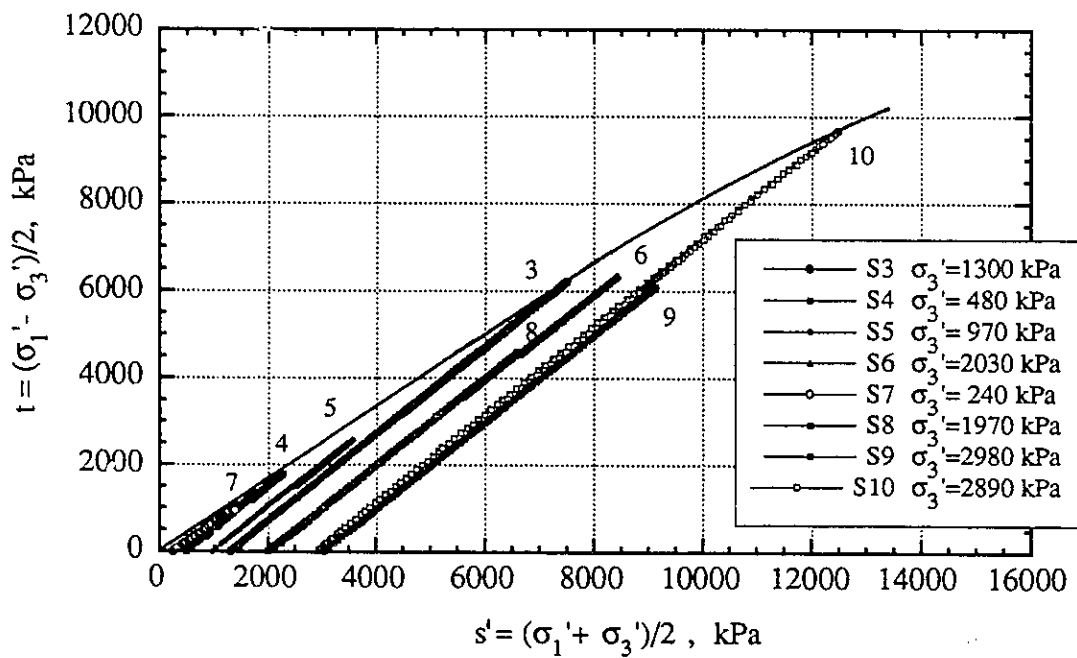


Figure 4.4 Stress Paths A_p and A_u , Effective Permeability to Water - Water Porosity

Figure 4.5 Stress Path B_e , Stress Ratio - Axial StrainFigure 4.6 Stress Path B_e , Deviatoric Stress - Axial Strain

Figure 4.7 Stress Path B_e, Volume Change - Axial StrainFigure 4.8 Stress Path B_e, Failure Envelope

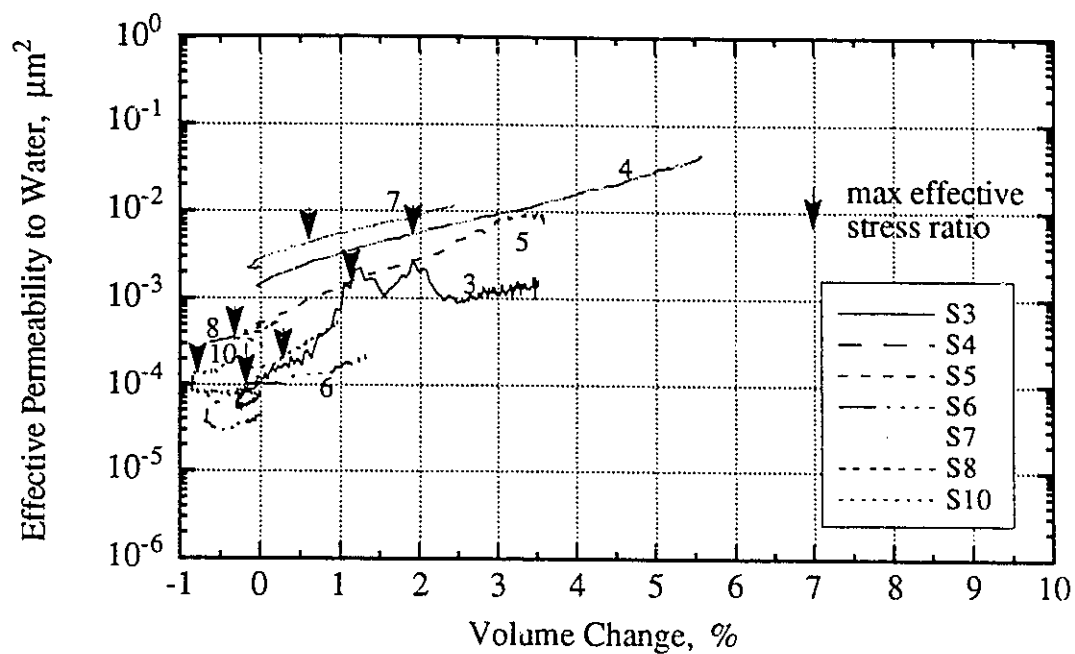


Figure 4.9 Stress Path B_e , Effective Permeability to Water - Volume Change

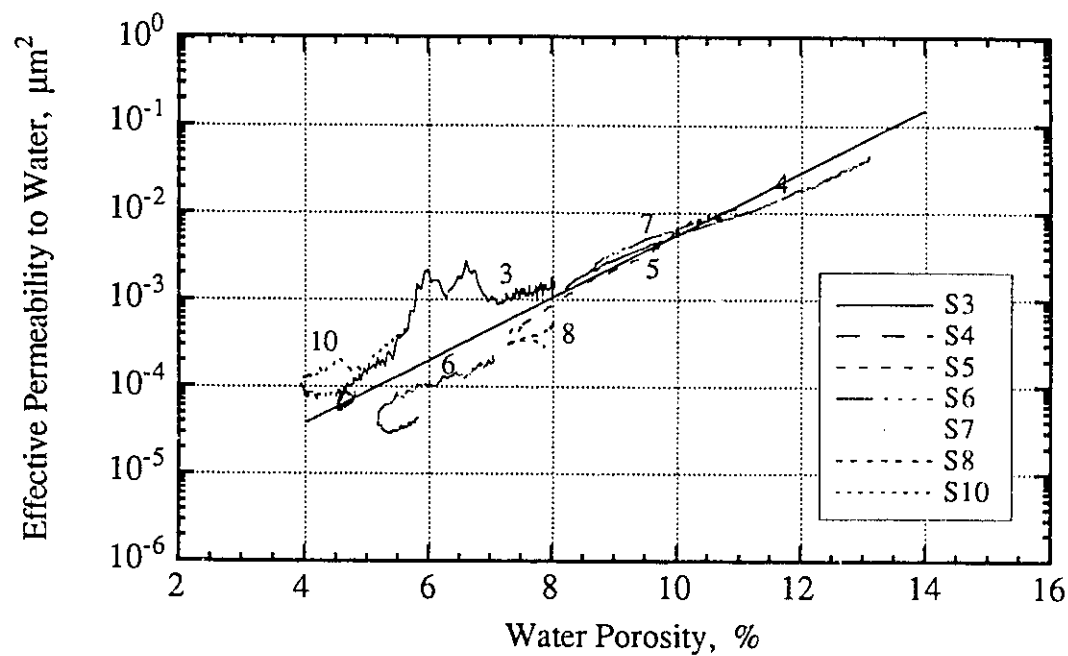


Figure 4.10 Stress Path B_e , Effective Permeability to Water - Water Porosity

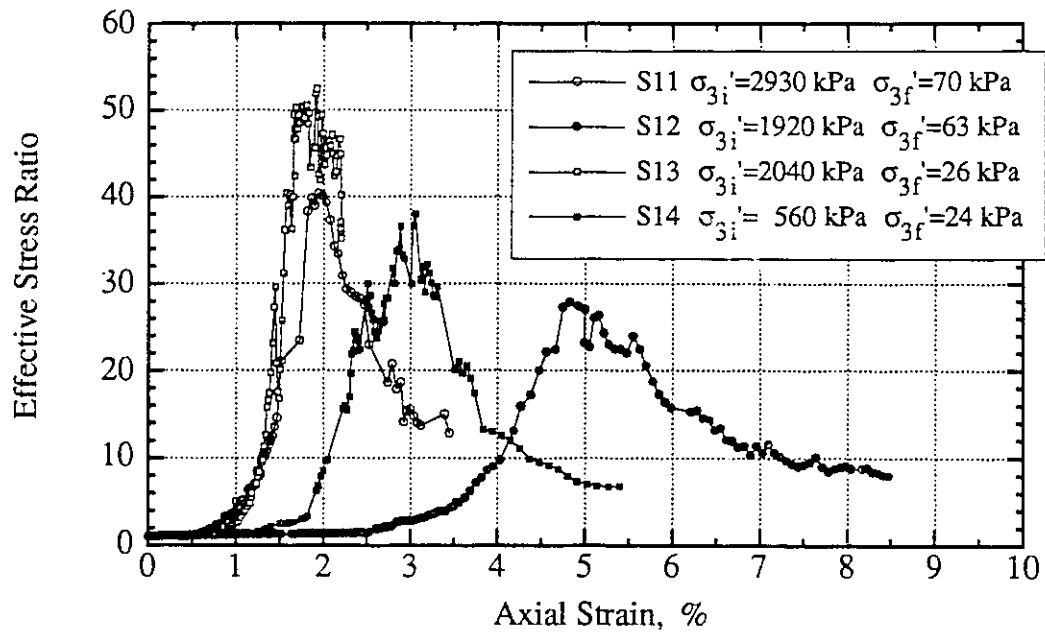


Figure 4.11 Stress Path G_p , Effective Stress Ratio - Axial Strain

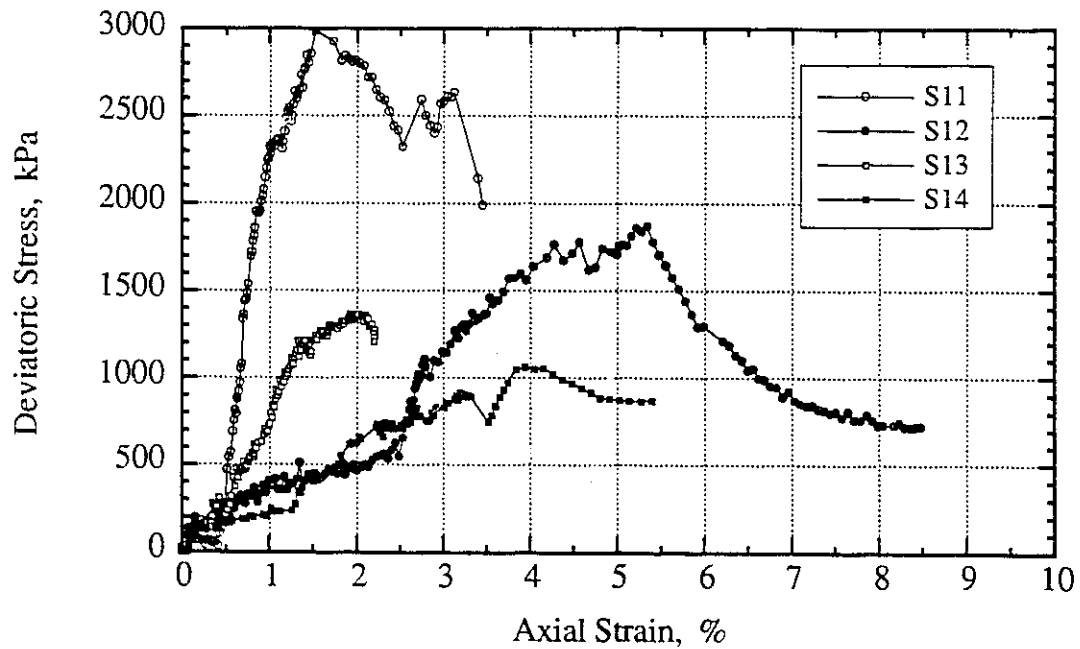


Figure 4.12 Stress Path G_p , Deviatoric Stress - Axial Strain

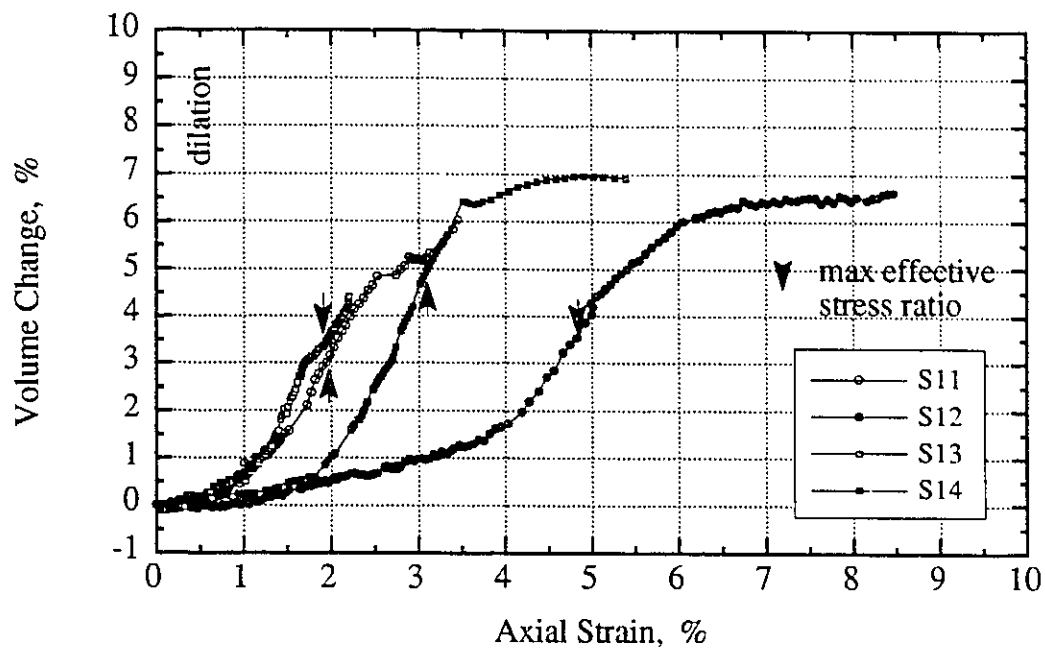


Figure 4.13 Stress Path G_p , Volume Change - Axial Strain

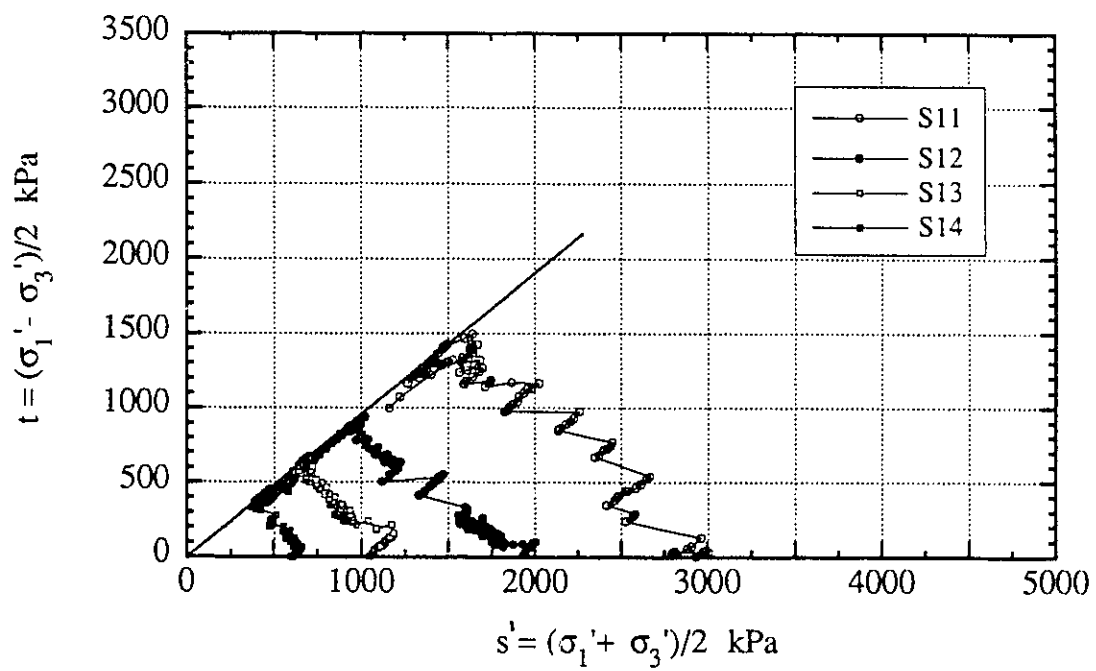


Figure 4.14 Stress Path G_p , Failure Envelope

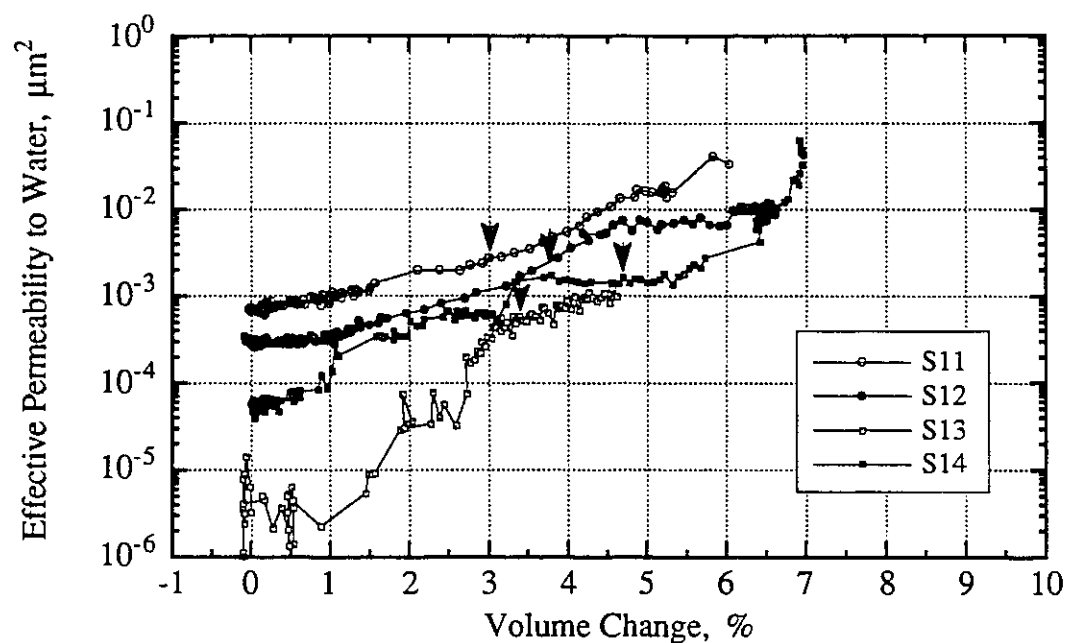


Figure 4.15 Stress Path G_p , Effective Permeability to Water - Volume Change

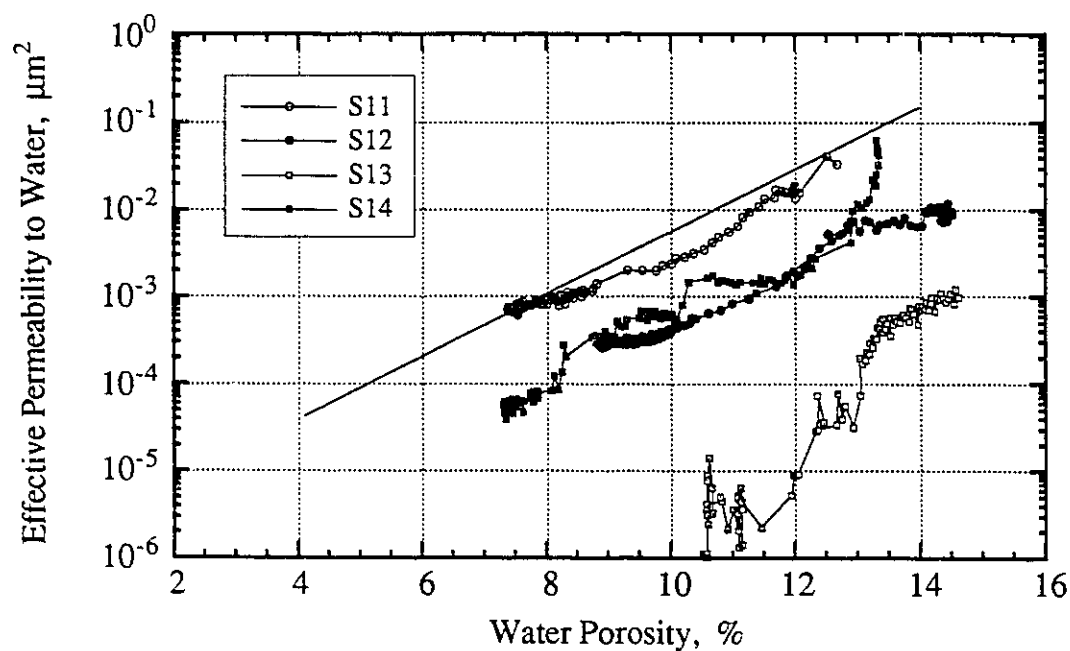


Figure 4.16 Stress Path G_p , Effective Permeability to Water - Water Porosity

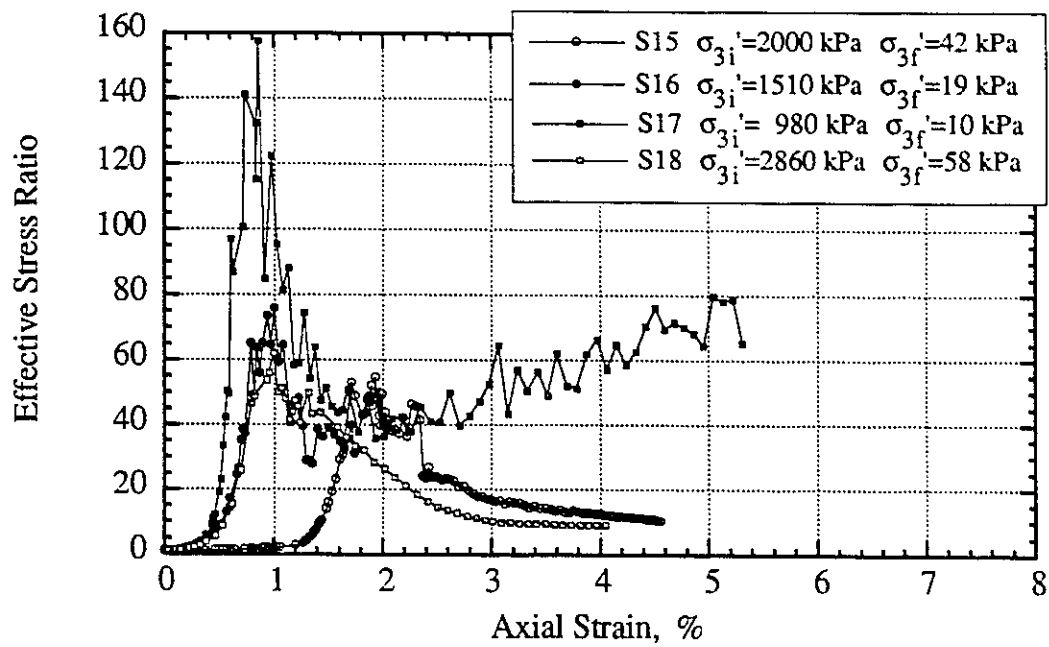


Figure 4.17 Stress Path G_u , Effective Stress Ratio - Axial Strain

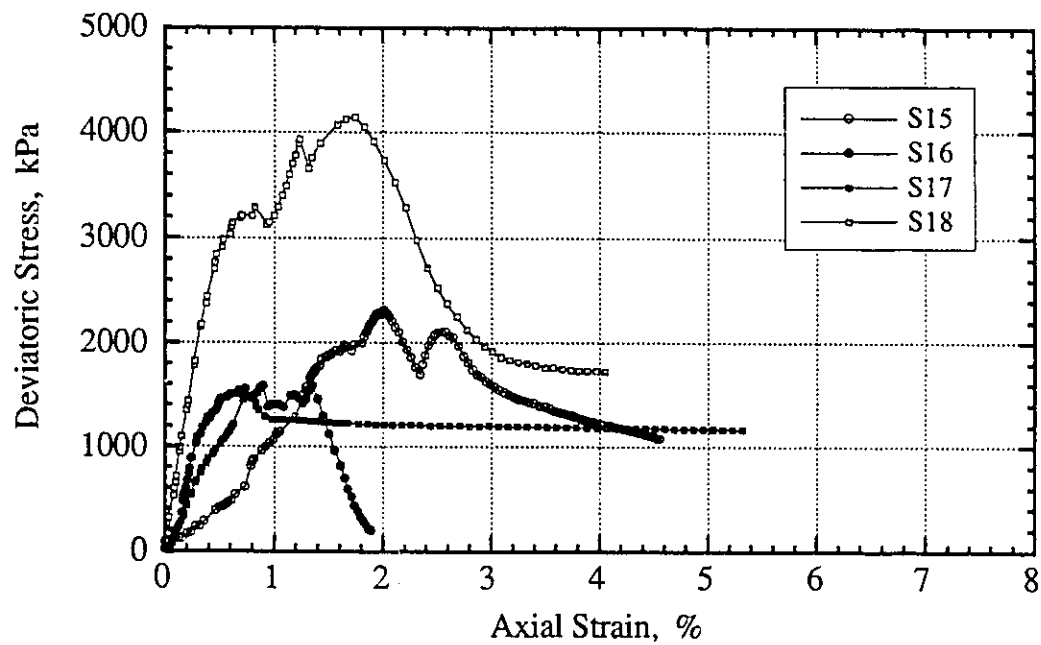


Figure 4.18 Stress Path G_u , Deviatoric Stress - Axial Strain

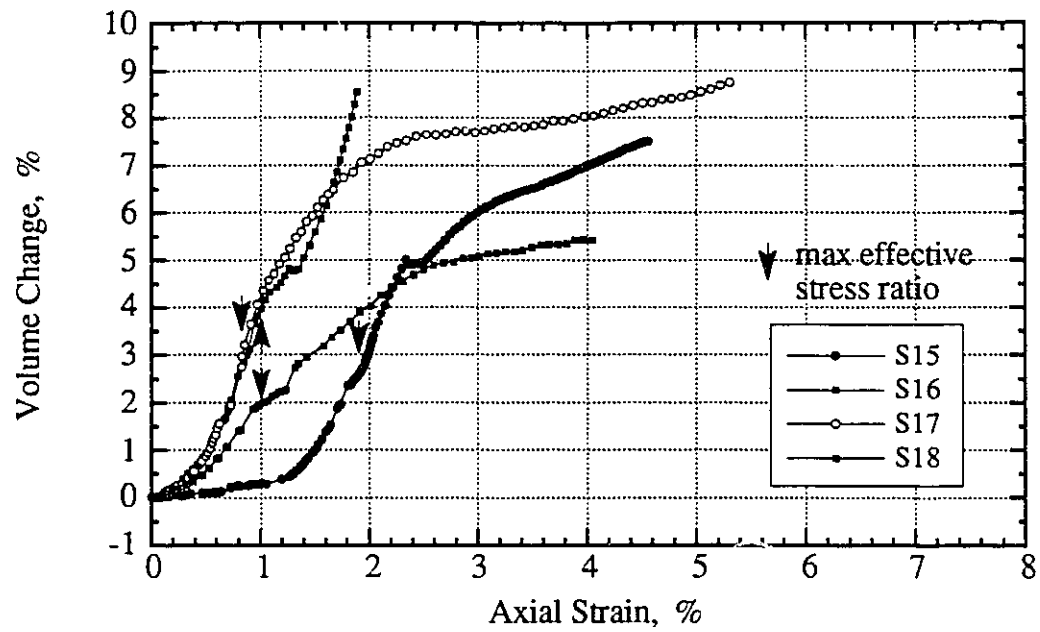


Figure 4.19 Stress Path G_u , Volume Change - Axial Strain

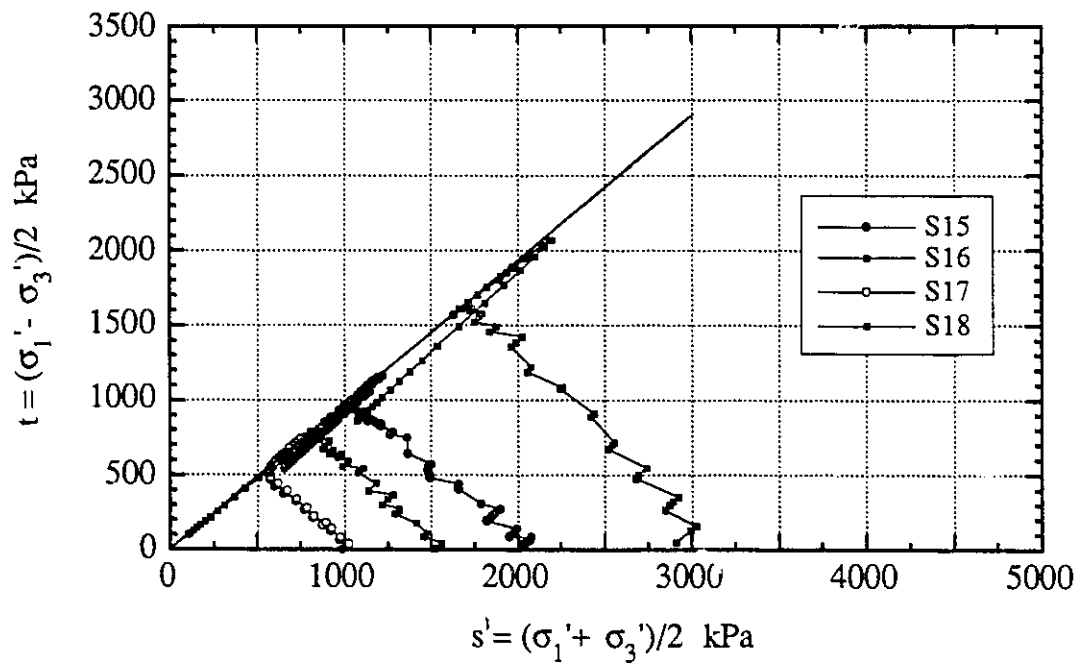


Figure 4.20 Stress Path G_u , Failure Envelope

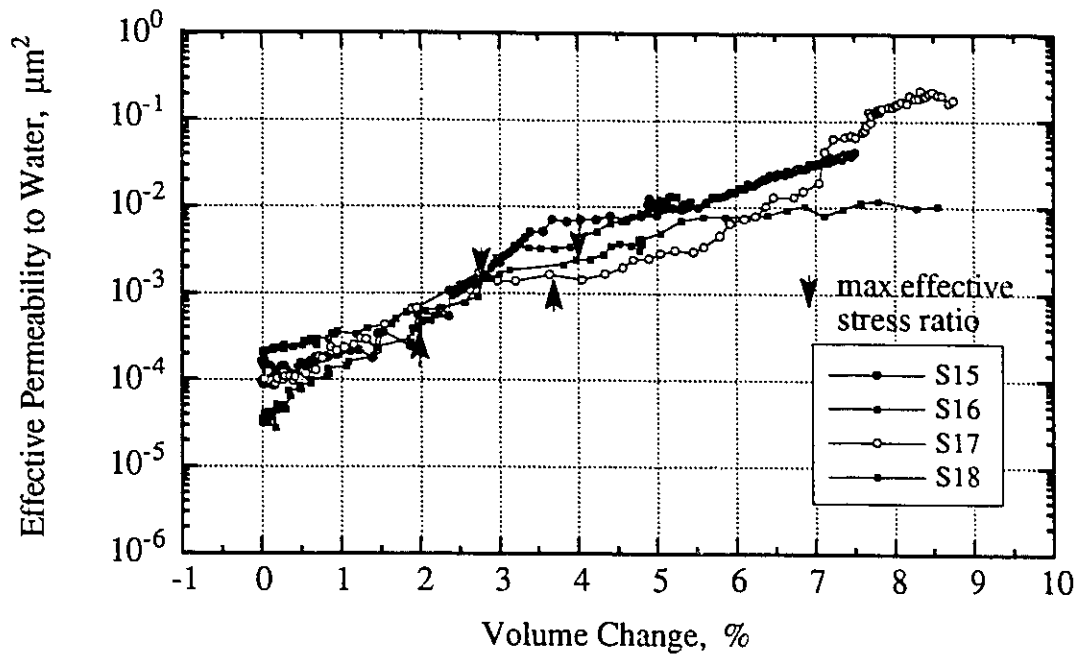


Figure 4.21 Stress Path G_u , Effective Permeability to Water - Volume Change

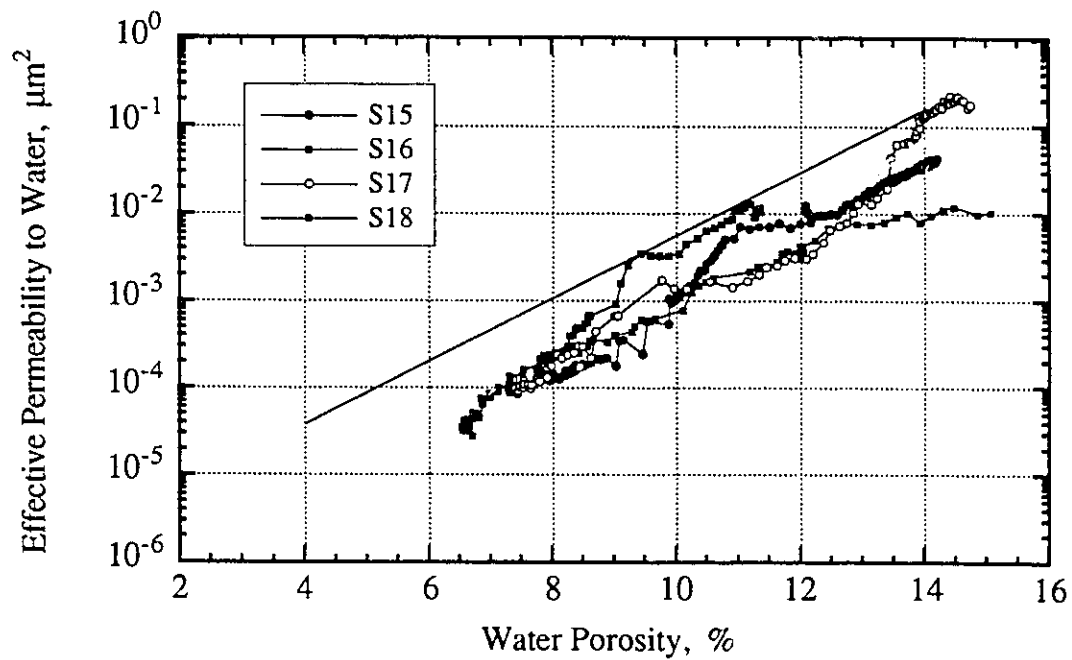


Figure 4.22 Stress Path G_u , Effective Permeability to Water - Water Porosity

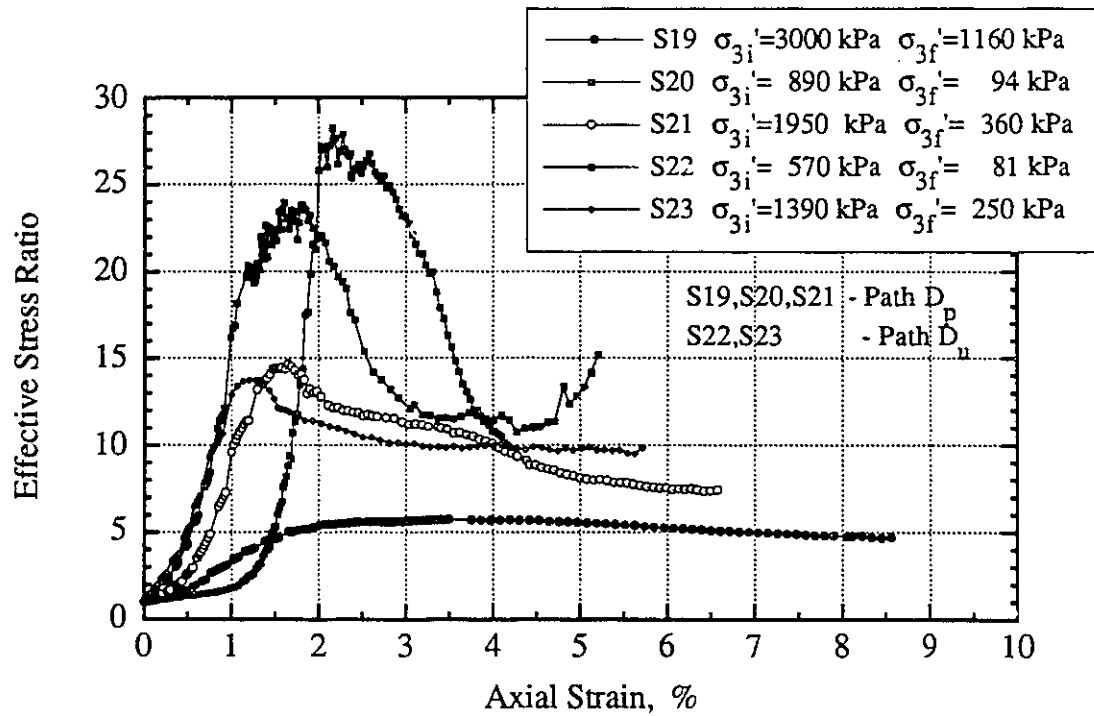


Figure 4.23 Stress Paths D_p and D_u , Effective Stress Ratio - Axial Strain

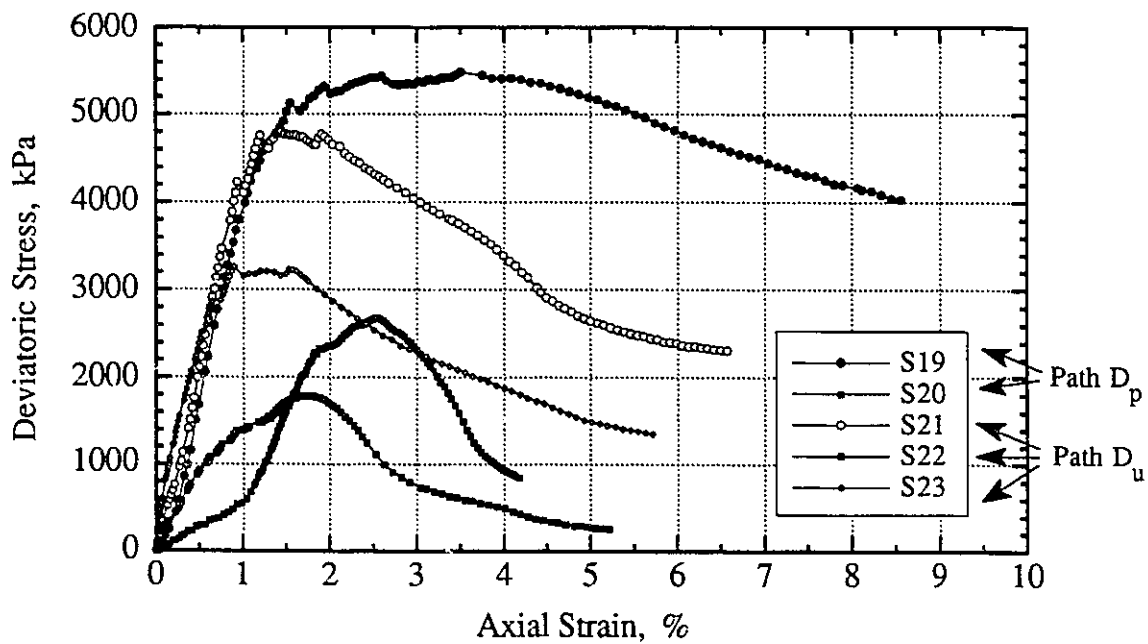


Figure 4.24 Stress Paths D_p and D_u , Deviatoric Stress - Axial Strain

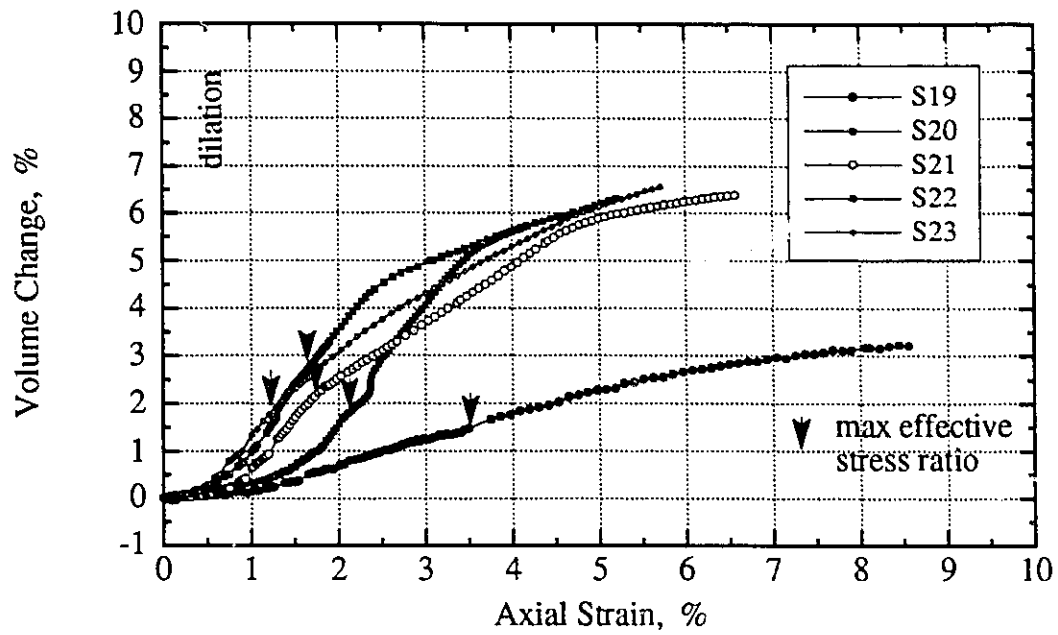


Figure 4.25 Stress Paths D_p and D_u , Volume Change - Axial Strain

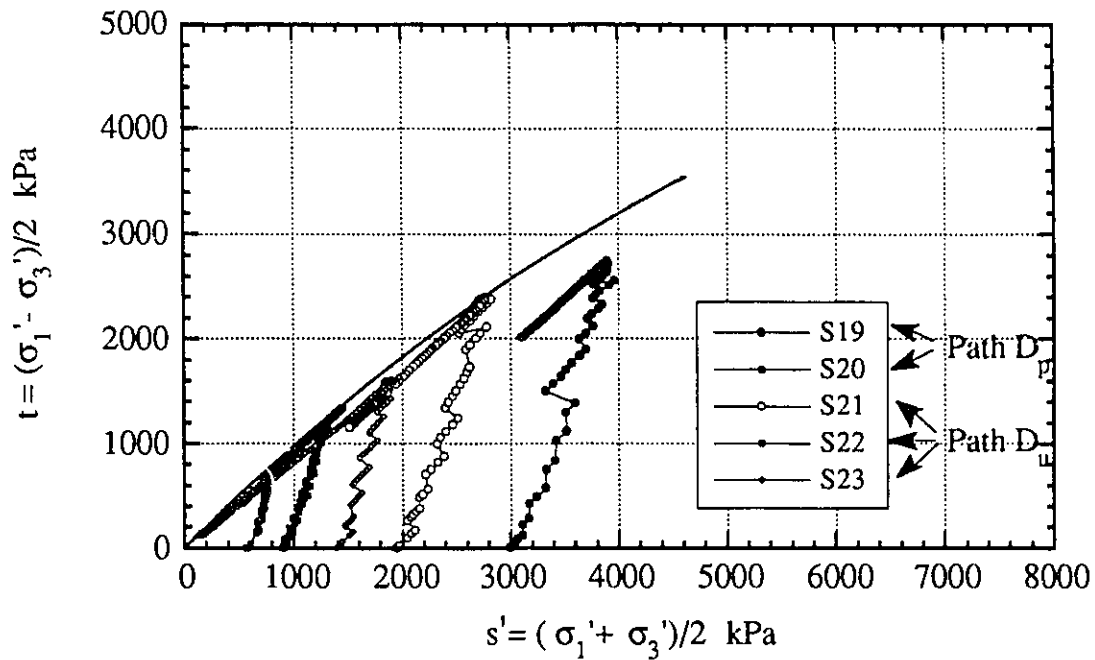


Figure 4.26 Stress Paths D_p and D_u , Stress Envelope

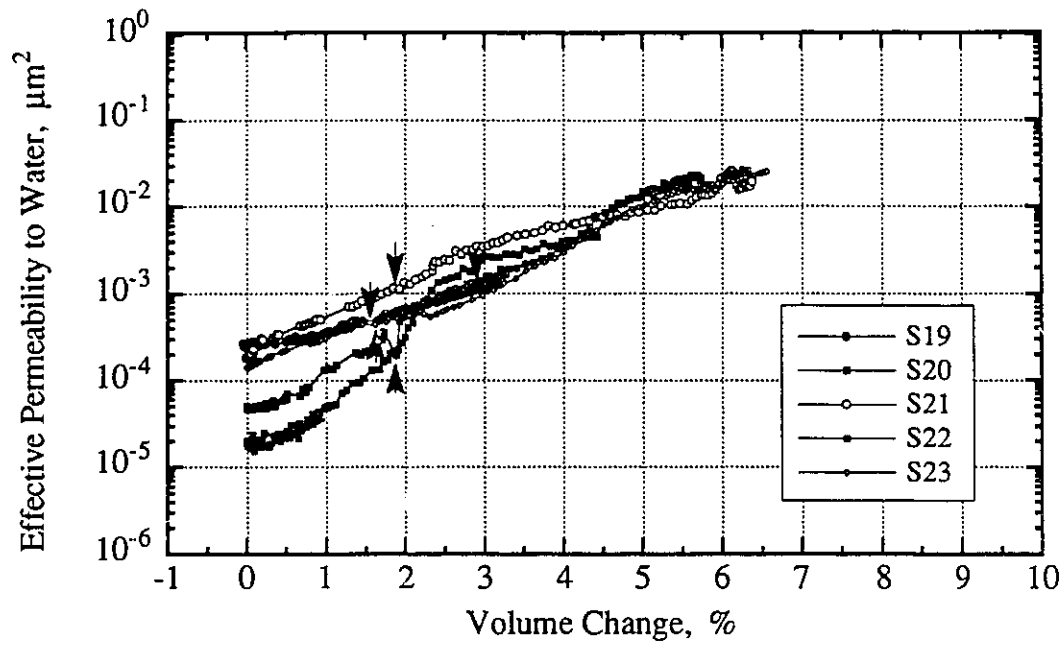


Figure 4.27 Stress Paths D_p and D_u , Effective Permeability to Water - Volume Change

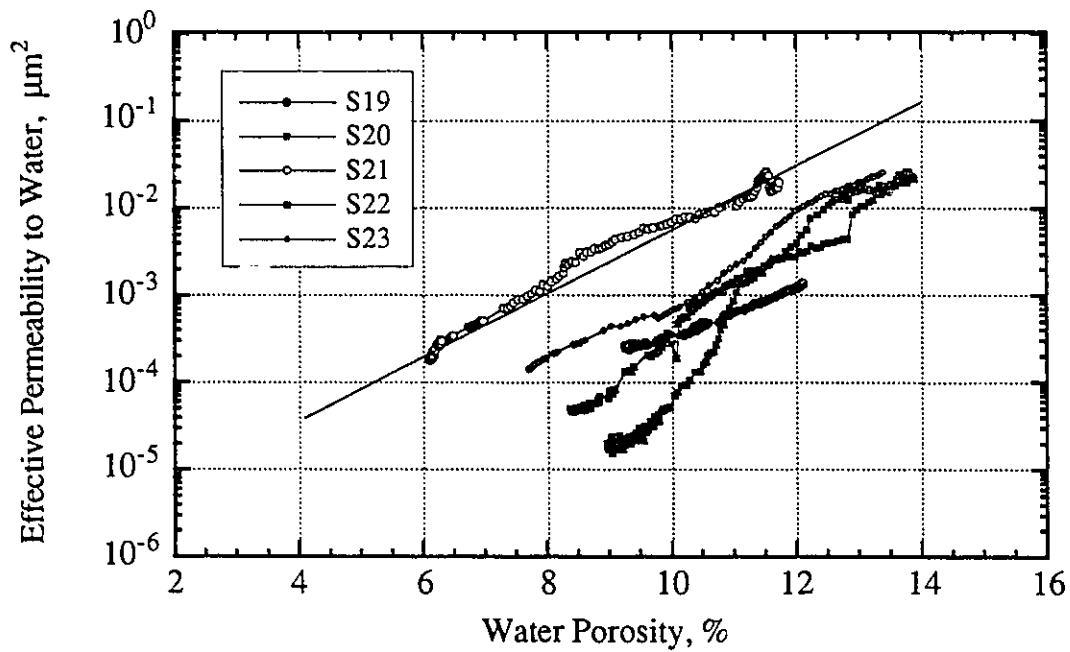


Figure 4.28 Stress Path D_p and D_u , Effective Permeability to Water - Water Porosity

Chapter 5. EFFECTIVE PERMEABILITY TO WATER - DISCUSSION OF TEST RESULTS

5.1 Specimen Saturation and Compressibility

The effective permeability to water tests on oil sands cores were conducted under conditions of complete liquid saturation, that is, any gas bubbles in the core were driven back into solution. The pore pressure parameter B (defined as the ratio of change in pore pressure to change in cell pressure) was measured for all specimens to ensure they were saturated. The oil sands isotropic compressibility, used for the calculation of the theoretical value of B , was determined from tests on five specimens (S19 to S23).

The complete saturation of specimens was achieved either by saturation after isotropic compression or before isotropic compression. Saturation after compression, conducted on specimens S3 to S19, was performed in order to reduce the amount of water needed to inject into the specimen to completely drive gas bubbles into solution. Because the need arose to measure specimen volume changes during isotropic compression, the remaining specimens were saturated before compression, so that volumetric changes could be measured with the EMA in the back pressure system. In both methods, saturation conditions were checked by observing changes in pore pressure parameter B (Equation 3.2). Complete saturation is obtained when B becomes constant with an increase in pore pressure (under unchanged effective stress). Figure 5.1 shows the changes in parameter B with changes in pore pressure for specimens S20 to S23.

The experimental values of B , obtained from completely saturated specimens, are shown in Table 4.3 and plotted versus the coefficient of isotropic compressibility (c_s) in Figure 5.2. The effective confining stresses (σ_3'), under which values of B were

determined, are also shown in Table 4.3. The compressibilities of specimens saturated after compression, as shown in Figure 5.2, were calculated using the equation obtained as a best fit to the test results (shown in Figure 5.3) from specimens S19 to S23 during isotropic unloading:

$$c_s = 0.00127 \cdot \sigma_3'^{-0.815} \quad (\text{Figure 5.4}) \quad 5.1$$

A curve following this equation is shown in Figure 5.4 together with the experimental compressibility data. The compressibilities of specimens saturated before compression were estimated from Figures A.7 and E.2 to E.5, all of which show plots of specimen volume changes against effective confining stresses.

Figure 5.2 shows that the pore pressure parameter value varies with changes in compressibility, which, in turn, is a function of effective confining stress and loading history. A scatter of B values also occurred at the same effective confining stress (the same compressibility). This variation could result from slight differences in the compressibilities of individual specimens and the average values are reflected by Equation 5.1.

The experimental results were compared to the theoretical relations between pore pressure parameter B and compressibility, as defined by the equation:

$$B = 1 / (1 + (\phi_w \cdot c_w + \phi_b \cdot c_b) / c_s) \quad 5.2$$

where: ϕ_w - water porosity (ratio of volume occupied by water to total specimen volume)

ϕ_b - bitumen porosity (ratio of volume occupied by bitumen to total specimen volume)

$c_w = 0.45 \cdot 10^{-6} \text{ kPa}^{-1}$ - compressibility of water

c_b - compressibility of bitumen

c_s - compressibility of oil sands structure or matrix

The typical porosities used in calculations were: $\phi_w = 7.5 \%$ and $\phi_b = 28.5 \%$. The compressibilities of oil sands specimens were calculated from Equation 5.1. Two theoretical curves were plotted for two different bitumen compressibilities to show how bitumen compressibility influences the B value. The bitumen compressibility value of $2.1 \cdot 10^{-6} \text{ kPa}^{-1}$ was taken from Plewes (1987). This compressibility value resulted in theoretical values of B higher than that given by the experimental results. A larger bitumen compressibility of $8.0 \cdot 10^{-6} \text{ kPa}^{-1}$ was used in Equation 5.2 and resulted in B values which more closely matched the experimental results.

The compressibility of bitumen used by Plewes was measured from core which originated from shallow deposits at the Syncrude open pit mine. The core used in this study was taken from deeper deposits (150 m) at the UTF site. The core was preserved in a frozen state from the moment of recovery to the time it was used in the experiments conducted at the in situ temperature of 8°C . The bitumen in the UTF core is saturated with gas at the in situ temperature and pore pressure, that is, it is a live oil. It, therefore, contains more dissolved gas than that contained in the core used by Plewes. An increase in the amount of gas dissolved in bitumen increases the compressibility of the bitumen.

5.2 Volume Changes

This section presents and interprets volume changes (as defined in 3.6.2) that occur in Athabasca McMurray Formation oil sands during stress-induced deformations. The volume changes are analyzed in the context of changes in mean effective stress and in shear stress, as well as in the context of the intergranular interactions and the mutual rearrangements of grains that are associated with sand structure deformations. Extending the proposal of Wong et al. (1993), the possible deformations have been grouped into

five different modes: contact elastic deformations, rearrangement, sliding (frictional sliding), rolling (shear contraction and dilation), and crushing (grain breakage).

5.2.1 Isotropic Unloading Tests

During the initial isotropic compression of specimens the dominant mode of deformation is the rearrangement of particles, with the elastic deformations of individual grains playing a lesser part. When the specimen is unloaded, only the portion of the work used to produce the elastic deformations is recovered. During the recompression cycle, on the other hand, contact elastic deformations are dominant. The hysteresis, which occurs between the unloading and reloading phases of a cycle, indicates a lag in the response of oil sands towards changes in forces. Comparisons made between the unloading and reloading cycles, shown in Appendix E, must be carried out with the recognition that the two stress paths were conducted with different time intervals between consecutive pressure changes.

Figure 5.5 shows total volume changes of the specimens measured during isotropic unloading tests carried out on samples S19 to S23, during which permeability measurements were conducted. The best curve fit to all data takes the form:

$$\epsilon_v = A_v + B_v \cdot \log \sigma_3' \quad 5.3$$

where: $\epsilon_v = \Delta V/V_0$ - volumetric strain (= volume change), %

σ_3' - effective confining stress, kPa

A_v, B_v - constants

The constants were calculated as: $A_v = 3.980$ and $B_v = -1.031$ ($R=0.991$). One curve was fitted to all the results of the five tests because of the obvious similarity between the different experimental curves (Figure 4.2).

The power function, often used to relate the change in bulk volume to the change in confining pressure (Wong, 1993), is less accurate. This curve is also shown in Figure 5.5 for comparison and is not considered further.

The pore volume changes (ϵ_{vp}) versus effective confining stresses are shown in Figure 5.6 and are curve fitted with the function:

$$\epsilon_{vp} = 11.1 - 2.86 \cdot \log \sigma_3'$$

5.2.2 Triaxial Shear Tests

The three types of triaxial shear tests differed in the way changes were made in the two components of the state of stresses, the mean effective stress and the deviatoric stress. However, the general picture of specimen deformations in all tests was similar to that which occurred during the conventional compression test, with an increase in compressive strain in the axial direction (imposed by the loading frame) and an increase in the expansive strain in the radial directions.

The mutual displacement of grains is more complex in triaxial compression tests than during isotropic unloading. During isotropic stress changes, the specimen increases or decreases its dimensions in all the principal directions. During the triaxial compression test, the specimen is compressed in the axial direction at a constant rate of strain and expands in the radial directions at the same time. At the initial stages of triaxial testing on dense sand specimens, contact elastic deformations and rearrangement dominate, resulting in a decrease in the net volume of the specimen. At higher stress ratios, sliding (the relative motion between groups of particles) and rolling dilation occur, which results in permanent (plastic) increases in volume. The grains forced to move laterally override one another causing this expansion in the volume of the pores in the specimen. At high confining stresses, dilation can be somewhat suppressed by the shearing and crushing of

sand grains. The McMurray Formation sands, being almost all quartz grains, withstand grain crushing except at very high stress levels which do not occur at the UTF site.

Figure 5.7 shows the relationships between volumetric changes and mean effective stresses (p'), as measured on specimens at shear failure (at the maximum effective stress ratio) and at the end of testing (residual shear strength condition). Similar relationships between pore volume changes and mean effective stresses are shown in Figure 5.8. The solid line represents volume changes at failure as a function of p' . The dashed line gives an approximation of the largest volume changes which would be expected to occur at a given p' value. The results of the tests indicate that the Athabasca McMurray Formation oil sands undergo a substantial increase in volume at shear failure if the mean effective stress is lower than about 3 MPa. This volume increase can occur at even larger mean effective stresses (up to 6 MPa) if sand is deformed to larger axial strains ($> 5\%$). At low mean effective stresses (< 0.5 MPa) volumetric changes can be substantial, exceeding 25 % of the initial pore volume or 10 % of the initial total volume of the specimen. It should also be noted that volume increase at failure constitutes only a fraction of the volume increase occurring at larger axial strains.

The relationship between volume change at failure and the mean effective stress, measured on different specimens following different stress paths, is fairly consistent. However, some scattering of points in Figure 5.7 follows from differences in specimen void ratios. The initial porosity or void ratio is another parameter having an influence on specimen volumetric changes. Its influence can be determined when comparing the results of tests following the same stress path. For example, specimens S3 and S8, both of which failed at mean effective stresses of about 5.3 MPa, displayed 0.4 % and -0.4 % volumetric strains, respectively. Figure 5.18, which plots void ratio versus mean effective stress, displays a difference in the initial void ratios of these specimens (0.52 and 0.57).

Figures 5.18 and 5.20 also illustrate that specimens having a lower initial void ratio have a larger potential for volumetric increase during shear. The figures also compare volumetric changes during shear tests with those that occur during isotropic unloading tests.

5.3 Effective Permeability to Water

5.3.1 Bitumen Mobility

In field extraction operations, the bitumen contained in Athabasca McMurray Formation oil sands can be considered immobile at reservoir temperatures. However, following these laboratory tests, conducted on short specimens (38.1 mm in length), small amounts of bitumen, ranging from about 2 to 9 % of the bitumen initially contained in the specimens, were found in the porous stones. Some of the bitumen could enter the porous stones because they were in direct contact with pressurized specimens. Nevertheless, various amounts of bitumen must have been displaced from the specimens as the result of other factors, such as specimen compression. The amounts of bitumen expelled from specimens, however, were relatively small and the resulting error in the measured effective permeability to water should not be greater than a few percent.

A broader discussion of the problem of bitumen mobility, as well as of the estimation of the error that could occur in calculated effective permeability to water, are carried out in Appendix D. The error resulting from the displacement of small amounts of bitumen from specimens influences calculations of the effective permeability to water. However, this influence is in the opposite direction to the error resulting from nonuniform specimen dilation brought about by friction between porous stones and

specimen, as described in Appendix B. One of these errors would tend to offset the other to a certain degree.

5.3.2 Influence of Fines on Permeability

No evidence was found of fines movement during the effective permeability to water tests, even though fresh water was used as a permeant. As discussed in Section 2.2.4, when fresh water is used as a permeant, it may cause problems by dispersing clays and allowing them to move which could decrease or increase permeability. Observations made during the initial stages of testing revealed that after the differential pressure across a specimen was established, the differential pressure often decreased, indicating a slight increase in permeability; however, given time, the pressure gradient stabilized. No increase in the pressure gradient took place that could indicate a permeability reduction caused by the movement of fines. The initial decrease in the differential pressure could be associated with the bitumen mobility described in the previous section or could simply follow from the reshaping of the channels through which water flowed.

Most of the fines in the specimens were contained in shale and silt fragments or layers, visible to the naked eye. The fragments varied in size from very small to several millimeters in length. The layers or lenses were longer and sometimes extended throughout the whole cross-sectional area. These shale fragments are detrital and cannot move without destroying the existing sand structure. Moreover, water in oil sands of low water saturation does not flow along the whole grain surfaces but through channels that are built of interconnected pendular rings (Section 2.1.3); therefore, the amount of authigenic fines that could possibly be entrained into flowing water was further limited to those which happened to border with the water channels. A noticeable reduction in

measured permeability did not take place, either because the amount of fine particles was not sufficient, or because the particles themselves were not free to move.

The fine particles did not create problems on a microscale level (in pore spaces). However, in many cases, shale fragments, as well as shale and silt layers, were obstacles to flow on the macroscale level. As a general rule, specimens which contained larger amount of fines, despite their larger total water content, had a significantly lower initial permeability than low fines specimens. Also, the rate of change in permeability with changes in porosity, in the initial stages of testing, was higher for specimens containing more fines (Figure 5.11). At larger volume changes, the rate of increase in permeability became similar for all specimens.

5.3.3 Initial Permeability of Oil Sand Cores

The effective permeabilities to water of core specimens, measured at the beginning of the triaxial shear tests or the isotropic unloading tests, are plotted in Figure 5.9. The permeabilities of tested specimens varied between $5.3 \cdot 10^{-6} \mu\text{m}^2$ and $2.3 \cdot 10^{-3} \mu\text{m}^2$. This significant difference in permeability values occurred for specimens of similar water porosity but different fines content.

The line plotted in Figure 5.9 represents the best linear semi-logarithmic fit to the test results from specimens S1, S3, S4, S5, S10, and S11. All these specimens contained only a small amounts of fines (<2 % particles smaller than $45 \mu\text{m}$) distributed in small separated fragments. Therefore, the differences in the permeability of these samples result from differences in their initial water porosities, which, in turn, was a function of the in situ water porosity, the degree of disturbance, and the effective confining stress applied during testing. This line shows a good relationship between water porosity and initial effective permeability to water for low fines oil sands.

The line plotted in Figure 5.9 follows the equation:

$$\log k_{ew} = -5.868 + 36.20 \cdot \phi_w \quad 5.4$$

where: k_{ew} - effective permeability to water, μm^2

ϕ_w - water porosity, fraction

From this equation, the change in effective permeability to water can be expressed as a function of change in porosity :

$$\log k_{ew2} - \log k_{ew1} = 36.2 \cdot (\phi_{w2} - \phi_{w1}) \quad 5.5$$

Deviations in specimen permeability values from the line described above were caused by such factors as higher fines content, the mode of fines distribution, and possibly grain size distribution.

The relationship between the initial effective permeability to water and fines content is presented in Figure 5.10. Larger fines contents are clearly associated with lower effective permeabilities to water. A bilinear line drawn in Figure 5.10 shows the approximate relationship at a constant water porosity of 8 % between fines content and the effective permeability to water of oil sands. The in situ oil sands, which are rich in bitumen, have a water porosity of approximately 4 %. For these rich oil sands with low fines content (<2%) the in situ initial effective permeability to water is $3.8 \cdot 10^{-5} \mu m^2$. A relationship between fines content and effective permeability to water for this water porosity is also shown. This bilinear relationship can be expressed by two equations for two different ranges of fines content:

$$\log k_{ew} = -4.420 \quad \text{for} \quad F < 2\% \quad 5.6$$

$$\log k_{ew} = -4.420 - 0.452 \cdot (F - 2) \quad \text{for} \quad 2\% < F < 5\% \quad 5.7$$

where: F = fines content, %

For fines contents over 5 %, the distribution of fines is in large clasts or laminations which result in a variable decrease in the initial effective permeability to water and cannot be modeled. As shown later, shear strains have a significant influence on increasing the permeability of these higher fines oil sands.

Fines contained in specimens can influence measured permeability values in two ways. First, the water contained in discontinuous shale clasts or in other agglomerations of fine particles (Takamura et al. 1982) is generally less mobile than that contained in the pendular rings at the contacts of sand grains and in the channels created between sand grains and the bitumen contained in pores. Consequently, the pore space involved in conducting water contributes to only a fraction of the total pore space occupied by water. Second, the shale fragments, lenses and layers may not only bind some pore water, but they also create restrictions to flow by reducing the area through which water can easily flow. The first reason given above appears to be the major cause for the scatter of the test data in Figures 5.9 and 5.10.

To summarize, the permeability of oil sands specimens, recompacted under 7 to 6 MPa confining effective stresses and unloaded to between 3000 and 240 kPa effective confining stresses, varied from $5.3 \cdot 10^{-6}$ to $2.3 \cdot 10^{-3} \mu\text{m}^2$. The measured permeability values were affected by such factors as specimen water porosity, fines content, the mode of fines distribution, and the grain size distribution of sand. Good relationships were obtained for low fines specimens (less than 2 % of particles $<45 \mu\text{m}$) and constant water porosity specimens (in situ water porosity of 4 %).

5.3.4 Isotropic Unloading

Changes in the effective permeability to water during isotropic unloading tests are shown in Figures 5.11, 4.3, and 4.4. Some additional test details are contained in Table 4.2.

The main feature of the plots shown in the figures is a relatively linear relationship between the logarithm of effective permeability to water (k_{ew}) and water porosity (ϕ_w). If the water porosity is small, a basically linear relationship also exists between k_{ew} and volumetric strain ($\epsilon_v = (\phi_w - \phi_{wi}) / (1 - \phi_{wi})$). The above relationship between k_{ew} and ϕ_w agrees with the findings of others (Rajani, 1988; Monte and Kritzen, 1976) who also proposed a bilinear fit to the absolute permeability - porosity experimental data. In the range of small porosity values ($\phi < 25-28\%$) Rajani proposes a semi-logarithmic relationship as follows:

$$\log k = A_2 + B_2 \cdot \phi_w \quad 5.8$$

A similar correlation was also suggested by Monicard (1980) for field studies in reservoir engineering (see Section 2.2.2). The relationship given in Section 5.3.3 (Equation 5.4) to fit the initial permeability data for specimens with small fines content had the same form. For the purpose of comparison, this relationship is shown in Figure 4.4 and Figure 5.11. The relationship between k_{ew} and ϕ_w for the isotropic unloading tests performed on the specimen with the highest permeability (S21) is the same as the relationship given by Equation 5.4.

Another significant feature of the effective permeability to water - water porosity plots is the relationship between the initial permeability values and the slope of the plots. The lower the initial permeability, the higher the slope. Because specimen initial permeability to water was mainly a function of the fines content and the mode of fines distribution, these two parameters also strongly affect the rate of change of the effective

permeability to water with changes in water porosity; this indicates that the constants in Equation 5.8 (A_2 and B_2) change with changes in the fines content and in the mode of fines distribution (clasts, layers, lenses or fine particles in small agglomerations). As shown in Section 5.3.3, for low fines oil sand ($F < 2\%$), $A_2 = -5.868$ and $B_2 = 36.20$. For higher fines oil sands ($2\% < F < 5\%$), constant A can be found from the relationship:

$$A_2 = -4.41 - 0.728 \cdot F \quad 5.9$$

Constant B_2 may increase with the fines content but can be taken as 36.2 as a first approximation.

5.3.5 Triaxial Shear Tests

The effective permeability to water of oil sands during triaxial shear tests was found to be a function of water porosity, the presence of fines, and the stress path followed.

The triaxial shear tests performed in this study were of three different types, each of which followed a different effective stress path. The permeability measurements performed during triaxial compression tests are presented in Figures 4.9 and 4.10. Permeability measurements performed during effective confining stress unloading tests are shown in Figures 4.15, 4.16, 4.21 and 4.22; those performed during constant p' tests are shown in Figures 4.27, 4.28, and 5.11. All plots depicting effective permeability to water versus water porosity contain the reference line given by Equation 5.4. Some irregularities in the plots shown in Figures 4.16, 4.22, 4.28 and 5.11 could have resulted from the manual change (in steps) of the cell pressure or pore pressure.

Figure 5.11 beside the constant p' tests results also presents results of the isotropic unloading tests performed earlier on the same set of specimens. For both types

of test the relationship between effective permeability to water and water porosity follows the same, approximately straight lines. In summary, whether volume increase occurs by isotropic unloading or by shear dilation, the resulting effective permeabilities are the same. The increase in effective permeability is a function only of change in water porosity; the stress path has little effect. As mentioned above, the fines content also has an effect on the increase in relative permeability to water; the higher the fines content, the greater is the rate of permeability increase.

5.3.5.1 Effect of Initial Shear Contraction on Effective Permeability to Water

Analyzing the compression shear tests results shown in Figure 5.12, it should be noted that for the specimens which initially contracted and then dilated with further shearing, the permeability increased even though the overall specimen net volume change was still contractive. At the shear strain when the specimen volumes had regained their initial values, the effective permeability to water had increased 100, 100, 50 and 200 %, respectively, for specimens S3, S6, S8 and S10, which were compressed under effective confining stresses of 1.3, 2.0, 2.0 and 3 MPa respectively. This permeability increase must have resulted from the manner in which the specimens were deformed. The specimens were compressed axially, and they expanded laterally from the beginning of shear testing. This specimen deformation caused a change in shape of the intergranular pores which tended to become flatter and wider. It appears that this mode of deformation opened up vertical channels which resulted in an enhanced effective permeability to water in the vertical direction. The width of the horizontal channels must have been reduced, so that the horizontal effective permeability to water probably decreased.

At this initial stage of specimen deformation, the effective permeability to water has rates of decrease and increase similar to that shown by the reference line in Figure 5.12. The results of the effective stress unloading tests and the constant p' tests provide support for this generalization. For these tests, specimen volumes increase from the beginning, and the relationship between effective permeability to water and water porosity generally follows the same slope as the reference line.

The contribution of this initial shear strain to the increase in permeability is small if the specimen subsequently experiences a significant increase in volume. However, it can be stated that the initial stages of triaxial compression tests induced anisotropic permeability conditions in oil sands cores. The result of this deformation induced anisotropy is permeability enhancement in the direction of the compressive stress at very small shear strains. This permeability enhancement can occur in spite of a decrease in specimen pore volume.

5.3.5.2 Effect of Water Porosity on Effective Permeability to Water

In most cases, the plots of permeability to water versus water porosity are linear semi-logarithmic and have the same slope as the reference line which shows the relationship between permeability to water and water porosity when unaffected by high fines content. This test result shows that water porosity is the dominant parameter affecting changes in the effective permeability to water.

Figure 5.13 presents the results of all triaxial shear and isotropic unloading tests. The specimens have different initial permeabilities because they contain different amounts of fines. The two straight lines in the figure show the bounds of increasing effective permeability to water with increasing water porosity. The lower line is parallel to the upper line for low fines oil sands (Equation 5.4). Specimens of exceptionally low

permeabilities, as produced by layers or lenses of shale, fall below the lower line. Low fines specimens, showing permeability enhancement through deformation-induced anisotropy, fall above the upper line. The two lines contain the permeabilities of specimens of high bitumen content Athabasca McMurray Formation oil sands in which the majority of fines were contained in separated small clasts not affecting oil sands permeability, on the scale of the tested specimens (38.1 mm diameter x 38.1 mm long). The initial permeability - water porosity relationship varies because of the different amount of water in the clasts which varied in number and size.

The higher slopes of some plots, occurring especially in the initial stages of the testing, were associated with a higher fines content comprised of larger clasts (several millimeters in diameter), shale lenses or layers. It would appear that small shear strains are effective in increasing the permeability through shale inclusions. The shear strains must develop shear bands with larger porosities through the shale inclusions.

5.3.6 Comparison with Other Experimental Works

5.3.6.1 Triaxial Shear Tests on Oil Sands

Only one other experimental study has been performed so far that could be used as a basis of comparison with these test results. Figure 5.13 includes the results reported by Wong (1991) of one triaxial compression test performed on the Athabasca McMurray Formation oil sands with effective permeability to water measured with a pressure pulse technique. The initial permeability of the core in Wong's test, $1 \cdot 10^{-5} \mu\text{m}^2$ at a water porosity of 5%, falls within the range of permeabilities measured in this study. However, in Wong's experiment, the rate of permeability change with water porosity change caused by shear dilation is significantly higher than the rate of change expressed by Equation 5.4.

The apparent discrepancy between the rates of change in the effective permeability to water may have occurred because of two differences in the testing programs. Wong used a pressure pulse technique at room temperature to measure permeability not a direct water flow technique at 8 °C as used in these tests. Compressibility of bitumen and other factors may cause a difference in the experimental results from the two different methods. Wong's specimen also failed on a shear band that was 4-6 mm thick and inclined at an angle of 70°. The real water porosity in the shear band might have been much higher than the average value calculated on the basis of total volumetric changes. This deformation-induced specimen nonhomogeneity with respect to porosity would result in an effective permeability to water larger than would have occurred if the specimen had expanded in a uniform manner.

A similar exceptionally high increase in effective permeability to water occurred during the test on specimen S3 in this study. For S3, the rapid increase in permeability took place after the peak stress ratio was exceeded. In the later stages of this test, water permeability assumed values that could be predicted using Equation 5.4. Specimen S3 was well preserved, having a disturbance index of only 3.9 % (after isotropic compression), so that it likely developed a shear band of a substantially larger porosity than the rest of the specimen. At large strains, more of the specimen probably was influenced by shear dilation. As shown in Appendix B, the mode of failure for these short specimens, except specimen S3, was by fairly uniform lateral expansion indicating a general state of shear.

The development of a shear band which has a very high water porosity, complicates the measurement of the increase in effective permeability to water, although its effect seems to be limited to the small strain state.

5.3.6.2 Absolute Permeability versus Porosity and Effective Permeability to Water versus Water Porosity

Figure 5.14 presents both the absolute permeability of bitumen-free oil sands and the effective permeability to water of oil sands core material. The horizontal axis in this figure shows oil sand porosity for bitumen-free oil sands and water porosity for high bitumen content oil sands cores. For these experiments where the bitumen is considered immobile, the water porosity is treated as porosity. The absolute permeability test results described in Chapter 3 were extrapolated to a lower range of porosities by using Equation 3.11 with $C_0 = 16.9 \mu\text{m}^2$ (Section 3.7.2.4). The results of all the tests for effective permeability to water are represented by the two limit lines described in Section 5.3.5, which show a linear semi-logarithmic relationship between k_{ew} and ϕ_w . Although the linear semi-logarithmic relationship between permeability and porosity is fairly consistent, this relationship only holds for a limited range of low porosities. The relationship is different for low porosity and high porosity ranges. Transition from the linear semi-logarithmic fit to the Kozeny-Carman equation fit takes place between 15 % and 20 % porosity.

A similar bilinear fit has been found to fit absolute permeabilities measured on Venezuela oil sands (Rajani, 1988). The values of absolute permeability versus porosity reported by Rajani are also shown in Figure 5.14. In this case, transition between the two fits takes place between 25 % and 28 % porosity.

Figure 5.14 also shows the results of absolute permeability tests measured on Ottawa Sand and crushed Westerly-Granite (Zoback, 1975). In these tests, the granular materials were subjected to large isotropic stresses to change their porosity through elastic deformation and the crushing of grains. The two linear semi-logarithmic relationships fit this experimental data better than Rajani's combination of a linear semi-logarithmic fit in the low porosity range and the Kozeny-Carman equation in the high porosity range.

It is also noticeable that oil sands cores have a significantly lower permeability to water than Ottawa Sand or crushed granite at the same porosity (water porosity). Therefore, the oil sands tested, in comparison with Ottawa Sand or crushed granite, must have much narrower channels through which water can flow.

To summarize, the relationship between water permeability and porosity is bilinear over a broad range of porosities for a number of different granular materials. The transition from one straight line to the other occurs at different porosities for different materials.

5.3.6.3 Effective Permeability to Water versus Water Saturation

Figure 5.15 compares the test results obtained in this study to the $k_{rw} - S_w$ relationship given in the Petroleum Production Handbook which is described by Equations 2.17 and 2.18. In terms of effective permeability to water, Equations 2.17 and 2.18 can be expressed in a general form:

$$k_{ew} = ((S_w - S_{wi}) / (1 - S_{wi}))^n \cdot k \quad 5.10$$

Assuming the equation must go through the point with coordinates $k_{ew} = 2.6 \cdot 10^{-4} \mu\text{m}^2$ and $S_w = 0.17$, which lies on the upper bound to the experimental results described by Equation 5.4 in Figure 5.13, the exponent n was calculated. It equals 3.70 and is slightly higher than the value, 3.5, given in the Petroleum Production Handbook for unconsolidated poorly sorted sands. An absolute permeability (k) of $1.52 \mu\text{m}^2$ (Section 3.7.2.2) an irreducible water saturation (S_{wi}) of 8.2 %, and an oil sands in situ porosity of 34 % were assumed for the purpose of calculations. These values are the averages obtained on the core specimens which contain less than 2 % fines and seem to be the most appropriate for the high grade, low fines Athabasca McMurray Formation oil sands

tested in this study. The curve described by Equation 5.10 correlates reasonably well with the experimental results over a relatively large range of water porosities. However, noticeable differences occur, especially at very low water porosities, at which Equation 5.10 gives lower values of the effective permeability to water than those obtained in this study. Also, the linear increase in permeability in the effective permeability tests is poorly modeled. Nevertheless, the model provides a transition from the range of low porosities to the range of high porosities. However, the bilinear relationship given in the previous section is a better model.

Any agreement between the results of this study and the Equation 5.10 are somewhat surprising if we consider the differences in testing procedures and analyses. The model expressed by Equation 5.10 was derived experimentally on the basis of tests during which water saturation was decreased through the injection of oil into sand specimens while specimen porosity remained constant. In this study, water saturation was increased, at constant oil saturation, through an increase in porosity. Besides the difference associated with the direction of the change in water porosity (drainage versus imbibition), the two processes seem to be intrinsically different. Nevertheless, their general influence on permeability appears to be similar.

The finding described above indicates that the change in the effective permeability to water caused by shear dilation can be approximated, in reservoir calculations, by correcting saturation ratio according to pore volume expansion. Pore volume changes from changes in confining stresses and shear stresses can be determined through geomechanical models. Some caution, however, is recommended in the low range of water porosities.

This method of correcting saturation ratio, however, can not be applied when the increase in the effective permeability to water is caused by anisotropic deformation without an increase in the porosity (Section 5.3.5.1). In this case, water permeability

changes must be related to linear deformations and levels of confining stress. The non-uniform deformations associated with the development of narrow shear bands (Section 3.3.6.1) also require a different approach.

5.4 Shear Strength of Athabasca McMurray Formation Oil Sands

A summary of the results of the triaxial shear tests performed on oil sand cores is presented in Table 4.4. The shear strength of all specimens is shown in terms of s' and t in Figure 5.16. The principal stress ratio criterion (defined as the maximum ratio of vertical effective stress to confining effective stress) was used to determine specimen strength.

The failure envelope drawn through the points representing the specimens of the highest strength is believed to represent the strength of in situ oil sand; the lower strength values reflect the influence of specimen disturbance. The failure envelope is curvilinear. Using the slope of this line, an angle of shearing resistance of 76° was estimated for low effective confining stresses (<200 kPa). This relatively high friction angle was measured during confining stress unloading tests and constant p' tests, during both of which confining stress was decreased to very low values to induce specimen failure. The results of the triaxial compression tests carried out at low confining stresses gave a linear failure envelope, indicating a lower angle of shearing resistance of 55° . At higher confining stresses, ranging from 1.3 to 3 MPa, the angle of shearing resistance decreased to 44° . This last value was obtained on the basis of only two measurements, performed on specimens S3 and S10, of which the second had a higher initial void ratio. A larger number of tests might give somewhat different results.

The failure envelope described above was taken as the upper bound envelope. However, the test results show that the strength of the oil sands specimens depends to a

great extent on their void ratio. Figures 5.17 and 5.18 show triaxial compression tests in the p' - q and p' - e coordinates. Similarly, Figures 5.19 and 5.20 show confining stress unloading tests and constant p' tests. In these plots, the effect of void ratio on oil sands strength is readily apparent. For example, specimens S6 and S8 were axially compressed at the same confining effective stress of 2 MPa, but their deviatoric stress at failure was 12.7 and 9.2 MPa, respectively, because their void ratios were different (0.56 and 0.58, respectively). Figures 5.17 to 5.20 illustrate that two variables are required to adequately describe the shear strength and stress state of Athabasca oil sands: mean effective stress and void ratio.

The curvilinear shape of the failure envelope follows from the fact that, at lower confining stresses, the stress ratio at failure is higher. Figure 5.21 presents the relationship between these two variables for all tested specimens. The effective stress ratio reaches tens or even hundreds at very low confining stresses. These high values can not arise merely from the shear strength of a granular material; rather, they must result from the high viscosity bitumen contained in the oil sands pores, which would create an apparent cohesion, that is, some degree of strength at zero confining stress, at the strain rates used during testing. As well, the locked sand structure may impart a cohesive strength to the oil sands. Hence, the effective stress ratio at failure is a function of bitumen viscosity, rate of shearing, effective confining stress, specimen disturbance, and initial void ratio.

The approximate location of the Critical State Line (referring to the state of sand at which shear deformation occurs without volume change) is also shown in Figures 5.17 to 5.20 to demonstrate the potential for volumetric change at different mean effective stresses (p'). The changes in the void ratios of specimens during isotropic unloading tests are shown for purpose of comparison.

5.5 Summary

5.5.1 Observations

1. The high grade, low fines Athabasca McMurray Formation oil sand cores (from Units E and D at the UTF Phase A Pilot) contain, in terms of mass, 1.1 % to 2.9 % water and 13.3 % to 15.2 % bitumen, with average values of 1.8 % and 14.5 %, respectively.
2. The in situ porosities varied from 32.5 % to 35.0 %, with an average value of 33.5%.
3. The in situ water saturations varied from 6.4 % to 17.5 %, with an average of 11.2%. Taking into account the nonhomogeneity of the whole formation, which contains a higher percentage of shale than the core specimens tested, the average in situ water saturation for the formation could be higher.
4. The irreducible water saturation of cores containing less than 2 % fines (<45 μ m) was measured to be 8 % (equivalent to a water porosity of 2.7 %).
5. The effective permeability to water of high grade oil sands, recompressed to porosities ranging from 34.4 % to 37.6 %, varied from $5.3 \cdot 10^{-6} \mu\text{m}^2$ to $2.3 \cdot 10^{-3} \mu\text{m}^2$. Lower permeability values are associated with higher fines content, even though specimens with more fines have a higher water porosity.
6. During isotropic unloading, the increase in the effective permeability to water can reach 500 % for a decrease in confining effective stress from 6 MPa to 0.1 MPa and a pore volume increase of 4.5 % or a total volume increase of about 1.6 %. The permeability change is a function of initial permeability. The lower is the initial permeability, the greater is the permeability change.

7. The effective permeability to water can increase by three orders of magnitude as the result of a 17 % increase in pore volume or a 6 % increase in total volume brought about by shear dilation.
8. The specimens in triaxial shear failed by fairly uniform lateral expansion indicating a general state of shear and a uniform volumetric strain. Only one specimen developed a discernible shear band.

5.5.2 Conclusions

1. The initial effective permeability to water of the Athabasca McMurray Formation oil sands is a function of water porosity, fines content, and the mode of fines distribution. The following equation describes the relationship between effective permeability to water (k_{ew}) and water porosity (ϕ_w) for low fines (<2%) oil sands, for the range of porosities occurring during testing:

$$\log k_{ew} = -5.868 + 36.20 \cdot \phi_w \quad 5.4$$

This equation can be used to extrapolate laboratory effective permeability to water results on cores to in situ oil sands.

2. The increase in the effective permeability to water caused by isotropic unloading and by shear dilation is mainly a function of the increase in water porosity and is independent of the stress path a specimen has followed to undergo this volume change. It should be realized, however, that the amount of volume change is a function of stress path. The rate of permeability change follows Equation 5.4, except for cores containing high amounts of fines.

3. During triaxial compression tests, the initial mode of core deformation, which involves axial compression and lateral expansion, can cause permeability enhancement even when specimen porosity does not increase. This type of permeability enhancement ceases to predominate when specimen porosity starts to increase by shear dilation.
4. During oil sands shear failure, the development of a shear band, which is associated with a large increase in localized porosity, can induce a very large increase in the effective permeability to water. The effect of a shear band, however, appears to become small at large strains after shear failure.
5. A bilinear relationship, on a semi-logarithmic plot, between permeability and water porosity was found to model the absolute permeability values at high porosities and the effective permeability to water values at low water porosities. The transition from one relationship to the other takes place between 15 % and 20 % porosity.
6. The increase in relative permeability resulting from the increased water porosity brought about by shear dilation can be approximated by existing models by correcting for water saturation. Agreement with experimental results, however, is poor in the low range of water porosities. The mechanisms which influence the increase in relative permeability to water include more than just the increase in water porosity. Volumetric changes cause a change in pore throat geometry and in capillarity effects between water and bitumen. These changes may also be highly influenced by surface chemistry.
7. Void ratio has a significant influence on the stress-strain relationship and must be considered, along with mean effective stress, as one of the two variables defining the shear strength and stress state of the oil sands tested.

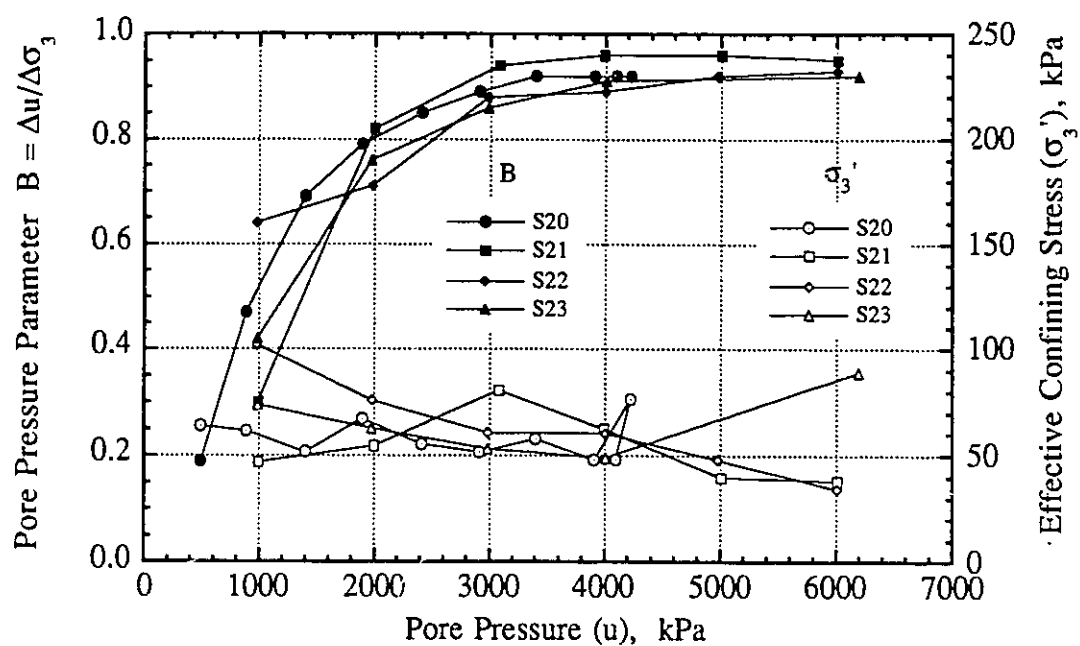


Figure 5.1 Saturation of Specimens by Pore Pressure Increase

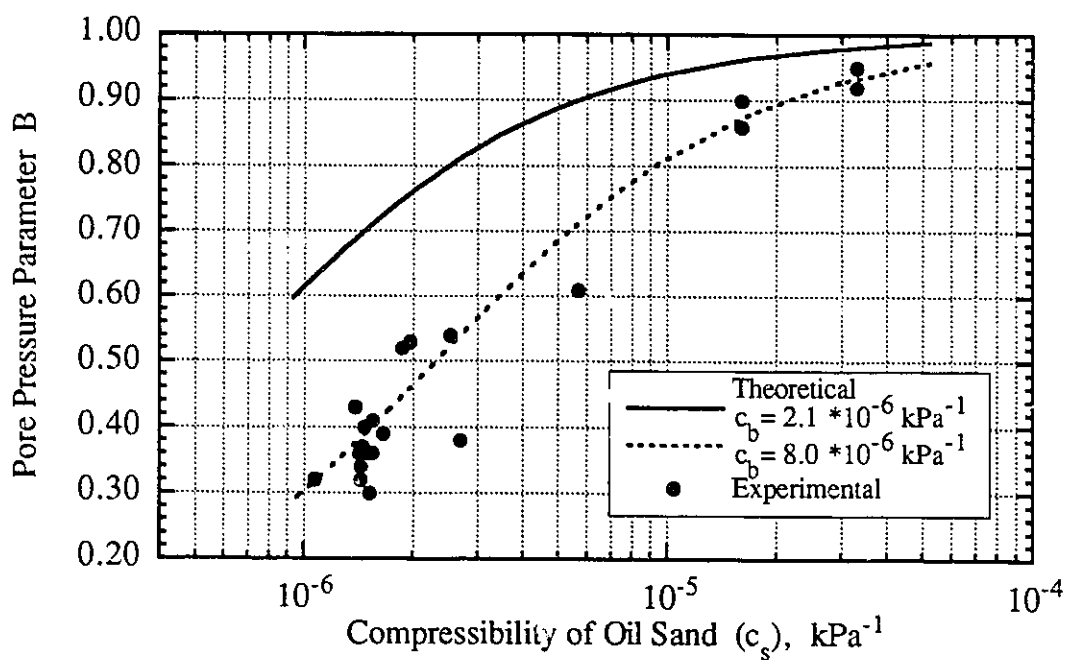


Figure 5.2 Relation Between Pore Pressure Parameter B and Compressibility of Oil Sands Core

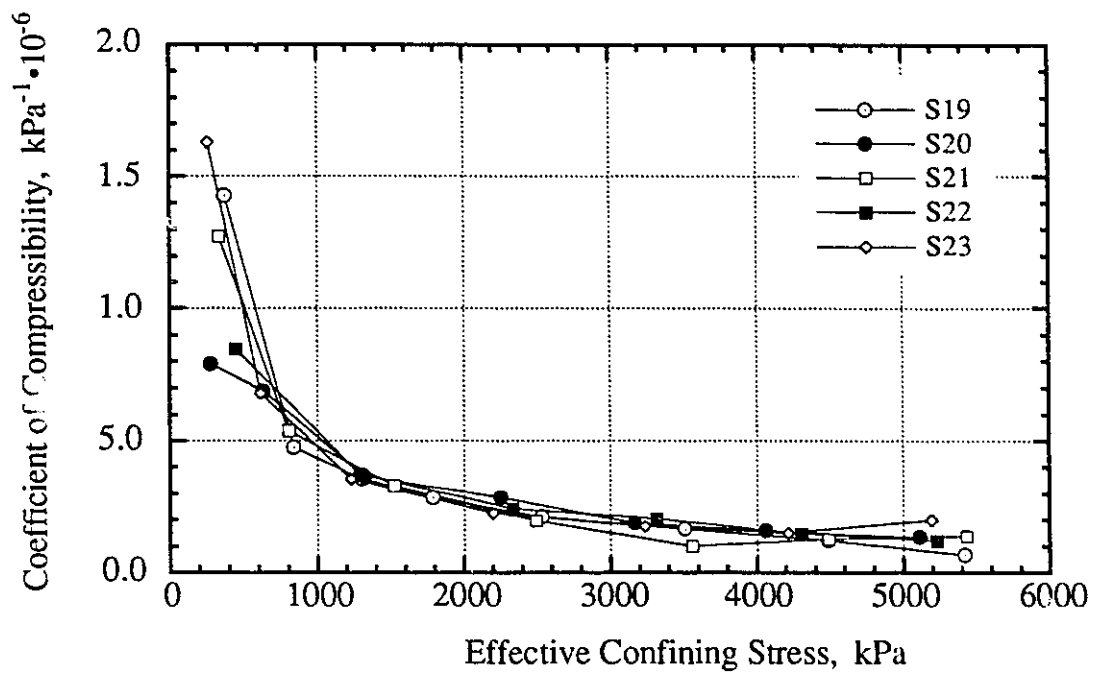


Figure 5.3 Isotropic Compressibility of Oil Sands Specimens (Unloading Phase)

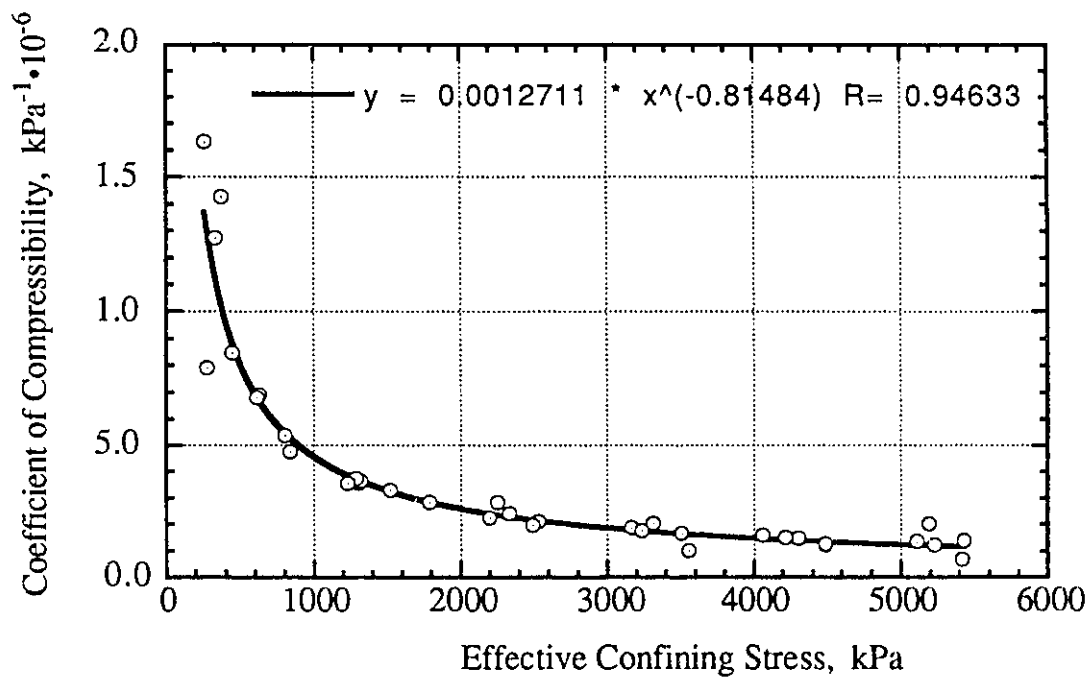


Figure 5.4 Isotropic Compressibility of Oil Sands Specimens - Curve Fit (Unloading Phase)

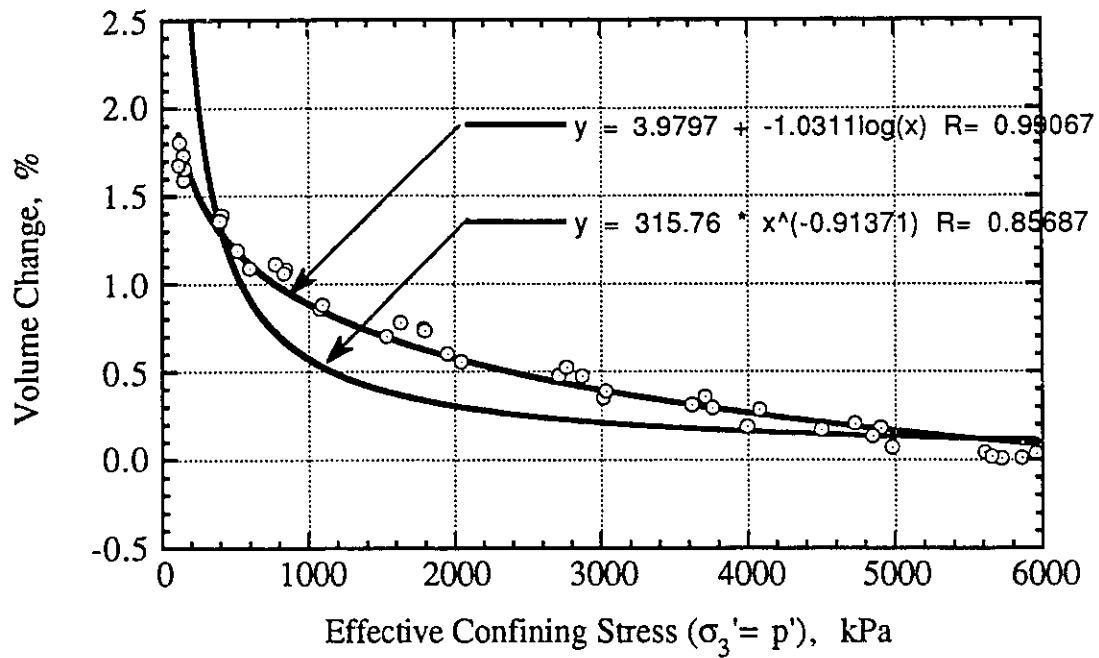


Figure 5.5 Volume Change During Isotropic Unloading, S19-S23

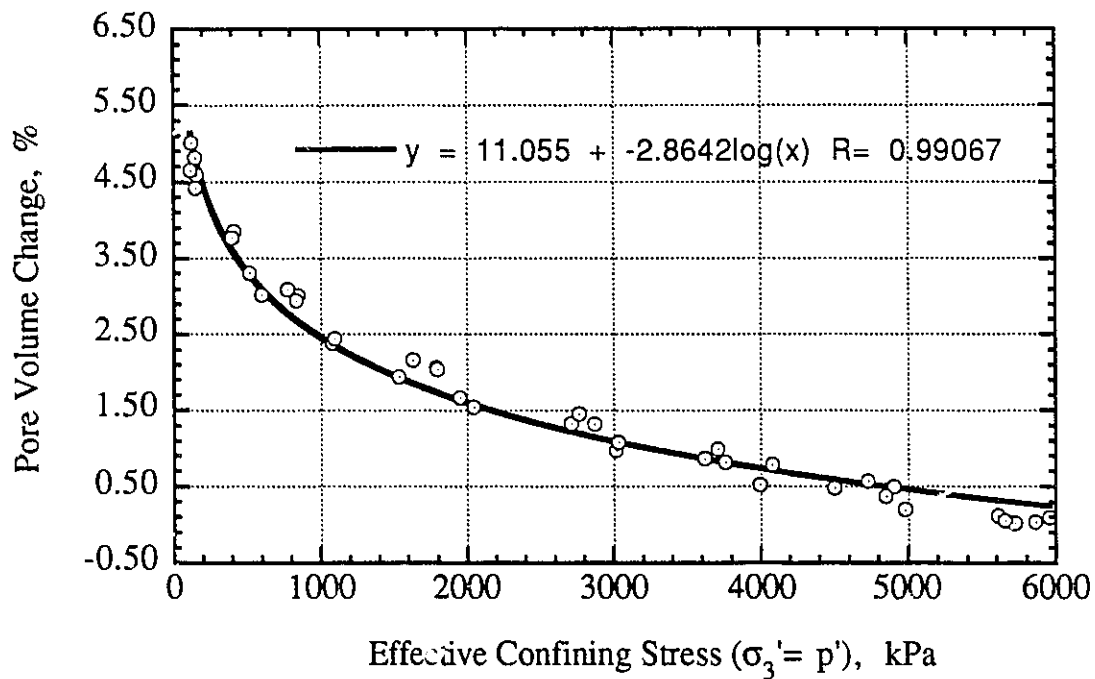


Figure 5.6 Pore Volume Change During Isotropic Unloading, S19-S23

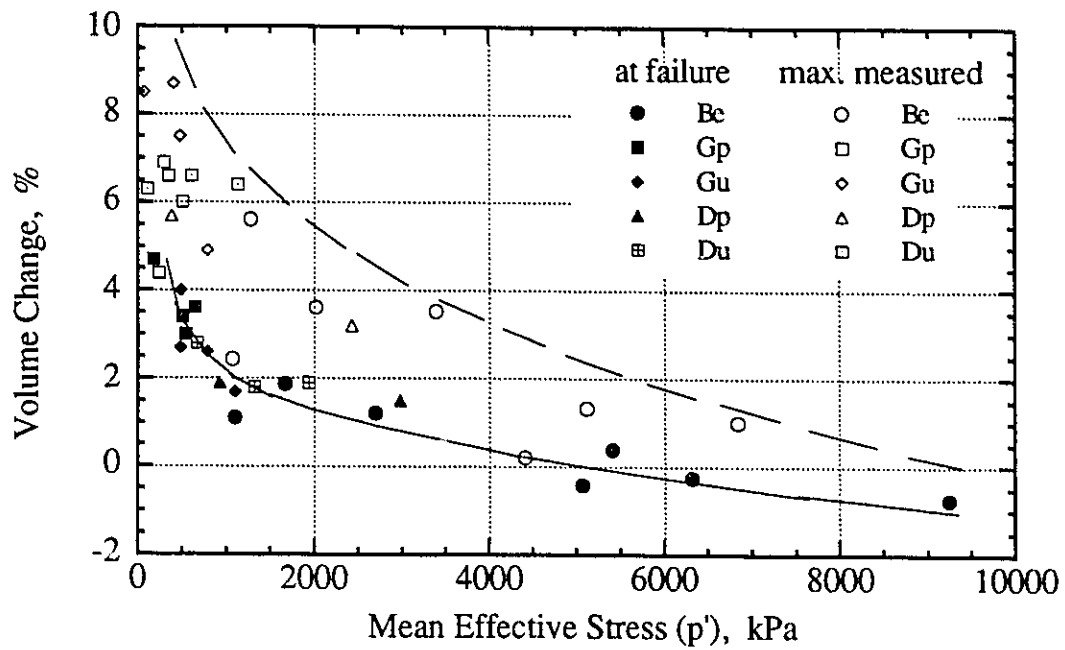


Figure 5.7 Volume Change During Triaxial Shear

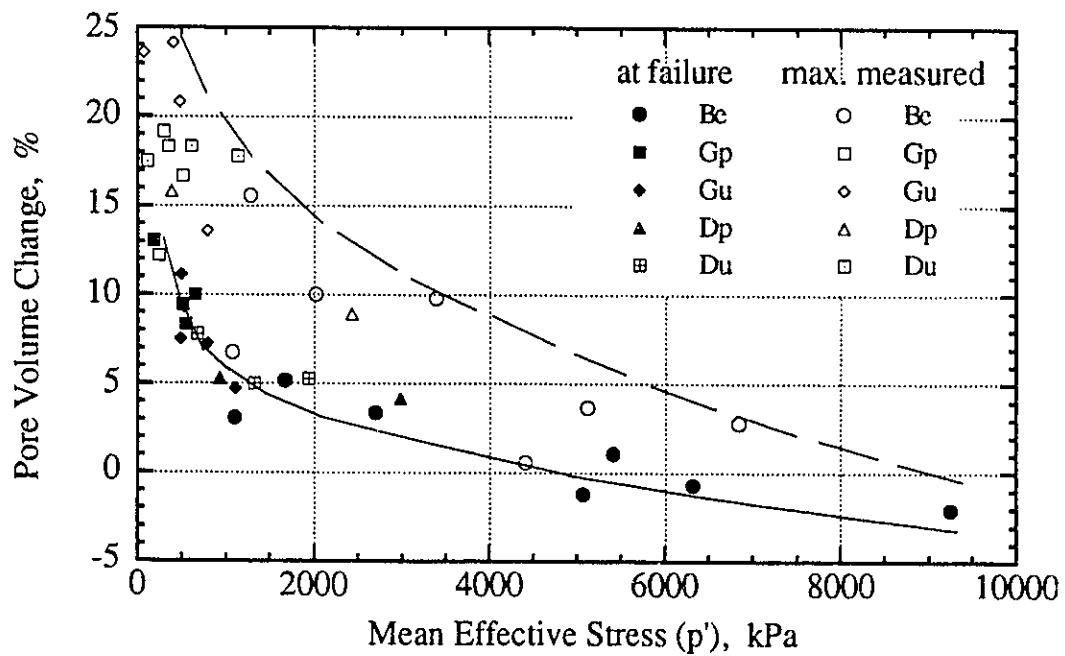


Figure 5.8 Pore Volume Change During Triaxial Shear

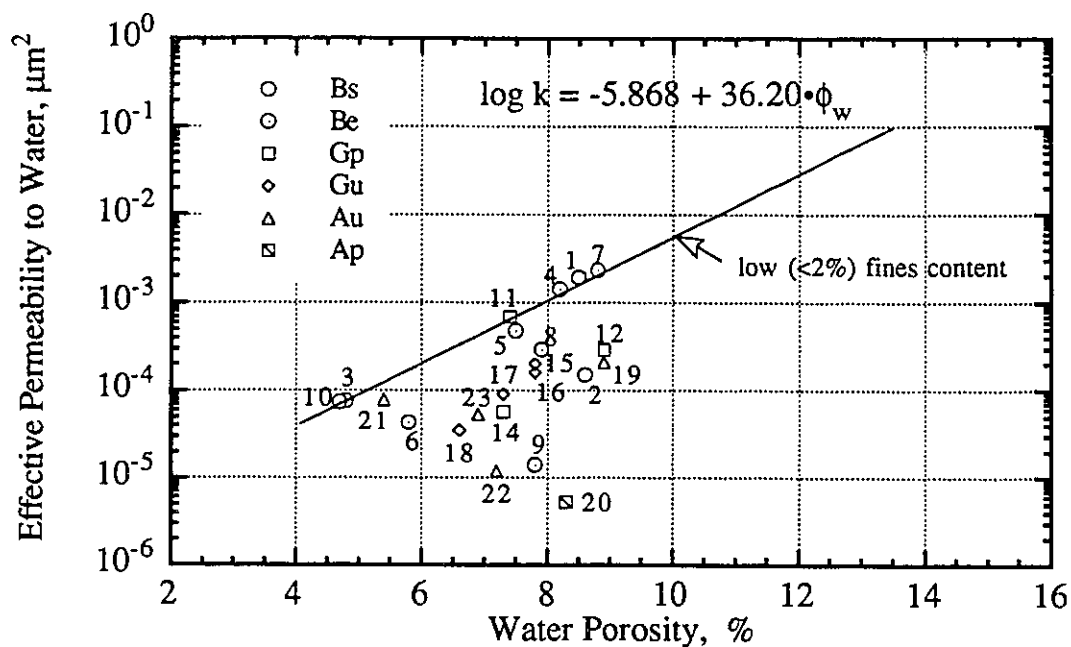


Figure 5.9 Effect of Water Porosity on Initial Effective Permeability to Water

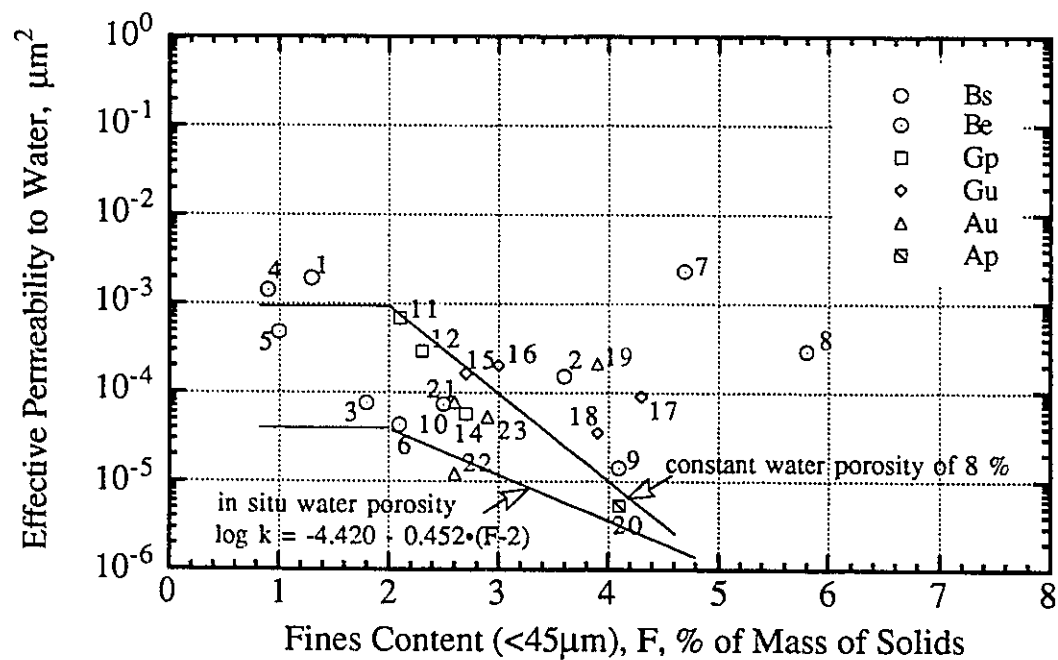


Figure 5.10 Effect of Fines Content on Initial Effective Permeability to Water

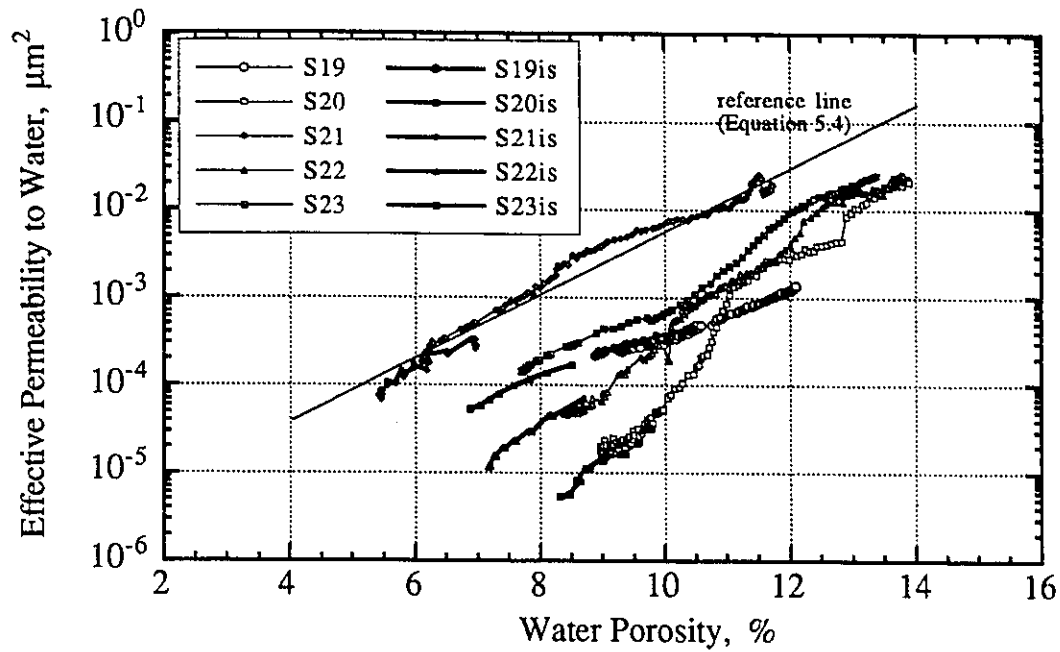


Figure 5.11 Effect of Isotropic and Triaxial Shear Volume Changes on Effective Permeability

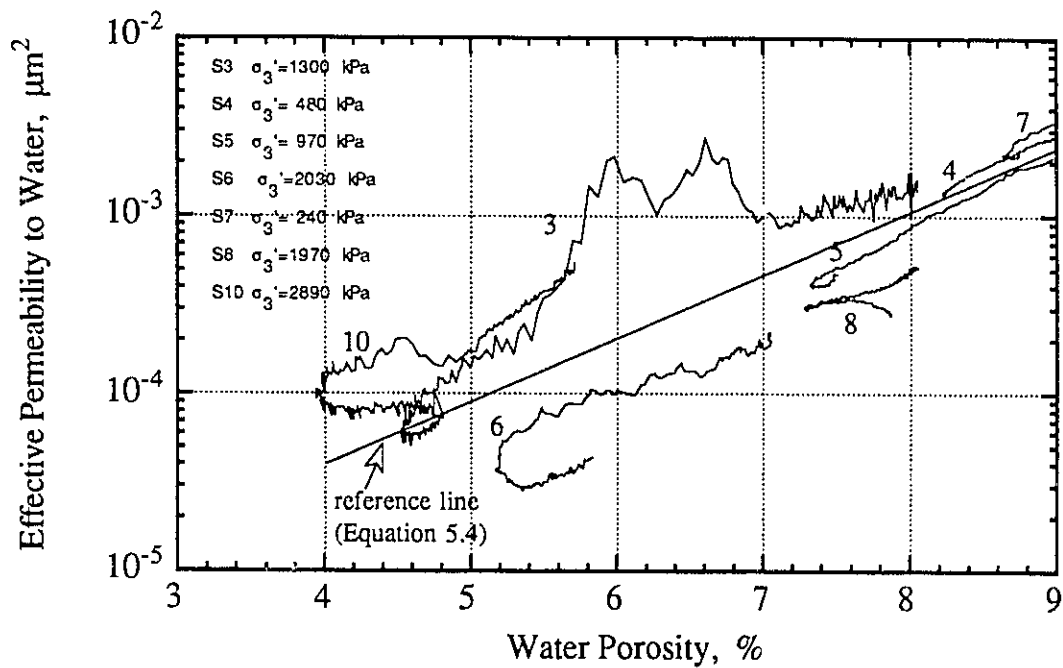


Figure 5.12 Increase in Effective Permeability Caused by Deformation During Specimen Contraction

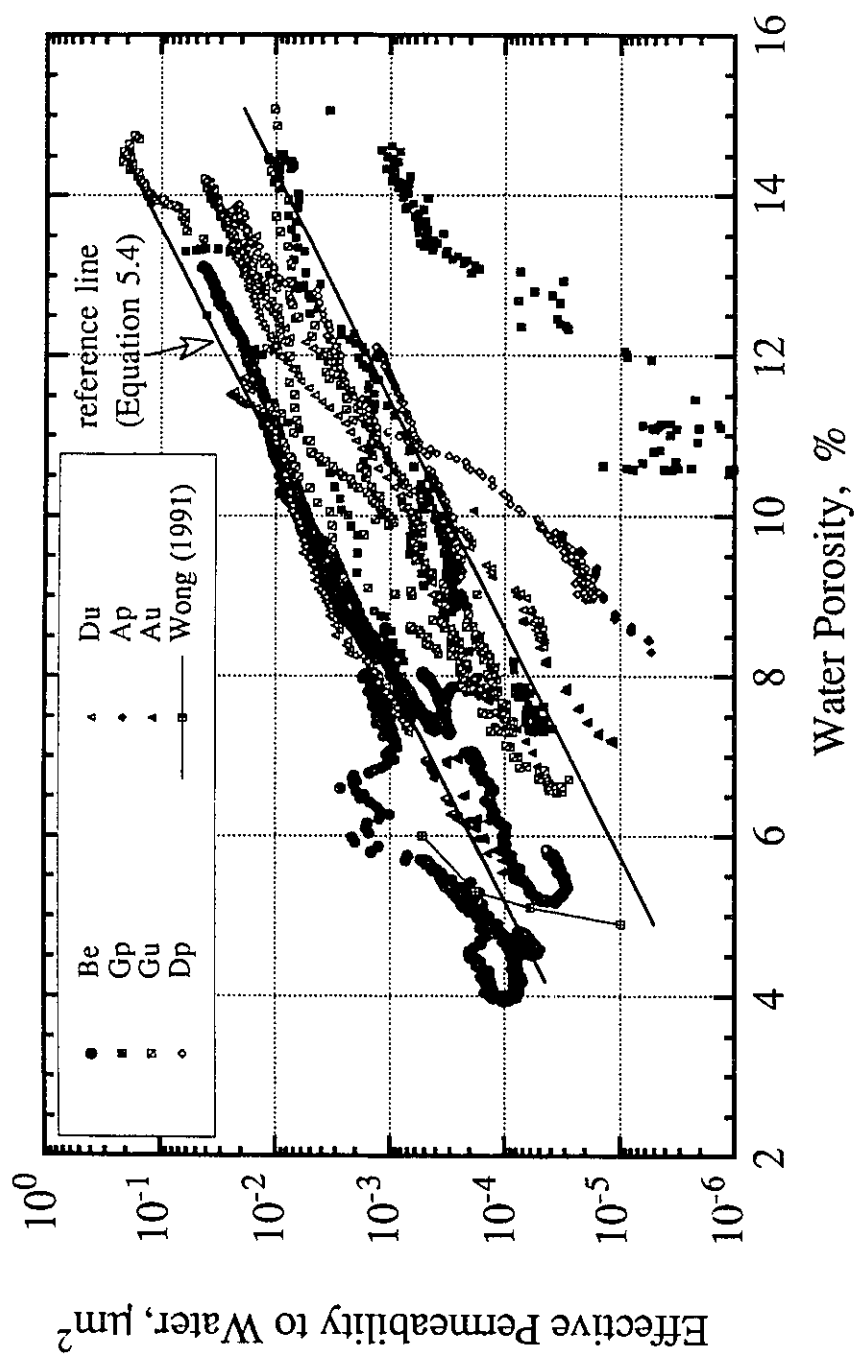


Figure 5.13 Effect of Water Porosity on Effective Permeability to Water During Isotropic and Triaxial Shear Tests

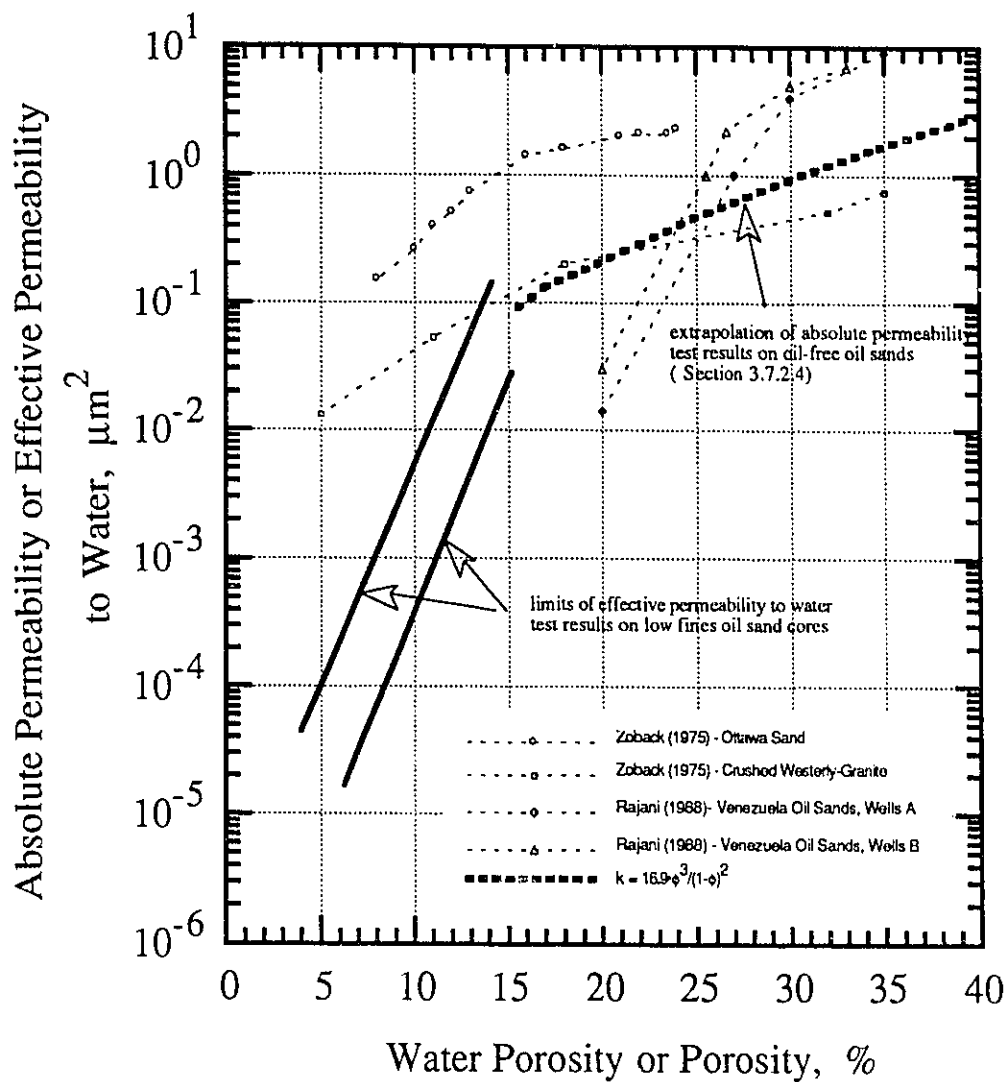


Figure 5.14 Effective Permeability to Water of Oil Sand Cores Compared to Absolute Permeability Test Results

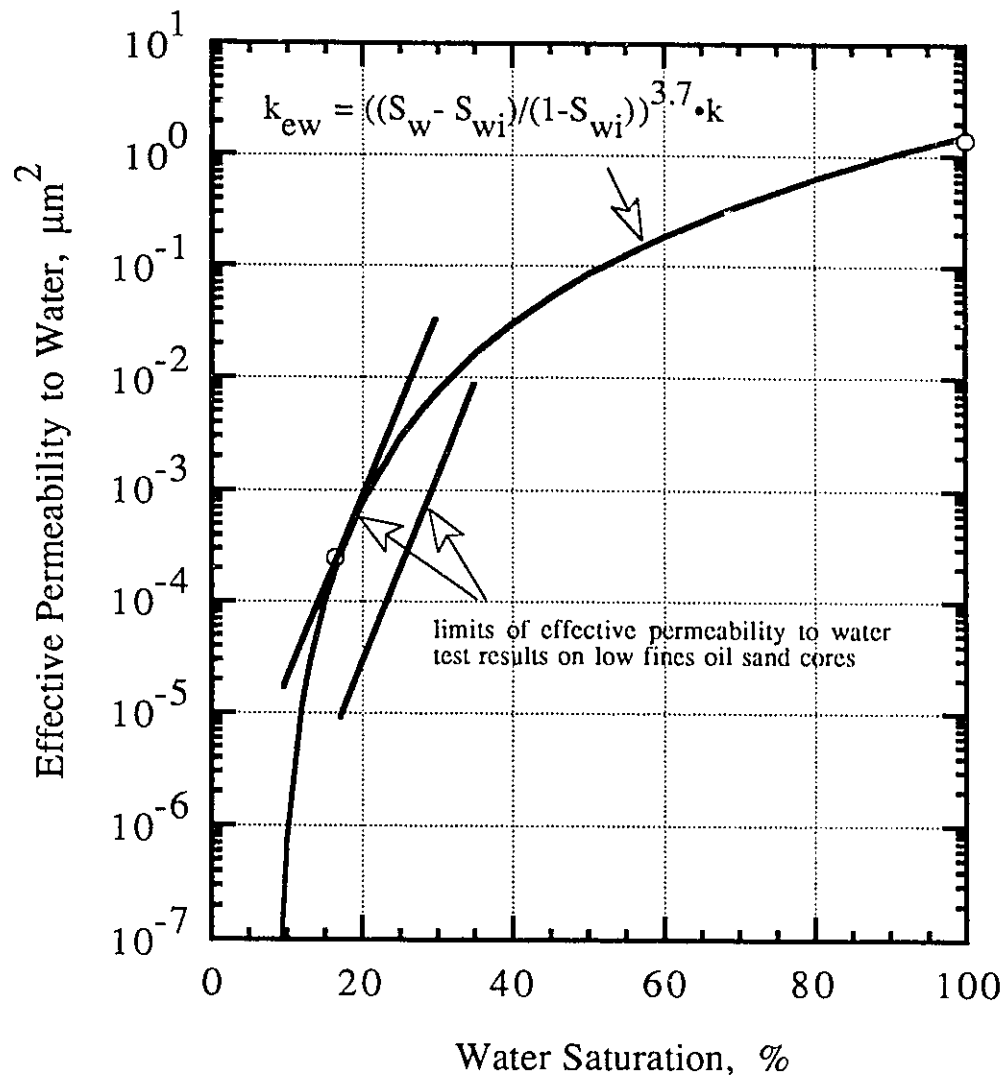


Figure 5.15 Comparison of Experimental Results with Mathematical Model

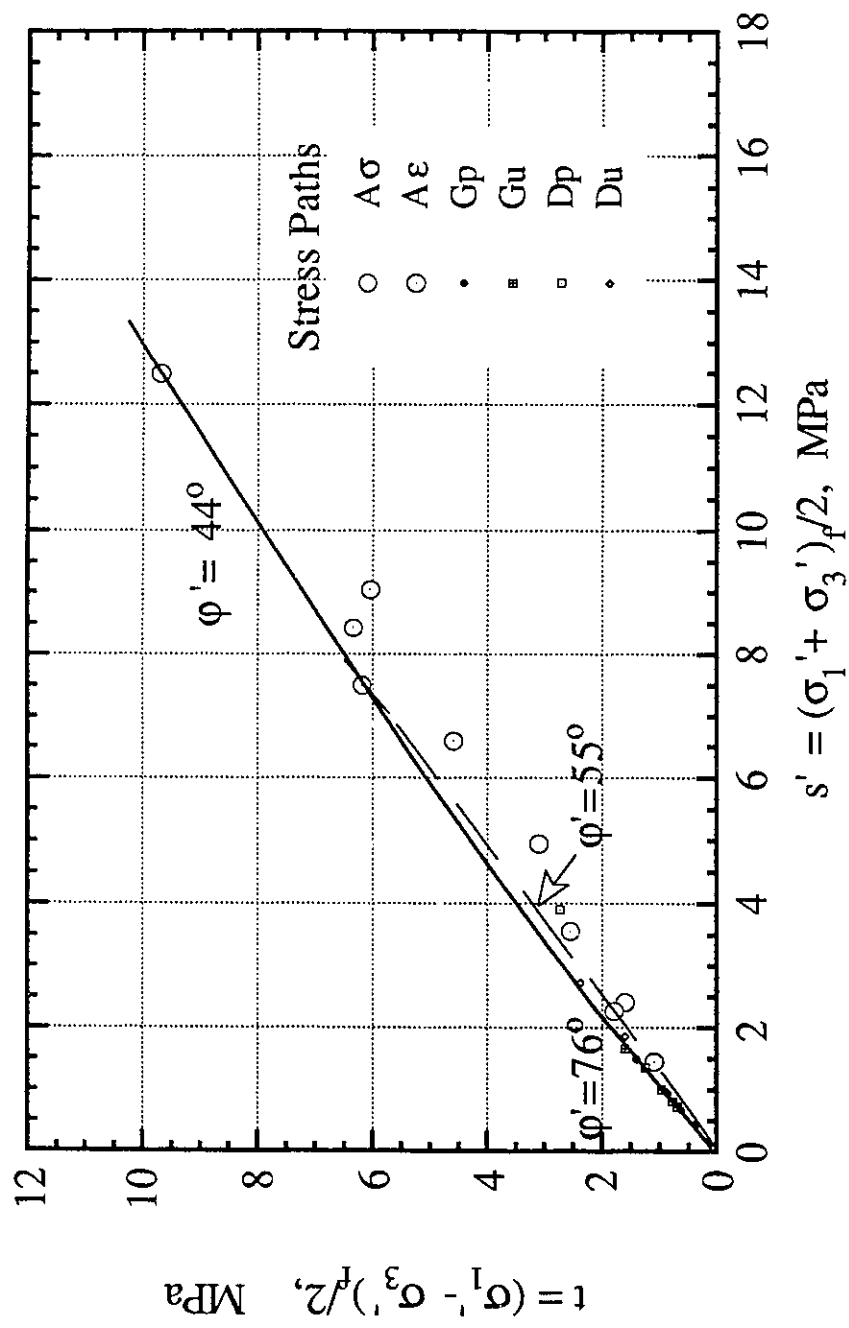
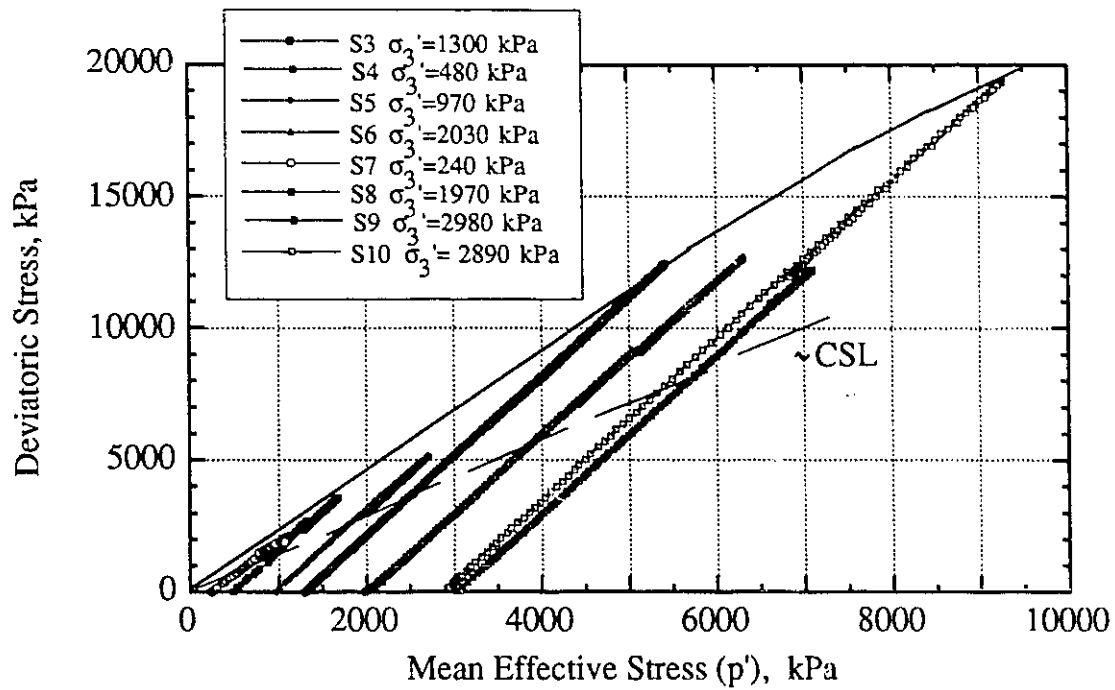
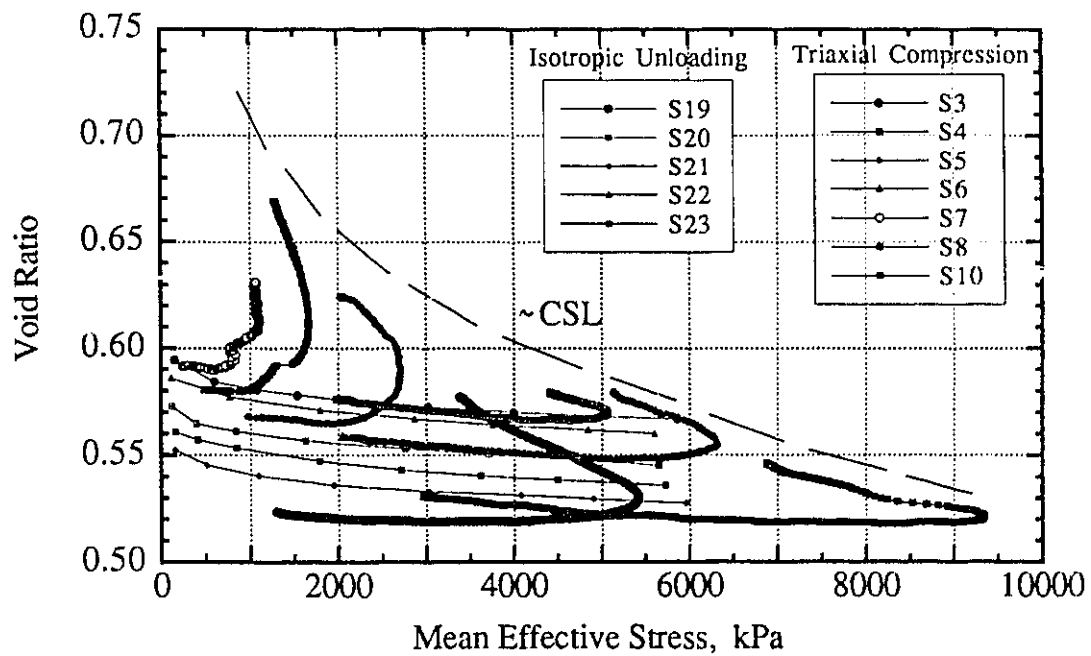


Figure 5.16 Failure Envelope for Athabasca McMurray Formation Oil Sands

Figure 5.17 Stress Path B_c in p' - q' Stress FieldFigure 5.18 Stress Path B_c and A, Void Ratio - Mean Effective Stress

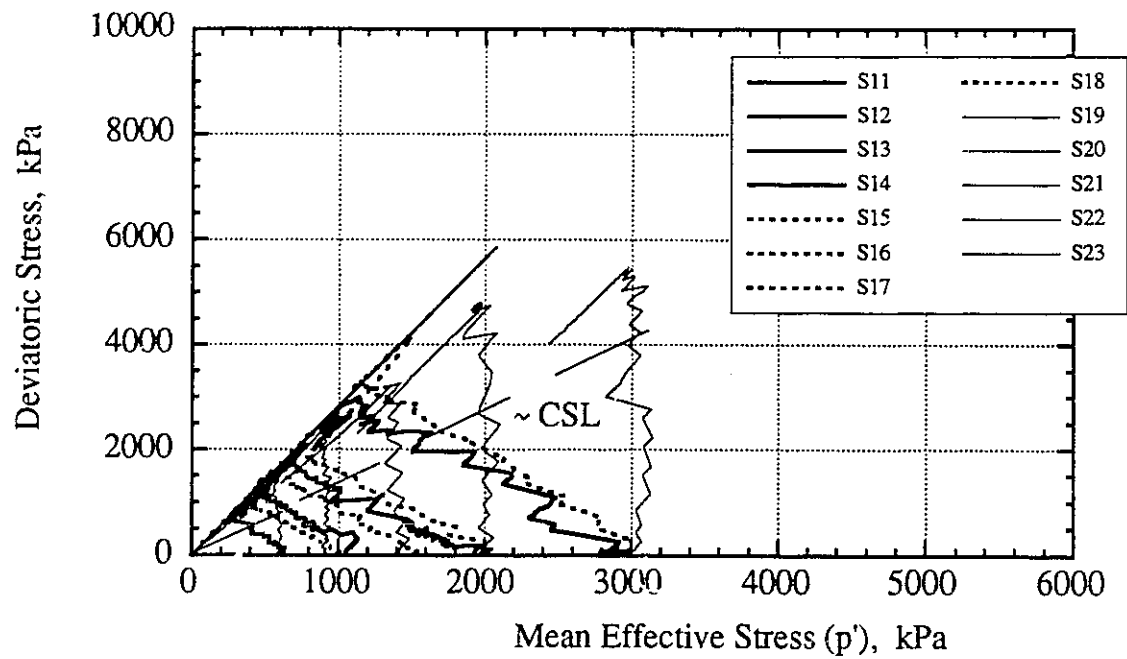
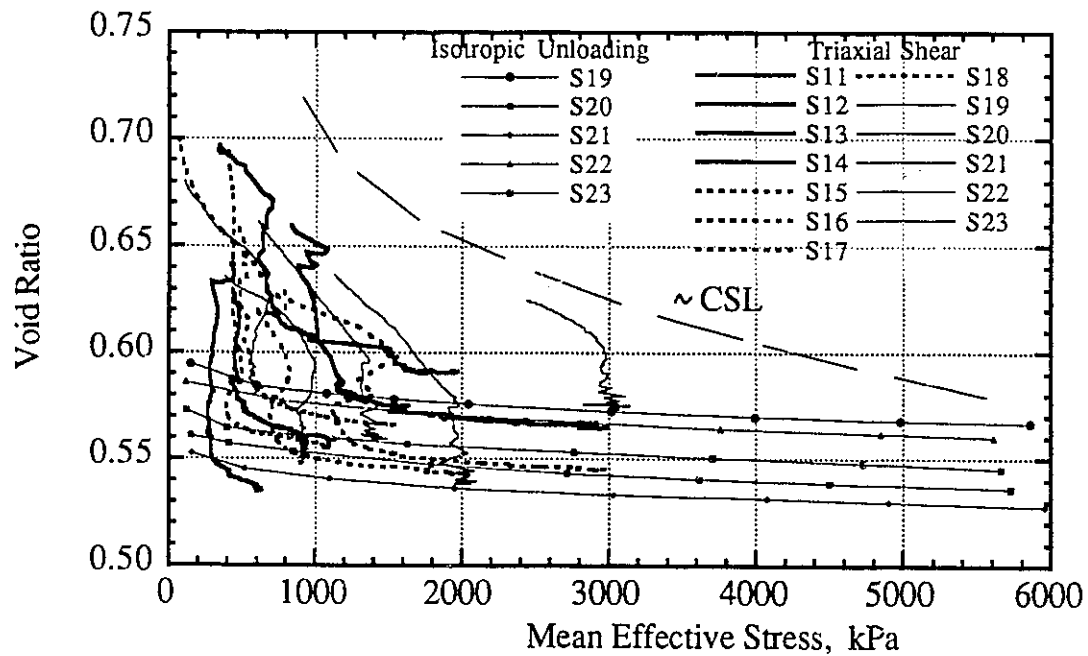
Figure 5.19 Stress Paths D and G in p' - q Stress Field

Figure 5.20 Stress Paths D and G, Void Ratio - Mean Effective Stress

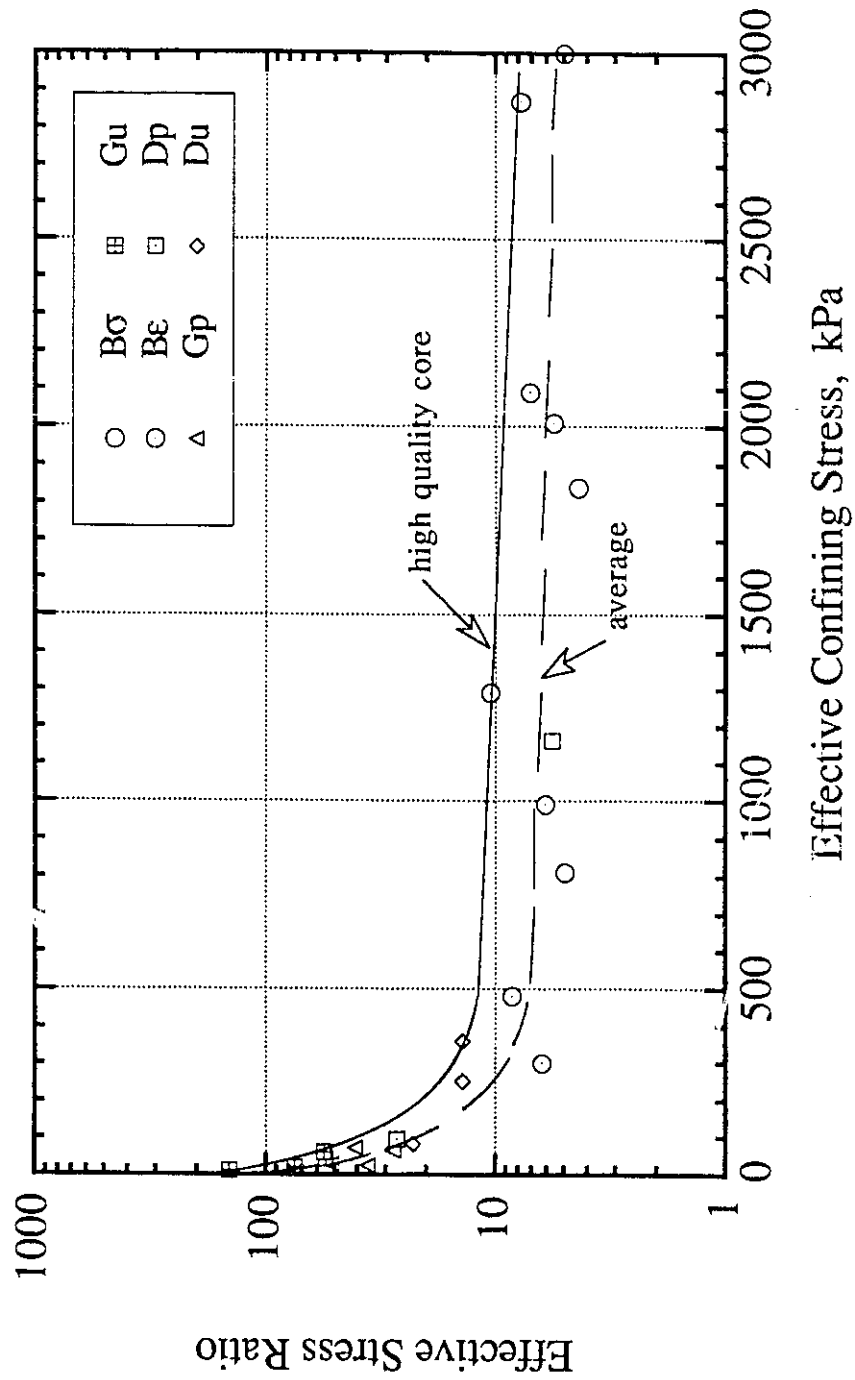


Figure 5.21 Effective Stress Ratio at Failure Versus Effective Confining Stress

Chapter 6. SUMMARY AND CONCLUSIONS

6.1 Factors Affecting Permeability of Oil Sands

1. The Athabasca McMurray Formation oil sands are a nonhomogeneous and anisotropic geotechnical material. They are generally composed of uncemented quartz sands with associated shales occurring in different forms: beds, stringers, layers, laminations, lenses, breccias, or separate shale fragments of different sizes.
2. Oil sands grains are water-wet and oil sands pores are filled with varying proportions of bitumen and formation brines. Recovered cores also contain gas, which has evolved from water and bitumen. The volume of pores filled with gas is an indication of the degree of sample disturbance. The in situ porosity of rich oil sands varies from 30 % to 35 % and oil saturation is up to 18 % by weight.
3. The in situ effective permeability to water of rich oil sands can be of the order of $10^{-5} \mu\text{m}^2$ or even lower. The absolute permeability of Athabasca and Cold Lake oil sands assumes values of the order of 1- 5 μm^2 .
4. The absolute permeability can sharply decrease when flow is changed from brine to fresh water. The permeability change depends on the rate of change in NaCl concentration. The sensitivity of a core to salt concentration changes can differ from field to field and must be checked every time a core from a new place is tested. The effective permeability to water of bitumen-rich oil sands is probably not significantly sensitive to the sequence of brine and water flow.

5. Shear stresses cause distortion and dilation of oil sand specimens if confining effective stresses remain below some critical value. This dilation is reflected in an increase in permeability.
6. In some instances (grouted sands (Mori and Tamura, 1986), some sandstones from North Sea (Rhett and Teufel, 1992)), anisotropic loading or unloading caused permeability enhancement without an increase in total volume.

6.2 Experimental Apparatus and Procedures

1. The experimental system designed for this program was able to measure the change in porosity and change in permeability constantly throughout isotropic unloading tests and throughout triaxial shear tests following different stress paths. A constant flow pump was used to maintain flow through the specimen in the triaxial system for permeability measurement and a sensitive differential pressure transducer was used to monitor the pressure difference induced across the length of the specimen.
2. The experiments were conducted at 8 °C, the in situ temperature at the AOSTRA Underground Test Facility. In addition, a very small flow rate of water through the cores was maintained in the effective permeability to water tests. These two experimental techniques were successful in preventing the movement of any significant amount of bitumen during the effective permeability to water tests.
3. The experimental procedure of using a constant flow pump simplified calculations of the average flow through the specimen by controlling the rate of flow into the

specimen and eliminating errors which are usually associated with calculations of the flow rate during the constant head method of permeability measurement.

6.3 Absolute Permeability of Athabasca Oil Sands

1. Experimental results of absolute permeability can be extrapolated from laboratory to in situ porosities using Kozeny and Carman's theory.
2. Absolute permeability change is a function of pore volume change and is independent of the stress path a specimen has followed to undergo this volume change.
3. For reservoir modeling purposes, a new permeability resulting from an increase in porosity of the Athabasca McMurray Formation oil sands can be calculated from the equation:

$$k_2 = k_1 + 16.9 \cdot (\phi_2^3 / (1 - \phi_2)^2 - \phi_1^3 / (1 - \phi_1)^2) \quad 3.12$$

4. The new permeability also can be calculated by using the equation:

$$k_2 = k_1 + 31 \cdot (\phi_2 - \phi_1) \quad 3.10$$

which agrees better with the experimental results.

5. The absolute permeability measured on reconstituted oil-free oil sands and on extracted oil sand cores falls within the same range when the porosities are similar.
6. Low fines (<2%) oil sands at a porosity of 34 % have an absolute permeability of $1.52 \mu\text{m}^2$.

6.4 Effective Permeability to Water of Athabasca McMurray Formation Oil Sands

1. The initial effective permeability to water of the Athabasca McMurray Formation oil sands is a function of water porosity, fines content, and the mode of fines distribution. The following equation describes the relationship between effective permeability to water (k_{cw}) and water porosity (ϕ_w) for low fines (<2%) oil sands, for the range of porosities occurring during testing:

$$\log k_{cw} = -5.868 + 36.20 \cdot \phi_w \quad 5.4$$

This equation can be used to extrapolate laboratory effective permeability to water results on core to in situ oil sands.

2. The in situ porosities varied from 32.5 % to 35.0 %, with an average value of 33.5%.
3. The increase in the effective permeability to water caused by isotropic unloading and by shear dilation is mainly a function of the increase in water porosity. The rate of permeability change follows Equation 5.4, except for cores containing high amounts of fines.
4. During isotropic unloading, the increase in the effective permeability to water can reach 500 % for a decrease in confining effective stress from 6 MPa to 0.1 MPa and a pore volume increase of 4.5 % or a total volume increase of about 1.6 %. The permeability change is a function of initial permeability. The lower is the initial permeability, the greater is the permeability change.

5. The effective permeability to water can increase by three orders of magnitude as the result of a 17 % increase in pore volume or a 6 % increase in total volume brought about by shear dilation.
6. During triaxial compression tests, the initial mode of core deformation, which involves axial compression and lateral expansion, can cause permeability enhancement even when specimen porosity does not increase. This type of permeability enhancement ceases to predominate when specimen porosity starts to increase by shear dilation.
7. The specimens in triaxial shear failed by fairly uniform lateral expansion indicating a general state of shear and a uniform volumetric strain. Only one specimen developed a discernible shear band.
8. During oil sands shear failure, the development of a shear band, which is associated with a large increase in localized porosity, can induce a very large increase in the effective permeability to water. The effect of a shear band, however, appears to become small at large strains after shear failure.
9. A bilinear relationship, on a semi-logarithmic plot, between permeability and water porosity was found to model the absolute permeability values at high porosities and the effective permeability to water values at low water porosities. The transition from one relationship to the other takes place between 15 % and 20 % porosity.
10. The increase in relative permeability resulting from the increased water porosity brought about by shear dilation can be approximated by existing numerical models by correcting for water saturation. Agreement with experimental results, however, is poor in the low range of water porosities.

5.5 Shear Strength of Athabasca Oil Sands

1. The failure envelope of the reconstituted oil-free Athabasca oil sands is curvilinear. At low effective confining stresses (up to 250 kPa), the angle of shearing resistance, ϕ' , is equal to 42° . At higher effective confining stresses, its value is lower and is a function of the stress path followed in the triaxial cell. The shear strength of the reconstituted oil-free Athabasca oil sands is similar to other fine, dense sands with uniform gradation of angular grains.
2. The shear strength of the Athabasca McMurray Formation core also changes non-linearly with the mean effective confining stress and shows a strong stress path dependency. An angle of shearing resistance of 76° was measured during effective confining stress unloading tests at effective confining stresses lower than 200 kPa. The angle of shearing resistance measured during triaxial compression tests varied from 55° at low confining stresses to 44° for effective confining stresses ranging from 1.3 MPa to 3 MPa.
6. Void ratio has a significant influence on the stress-strain relationship and must be considered, along with mean effective stress, as one of the two variables defining the shear strength and stress state of the oil sands tested.

6.6 Suggestions for Future Work

1. The investigations on absolute permeability described in this study were performed on recompacted bitumen-free oil sands. Reviewing similar published results it appears necessary to verify the findings of this study by performing experiments on extracted or naturally bitumen-free oil sands core.

2. Effective permeability to water measurements during initial stages of the triaxial compression tests indicate that permeability enhancement can occur without porosity increase, caused only by sample deformations. To quantify these permeability changes with the axial and radial deformations, additional tests at a higher range of confining stresses are required.
3. To further develop the experimental apparatus used for permeability investigations in this study, a constant temperature cell is suggested which should enclose all elements of the apparatus. Better temperature control would allow the reliable measurement of lower permeabilities at lower flow rates.

REFERENCES

- Adhikary, D.P. 1991. **Laboratory Investigation of Effects of Stress Changes on Hydraulic Conductivity of Reconstituted Oil Sands**. M.Eng. Report, University of Alberta, 99 p.
- Agar, J. 1984. **Behaviour of Oil Sands at Elevated Temperatures**. Ph.D. Thesis, University of Alberta, Edmonton, 906 p.
- Agar, J.G., Morgenstern, N.R. and Scott, J.D. 1986. **Fluid Transport Properties of Athabasca Oil Sand at Elevated Temperatures and Confining Stresses**. Report, University of Alberta, 36 p.
- Aggour, M.A., Mallk, S.A. and Harari, Z.Y. 1989. **Effect of Cyclic Formation-Pressure Changes on Permeability**. SPE Reservoir Engineering, Vol. 4, No. 1, February, pp. 91-96.
- Ahmed, U., Crary, S.F. and Coates, G.R. 1991. **Permeability Estimation: the Various Sources and Their Interrelationships**. Journal of Petroleum Technology, May, pp. 578-587.
- Batycky, J.P., McCaffery, F.G., Hodgous, P.K. and Fisher, D.B. 1981. **Interpreting Relative Permeability and Wettability from Unsteady State Displacement Measurements**. SPEJ, June, 296 p.
- Beattie, C.I., Boberg, T.C. and McNab, G.S. 1989. **Reservoir Simulation of Cyclic Steam Simulation in the Cold Lake Oil Sands**. Paper SPE 18752, presented at SPE California Regional Meeting, Bakersfield, California, April 5-7, pp. 69-82.
- Bear, J. 1972. **Dynamics of Fluids in Porous Media**. American Elsevier Publishing Co., New York, 760 p.

- Bishop A.W. and Green, G.E. 1965. **The Influence of End Restraint on the Compression Strength of a Cohesionless Soil.** Geotechnique, Vol. 15, No. 3, pp. 243-266.
- Caney, R.C., Stevens, E. and Sheth, N. 1979. **Suggested Test Methods for Determination of Degree of Saturation of Soil Samples by B Value Measurement.** Geotechnical Testing Journal, Vol. 2, No. 3, September, pp. 158-162.
- Cerda, C.M. and Non-Chhom, K. 1988. **Laboratory Study of Permeability Reduction Due to the Flow of Kaolinite Fines.** Paper No. 20, presented at the 4th UNITAR/UNDP International Conference on Heavy Crude and Tar Sands, Edmonton, August 7-12, pp. 399-408.
- Coskuner, G. and Maini, B. 1988. **Fines Migration in Heavy Oil Reservoirs.** Paper No. 119, presented at the 4th UNITAR/UNDP International Conference, Edmonton, August 7-12, pp. 371-382.
- Cottrell, J. H. 1963, **Development of an Anhydrous Process for Oil Sand Extraction in The K. A. Clark Volume.** M. A. Carrigy Ed., Alberta Research Council, Edmonton, pp. 193-206.
- Dusseault, M.B. 1977. **Stress State and Hydraulic Fracturing In the Athabasca Oil Sands.** Canada-Venezuela Oil Sands Symposium, Edmonton, May 30 - June 3, pp. 27-35.
- Dusseault, M.B. and Morgenstern, N.R. 1978. **Shear Strength of Athabasca Oil Sands.** Canadian Geotechnical Journal, Vol. 15, No. 2, pp. 216-238.
- Dusseault, M.B. and Morgenstern, N.B. 1979. **Locked Sands.** Quarterly Jour. Eng. Geol., Vol 12, No. 2, pp. 117-131.
- Dusseault, M.B. and Rothenburg, L. 1988. **Shear Dilatancy and Permeability Enhancement in Oil Sands.** Paper No. 32, presented at 4th UNITAR/UNDP International Conference, Edmonton, August 7-12, pp. 55-65.

- Gabriel, G.A. and Inamdar, G.R. 1983. **An Experimental Investigation of Fines Migration in Porous Media**. Paper SPE 12168, presented at SPE Annual Technical Conference and Exhibition, San Francisco, October 5-8.
- Gobran, B.D. 1981. **The Effect of Confining Pressure, Pore Pressure, and Temperature on Absolute Permeability**. Ph.D. Dissertation, Stanford University, California, 107 p.
- Gronseth, J.M. 1989. **Geomechanics Monitoring of Cyclic Steam Simulation Operations in the Clearwater Formation**. Paper No. 34, presented at the Fourth District 5 Meeting, CIM, Calgary.
- Gronseth, J.M. 1990. **What Role Does Heave/Subsidence Play in Thermal Heavy Oil Recovery Operations ?** Minutes of Quarterly Meeting of the Canadian Heavy Oil Association, Calgary, May 15, 2 p.
- Gruesbeck, C. and Collins, R.E. 1982. **Entrainment and Deposition of Fine Particles in Porous Media**. Society of Petroleum Engineers Journal, December, pp. 847-856.
- Gunter, W.D., Bird, G.W. 1989. **Inorganic Chemistry in AOSTRA Technical Handbook on Oil Sands, Bitumens and Heavy Oils**. L.G. Hepler and Ch. Hsi Ed. AOSTRA Technical Publication Series No. 6, pp. 204-258.
- Hackbarth, D.A. and Nastasa, N. 1979. **Hydrogeology of the Athabasca Oil Sands Area**, Alberta. Alberta Research Council, Bulletin 38, 39 p.
- Harris, M.C. and Graham, J.P. 1989. **MINI-FRAC Testing Well AO-83, UTF Site**. Report Submitted to AOSTRA. Thurber Consultants Ltd, 24 p.
- Hassan, D. 1990. **Importance of Geomechanics in Oil Sands and "One Minute" Comments**. Quarterly Meeting of the Canadian Heavy Oil Association, Calgary, May 15.

- Head, K.H. 1985. **Manual of Soil Laboratory Testing**, Vol. 3. John Wiley and Sons, New York-Toronto, 1238 p.
- Henkel, D.J. and Gilbert, G.D. 1952. **The effect of the Rubber Membrane on the Measured Triaxial Compression Strength of Clay Samples**. *Geotechnique*, Vol. 3, No. 1, pp. 20-29.
- Holt, R.M. 1990. **Permeability Reduction Induced by a Nonhydrostatic Stress Field**. *SPE Formation Evaluation*, December, pp. 444-448.
- Honarpour, M., Koederitz, L. and Harvey, A.H. 1986. **Relative Permeability of Petroleum Reservoirs**. CRC Press, Inc, Boca Raton, Florida, 143 p.
- Hycal Energy Research Laboratories Ltd. 1990. **Special Core Studies - Coring, Preserving and Testing**. 509 p.
- Kezdi, A. 1974. **Handbook of Soil Mechanics, Vol.1- Soil Physics**. Elsevier Scientific Publishing.
- Kosar, K.M. 1983. **The Effects of Heated Foundations on Oil Sand**. M.Sc. Thesis, University of Alberta, Edmonton, 248 p.
- Kry, P.R. 1989. **Field Observations of Steam Distribution During Injection to the Cold Lake Reservoir**. Paper No 31, presented at the Fourth District 5 Meeting, CIM, Calgary.
- Kwan, M.Y., Okazawa, T. and Fortier, R.A. 1986. **Application of the Pulse-Decay Technique to the Measurement of Heavy Oil Core Fluid Mobilities and Porosity**. *Journal of Canadian Petroleum Technology*, September-October, Vol 27, No. 5, pp. 92-98.
- Kwan, M.Y., Cullen, M.P., Jamieson, P.R. and Fortier R.A. 1988. **A Study of Fines Migration Related Permeability Damage in Extracted Cold Lake Heavy Oil Cores**. Paper No. 59, presented at the 39th Annual Technical

Meeting of the Petroleum Society of CIM, Calgary, June 12-16, pp. 59-1 to 59-18.

Laing, J.M., Graham, J.P., Stokes, A.W. and Collins, P.M. 1991. **Geotechnical Instrumentation and Monitored In Situ Behaviour of Oil Sands During Steaming at the AOSTRA UTF Phase A Trial**. Paper No. 89, presented at 44th Canadian Geotechnical Conference, Calgary, pp. 89-1 to 89-9.

Laing, J.M., Scott, J.D., Stokes, A.W., Suggett, J.C. and Wood, J.C., 1988. **Geotechnical Instrumentation of the AOSTRA Mine-Assisted Underground Steaming Trial**. Paper No. 112, presented at 4th UNITAR/UNDP International Conference, Edmonton, August 7-12, pp. 112-1 to 112-18.

Lambe, T.W. and Whitman, R.V. 1979. **Soil Mechanics**. SI Version, John Wiley, New York, 553 p.

Leshchyshyn, T.H. and Seyer, W.G. 1990. **Three Field Techniques to Estimate the Effective Permeability in the Athabasca Oil Sands**. Paper No. CIM/SPE 90-53, presented at the International Technical Meeting of the Petroleum Society of CIM and the Society of Petroleum Engineers, Calgary, June 10-13, pp. 53-1 to 53-26.

Lowe, J. and Johnson, T.C. 1960. **Use of Back Pressure to Increase Degree of Saturation of Triaxial Test Specimens**. ASCE Research Conference on Shear Strength of Cohesive Soils, Boulder, Colorado, USA, pp. 819-836.

Mainland, G.G. 1983. **The Development of In Situ Recovery Technology at Cold Lake**. Alberta Oil Sands Technology and Research Authority, Proceedings of the 4th Annual Conference on Advances in Petroleum Recovery Technology, Calgary, 13 p.

Mattison, B.W. 1987. **Ichtiology, Paleontology and Depositional History of the Lower Cretaceous Mc Murray Formation, Athabasca Oils Sands**

- Area, Northeastern Alberta.** M.Sc. Thesis, Dept. of Geology, University of Alberta.
- Monicard, R.P. 1980. **Properties of Reservoir Rocks: Core Analysis.** Editions Technip, Paris, 165 p.
- Monte, J.L. and Krizen, R.J. 1976. **One Dimensional Mathematical Model for Large-Strain Consolidation,** *Geotechnique*, Vol. 26, No. 3, pp. 495-510.
- McKay, J.G. 1989. **Undisturbing Oil Sand Sampling and Sample Quality Evaluation.** M.Sc. Thesis. University of Alberta, Edmonton, 227 p.
- Morgenstern, N.R., Fair, A.E., and McRoberts, E.C. 1988. **Geotechnical Engineering Beyond Soil Mechanics - a Case Study.** *Canadian Geotechnical Journal*, Vol. 25, No. 4, November, pp. 637-661.
- Mori, A. and Tamura, M. 1986. **Effect of Dilatancy on Permeability in Sands Stabilized by Chemical Grout.** *Soils and Foundations* (Japanese Society of SM and FE), Vol. 26. No. 1 March, pp. 96-104.
- Morita, N., Gray, K.E., Srouji, F.A.A., and Jogi, P.N. 1984. **Rock Property Change During Reservoir Compaction.** Paper SPE No. 13099, presented at the 59th Annual Technical Conference and Exhibition of the Society of Petroleum Engineers, Houston, Texas, September 16-19, 17 p.
- Mossop, G.D. 1980. In **Facts and Principles of World Petroleum Occurrence.** A.D. Miall Ed., Can. Soc. Petrol. Geol. Memoir 6, pp. 609-632.
- Mossop, G.D. 1980. **Geology of the Athabasca Oil Sands.** *Science*, Vol. 207, No. 11, January, pp. 145-152.
- Mungan, N. 1965. **Permeability Reduction Through Changes in pH and Salinity.** *Journal of Petroleum Technology*. July-September, pp. 1449-53.

- Muecke, T.W. 1979. **Formation Fines and Factors Controlling Their Movement in Porous Media** Journal of Petroleum Technology, February, pp. 144-150.
- Nasr-El-Din, H.A., Maini, B.B. and Stanislav, P. 1991. **Fines Migration in Unconsolidated Sand Formations.** AOSTRA Journal of Research, No. 7, 15 p.
- Peacock, D.H. 1988. **Gas Evolution in Athabasca Oil Sands.** M.Sc. Thesis, University of Alberta, Edmonton.
- Petroleum Production Handbook**, 1962. Society of Petroleum Engineers of AIME, Dallas, Texas, Frick Thomas C., Ed.
- Plewes, H.D. 1987. **Undrained Strength of Athabasca Oil Sands.** M.Sc. Thesis, University of Alberta, Edmonton, 267 p.
- Rajani, B.B. 1988. **A Simple Model for Describing Variation of Permeability with Porosity for Unconsolidated Sands.** In-Situ, Vol.12, No.3, pp. 209-226.
- Rhett, D.W. and Teufel, L.W. 1992. **Effect of Reservoir Stress Path on Compressibility and Permeability of Sandstones.** Paper SPE No 24756, presented at the 67th Annual Technical Conference and Exhibition of the Society of Petroleum Engineers, Washington, DC, October 4-7, pp. 965-972.
- Rottenfusser, B.A., Alwast, N.K., Kidston, C.R. and Cotterill, D.K. 1989. **Geology of UTF Phase A.** Report to AOSTRA. Alberta Geological Survey, Alberta Research Council.
- Rottenfusser, B.A., Pelfreyman, J.E. and Alwast, N.K. 1988. **Geology of the AOSTRA Underground Test Facility Site.** Paper No. 115, presented at the 4th UNITAR/UNDP Conference, Edmonton, August 7-12, pp. 115-1 to 115-2.

- Scott, J.D., Adhikary, D. and Proskin, S.A., 1991a. **Volume and Permeability Changes Associated with Steam Stimulation in an Oil Sands Reserwoir**. Paper No. CIM and AOSTRA 91-63, presented at the Petroleum Society of CIM and AOSTRA Technical Conference, Banff, Alberta, April 21-24, 14 p.
- Scott, J.D., Chalaturnyk, R. J. Stokes, A.W., Collins, P.M. 1991b. **The Geotechnical Program at the AOSTRA Underground Test Facility**. Paper No. 88, presented at 44 th Canadian Geotechnical Conference, Calgary, September 29 - October 2, 8 p.
- Scott, J.D., Proskin, S.A., Adhikary, D. 1992. **The Relationship Between Absolute Permeability and Stress State for Heavy Oil Sand**. Univerity Of Alberta, 10 p.
- Settari, A., Ito, Y., Fukushima, N. and Vaziri, H. 1990. **Geotechnical Aspects of Recovery Processes in Oil Sands**. 11 p.
- Selby, R.J. and Ali, S.M.F. 1988. **Mechanics of Sand Production and the Flow of Fines in Porous Media**. JCPT, May.
- Smith, G. 1990. **Geomechanics**. Minutes of Quarterly Meeting of the Canadian Heavy Oil Association, Calgary, May 15, 2 p.
- Takamura, K. 1982. **Microscopic Structure of Athabasca Oil Sand**. The Canadian Journal of Chemical Engineering, Vol. 60, August, pp. 538-545.
- Torsaeter, O. and Beldring, B. 1987. **The Effect of Freezing of Slightly Consolidated Cores**. SPE Formation Evaluation, Vol.2, No.3, September, pp. 345 - 340.
- Tortike, W.S. and Farouq Ali, S.M. 1991. **Prediction of Oil Sand Failure Due to Steam-Induced Stresses**. The Journal of Canadian Petroleum Technology, Vol. 30, January-Ferbruary, pp. 87-96.

- Wei, K.K., Morrow, N.R. and Brower, K.R. 1986. **Effect of Fluid, Confining Pressure, and Temperature on Absolute Permeabilities of Low-Permeability Sandstones.** SPE Formation Evaluation, August, pp. 413-423.
- Wightman, D., Rottenfusser, B., Kramers, J. and Harrison, R. 1989. **Geology of the Alberta Oil Sands Deposits in AOSTRA Technical Handbook on Oil Sands, Bitumens and Heavy Oils.** L.G. Hepler and Ch. Hsi Ed. AOSTRA Technical Publication Series No.6, pp. 1-9.
- Wong, R.C.K., Barr, W.E., To, N.M. and Paul, R. 1991. **Laboratory Measurement of Effective Permeability to Water and Compressibility in Unconsolidated Athabasca Oil Sands Cores.** Proceedings of 44th Canadian Geotechnical Conference, Calgary, pp. 56-1 to 56-7.
- Wong, R.C.K., Barr, W.E. and Kry, P.R. 1993. **Stress-Strain Response of Cold Lake Oil Sands.** Geotechnical Journal. Vol 30, No 2, pp. 220-235.
- Zoback, M.D. 1975. **High Pressure Deformation and Fluid Flow in Sandstone, Granite, and Granular Materials.** Ph.D. Dissertation, Stanford University, California, 210 p.

APPENDIX A

Initial Tests on Oil Sand Cores, Stress Path B₀

This appendix presents results of the triaxial compression stress-controlled tests performed on oil sands cores. Factors that led to the changes introduced into the conditions of the following tests are also discussed.

Two triaxial compression stress-controlled tests were performed on specimens S1 and S2. The size of these specimens, which had a height to diameter ratio of 2 to 1, was different than the size of all the remaining oil sand specimens (1 to 1). The test on specimen S1 was conducted at a room temperature of 23 °C while the test on specimen S2 was carried out at 15 °C. In these tests, frictionless porous stones, described in Appendix B, were used and the Bellofram load frame was utilized to apply a constant vertical load. Specimen initial parameters and test results are shown in Tables 4.1 to 4.4.

Saturation and Isotropic Compression

The specimens were thawed under a cell pressure of 200 kPa and with back pressure lines open to atmospheric pressure. Then, the cell and back pressures were alternately increased in steps of 200 kPa until a back pressure of 3 MPa was reached. The effective confining pressure was always maintained higher than 200 kPa when pressure was being increased. The specimens were left to saturate overnight. Next, the cell and back pressures were increased in steps of 200 kPa until cell pressures of 5.4 MPa for specimen S1 and 6.2 MPa for specimen S2 were reached. The coefficient of pore pressure, B , equaled 0.87 and 0.89 respectively during these two tests. To compress the specimens isotopically, cell pressure was reduced in stages down to 1 MPa. Plots of volume change versus effective confining pressure during isotropic compression tests are shown in Figure A.7.

Triaxial Compression

The triaxial compression tests on specimens S1 and S2 were performed at effective confining stresses of 800 kPa and 1840 kPa respectively. After the isotropic compression was completed, cell pressure was decreased gradually until the required effective confining stress was reached. Next, flow through the two specimens was started at 4 ml/hr and 0.55 ml/hr respectively. The differential pressure became stabilized in 2 hr and 6.5 hr for specimens S1 and S2 respectively. During the triaxial compression test, the vertical load was increased in several stages until the specimen failed.

Test Results

Specimen S1 failed abruptly. The specimen slipped to one side of the base pedestal, and a wedge of the cylinder split at the bottom. Specimen S2 bulged and expanded radially, rather uniformly over the lowest half of the specimens height. Sketches of the specimens after failure are shown in Figure A.8.

The stress-strain curves for S1 and S2 are shown in Figures A1 and A.2. At failure, stress ratios of 5.0 and 4.4 and deviatoric stresses of 3.2 MPa and 6.2 MPa at axial strains of 5.0 % and 3.5 % were measured for specimens S1 and S2 respectively.

The volume change-axial strain curves are shown in Figure A.3. During the initial stages of testing, the two specimens contracted by 0.27 % and 0.30 % respectively. At failure, specimen S1 had dilated by 1.2 %, but the volume of specimen S2 was still about 0.10 % less than the initial specimen volume. One measurement on specimen S2, performed at a large axial strain of 12 %, showed dilation of 0.76 %.

The effective permeability to water versus, first, changes in water porosity and, second, changes in volume are shown in Figures A5 and A6. Specimen S1 initially experienced a decrease in permeability even when the specimen volume increased.

Changes in the effective permeability to water of specimen S2 are more consistent with changes in water porosity.

Discussion and Conclusions

The strength of specimens S1 and S2 was somewhat lower than that of the specimens tested in the triaxial compression strain-controlled tests along stress path Be (Figure 5.16). The axial strain at failure for both specimens was larger than the strain at failure measured for the other specimens during strain-controlled tests. The lower strength and larger strain at failure of specimens S1 and S2 can be attributed to their premature failure. This could result from slippage of the specimen off the pedestal on the surfaces coated with silicon grease from a horizontal component of the external load developed. Larger axial strains at failure also could follow from the mode of the vertical load change. Rapid increases in vertical load result in rapid increases in the mean effective stress, which produces specimen contraction. This, in turn, involves an instantaneous increase in pore pressure and a decrease in the effective confining stress. Dissipation of this excessive pore pressure can be a relatively slow process, as a result of the low permeability of oil sands.

The differences in the effective confining stress between the top and the bottom of the specimen, due to the differential pressure developed during permeability tests, proved large enough to cause specimen failure through expansion of its lower zone. This was the main reason why the height to diameter ratio of specimens was changed in the tests that followed. Across a shorter specimen, lower differential pressure is created at the same flow rate, so that bulk failure is expected to develop in a larger part of a specimen.

Problems also occurred in permeability measurements. During the two tests, small quantities of bitumen were eroded from the specimens and deposited in the frictionless porous stones and the small porous stone placed centrally in the top cap

(Appendix B), possibly clogging some of their pores . The test on specimen S2 was conducted at a lower temperature (15 °C) than the test on specimen S1 (23 °C), resulting in improved permeability measurements.

To reduce the influence of these shortcomings on test results, the following measures were adopted in later testing:

1. Shorter specimens, with a height to diameter ratio of 1 to 1 (38.1 mm in diameter and 38.1 mm in length), were used to decrease differential pressure across the specimen (to about 100 kPa), cause more uniform distribution of the effective confining pressure, and, in effect, almost uniform shear dilation along the specimen.
2. Conventional porous stones were used to eliminate accidental splitting of the specimen in its lower part or slipping off the pedestal during testing.
3. Only strain-controlled tests were conducted, applying constant and very low rates of axial strain to assure low rates of volume change. Any manual changes in pressure were carried out in very small increments. The strain-controlled tests also allowed the measurement of specimen behavior in the post-peak region. The volumetric changes that occur before peak strength is reached constitute only part of the total volumetric changes measured at higher axial strains in the post-peak region.
- 4 The testing temperature was lowered to its in situ value of 8 °C to increase bitumen viscosity and thus reduce its mobility.

The applied measures eliminated, to a satisfactory degree, the difficulties that were encountered during tests on specimens S1 and S2 and improved the quality of the measurements of the effective permeability to water.

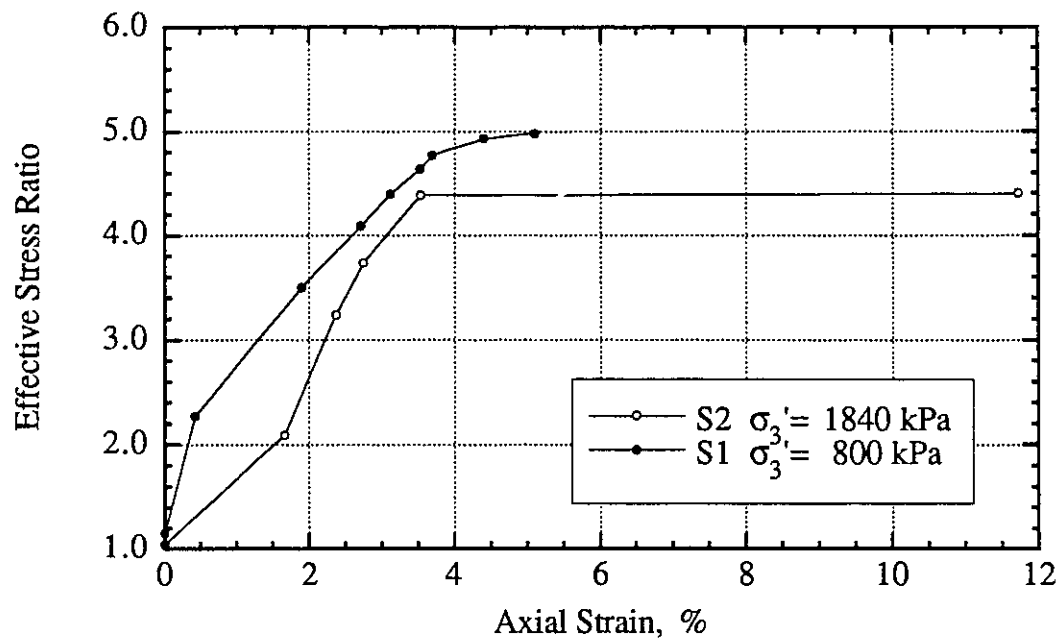


Figure A.1 Stress Path B_o , Volume Change-Axial Strain

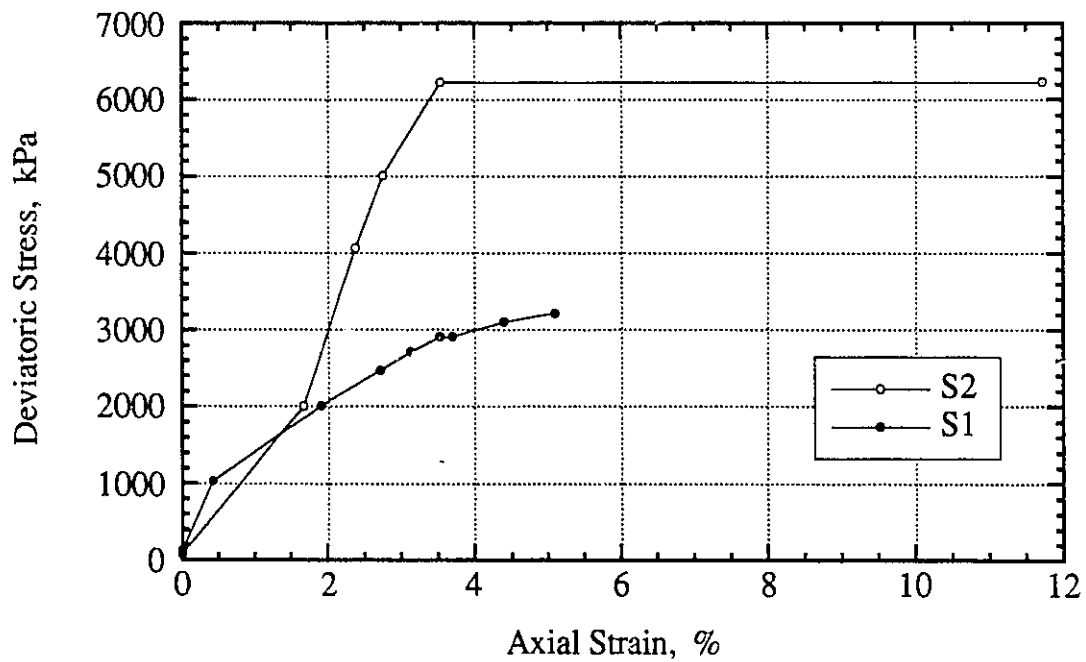
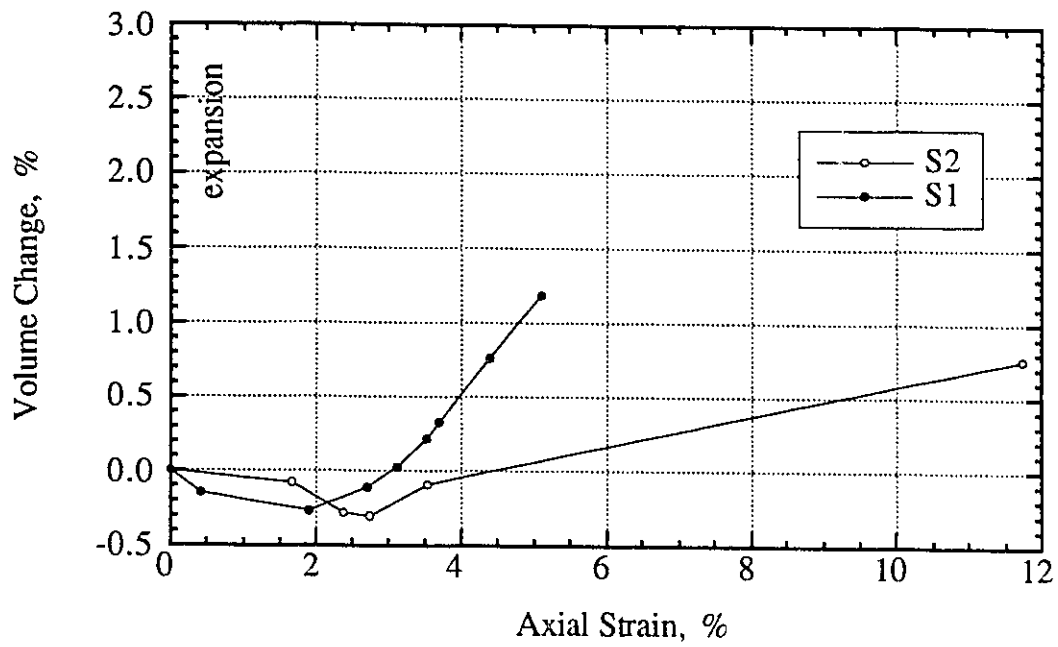
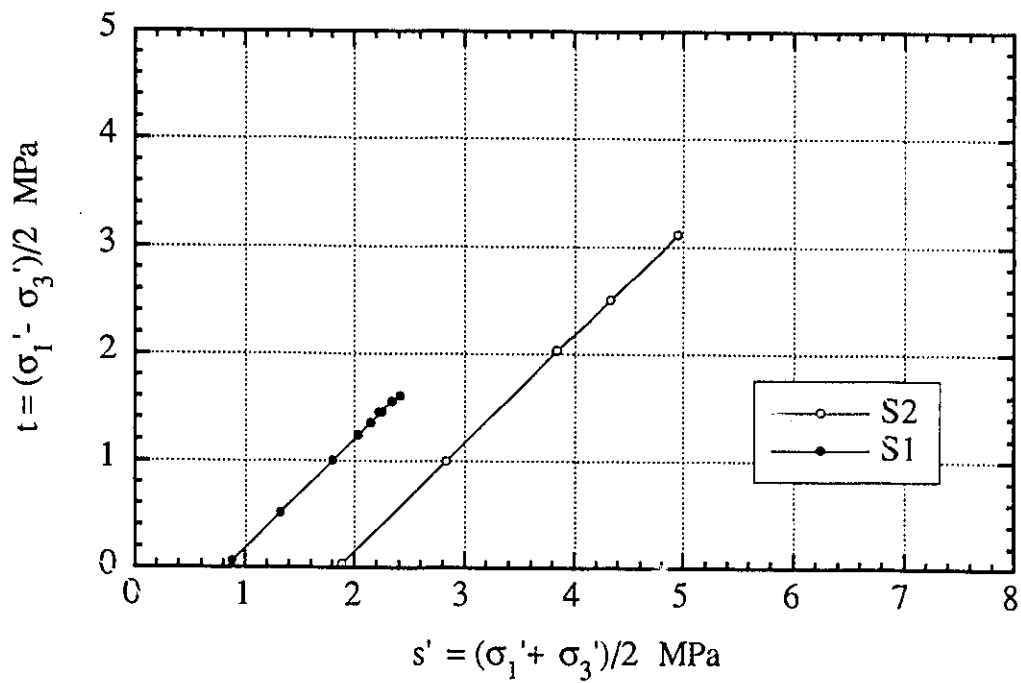


Figure A.2 Stress Path B_o , Deviatoric Stress- Axial Strain

Figure A.3 Stress Path B_o , Volume Change-Axial StrainFigure A.4 Stress Path B_o

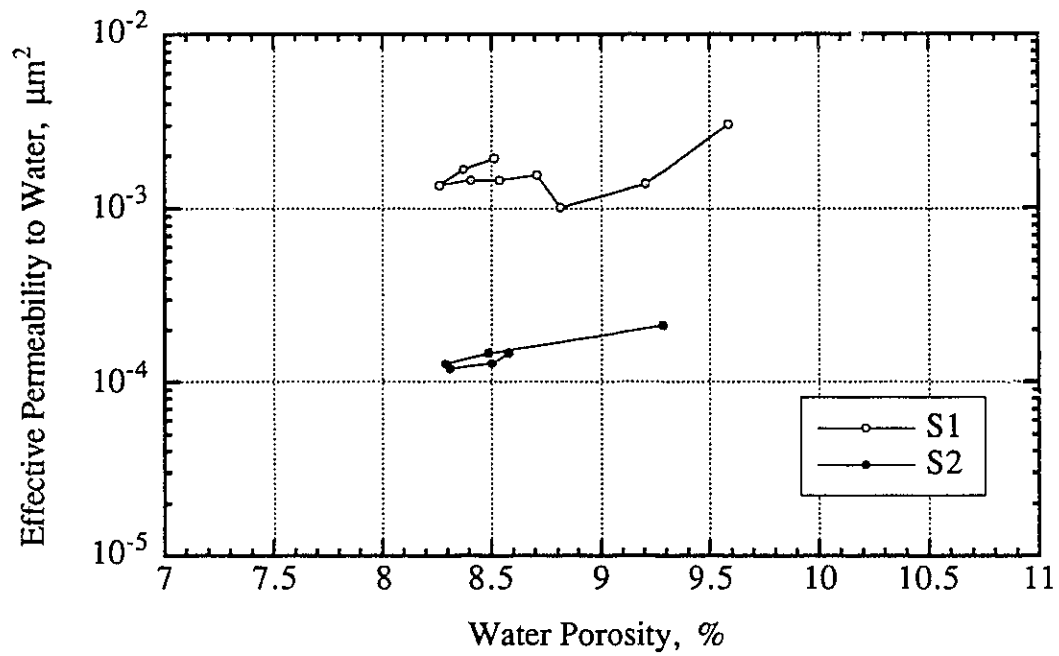


Figure A.5 Stress Path B_o, Effective Permeability to Water-Water Porosity

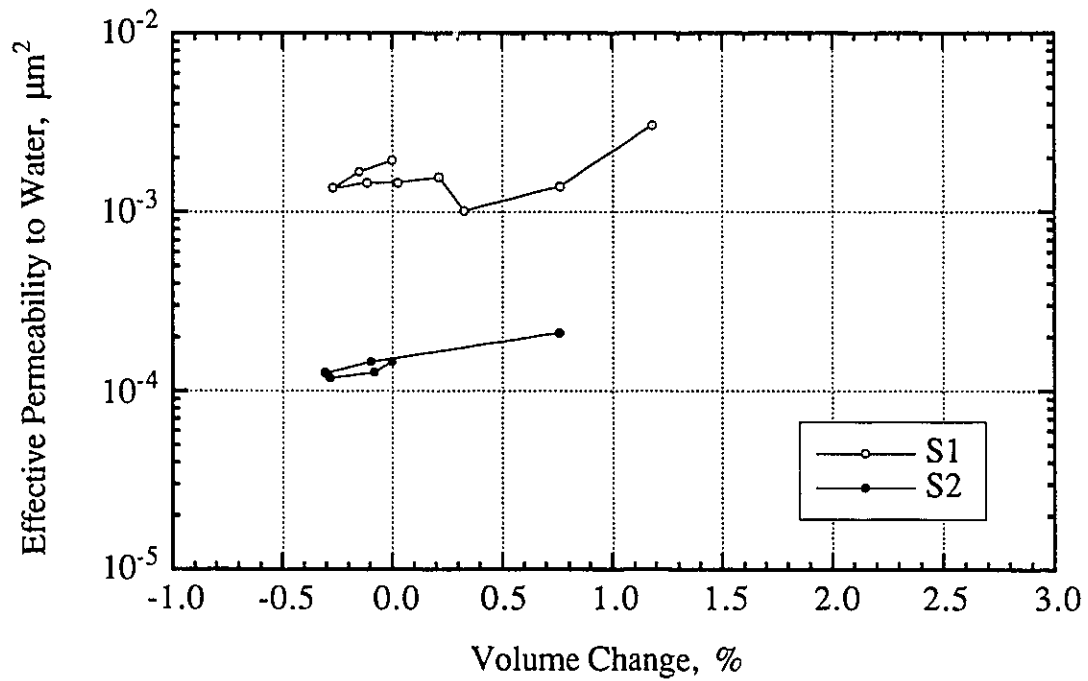


Figure A.6 Stress Path B_o, Effective Permeability to Water-Volume Change

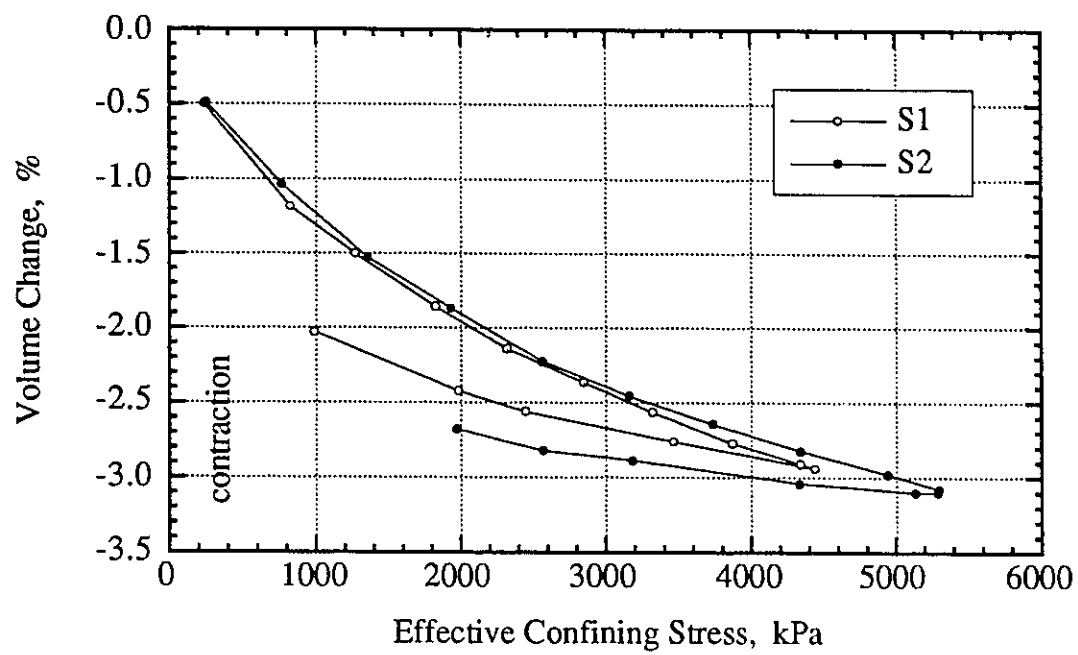
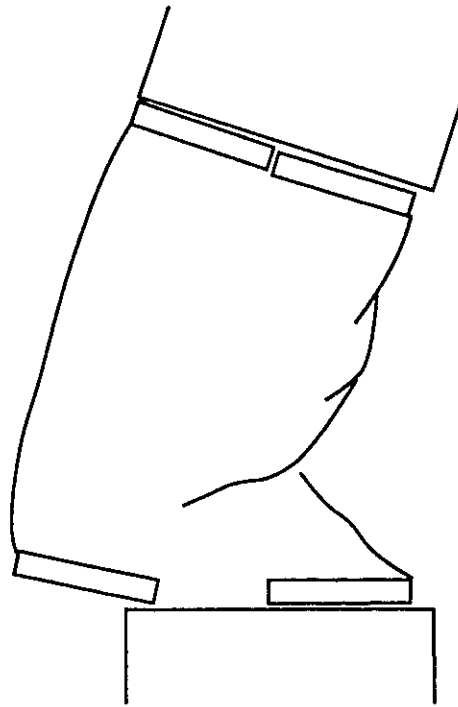
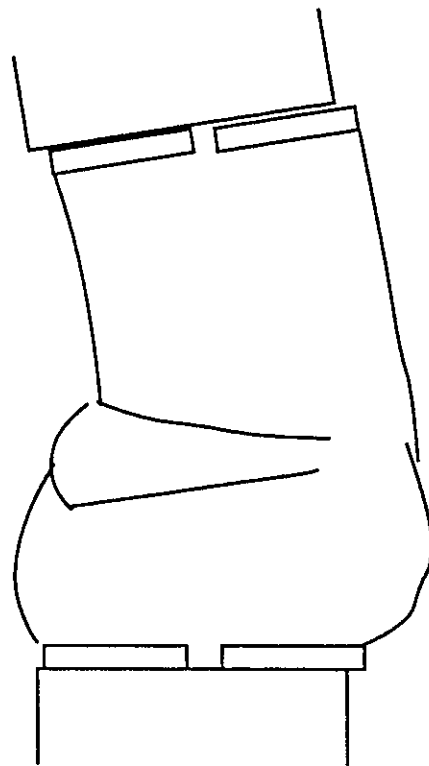


Figure A.7 Volume Change During Isotropic Compression



Specimen S1



Specimen S2

Figure A.8 Shape of Specimens S1 and S2 After Failure

APPENDIX B

Frictionless Porous Stones

Although the attempt to design and use frictionless porous stones was not brought to a successful end, it cast additional light on the permeability test results.

It is commonly known that boundary restraint, resulting from the use of rigid loading platens, influence specimen strength as well as the relationships between stress, strain, and volume change. This influence manifests itself in higher strength, as well as lower volume change and lower axial strain at failure, for specimens with non-lubricated ends than for those with lubricated ends. Tests reported by Bishop and Green (1965), performed on Ham River medium to fine sand samples, showed that differences between samples (1 to 1) with lubricated ends versus those with non-lubricated ends can be significant. Oil sands are a geotechnically different material, exhibiting less axial strain to failure, greater strength, a larger maximum rate of volume change, and a lower porosity as compared to Ham River sands, therefore, the effect of boundary restraint on the strength and volumetric changes of oil sands could be different.

The location of the frictionless porous stones in the assembly is shown in Figure B.1. The two conventional circular porous stones were cut into six segments each and separated from the base pedestal and the top cap by two layers of rubber membranes. Water from the specimen drains through the porous stone segments and then through a central hole in the rubber membranes into a small circular porous stone placed centrally in the top cap. Water can enter the specimen by passing through a similar small porous stone situated in the base pedestal, a hole in the rubber membrane, and another set of segmented porous stones. The surfaces between the rubber membranes and between the membranes and the base pedestal and top cap were lubricated with silicone grease. The porous stone segments were designed with the assumption that they would be free to

move radially along with the expanding ends of the specimen. In the overall picture, this did take place but, at the same time, some difficulties appeared.

Frictionless porous stones were used in four tests: one on reconstituted extracted oil sands (specimen PI4), two on oil sands specimens having a height to diameter ratio of 2 to 1 (S1,S2), and one on an oil sands specimen having the ratio of 1 to 1 (S5). During isotropic unloading, specimen PI4 underwent only a slightly larger volumetric expansion than the specimens not tested with expanding (frictionless) porous stones (PI1 to PI3). Differences in the rate of the volume change were more noticeable at lower effective confining stresses (Figure 3.7). During triaxial compression, specimen PI4 failed at a lower stress ratio than specimen PI3, by about 6 % (Figure 3.33), although specimen PI3 was sheared under lower effective confining stress. Some influence on the difference in the stress ratio at failure could be caused by the premature specimen failure described in Appendix A. The average rate of permeability increase in case of specimen PI4 was similar to that of specimen PI3 (Figure 3.20). The initial porosities of both specimens were about 39 %. After the test on specimen PI4, the upper porous stone segments did not show any displacement but the lower porous stone segments were displaced radially.

During the triaxial compression tests on oil sands cores, specimen S1 failed abruptly due to shear failure at its lower part, which was brought about by the uneven radial displacement of the segments of the porous stone. The specimen, in consequence, slipped off the base pedestal (Figure A.8). Specimen S2 failed by bulging disproportionately at the base rather than at the top.

Another difficulty that appeared when frictionless porous stones were used was that, during permeability tests, even a very small amount of bitumen displaced from the specimens could significantly reduce permeability of the small porous stone placed centrally in the top cap. The continuous decrease in permeability during the test on specimen S1, which took place even when specimen volume was increasing, is believed

to follow from the partial clogging of the small porous stone by bitumen. After the test, bitumen was found in the porous stone segments, in the small porous stone, and farther up in the top cap holes. The test on specimen S1 was carried on at a room temperature of 23 °C.

Bitumen mobility during the triaxial compression test on specimen S5 (38.1 mm in diameter and 38.1 mm in length) performed at 8 °C did not cause problems, as virtually no bitumen was flushed out of this specimen, however, the frictionless porous stones caused an undesirable mode of specimen failure. Part of the specimen, in the shape of a wedge, was split from the specimen cylinder and excessively displaced horizontally to one side of the base pedestal (Figure B.3), which, thus, still showed a tendency for specimen failure to be concentrated at the bottom. Also, some obstruction to the radial movement of the porous stones was observed, due to the bending of the sharp tips of the porous stone segments at the center of the top cap and the base pedestal.

There were no tests with conventional porous stones performed at a similar effective confining stress, therefore, it is difficult to evaluate precisely the influence of the frictionless porous stones on the strength and volume change of the specimen. However, the plots of effective permeability to water against water porosity (Figures 4.9 and 4.10) show only a slightly higher rate of permeability change during the test on specimen S5 as compared to the other tests, performed without frictionless porous stones.

Because of the aforementioned difficulties associated with the application of the frictionless porous stones and lack of evidence that the conventional porous stones would excessively affect the effective permeability to water - water porosity relationship, all remaining tests were conducted with conventional (non-expanding) porous stones.

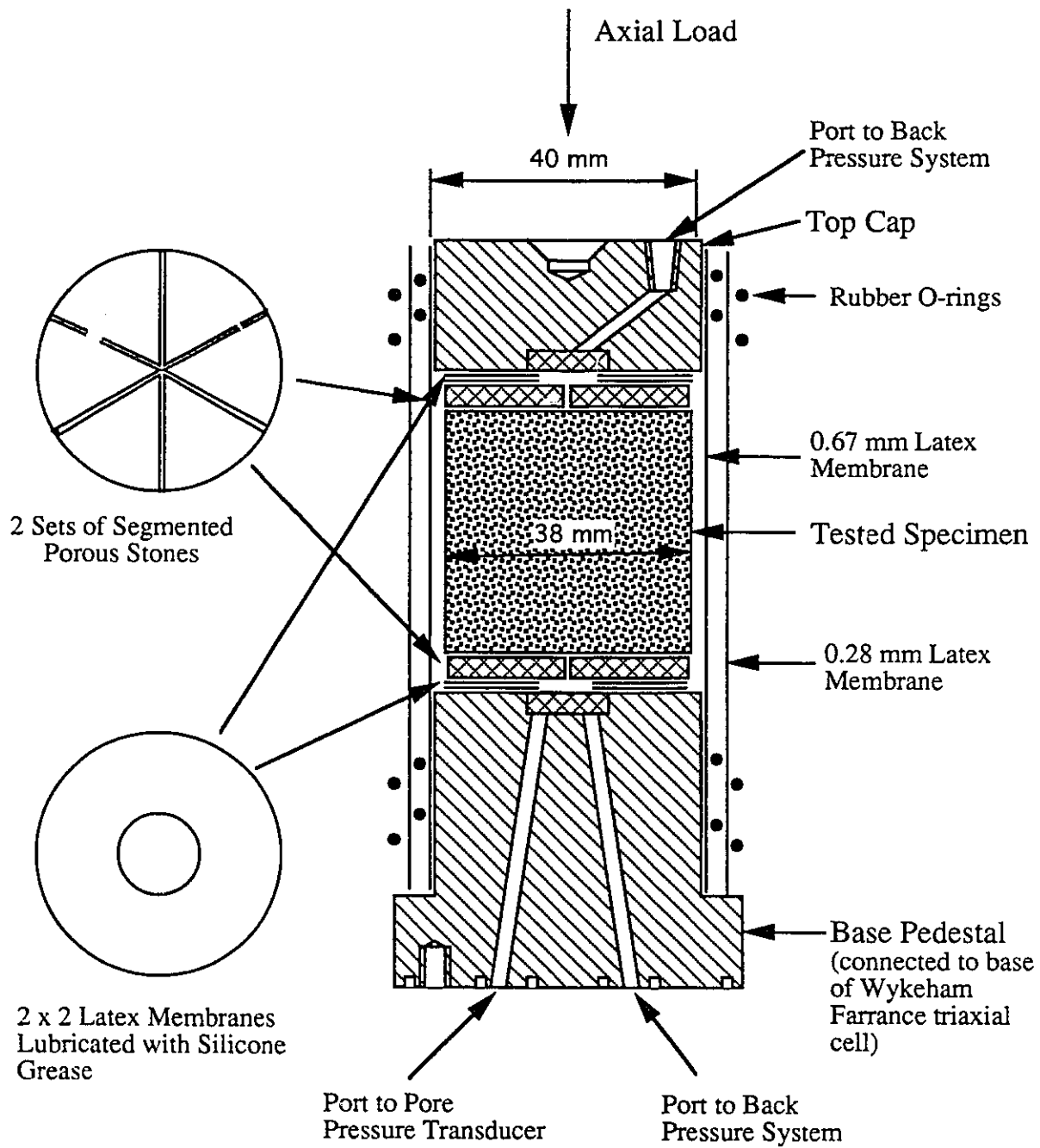


Figure B.1 Assembly of Frictionless Porous Stones

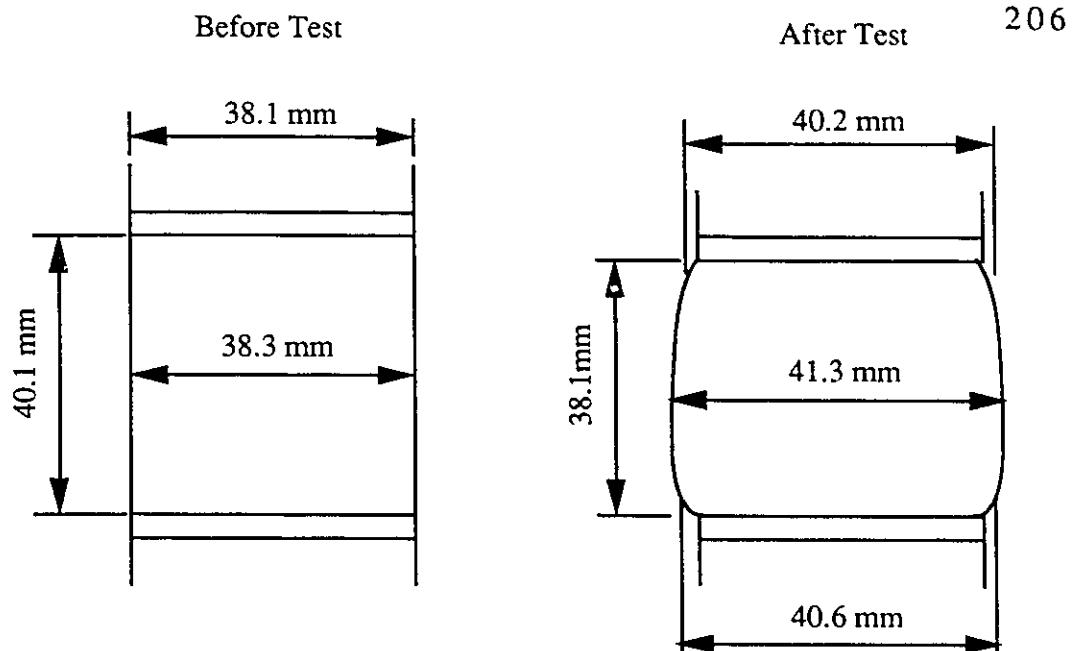


Figure B.2 Dimensions of Specimen S4 After Test as an Example of Specimen Deformations with Conventional Porous Stones

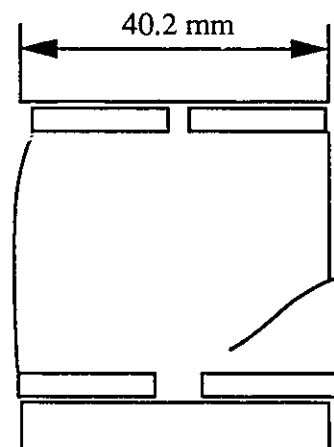


Figure B.3 Schematic Diagram of Specimen S5 with Frictionless Porous Stones After Failure

APPENDIX C

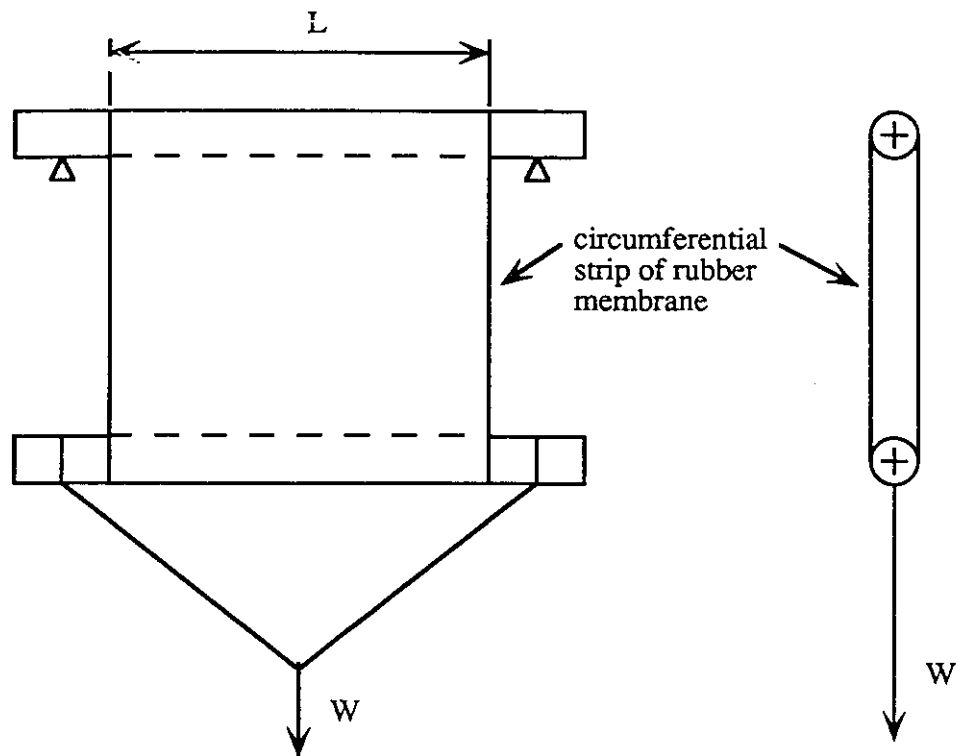
Effect of Rubber Membrane on Triaxial Test Results

The influence of the rubber membrane on the measured strength of specimens in conventional triaxial compression tests at confining stresses greater than 100 kPa is considered to be negligible. However in the case of the confining stress unloading tests carried on in this study, the effective confining stress at failure was as low as 10 kPa; hence, neglecting the effect of the membrane could lead to significant errors in calculated stress ratios.

There are two modes in which the membrane can act on a specimen during deformations (Henkel and Gilbert, 1952). The membrane can work as a reinforcing compression shell bearing vertical loads, or it can exert a confining pressure on the specimen due to the hoop tension associated with the extension of rubber as the diameter of the specimen increases. The actual effect of the membrane on the specimen is a combination of these two modes. Under special circumstances, one mode may dominate. In the case of a clay specimen in a undrained or constant volume test at a high confining stress, the membrane and specimen can probably deform as a unit because the Poisson's ratios of clay and rubber are similar. In the case of a sand specimen in a drained test under a very low confining stress, there is an increase in specimen diameter and the membrane stretches and exerts pressure on the specimen. This added confining pressure has to be added to cell pressure when the effective confining stress is calculated. To illustrate how the membrane correction affects the calculation of stress ratio, the test results on specimen S17 will be discussed. The specimen failed at a confining stress of 10.6 kPa. The membrane correction amounted to 20 % of the value of the effective confining stress. If it were neglected, the calculated stress ratio would also be higher by 20 %. Specimen S17 reached its peak stress ratio at an axial strain of 0.8 %. If the peak

stress ratio were reached at larger strains, then neglecting to correct for the effect of the membrane on the effective confining stress would result in an even larger error.

The schematic layout of the rubber extension test is shown in Figure C.1. On the next page, the confining pressure correction is derived. Figures C.3 and C.4 show the results of the rubber membrane extension tests on two membranes, 0.76 mm and 0.28 mm thick.



Extension Modulus $M = F / ((S - S_0) / S_0)$

where: $F = W / 2L$

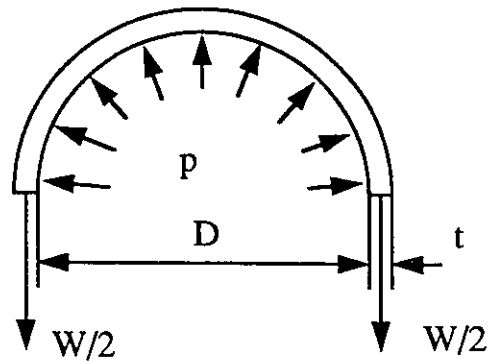
W - load

L - length of membrane segment

$S_0 = 38.1 \text{ mm}$ - initial length of membrane circumference

S - length of stretched membrane circumference

Figure C.1 Measurement of Extension Modulus of Rubber Membrane



The pressure exerted on a specimen by an extended membrane is equal:

$$p = W/(D \cdot L) = (2F \cdot L)/(D \cdot L) = 2F/D$$

From the extension modulus definition:

$$F = M \cdot (S - S_0)/S_0 = M \cdot (D - D_0)/D_0$$

since

$$S = \pi(D+t) - \pi D$$

$$S_0 = \pi D_0$$

The confining pressure correction due to membrane extension:

$$p = 2M \cdot (D - D_0)/(D \cdot D_0)$$

Figure C.2 Calculation of Confining Pressure Correction

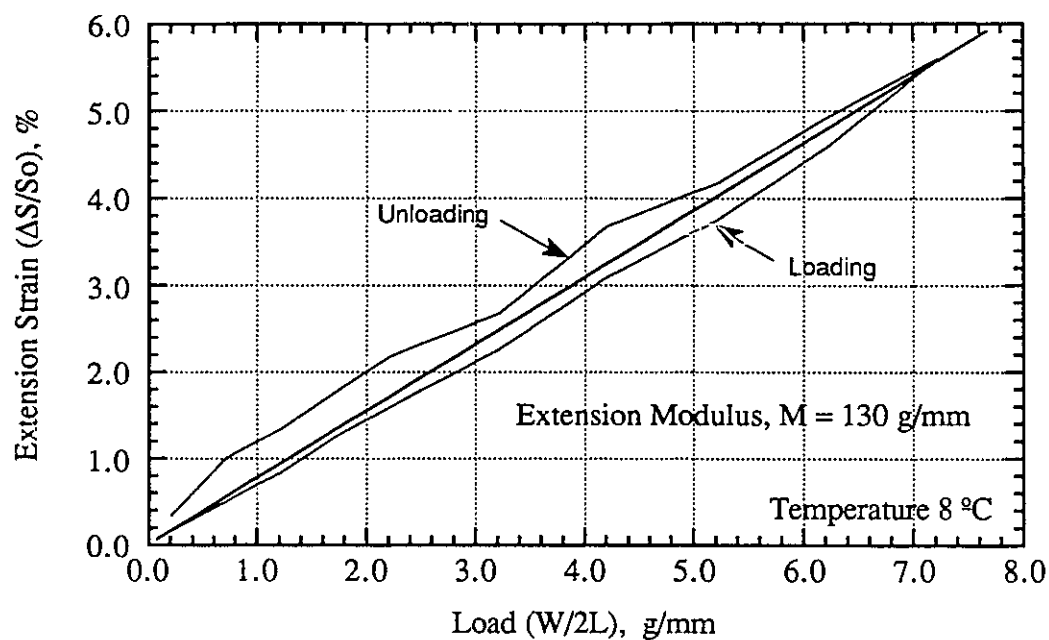


Figure C.3 Rubber Membrane Extension Test - 0.67 mm thick

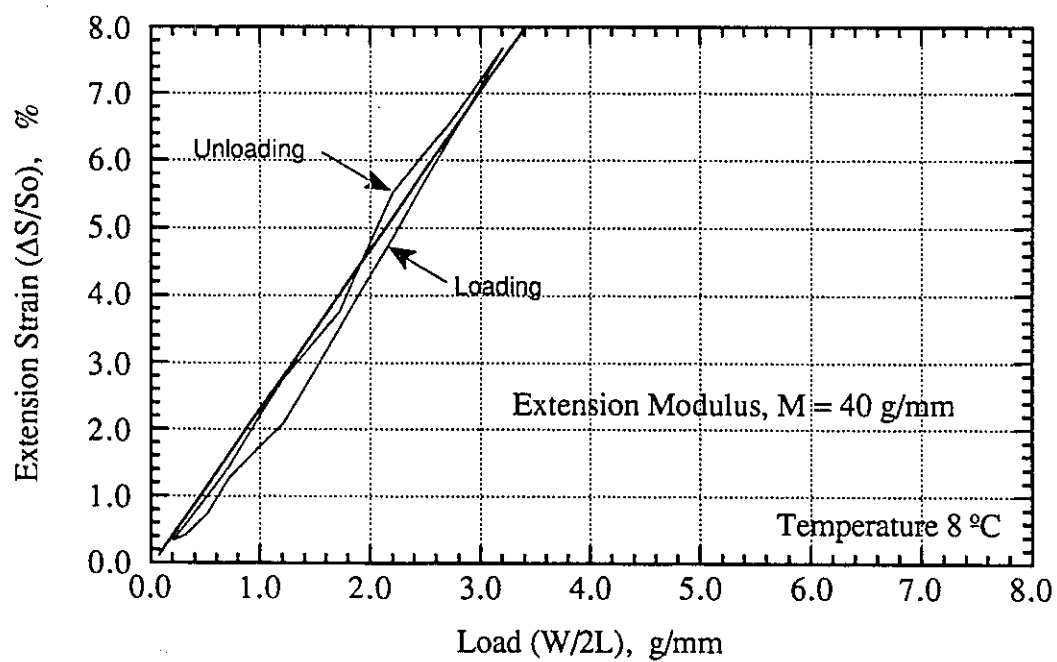


Figure C.4 Rubber Membrane Extension Test - 0.28 mm thick

APPENDIX D

Bitumen Mobility During Testing

In this study, effective permeability to water calculations were performed under the assumption that the bitumen filling the pore space in oil sands is totally immobile. Because this assumption did not prove to be completely true, the following discussion is made in order to show that the error in permeability estimation, resulting from the displacement of a small amount of bitumen, was small. In most cases, this error was much smaller than 9 %, as can be inferred from the quantities of displaced bitumen.

In the natural state, the viscosity of the bitumen contained in the Athabasca oil sands is so high (of the order of 10^7 mPa•s) that it is considered immobile. In these tests, the temperature was maintained at the in situ level of 8 °C to keep the bitumen viscosity high. However, it was observed that the amount of bitumen extracted from specimens after testing was lower than the amount of bitumen that was calculated on the basis of the composition of trimmings. This difference could be because the bitumen content in the specimens really was lower than in the trimmings, since the specimens, in most cases, contained higher amounts of fines than the trimmings (Figure D.2); higher fines content is associated with higher water and lower bitumen contents (Figure D.1). Nevertheless, flushing or squeezing of the bitumen out of the specimens also took place. Various amounts of bitumen were found in the porous stones after testing, although bitumen never entered the channel in the top cap (except in the case of specimen S1 described in Appendix A). More specific measurements and analysis of bitumen mobility were performed during testing on specimens S19 to S23. Table D.1 shows bitumen contained in specimens calculated after testing, bitumen displaced from specimens, applied flow rate, duration of tests, and initial permeability. No clear relation was found between these

parameters and the amount of displaced bitumen, which indicates that the effects of these parameters are complex and interdependent.

One factor that could play a role in squeezing bitumen out of the specimens was the consolidation processes or, more precisely, the rate of consolidation pressure change. A rapid increase in the effective confining stress could lead to substantial pressure gradients inside the specimen because of the low permeability to water of oil sands. In some cases, bitumen was found in the lower porous stone. This bitumen could not have been displaced there by flowing water because the flow direction was upward.

Another factor that could lead to bitumen displacement was the "end effect", according to which the ends of the strongly water wet core tend to imbibe water spontaneously rather than produce it. As a result, a stagnant zone of water forms near the outlet end of the core. Bitumen is then expelled from this zone. The thickness of this end zone, as reported by researchers, is a function of flow rate; the higher the flow rate, the shorter the end zone. It is possible that, although the natural mobility of bitumen contained in specimens was very low, bitumen could still be removed from the end zone because of the additional force associated with the "end effect".

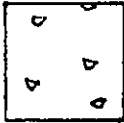




In the event that a water-saturated end zone develops, the effective permeability to water should be calculated by taking into account the specimen length corrected by the thickness of the zone bitumen-discharged. For instance, if the end zone covered 9 % of the specimen length (9 % of the bitumen mass expelled, as in the case of specimen S19), the real permeability would be 9 % lower than calculated. Compared to measured increases in effective permeability to water, which can reach thousands or tens of thousands percent, the error caused by the "end effect" would not be very significant.

Two observations support the assumption that the amount of bitumen expelled from the specimens did not have a large influence on measured changes in permeability. Figure 5.11 shows the results of two types of tests, the isotropic unloading and constant

p' tests, performed on the same set of specimens (S19 to S23). In the isotropic unloading tests, specimens were unloaded either to very low confining stresses (150 kPa) and then reconsolidated under the effective confining stresses at which the shear tests were started (S21 to S23) or the specimens were restressed back to 6 MPa and then pressure was adjusted to create the initial conditions of the shear tests (S19 and S20). In both types of tests, permeability measurements were similar at the same water porosity. In general, the plots of permeability change versus water porosity change for shear tests are a continuation of the isotropic unloading test results.

The other observation, also supporting the hypothesis that errors in permeability estimation were not large, is that there were no differences in the slopes of test plots in Figure 5.11 that could be clearly attributed to the amount of bitumen removed from individual specimens. The differences in the slopes of plots in the initial stages of testing resulted rather from differences in fines content and the mode of their distribution.

Table D.1 Bitumen Mobility Analysis

Specimen	S19	S20	S21	S22	S23
Displaced bitumen found in (g):					
Upper porous stone	0.87	0.51	0.67	0.59	0.29
Lower porous stone	0.28	0.20	0.03	0.04	0.04
On the top cap	0.10	0.19	0.03	0.04	0.00
Total amount of displaced bitumen (g):	1.25	0.90	0.73	0.67	0.30
Bitumen contained initially in specimens (g):	13.3	12.6	13.9	14.7	13
Initial bitumen porosity (%):	27.3	26.6	29.1	28.7	28.4
Percent of displaced bitumen:	9.4	7.2	5.3	4.5	2.3
Initial water permeability (μm^2):	$21 \cdot 10^{-5}$	$0.53 \cdot 10^{-5}$	$7.4 \cdot 10^{-5}$	$1.0 \cdot 10^{-5}$	$5.3 \cdot 10^{-5}$
Flow rate (cm^3/hr):	1.5	0.046	0.43	0.14	0.6
Max. pressure drop across specimen (kPa):	103	124	81	185	153
Total duration of flow (hr):	50	94	69	67	59
Mode of fines distribution:	shale fragments 	lenses of shale 	shale fragments 	silt+mica layers 	silt+mica layers 

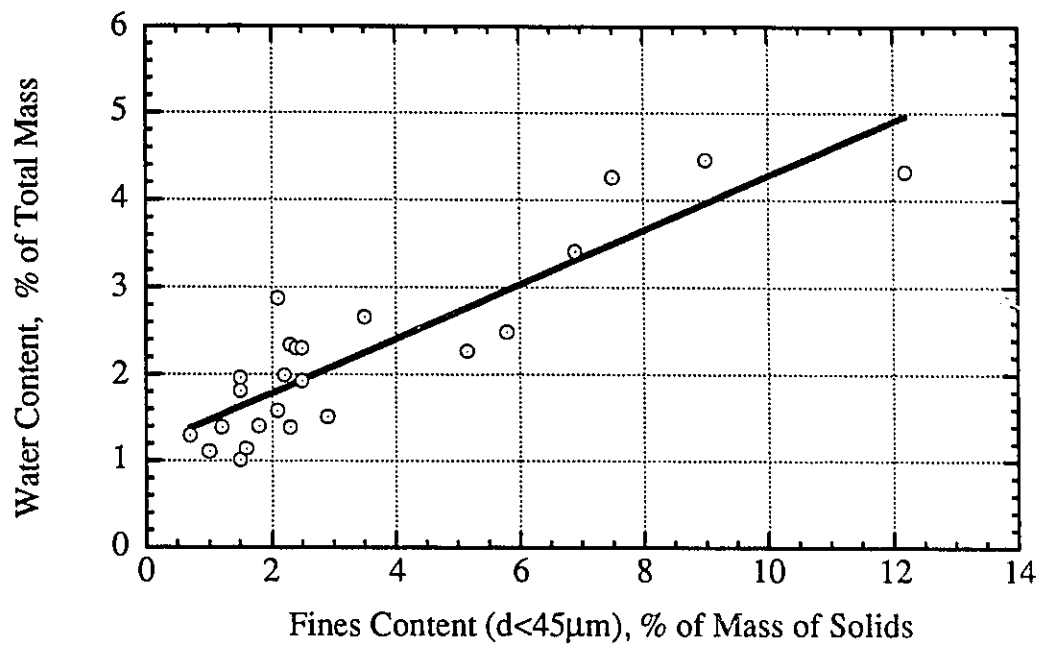


Figure D.1 Relationship Between Water Content and Amount of Fines Measured on Trimmings

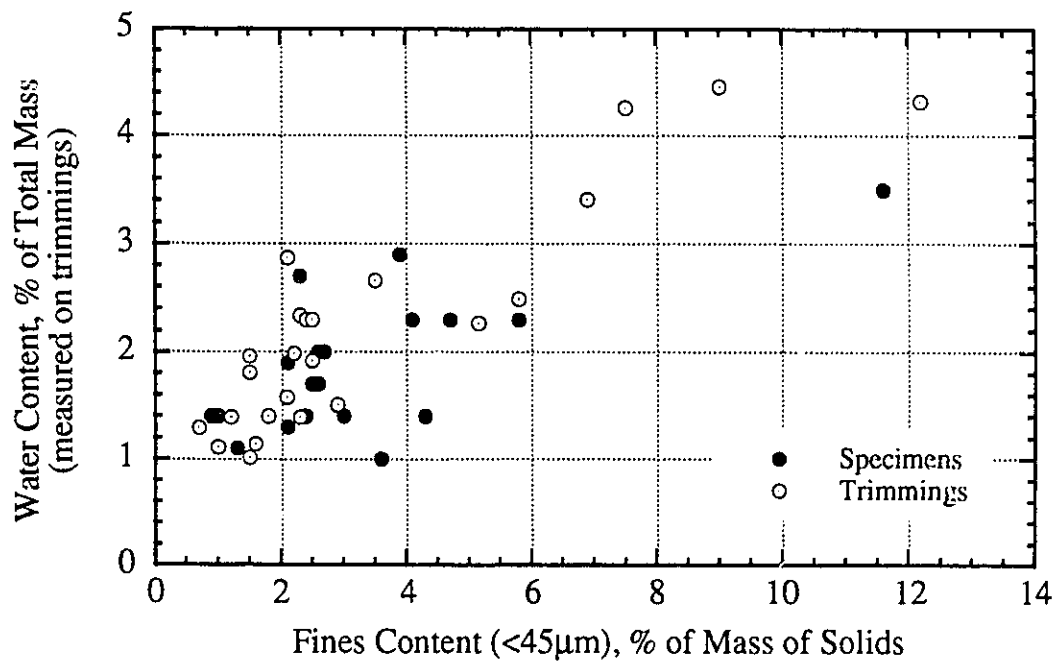


Figure D.2 Comparison of Amount of Fines Measured on Trimmings and Specimens

APPENDIX E**Compression Curves for Specimens S19 to S23**

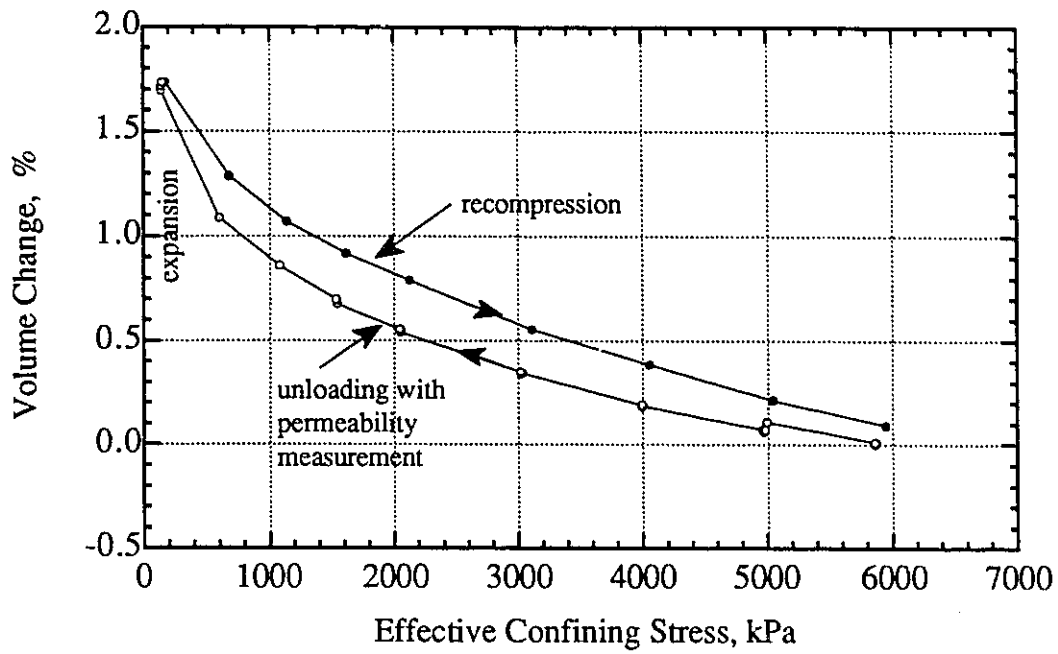


Figure E.1 Isotropic Unloading and Recompression, Specimen S19

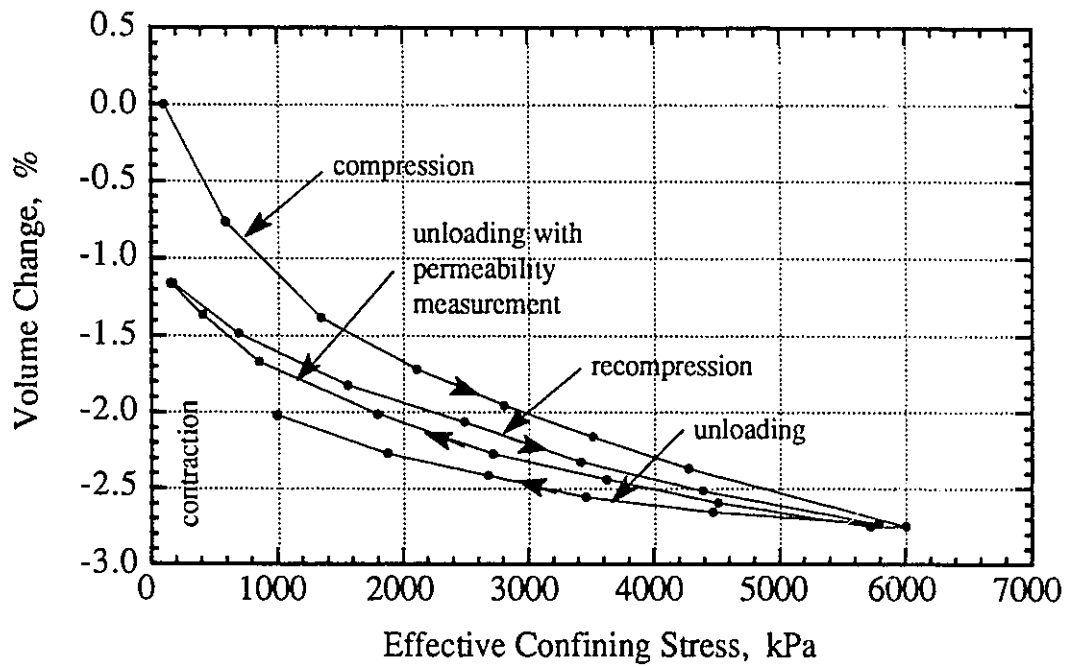


Figure E.2 Isotropic Compression and Unloading, Specimen S20

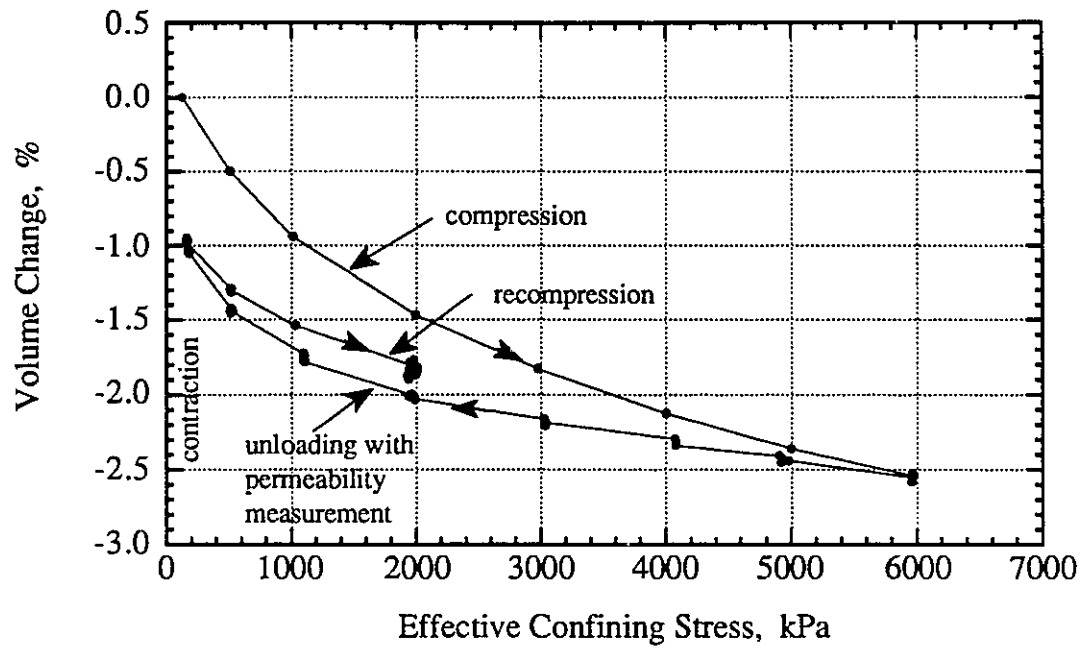


Figure E.3 Isotropic Compression and Unloading, Specimen S21

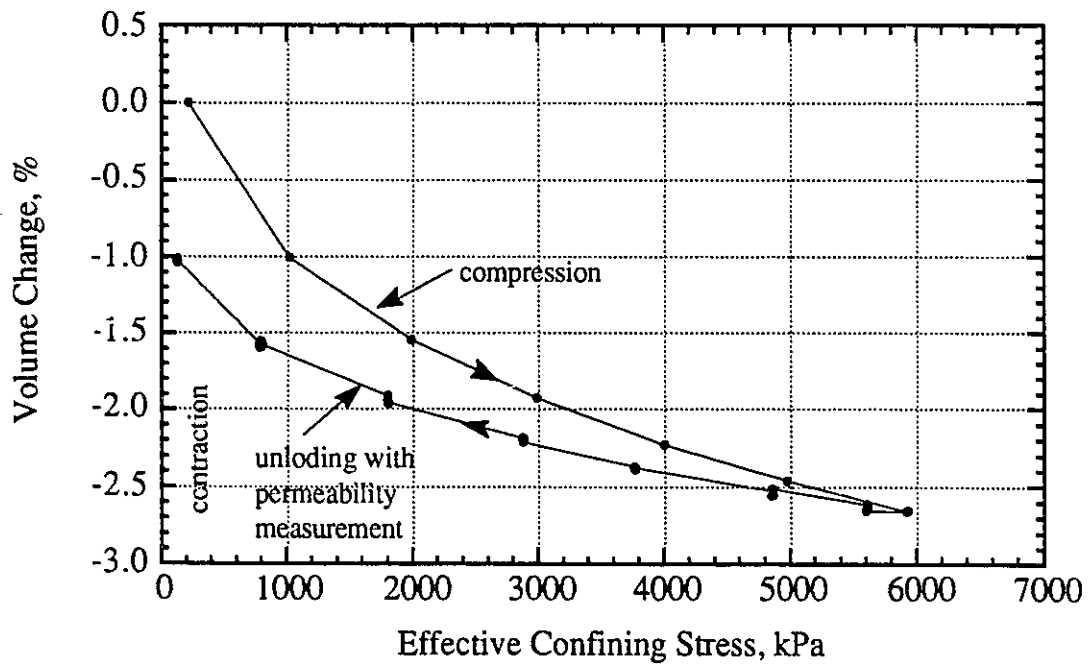


Figure E.4 Isotropic Compression and Unloading, Specimen S22

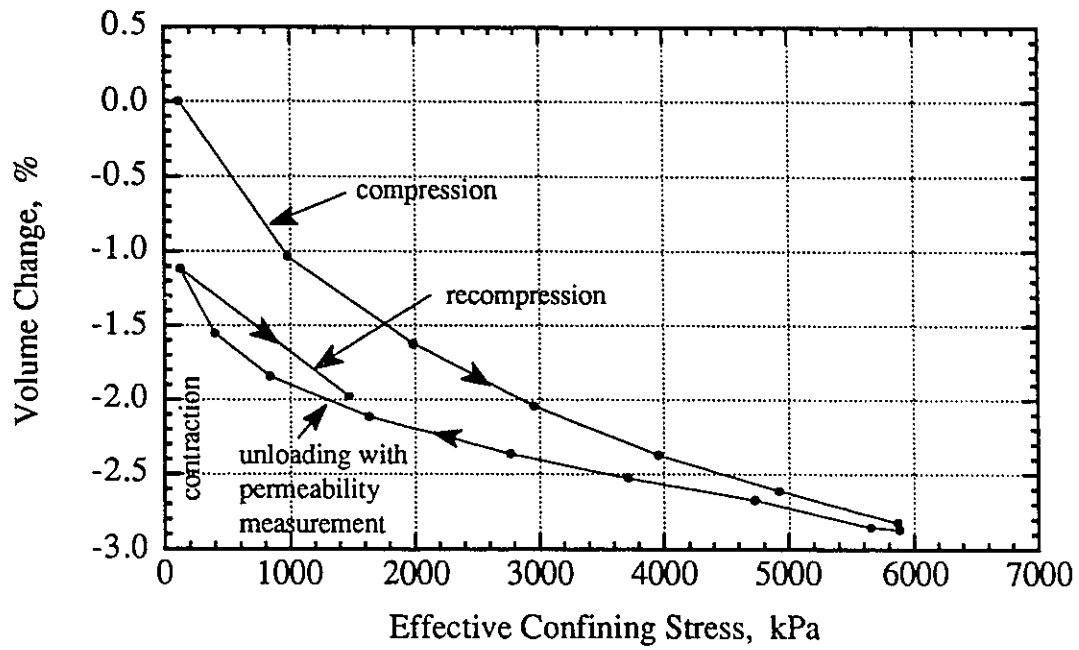


Figure E.5 Isotropic Compression and Unloading,
Specimen S23

APPENDIX F

Grain Size Analysis

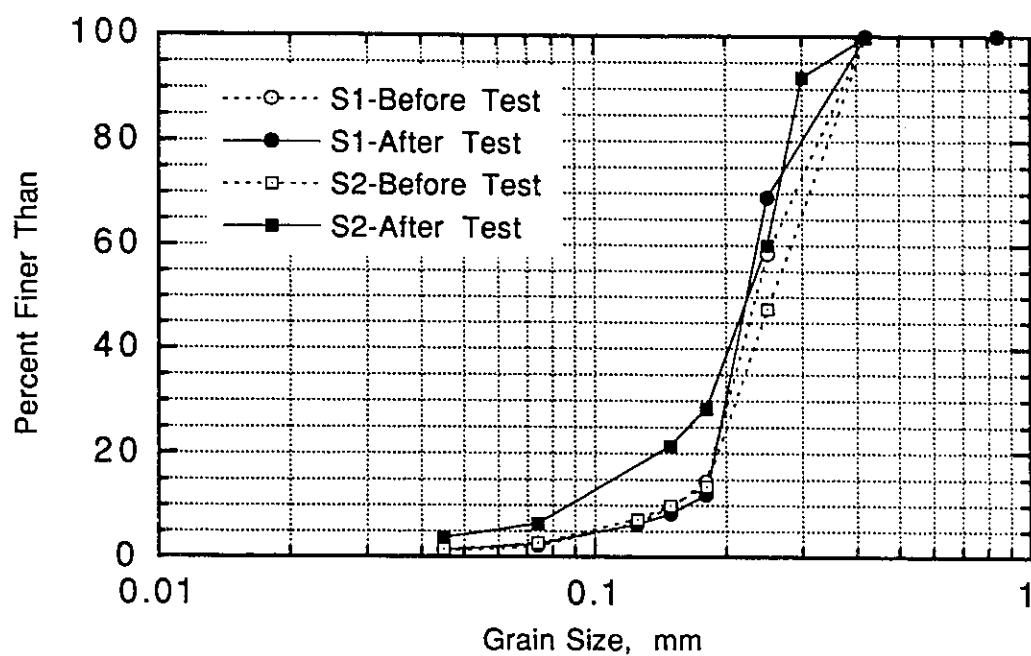


Figure F.1 Grain Size Distribution-Specimens S1 and S2

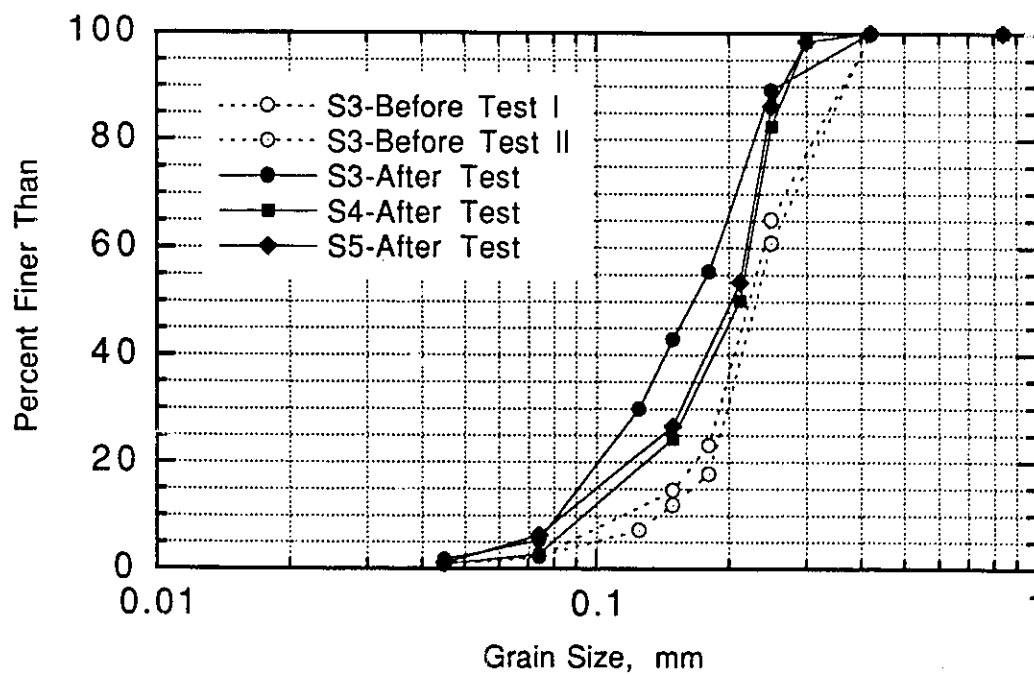


Figure F.2 Grain Size Distribution-Specimens S3-S5

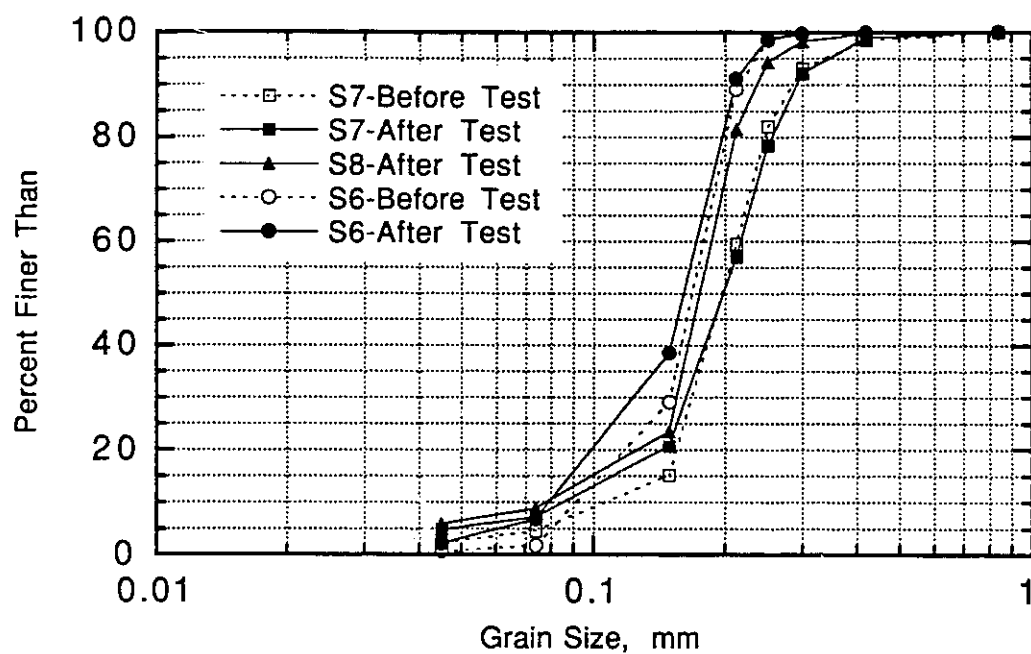


Figure F.3 Grain Size Distribution-Specimens S6-S8

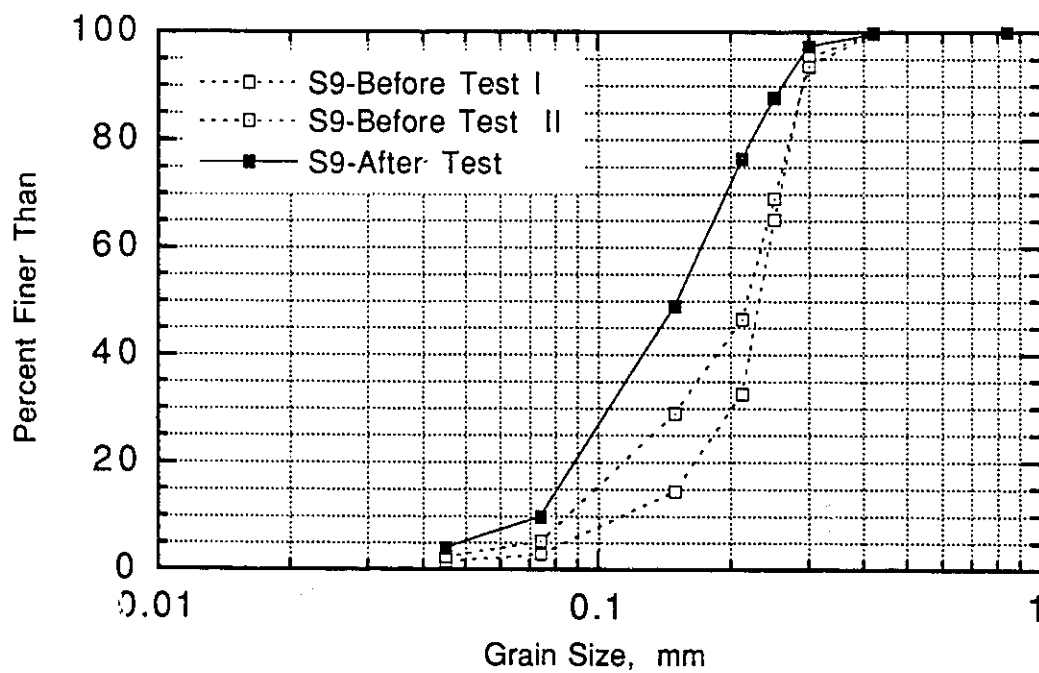


Figure F.4 Grain Size Distribution-Specimen S9

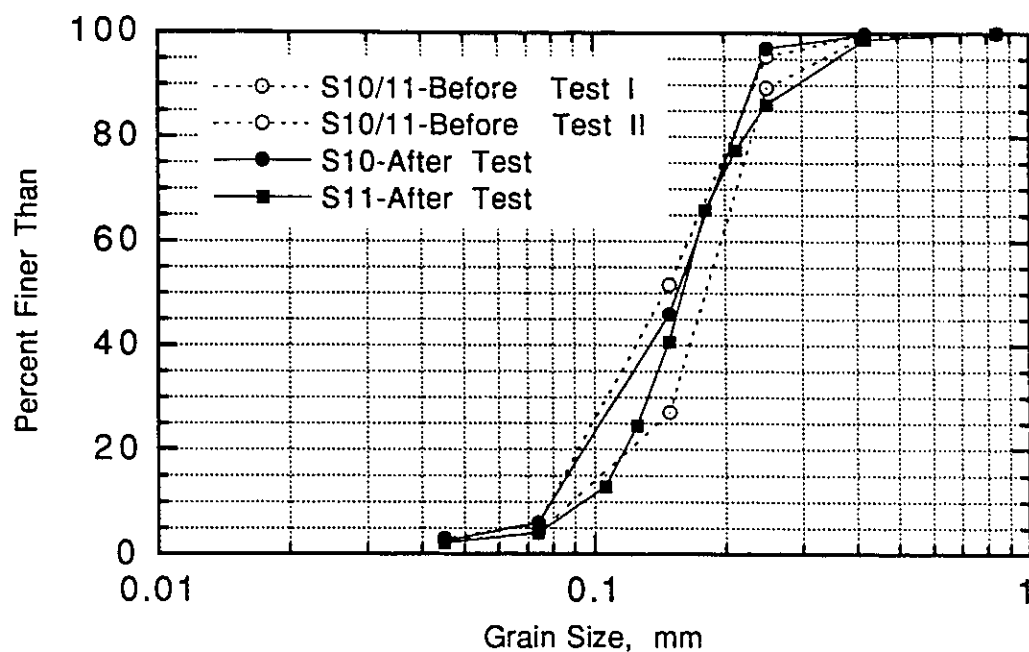


Figure F.5 Grain Size Distribution-Specimens S10 and S11

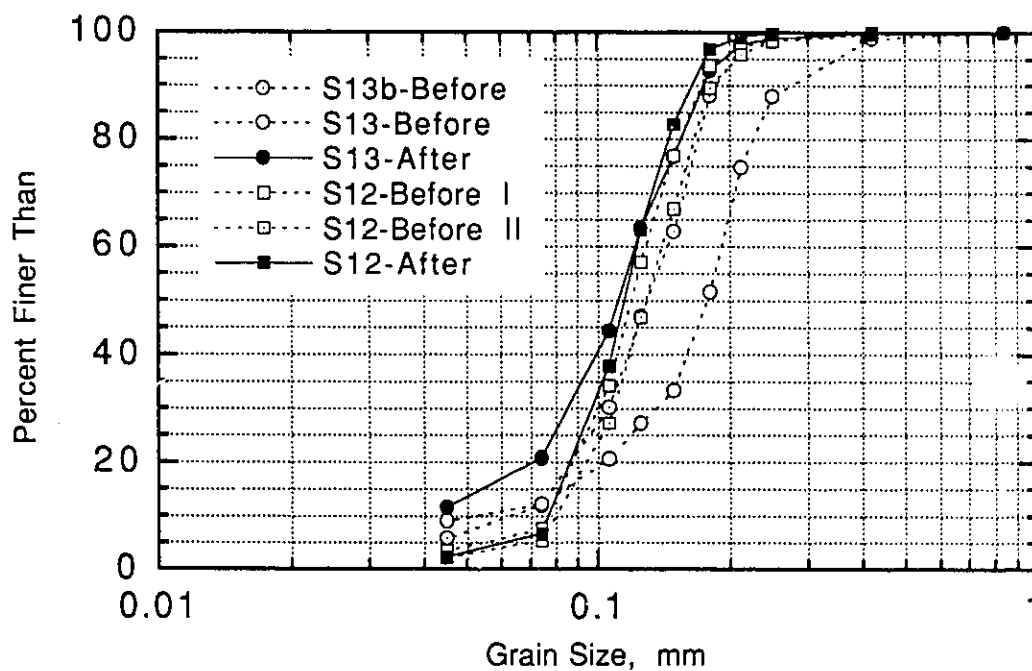


Figure F.6 Grain Size Distribution-Specimens S12 and S13

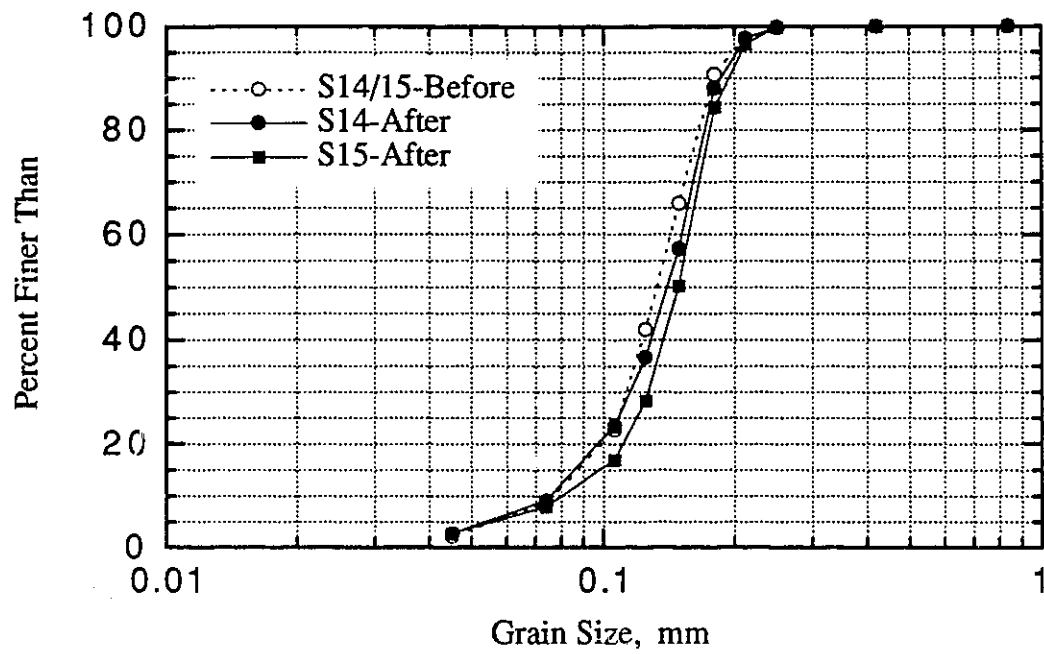


Figure F.7 Grain Size Distribution-Specimens S14-S15

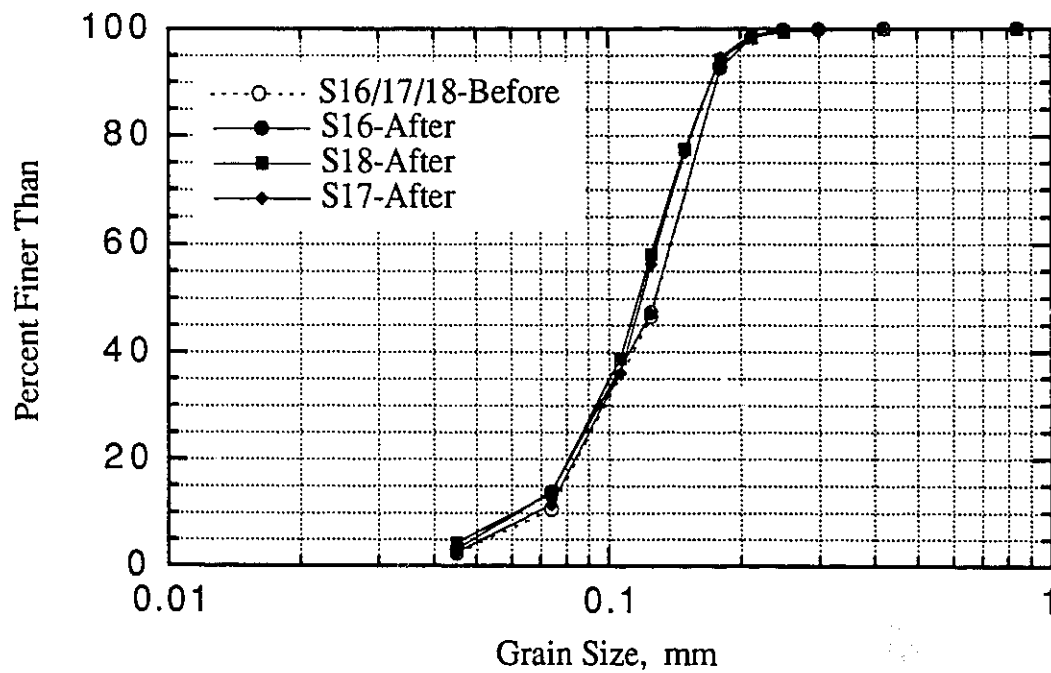


Figure F.8 Grain Size Distribution-Specimens S16-S18

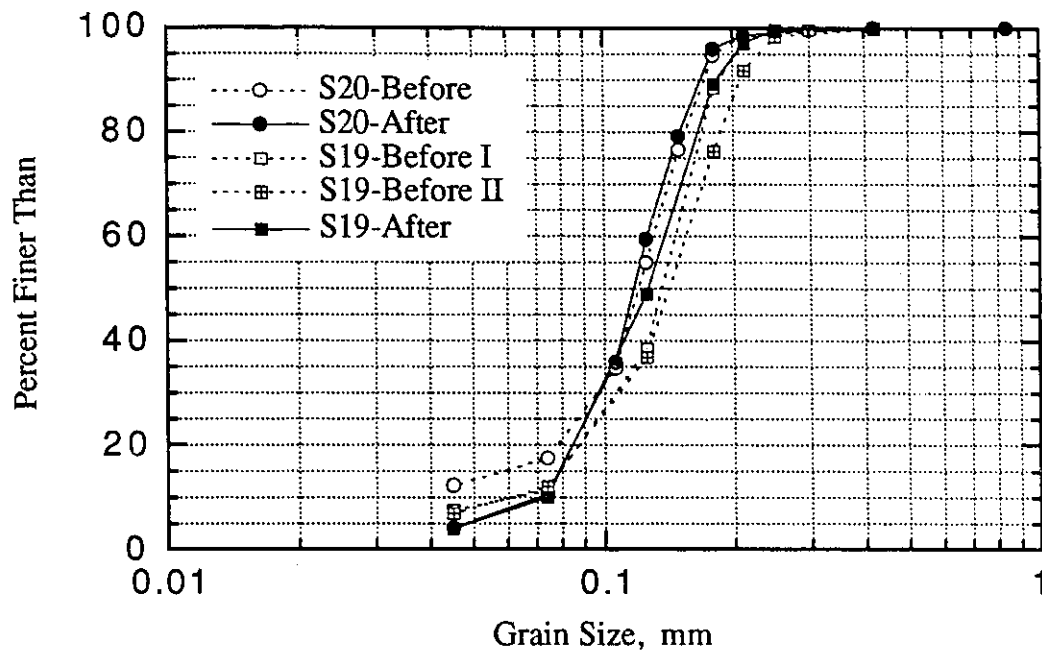


Figure F.9 Grain Size Distribution-Specimens S19 and S20

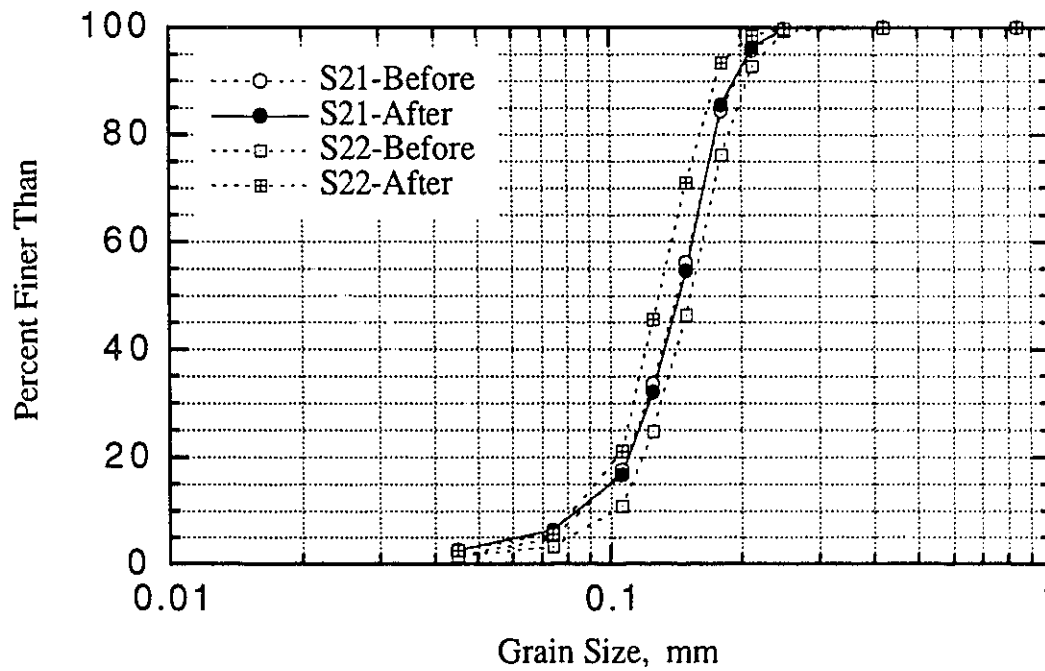


Figure F.10 Grain Size Distribution-Specimens S21 and S22

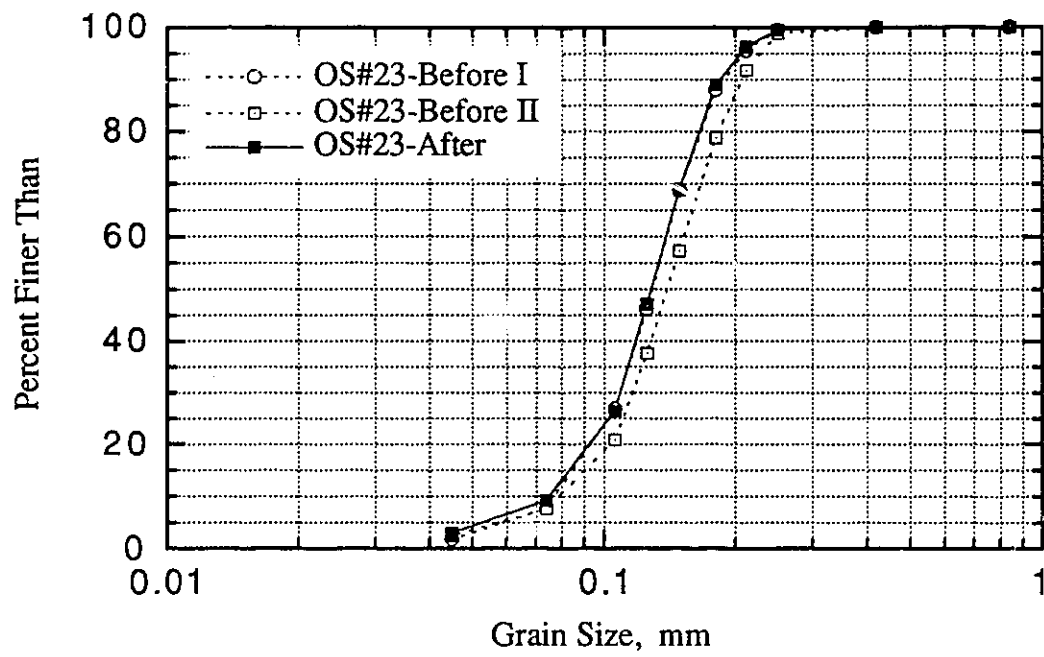


Figure F.11 Grain Size Distribution-Specimen, S23